State of Florida
Department of Transportation

Submitted by the
TEXAS A&M TRANSPORTATION INSTITUTE
In cooperation with
UNIVERSIDAD DE LOS ANDES

UNDERSTANDING MECHANISMS OF RAVELING TO EXTEND OPEN GRADED FRICTION COURSE (OGFC) SERVICE LIFE

BDR74–977–04

FINAL REPORT

Texas A&M Transportation Institute

March 2016

DISCLAIMER

The opinions, findings, and conclusions expressed in this publication are those of the authors and not necessarily those of the State of Florida Department of Transportation.

CONVERSION TABLE

SYMBOL	WHEN YOU KNOW	MULTIPLY BY	TO FIND	SYMBOL
LENGTH				
mm	millimeters	0.039	inches	in
m	meters	3.28	feet	ft
m	meters	1.09	yards	yd
km	kilometers	0.621	miles	mi

SYMBOL	WHEN YOU KNOW	MULTIPLY BY	TO FIND	SYMBOL
AREA				
mm^2	square millimeters	0.0016	square inches	in^2
m^2	square meters	10.764	square feet	ft^2
m^2	square meters	1.195	square yards	yd^2
ha	hectares	2.47	acres	ac
km^2	square kilometers	0.386	square miles	mi^2

SYMBOL	WHEN YOU KNOW	MULTIPLY BY	TO FIND	SYMBOL
VOLUME				
mL	milliliters	0.034	fluid ounces	fl oz
L	liters	0.264	gallons	gal
m^3	cubic meters	35.314	cubic feet	ft^3
m^3	cubic meters	1.307	cubic yards	yd^3

SYMBOL	WHEN YOU KNOW	MULTIPLY BY	TO FIND	SYMBOL
MASS				
g	grams	0.035	ounces	oz
kg	kilograms	2.202	pounds	lb
Mg (or "t")	megagrams (or "metric ton")	1.103	short tons (2000 lb)	T

SYMBOL	WHEN YOU KNOW	MULTIPLY BY	TO FIND	SYMBOL
TEMPERATURE (exact degrees)				
°C	Celsius	1.8C+32	Fahrenheit	°F

SYMBOL	WHEN YOU KNOW	MULTIPLY BY	TO FIND	SYMBOL
ILLUMINATION				
lx	lux	0.0929	foot-candles	fc
cd/m^2	$candela/m^2$	0.2919	foot-Lamberts	fl

SYMBOL	WHEN YOU KNOW	MULTIPLY BY	TO FIND	SYMBOL
FORCE and PRESSURE or STRESS				
N	newtons	0.225	poundforce	lbf
kPa	kilopascals	0.145	poundforce per square inch	lbf/in^2

Technical Report Documentation Page

1. Report No.	2. Government Accession No.	3. Recipient's Catalog No.
4. Title and Subtitle Understanding Mechanisms of Raveling to Extend Open Graded Friction Course (OGFC) Service Life		5. Report Date March 2016
		6. Performing Organization Code
7. Author(s) Edith Arámbula-Mercado, Ryan A. Hill, Silvia Caro, Laura Manrique, Eun Sug Park, Emmanuel Fernando		8. Performing Organization Report No.
9. Performing Organization Name and Address Texas A&M Transportation Institute 3135 TAMU College Station, TX 77843		10. Work Unit No. (TRAIS)
		11. Contract or Grant No. BDR74–977–04
12. Sponsoring Agency Name and Address Florida Department of Transportation 605 Suwannee Street, MS 30 Tallahassee, FL 32399		13. Type of Report and Period Covered Final Report 4/14/2014 – 3/31/2016
		14. Sponsoring Agency Code
15. Supplementary Notes		

16. Abstract

To understand the mechanisms of raveling in open graded friction course (OGFC) mixtures, this project was divided into experimental measurements and finite element (FE) modeling. For the experimental part, mixtures with good and poor field performance with respect to raveling were selected and some variations were added. A field visit and forensic analysis of cores obtained from the corresponding field projects revealed poor drainability, lower binder content, and finer gradation than the mix design requirements. The aggregates and binders were characterized using standard and advanced techniques to determine their propensity to raveling. The six mixtures included in the study were also characterized in the laboratory using permeability, Cantabro loss, indirect tensile (IDT) strength, and Hamburg wheel tracking test. The Cantabro loss test was the best predictor of the durability of the mixtures when compared to observed field performance. AASHTO T 283 and the moisture induced stress tester (MIST) device were used to evaluate the effect of moisture on the mixtures' IDT strength and Cantabro loss. All mixtures showed minimal impact from the conditioning protocols, especially MIST conditioning.

A finite element numerical model was also developed to better identify the mechanisms associated with the initiation and progression of raveling in OGFC. The two-dimensional model consisted of a moving wheel load passing over a typical OGFC layer on top of a regular pavement structure. The OGFC was modeled using microstructures obtained with X-ray computed tomography techniques. Various parameters related to the OGFC mixture (i.e., internal factors) and to climatic, traffic, and pavement conditions (i.e., external factors) were evaluated. The results were analyzed using probabilistic principles and suggested that the most relevant mixture-related factors increasing the chances of raveling are binder content and air void content. Extreme temperatures, high traffic loads, and slow speed vehicles were also identified as detrimental, while the structural capacity of the pavement located underneath the OGFC was identified as the least significant parameter in promoting raveling.

17. Key Word	18. Distribution Statement
Open Graded Friction Course, OGFC, Permeable Friction Course, PFC, X-ray Computed Tomography, Finite Element, Numerical Modeling, Pavement Performance, Moisture Susceptibility, Raveling	No restrictions

19. Security Classif. (of this report)	20. Security Classif. (of this page)	21. No. of Pages	22. Price
	Unclassified	250	

Form DOT F 1700.7 (8-72) Reproduction of completed page authorized

ACKNOWLEDGMENTS

The authors would like to thank Sungho Kim and Tanya Nash from the Florida Department of Transportation for their guidance and support throughout the execution of this project. Gratitude is also extended to Rick Canatella, research technician, Fan Yin, graduate assistant, and Katherine E. Klentzman, Jonathan M. Chiou, and Javier de la Cerda, student workers, for their help in laboratory-related activities. The authors would also like to acknowledge the creativeness and persistence of Daniel Y. Carrizosa on the acquisition and processing of the X-ray computed tomography images. Finally, Arif Chowdhury, assistant research engineer, is gratefully acknowledged for his diligent efforts in coordinating and executing the evaluation of field sections.

EXECUTIVE SUMMARY

The objective of this project was to understand the mechanisms of raveling in open graded friction course (OGFC) mixtures by conducting experimental analysis and a two-dimensional (2D) finite element (FE) model. For the experimental component of the project, the Florida Department of Transportation (FDOT) identified two mixtures with good field performance and one mixture with poor field performance with respect to raveling. Another three mixtures were added by modifying the aggregate and binder type. Field projects on US-1 and I-75 corresponding to the good and poor performing mixtures, respectively, were visited to conduct a visual inspection, measure on-site permeability, and obtain field cores. The OGFC surface layer on both field projects was considered impermeable, with water flow values measured via permeameter of more than 5 min. A forensic evaluation on the field cores revealed that the good performing mixture had 1.3 percent lower binder content than the target value specified in the mix design, while the poor performing mixture had 1.5 percent less binder content than the mix design specification. Even though both mixtures had lower binder content as compared to the mix design requirement, the good performing mixture had higher binder content (i.e., 5.8 percent) as compared to the poor performing mixture (i.e., 4.6 percent).

The component materials used in the selected mixtures (Martin Marietta granite, White Rock Quarries limestone, performance grade [PG] styrene-butadiene-styrene [SBS] modified PG 76-22 or polymer modified asphalt with and without antistrip agent, and asphalt rubber PG 76-22 or asphalt rubber binder with and without antistrip agent) were facilitated by FDOT and characterized per traditional and novel test methods. For the aggregates, the bulk specific gravity, Los Angeles abrasion, water absorption, and insoluble residue were provided by FDOT. In addition, the Aggregate Image Measurement System was used to determine form, texture, and angularity, and the Universal Sorption Device was used to measure the surface free energy (SFE) components of the granite and limestone aggregates. For the binder, PG verification, master curves, and Glover-Rowe parameter were obtained via rheological testing. In addition, the Wilhelmy Plate was used to estimate the SFE components. Several of these properties were used in the FE model.

The mixtures were also characterized in the laboratory by preparing Superpave gyratory compactor (SGC) specimens to a target air void (AV) content of 20 ± 2 percent. The AV content was measured via dimensional analysis. A washed sieve analysis was done first to account for differences in the current gradation of the aggregates and the one specified in the mix design. Adjustments to the specimen fabrication protocol had to be made to account for subtle but significant expansion that occurred after the specimens were extracted from the SGC molds. Various performance tests were conducted on the mixtures, including permeability, Cantabro, indirect tensile (IDT) strength, and Hamburg Wheel Tracking Test (HWTT). All mixtures had low permeability as compared to the recommended threshold of 100 m/day, and the values seemed correlated to the number of SGC gyrations required to compact the specimens. The granite mixtures required more compaction effort to achieve the target AV and showed lower values of permeability as compared to the limestone mixtures. HWTT results indicated that all six asphalt mixtures never reached the stripping number, which is the change in curvature in the rut depth versus load cycle curve, and thus, according to this test, were likely not susceptible to moisture damage. Cantabro loss was the only test able to differentiate the mixtures according to observed field performance.

Two conditioning protocols were used to evaluate the effect of moisture on the mixture's IDT strength and Cantabro loss: (a) modified Lottman per American Association of State and Highway Transportation Officials (AASHTO) T 283, and (b) moisture induced stress tester (MIST) per American Society for Testing and Materials (ASTM) D7870. AASHTO T 283 was performed with the modifications outlined in AASHTO PP 77-14, which recommends one freeze/thaw cycle after subjecting the specimens to vacuum for 10 min without regard of the degree of saturation. MIST conditioning was done using 1,000 cycles, 40 psi pressure, and a water temperature of 60°C. After conditioning, specimens were air dried for 48–72 hr and subjected to CoreDry to ensure all free moisture had been removed before performance testing. The experimental results from the IDT and Cantabro loss tests showed that the moisture conditioning protocols did not produce the desired level of moisture damage. Based on a statistical analysis of variance, the mixtures were more sensitive to the AASHTO T 283 conditioning protocol as opposed to the MIST protocol, but still, several of the mixtures resulted in equivalent or larger values of IDT strength and equivalent or lower values of Cantabro loss after conditioning, which is opposite to the expected behavior. A small study was conducted varying the MIST test parameters and the drying of the mixtures after conditioning. It was apparent that testing the specimens soon after conditioning (without air dry and CoreDry procedures) had a significant effect on the moisture susceptibility of the mixture. In general, the six mixtures that were evaluated demonstrated adequate moisture resistance in the laboratory, and further investigation to develop adequate moisture conditioning methods or adjust the protocols of existing methods to FDOT OGFC mixtures was recommended.

The experimental results and field observations were complemented with the design and implementation of a 2D FE model of raveling in OGFC. The objective of this model was to identify mechanisms associated with the initiation and progression of raveling, as well as to quantify the relative impact of different factors in raising the tendency of OGFC to this distress.

The FE model was developed in the commercial software Abaqus® and consisted of a pavement structure composed of three layers: (a) an OGFC, (b) an equivalent base layer that represents all the layers of the structure, and (c) a subgrade. While the OGFC was modeled using micromechanics principles (i.e., the actual microstructure of the layer was considered), the other two layers were assumed to be a continuum media with linear elastic material properties. The microstructures of the OGFC were obtained through X-ray computed tomography and image analysis techniques on compacted specimens representing two of the mixtures evaluated. The images were used to extract segments that represented the thin OGFC layers in the pavement model. These segments were fully characterized in terms of the number and length of their stone-on-stone contacts.

In the model, the OGFC had three constitutive phases: (a) aggregates, (b) air voids, and (c) mastic (i.e., binder and filler). All aggregates were assumed to be coated by a thin layer of mastic material. The thickness of this layer was determined based on the binder content of each mixture. The FE pavement structure was subjected to the pass of a wheel load, and the mechanical processes occurring in the mastic material located at contact or stone-on-stone areas were analyzed.

The sensitivity of different internal and external factors to the propensity of the OGFC to initiate raveling was evaluated through 82 different simulations. In each simulation, internal or external factors of the OGFC were modified. The internal factors included the combination of materials (i.e., type of mixture), the OGFC binder content, the total AV content of the mixture, and the thickness of the OGFC layer. The external factors included the structural capacity of the pavement beneath the OGFC, the pavement temperature, the magnitude and speed of the wheel load traveling on the OGFC layer, the longitudinal forces that exist at the vehicle-pavement contact, and the presence of moisture diffusion processes and pore pressure.

Probabilistic principles were used to quantify the extreme values of stresses and strains associated with Mode I and Mode II of failure (i.e., opening and shear modes of failure) at each stone-on-stone contact. These values were used to define a raveling index that permitted researchers to quantify the propensity of each contact to fracture or raveling. Additionally, some further simulations were conducted using the Cohesive Zone Modeling (CZM) theory to evaluate actual fracture processes occurring in the mixtures after the binder had suffered oxidative hardening.

The results obtained from the simulations demonstrated that raveling is a mechanical phenomenon that occurs with higher probability under a Mode I (opening mode) of failure. Therefore, the mechanical properties of the individual constitutive phases of the mixture and their structural capacity, represented by the quality of the mixture's internal microstructure (i.e., number and length of stone-on-stone contacts, AV content, and mastic thickness), are critical in determining the resistance of an OGFC to raveling. Besides, it was observed that the structural capacity is affected by an increase in the total AV content of the mixture. An increase in pavement temperature and the presence of moisture were also observed to raise the mixture's susceptibility to raveling. In this sense, the use of antistripping materials seems to be an adequate strategy to obtain durable OGFC mixtures. Also, it was proved that pore pressure under saturated undrained conditions (i.e., when the mixture is clogged) could also impact the durability of the mixture. In terms of the effect of traffic conditions, the results suggest that the durability of OGFC could be compromised when used in low or low-medium speed roads, in areas where vehicles have to brake frequently, or in roads subjected to the effects of unusually high axle loads. The results of the impact of the OGFC thickness on the durability of the mixture were not conclusive, so simulations with more geometries to better understand the influence of this parameter are recommended. Finally, the results from the simulations that included CZM techniques showed that although initially one of the mixtures was more prone to raveling, under aged conditions, both mixtures had equivalent raveling susceptibility.

TABLE OF CONTENTS

LIST OF FIGURES

LIST OF TABLES

LIST OF ABBREVIATIONS AND ACRONYMS

2D	Two-dimensional
3D	Three-dimensional
AASHTO	American Association of State Highway and Transportation Officials
AIMS	Aggregate Image Measurement System
ANOVA	Analysis of Variance
ARB	Asphalt Rubber Binder
ASTM	American Society for Testing and Materials
AV	Air Voids
AC	Asphalt Content
CAPA	Computer Aided Pavement Analysis
CT	Computed Tomography
CZM	Cohesive Zone Modeling
DSR	Dynamic Shear Rheometer
ESAL	Equivalent Single Axle Load
FC	Friction Course
FDOT	Florida Department of Transportation
FE	Finite Element
FHWA	Federal Highway Administration
FIU	Florida International University
FM	Florida Method
GDOT	Georgia Department of Transportation
G-R	Glover-Rowe
HMA	Hot-Mix Asphalt
HSD	Honest Significant Differences
HWTT	Hamburg Wheel Tracking Test
IDT	Indirect Tensile
IRI	International Roughness Index
JMF	Job Mix Formula
LC_{SN}	Load Cycles to Stripping Number
LOT	Lifetime Optimization Tool
LSM	Least Squares Means
MIST	Moisture Induced Stress Tester
MDOT	Mississippi Department of Transportation
NCAT	National Center for Asphalt Technology
NCHRP	National Cooperative Highway Research Program
NMAS	Nominal Maximum Aggregate Size
OBC	Optimum Binder Content
OGFC	Open Graded Friction Course
PA	Porous Asphalt
PAV	Pressure Aging Vessel
PCC	Portland Cement Concrete
PCS	Pavement Condition Survey
PFC	Permeable Friction Course
PG	Performance Grade
PGA	Porous Graded Asphalt
PMA	Polymer Modified Asphalt
PMS	Pavement Management System
RH	Relative Humidity
R.I.	Raveling Index
RTFO	Rolling Thin Film Oven
SBR	Styrene-Butadiene-Rubber
SBS	Styrene-Butadiene-Styrene
SFE	Surface Free Energy
SGC	Superpave Gyratory Compactor
SMA	Stone Matrix Asphalt
SMO	State Materials Office
SN	Stripping Number
STOA	Short-Term Oven Aging
TSR	Tensile Strength Ratio
TxDOT	Texas Department of Transportation
USD	Universal Sorption Device
VMA	Voids in the Mineral Aggregate
WFV	Water Flow Value
WP	Wilhelmy Plate

CHAPTER 1 . INTRODUCTION

The objective of this project was to understand the mechanisms of raveling in open graded friction course (OGFC) mixtures. Mechanisms in this context are defined as any process that modifies the internal and/or external condition of the OGFC mixture and that can lead to a change in the original properties of the material. Raveling of asphalt mixtures is a complex phenomenon involving various physical, chemical, and mechanical processes, which occur at different rates and magnitudes. Physical and chemical properties of the individual materials as well as the characteristics of the mixture and other external factors such as the environment and traffic conditions play a key role in the expected performance of the mixture. In addition, when moisture is present in the microstructure, the mechanisms by which it interacts with the microstructure of the mixture and other factors usually compound or accelerate the onset and progression of raveling.

The first step in the execution of this project was to conduct a literature review, which is summarized in Chapter 2. The topics explored as part of this effort included national and international experience and specifications for OGFC, recent Florida Department of Transportation (FDOT) research and performance monitoring for OGFC, and numerical modeling of raveling.

Afterwards, with the help of FDOT, several mixtures were selected based on their observed field performance. A total of six mixtures were considered. Two good performing and one poor performing mixture with respect to raveling as reported by FDOT project BDV29-820-1, "FC-5 Raveling Study," were selected, and a modified version of the poor performing mixture was added, employing the same aggregate gradation but different binder type. In addition, a granite mixture listed in FDOT project BDS15 977-01, "Evaluate the Contribution of the Mixture Components on the Longevity and Performance of FC-5," was included, along with a modified version that included the same aggregate gradation but a different binder type. FDOT project BDS15 977-01 did not present field performance information for the granite mixtures. The good and poor performing mixtures with respect to raveling reported in FDOT project BDV29-820-1 correspond to field projects on US-1 and I-75, respectively, located in south Florida. Site visits to these field projects were done in October 2015 to conduct a visual inspection, measure on-site permeability, and obtain cores. The cores were used to perform a forensic analysis to help understand the observed field performance. Details of all mixtures and field projects are presented in Chapter 3.

Chapters 4 and 5 document the material and mixture characterization, including properties of the aggregate and binders, details of laboratory mixture specimen preparation, volumetrics, and moisture conditioning. Various performance tests were conducted to characterize the mixtures, including permeability per Florida Method (FM) 5-565, Cantabro abrasion loss per American Association of State and Highway Transportation Officials (AASHTO) TP 108, indirect tensile (IDT) strength per AASHTO T 283, and Hamburg wheel tracking test (HWTT) per AASHTO T 324. Specifics of the performance of the six mixtures are included in Chapter 5 along with a summary of the laboratory test results and correlation to observed field performance.

The numerical finite element (FE) model described in Chapter 6 allowed performing a comprehensive evaluation of the impact of internal and external factors on the likelihood of raveling in OGFC mixtures. As part of the literature review, it was determined that existing numerical models had made significant progress in understanding the micromechanical interaction within OGFC mixtures. Nevertheless, no numerical model had studied the micromechanical behavior of OGFC mixtures under repeated loads and the explicit presence of moisture using a realistic geometry. Therefore, the modeling approach used in this project included several novel and critical aspects that have not been considered in previous numerical studies. As detailed in Chapter 6, the FE model used actual images of the internal structure of OGFC mixtures and focused on the critical areas where raveling is expected to occur. The modeling approach also analyzed the influence of water diffusion (moisture damage) and pore pressure on the susceptibility of the OGFC mixture to undergo raveling. This is a crucial aspect since water is usually present in OGFC pavements and it is well known that it could degrade the adhesive and cohesive properties of the binder. The model was developed using commercial FE software Abaqus®, which will allow FDOT to easily reproduce the models or continue their development in the future.

Finally, conclusions and recommendations from the materials and mixture characterization and numerical modeling efforts are listed in Chapter 7.

CHAPTER 2 . LITERATURE REVIEW

OGFC pavements (also commonly called porous graded asphalt [PGA], porous asphalt [PA], or permeable friction course [PFC] pavements) are used to provide safety and environmental benefits. Compared to other types of surface mixtures, OGFCs have higher air void (AV) content (above 18 percent), higher binder content, and stiffer modified binders with or without additives (Cooley et al. 2009). The resulting OGFC surface layer yields the following benefits (Brown 1973; Ruiz et al. 1990; Khalid and Pérez 1996; Button et al. 2004; Kearfott et al. 2005):

- Reductions in:
  - Hydroplaning.
  - Wet-weather splash and spray.
  - Tire/pavement noise level.
  - Glare at night and in wet weather.
  - Pollutants in storm water runoff.
  - Number of wet-weather accidents, injuries, and fatalities.
- Improvements in:
  - Wet skid resistance.
  - Ride quality and vehicle handling.
  - Pavement marking visibility.

The performance of OGFC is often expressed in terms of durability and functionality. The benefits listed above result from the functionality of the PGA mixture, which mainly stems from the higher AV content in the mixture and thus increased permeability. The reduced tire/pavement noise level also depends on the aggregate gradation and binder type. Table 2-1 presents a comparison of different pavement surface materials with respect to the average noise level generated at the tire/pavement interface of a conventional dense-graded hot-mix asphalt (HMA) mixture.

Table 2-1. Average Comparative Noise Levels of Different Surface Mixtures (Kandhal 2004)

Mixture Type	Relative Noise Level, dB(a)
Open Graded Friction Course	−4
Stone Matrix Asphalt (SMA)	−2
Dense-Graded HMA	0 (reference)
Portland Cement Concrete (PCC)[a]	+3

[a] PCC noise level is likely to be significantly higher if PCC has transverse grooves or tinning.

The durability of OGFC pavements relates to the resistance of the surface mixture to distress/failure. One disadvantage associated with the use of OGFC is the reduced expected service life, ranging between 6−12 years versus about 12−18 years for a dense-graded HMA. The typical OGFC service life reported by the Transport Research Laboratory for a traffic level of 4000 commercial vehicles per lane, per day, is about 12 years (Yildirim et al., 2007). Table 2-2 lists the typical service life of various OGFC and PA mixtures according to various references.

Table 2-2. Typical Service Life of Open Graded Friction Course and Porous Asphalt Pavements (Alvarez et al. 2006)

Typical Service Life (years)	Type of Mixture	Country	Reference
8 or more	OGFC	United States	Mallick et al. (2000)
13	Rubber-modified OGFC (Arizona)	United States	Huber (2000)
15	OGFC (Wyoming)	United States	Huber (2000)
6 to 9	OGFC	United States	Yildirim et al. (2007)
7 to 10	Porous Asphalt	United Kingdom	Nicholls and Carswell (2001)
7	Porous Asphalt	Denmark	Nielsen et al. (2005)
8 to 12	Porous Asphalt	France	Huber (2000)
5 to 18	Porous Asphalt	Netherlands	Huurman et al. (2010b)

Raveling has been reported as the most common distress affecting OGFC mixtures (Huber 2000; Cooley et al. 2009) and thus one of the main causes impacting the durability of these types of pavements. Raveling is defined as the loss of aggregates at the surface of the pavement caused by repeated abrasion by traffic and often aggravated by the presence of moisture.

Molenaar and Molenaar (2000) identified two forms of raveling, each one caused by different mechanisms: (a) short-term raveling, and (b) long-term raveling. Short-term raveling is likely caused by intense shearing forces at the tire-pavement interface that develop within newly placed OGFC mixtures. Conditions that could enhance the potential for short-term raveling include mixture placement at low temperature, partial stone-on-stone contact achieved by the aggregates during compaction, and draindown segregation (areas where binder content is low). Long-term raveling, on the other hand, is considered a result of long-term segregation of the binder from the aggregates due to gravity. As the binder drains from the coarse aggregates under the effect of gravity, the aggregates near the surface of the layer become progressively less and less coated. The action of traffic, combined with binder oxidation and embrittlement, results in raveling. Long-term draindown of the binder occurs more frequently when unmodified, lower viscosity binders are used.

Raveling may also be compounded by poor bonding to the surface right beneath the pavement. Because of the open aggregate gradation in the OGFC mixture, there is limited aggregate surface area, which results in a relatively thick film of binder coating the aggregates and a reduced contact surface between the OGFC mixture and the underlying surface. Partial stone-on-stone contact achieved by the aggregates during construction and inadequate tack coat rates or conditions during application (e.g., dusty surface) can cause a reduction in the bond strength between the two layers. Thermal and aggregate segregation also plays a role in the development and progression of raveling in OGFC mixtures.

The type of binder used in OGFC is one of the most important factors influencing resistance to raveling. After several experiences using unmodified binders led to premature raveling degradation (e.g., in the State of Georgia; Watson, Johnson, et al. 1998), several transportation agencies and new studies reported improved durability of OGFC mixtures when using modified binders, such as tire rubber, styrene-butadiene-styrene (SBS) modified, and styrene-butadiene-rubber (SBR) modified binders (Huber 2000; Chen et al. 2013). In fact, nowadays the use of modified binders is considered standard practice in several states.

Raveling in OGFC pavements progresses rapidly and accelerates the appearance of other distresses that reduce the overall service condition of the pavement, increase the cost of maintenance, and reduce the road network capacity and serviceability (Alvarez et al. 2006; Mo et al. 2007; Cooley et al. 2009). In summary, raveling can be associated with the following materials, mix designs, and construction factors (California Department of Transportation [Caltrans] 2006):

- Incompatibility between binder and aggregate.
- Placement of the mixture at low ambient temperature.
- Inadequate compaction.
- Insufficient binder content.
- Early stop-and-go traffic.
- Moisture sensitivity of the mixture.
- Binder draindown.
- Binder aging.
- Binder softening generated by oil and fuel drippings.

Therefore, raveling in OGFC mixtures is a complex phenomenon depending on both the quality of the mixture components and the production and construction process. Understanding the mechanisms of raveling in OGFC pavements is necessary to formulate appropriate strategies to prevent this type of distress. The objectives of the literature review were to examine information on previous and current research and field experience focused on performance issues related to raveling of OGFC pavements and to summarize the most relevant numerical works that have been developed to better understand raveling. The review is divided into the following topics:

- National and international experience with OGFC.
- National and international specifications for OGFC.
- Recent and FDOT research studies on OGFC.
- Recent and OGFC performance monitoring in Florida.
- Numerical modeling of raveling in binder pavements.

2.1. National and International Experience with OGFC

2.1.1. National Experience

Recent research projects on the topic of porous/permeable pavements at the national level include the National Cooperative Highway Research Program (NCHRP) Project 9-41, "Performance and Maintenance of Permeable Friction Courses," and testing at the National Center for Asphalt Technology (NCAT) test track. NCHRP 9-41 includes a worldwide literature review and a survey of local and worldwide highway agencies to gather information on design, construction, maintenance, safety, performance, and use of OGFC mixtures. Its main objective was focused on recommending guidelines for design, construction, and maintenance of PFC mixtures based on the state of the practice and literature review (Cooley et al. 2009). A more detailed account of this project's recommendations is provided below.

With regard to PFC testing at NCAT, seven different PFC sections were constructed and tested at the test track, including sections W3, W4, and W5 constructed in June 2000; S4 and W8 constructed in August 2003; and N13 and S3 constructed in August and October 2006, respectively. Sections W3, N13, and S3 received approximately 10 million equivalent single axle loads (ESALs) at the termination of testing, and the remaining sections received approximately 20 million ESALs. Relevant data collected on these sections included sound pressure levels with the NCAT noise trailer, sound intensity levels, macro-texture measurements (sand patch and CT meter), skid (ASTM E274 skid numbers and dynamic friction test results), and roughness profiles (International Roughness Index [IRI]).

Section S3 corresponded to a 33 mm PFC using 100 percent gravel aggregate on top of a gravel SMA mixture built by the Mississippi DOT (MDOT). The mix utilized 6.4 percent performance grade (PG) 76-22 SBS modified binder, gravel aggregate, 1 percent lime, and 0.3 percent fibers. The 12.5 mm nominal maximum aggregate size (NMAS) PFC performed well through the third cycle (i.e., 2006–2008), and based on the good performance of the mixture, MDOT began utilizing this type of mix on several interstate highways in 2009.

Trafficking continued on section S3 during the next cycle (i.e., 2009–2011), and during that period, a steady progression of raveling was observed. The distress was more severe at the beginning portion of the section. Researchers reported the probable cause as a common construction defect with PFC, where the mixture placed first cools excessively as it comes in contact with the unheated parts of the transfer device and paver (West et al. 2012). For this reason, the first 7.6 m of every test section of the test track were excluded from the analysis due to transition effects and constructions issues. The rest of the pavement section was in better condition but still showed signs of raveling. This finding was confirmed via texture measurements, which showed a steady increase after about 10 million ESAL repetitions. The smoothness and drainability of the pavement were excellent and remained relatively constant with time.

Noise measurements were also performed on several OGFC sections of the NCAT test track using the on-board sound intensity method. Important conclusions from the observations include: (a) pavement age does not influence the noise level, and (b) the OGFC is louder at low 1/3-octave band frequencies (i.e., below 1,000 Hz) and quieter at frequencies above 1,500 Hz as compared to the other types of pavements analyzed, including fine and coarse-graded Superpave mixtures and SMA. The opposite was true for the Superpave and SMA mixtures, which had low noise levels at the low frequencies but high noise levels at the high frequencies. The higher the noise level at the high frequencies, the more bothersome the tonal noise perceived by the user.

Permeability was also measured on six OGFC sections. One section was constructed in 2003 (S4), two sections in 2006 (S3 and N13), and three sections in 2009 (N1, N2, and S8). The thickness of the lift for sections N1 and N2 was thinner (i.e., 20 mm) as compared to the other PFC sections. These mixtures showed a greater reduction in permeability over time. The use of heavier tack coat application rates did not seem to impact the permeability of the PFC. Sections N2 and S8 had the same mixture type and tack coat application rate; the only difference between them was the thickness of the lift (i.e., N2 was 20 mm and S8 was 33 mm). The thicker section was twice as permeable as the thin section, and the difference between them increased once they were subjected to traffic. The additional lift thickness helped increase and maintain the permeability of the OGFC pavement.

With reference to surface maintenance activities on OGFC pavements, according to a survey conducted as part of NCHRP Synthesis 284, there are no reports in the United States on the application of major maintenance for OGFC (Huber 2000). From 17 states that reported their use, only New Mexico, Wyoming, South Carolina, and Oregon employed fog seals to perform preventive maintenance. Although quantitative information about the significance of these treatments is not available, it is expected that fog seals extend the life of porous mixtures since they provide a small film of unaged binder at the surface (Rogge 2002). The downside is that fog seal treatments can also reduce the functionality of the OGFC pavement in terms of permeability (Huber 2000). The Federal Highway Administration (FHWA) recommends fog seal application in two passes (at a rate of 0.05 gal/yd^2 for each pass) using a 50 percent dilution of emulsion without any rejuvenating agents (FHWA 1990). Research in Oregon regarding permeability reduction and changes in pavement friction on certain PFC pavements generated by fog seals concluded that the mixtures still retained porosity and kept the rough texture related to its capability to reduce the potential for hydroplaning (Rogge 2002). However, quantitative conclusions regarding the changes in these parameters were not included. A decrease in pavement friction was noticed immediately after fog seal application, but during the first month, it increased considerably by traffic action.

2.1.2. International Experience

As in the United States, durability issues with PFC worldwide are mainly associated with raveling. In the Netherlands, over 80 percent of the highway system has some kind of PA wearing course, and more than 90 percent of the maintenance performed on these pavements is to address raveling (Van der Zwan 2011). The country has significant snowfalls and frequent freeze/thaw cycles, which aggravate the raveling problem. As a result, every year, 5–7 percent of the PFCs are replaced under standard maintenance. Several harsh winters in recent years have cause severe damage to PFCs and other types of pavements in the Netherlands. Not only the low temperature, but also the amount of moisture (snow or very wet weather prior to freezing) and the number of freeze/thaw cycles seem to be contributing factors. Recent extreme winter occurrences in in 2008–2009 and 2009–2010 caused damage in about 1.7 percent of the highway system. The roads affected were primarily the ones scheduled for maintenance the following year, and thus it was believed that part of the problem was the shifting forward of the maintenance schedule.

In other countries, the raveling issue has been minimized by introducing special laboratory tests. In Spain, a requirement of maximum Cantabro loss on wet samples was established (Ruiz et al. 1990) to prevent problems related to the use of hydrophilic fillers or binders with low adhesive bond properties.

Besides raveling, accelerated loss of permeability and noise reduction capacity due to clogging of AV are the main functional concerns for PFC pavements. A wide range of service lives has been reported in various countries. In Spain, for example, some PFCs retained their drainability for at least 9 years when subjected to medium traffic, whereas after 2 years, clogging was reported in mixtures operating under heavy traffic (Khalid and Pérez 1996). In Britain, the reduction in the suppression of noise capacity and permeability and some increase in spray levels were recognized, but the material retained its noise reduction capacity and similar performance in terms of spray generation compared to thin surfacing (Highways Agency 1999).

To assure the functional characteristics of the PFC over a longer period, certain European countries like Denmark use periodic cleaning procedures (using high-pressure water and a large vacuum machine) and the construction of a two-layer pavement system—a bottom layer of coarse PFC and a top layer of fine PFC (Thomsen et al. 2005; Van der Zwan 2011). The cleaning procedures are aimed to maintain the drainability of the pavement, while the two-layer pavement system provides greater noise reduction.

Countries that apply PFC cleaning techniques routinely also include the Netherlands and Japan. The frequency of cleaning varies among agencies. Some countries apply the function recovery concept in which cleaning activities are applied about twice per year with equipment that advances at slow speeds, applying high-pressure water and suction/removal in a single pass (Sandberg and Masuyama 2005; Thomsen et al. 2005). Other countries apply the function maintenance concept of operation with more frequent cleaning activities (i.e., every 1–2 weeks) with faster-moving equipment but achieving only partial debris removal.

In the United States, these cleaning practices on OGFC pavements have not been implemented. Local agencies assume that the material can self-clean due to action of the rolling tires at high speeds, although a recent study did not show differences between field measurements of water flow values performed on the wheel path and between the wheel paths of several field pavements (Arambula et al. 2012). In addition, it is assumed that high AV content of the mixture can ensure adequate drainage capacity for the entire service life of the pavement (Tappeiner 1993).

The Danish Road Institute performed noise measurements on thin porous pavement sections and found that noise levels could be correlated to loss of permeability and allowed for an earlier identification of clogging issues as compared to permeability tests (Bendtsen et al. 2002). Cores obtained from these pavements revealed that the clogging of the layer occurred in the upper 10–25 mm (0.39–1 inch).

There are no formal methods for determining the typical thickness of PGA surface courses. Nevertheless, some authors such as Ranieri (2002) and Cooley et al. (2009) have proposed some methodologies based on the hydraulic conductivity and the rainfall intensity of the zone of the project. Generally speaking, agencies have standard thickness values of these layers that have been defined based on experience. These values range between 20 mm and 50 mm; a summary of typical layer thickness values used worldwide is presented in Table 2-3.

Table 2-3. Typical Thickness of OGFC Surface Courses (after Stanard et al. 2007)

Country / State	Layer Thickness (mm)	Reference
Belgium	40	Van Heystraeten and Moraux (1990)
Germany	40	Stotz and Krauth (1994)
Netherlands	50	Van der Zwan et al. (1990)
Spain	40	Ruiz et al. (1990)
Switzerland	28–50	Isenring et al. (1990)
California	30.48	Caltrans (2006)
Georgia	30	Watson et al. (1998)
Mississippi	19.0–31.75	Cooley and James (2008)
New Jersey	19.0–31.75	NJDOT (2007)
Oregon	50	Moore et al. (2001)

2.2. National and International Specifications for OGFC

NCHRP Project 9-41 was conducted from 2005 to 2009 and produced NCHRP Report 640, including NCHRP Web-Only Document 138 (Cooley et al. 2009). As mentioned above, this project produced an annotated literature review and a survey of state departments of transportation (DOTs) to develop a state-of-the-practice summary on the use of permeable pavements and propose mix design, construction, maintenance, and rehabilitation guidelines to maximize advantages and minimize disadvantages associated with the use of permeable pavements. The resulting mix design recommendations are summarized in Table 2-4 along with the current specifications used by FDOT, the Texas Department of Transportation (TxDOT) and the Netherlands (TxDOT 2004; Voskuilen 2005; European Standard 2006; FDOT 2014c).

In the case of NCHRP 9-41, a balanced mix design to determine a range of optimum binder content (OBC) was suggested with draindown (AASHTO T 305) providing the upper bound and Cantabro loss (ASTM D7064/7064M) providing the lower bound. Section 337 of FDOT specifications details the requirements for asphalt concrete friction courses, including OGFC or FC-5 mixtures. The method for determining the OBC for FC-5, which is the pie-plate method, is detailed in FM 5-588. Besides the OBC determination, no other performance tests or indicators are required during the design of the FC-5 mixtures. FDOT designs all FC-5 mixtures. In the case of TxDOT, several recent research projects have prompted a series of revisions to their specifications. Currently, fine and coarse gradations are prescribed for both types of binders used in TxDOT PFC mixtures (PG 76 and asphalt rubber binders). The Hamburg, Overlay, and Boil tests are performed for informational purposes only; the only mixture that has limits for all three mentioned tests is the fine PG 76 mixture.

The mix design requirements used in the Netherlands are also listed in Table 2-4. A European Standard governs the design for this type of mixture, although it can be modified or adapted by each country. The size of the aggregates used in PA mixtures is set (within range), but the Netherlands often uses a two-layer PA system with a finer mix on top of a coarser mix. In addition, it utilizes a single type of binder and fixed OBC (4.5 or 5.5 percent with fibers). Apparently, there are several performance tests the Netherlands performs on a routine or research basis (Ongel et al. 2007), but no limits on the parameters resulting from these tests were found in the literature. It is assumed that the Netherlands evaluates the results of these tests based on past experience to classify a mixture as acceptable or unacceptable.

Table 2-4. Comparison of Mix Design Methods

Parameter	NCHRP 9-41	Florida DOT	Texas DOT	The Netherlands
MATERIAL SELECTION				
Coarse Aggregate	Los Angeles (LA) abrasion (AASHTO T96), 30% max Flat and elongated (ASTM D4791), 50% max Soundness (AASHTO T104), 10% maximum with sodium sulfate and 15% maximum with magnesium sulfate Uncompacted voids (AASHTO TP56 Method A), 45% minimum	100% crushed granite or 100% crushed oolitic limestone LA abrasion, 45% maximum Flat and elongated, 10% maximum Soundness, 12% maximum with sodium sulfate	LA abrasion, 30% maximum Flat and elongated, 10% maximum Soundness, 20% maximum with magnesium sulfate Angularity, 95% minimum Deleterious material, 1% maximum Decantation, 1.5% maximum	85–90% crushed stone 6 mm–16 mm
Fine Aggregate	Soundness (AASHTO T104), 10% maximum with sodium sulfate and 15% maximum with magnesium sulfate Uncompacted voids (AASHTO T304 Method A), 45% minimum Sand equivalent (AASHTO T176), 50% minimum	Design gradation range prescribes mostly aggregates larger than the No. 8 sieve (see Table 2-5)	Use of fine aggregate is not recommended in PFC	10–15% crushed sand 0.063 mm–2 mm
Binder	PG + 1 grade PG + 2 grades for high traffic	PG 76-22 polymer modified asphalt (PMA) or PG 76-22 asphalt rubber binder (ARB) with at least 7% ground tire rubber	PG 76-XX or ARB with at least 15% crumb rubber modifier	Pen grade 70/100
Additives	Cellulose fiber, mineral fiber, crumb rubber, or polymers can be used to minimize draindown	0.4% mineral (basalt, diabase, or slag) fibers or 0.3% cellulose fibers by wt. of mix; 1% hydrated lime for granite mixtures; 0.5% antistrip additive for limestone mixtures	0.2–0.5% cellulose or mineral fibers required for PG 76-XX mixtures; 1% lime required for all mixtures; antistrip agents may be used	Limestone filler 0.3–0.7% fibers (drainage inhibitors)
Aggregate Gradation	Gradation bands for 3 PFC sizes: 9.5 mm, 12.5 mm, 19 mm	Single requirement for FC-5 (see Table 2-5)	Fine and coarse gradations for each binder type	–
SPECIMEN FABRICATION	Short-term oven aging (STOA) per AASHTO R30 N = 50 in the SGC	FDOT designs all FC-5 mixtures	STOA 2 hr @ $T_{compaction}$ N = 50 in the SGC	4 Marshall specimens (50 blows per face)
VOLUMETRICS				
G_{mb}	Dimensional analysis	N/A	Dimensional analysis	Dimensional analysis
G_{mm}	@ Trial %ac	N/A	Calculate G_{se} based on measured G_{mm} @ 2 low %ac (i.e., 2.0–3.0%); Calculate G_{mm} @ trial %ac	N/A
AV	Total = 18–22%	N/A	Total = 18–22%	Minimum 20%

Table 2-4 (Continued). Comparison of Mix Design Methods

Parameter	NCHRP 9-41	Florida DOT	Texas DOT	The Netherlands
Optimum Binder Content	3 trial % binder contents; minimum 6–6.5% for $G_{sb} \leq 2.75$; draindown @ $T_{production}$ + 15°C w/ No. 8 sieve basket < 0.3%	3 trial %ac with PG 67-22; 5.5–7.5% for granite and 6.5–8% for limestone; draindown via pie-plate method 320°F for 1 hr and visual examination; OBC for ARB = OBC x 1.12	3 trial %ac; 6–7% for PG 76-XX mixtures, 7–10% for ARB mixtures; draindown @ OBC < 0.1%	4.5% for PA and 5.5% for PA+
DURABILITY				
Abrasion	Dry Cantabro < 15%	N/A	Dry Cantabro ≤ 20%	Dry Cantabro; rotating surface abrasion test @ 68°F (20°C)
Stone-on-Stone Contact	Ratio of the voids in the coarse aggregate of the mix to the voids in the coarse aggregate of the aggregate blend VCA_{mix}/VCA_{DRC} < 1.0; coarse aggregate fraction defined with breakpoint sieve	N/A	N/A	N/A
Fracture	Tensile strength ratio (TSR) > 0.7; moisture conditioning per AASHTO T283 with 10 min vacuum, 1 freeze/thaw cycle while submerged in water	N/A	N/A	Semi-circular bending test; retained indirect tensile strength after 68 hr in 104°F (40°C water)
FUNCTIONALITY				
Permeability	> 100 m/day (optional)	N/A	N/A	N/A

2.3. Recent FDOT Research Studies on OGFC

FC-5 is an asphalt concrete (AC) friction course with specific grading requirements (i.e., open gradation), as noted in Table 2-5. As mentioned previously, FDOT designs all FC-5 mixtures. This type of surface course is used in higher-speed roads, as noted in Table 2-6. The other two types of asphalt concrete friction courses are FC-9.5 and FC-12.5, which follow the standard Superpave fine mix SP-9.5 and SP-12.5 requirements (i.e., dense gradations).

Table 2-5. FC-5 Gradation Design Range (FDOT 2014c)

Sieve Size	¾ inch	½ inch	⅜ inch	No. 4	No. 8	No. 16	No. 30	No. 50	No. 100	No. 200
Percent Passing	100	85–100	55–75	15–25	5–10	–	–	–	–	2–4

Table 2-6. Asphalt Concrete Friction Course Selection Guide (FDOT 2008)

Design Speed (mph)	Two Lane	Multilane
35–45	FC-12.5 or FC-9.5	FC-12.5 or FC-9.5
50 or greater	FC-12.5 or FC-9.5	FC-5

Several recently completed research projects on OGFC mixtures have been sponsored and directed by FDOT, including:

- BC-354-81: Evaluation of Thick Open Graded and Bonded Friction Courses for Florida—Completed in 2006.
- BD-545-53: Introduction of Fracture Resistance to the Design and Evaluation of Open Graded Friction Courses in Florida—Completed in 2009.
- BDS15-977-01: Evaluate the Contribution of the Mixture Components on the Longevity and Performance of FC-5—Completed in 2014.
- BDV25-820-1: Determination of the Optimum Binder Content of Open-Graded Friction Course (OGFC) Mixtures Using Digital Image Processing—Completed in 2015.
- BDV29-820-1: FC-5 Raveling Study—Completed in 2015.

A brief description of these projects is provided next.

2.3.1. BC-354-81: Evaluation of Thick Open Graded and Bonded Friction Courses for Florida

Birgisson et al. (2006) conducted a study to revise the mix design method for friction courses and proposed a draft specification for OGFC (i.e., FC-5) and PFC, which was introduced as a thicker OGFC mixture alternative. The basis of the study was the porous European mixtures and the Georgia DOT OGFC mix design methods. Based on the results of the study and field evaluations, researchers recommended the following as part of the proposed draft specification:

- Separate aggregate gradation requirements for PFC and FC-5 mixtures.
- Slightly lower upper bound for the binder content range used for the granite mixtures (i.e., 7.0 vs. 7.5 percent).

- Design criteria for PFC mixtures using Superpave Gyratory Compactor (SGC) specimen at 50 gyrations, selection of OBC based on the voids in the mineral aggregate (VMA), AV content of the compacted specimen between 18–22 percent, and exclusive use of PG 76–22 binder.
    - A four-step mix design method for mix design of PFC consisting of:
        1. Selection of trial binder contents (5.5, 6.0, 6.5, and 7.0 percent).
        2. Determination of OBC at minimum VMA and film thickness of at least 34 microns.
        3. Evaluation of draindown at OBC via modified AASHTO T 305.
        4. Moisture susceptibility evaluation via modified AASHTO T 283.

Most of the mix design components listed above are in line with the recommendations of NCHRP Project 9-41.

2.3.2. BD-545-53: Introduction of Fracture Resistance to the Design and Evaluation of Open Graded Friction Courses in Florida

In 2009, Roque et al. conducted another study to evaluate the fracture resistance of Florida's OGFC mixtures. The researchers found that OGFC mixtures had lower resilient modulus and failure limits than dense-graded asphalt mixtures, which resulted in lower fracture energies. They further noted that this finding was expected since an OGFC mixture generates its strength from stone-on-stone contact because of the lack of true mortar or mastic in the mixture. Additional testing on composite mixtures by Roque et al. (2009) indicated that the fracture resistance of OGFC mixtures improved in pavements employing polymer modified bonding agents between the OGFC and binder course. However, test results from the NCAT road test facility did not support this finding. FDOT sponsored two pavement test sections at the NCAT test facility to examine the field performance of an FC-5 mixture with two different bonding materials: (a) polymer modified tack, CRS-2P (SBS) at 0.2 gal/yd^2; and (b) trackless tack (NTSS-1HM) at 0.05 gal/yd^2. Both sections developed longitudinal cracking throughout their entire length. However, it could not be determined from cores whether the cracking that developed was top-down or reflected upward from the underlying binder course.

A comparison of the effective binder contents between the two test sections and Section S3 of the NCAT test track, which was an older section built with lower-quality aggregate but that exhibited no cracking at the time of the study (detailed description in Section 2.1.1 above), showed that the FDOT sections had a lower effective binder content of 4.9 percent compared to 5.7 percent for Section S3. In addition, the two test sections had 15 percent recycled asphalt pavement (RAP), which could mean that the effective volume of binder might actually be less than the estimated amount. The report theorizes that a major probable cause of cracking in FC-5 mixes is insufficient volume of effective binder.

2.3.3. BDS15-977-01: Evaluate the Contribution of the Mixture Components on the Longevity and Performance of FC-5

Like several other agencies, FDOT has observed that the in-service life of FC-5 mixtures is less than the service life of dense-graded friction course mixtures. The current expected service life of FC-5 mixtures is between 8 to 10 years. Thus, FDOT funded a study with Rutgers University to evaluate the field performance and mixture components of the FC-5 mixture to improve its longevity. During field visits of FC-5 sections, researchers observed raveling but found that the cracking on these sections resulted from reflection cracking and not from top-down cracking as originally thought. Thus, field performance of FC-5 mixtures appears to be a function of mixture durability, which is related to the effective binder content.

During the FC-5 mixture design phase, researchers found that by using the binder that would be utilized during actual field production (i.e., PG 76-22 or ARB-12) instead of the PG 67-22 that FDOT currently uses in OGFC mix design by the pie-plate method, higher OBCs could be determined. Researchers attributed this change to the increased viscosity of the binders. When researchers evaluated the increased binder content, they determined that the durability of the mixtures in the Cantabro abrasion loss test increased while having no detrimental impact on the draindown of the mixture. The possible use of a 9.5 mm NMAS FC-5 mixture was evaluated using current FDOT practices and a recommended aggregate gradation based on previous NCHRP studies. The laboratory evaluation found that although the 9.5 mm NMAS mixtures improved durability and fatigue resistance, rutting/stability issues as measured by the HWTT might exist.

Aging using the long-term oven aging procedure in AASHTO R30 also showed that additional 0.6 percent binder, determined as optimum for the PG 76-22 and ARB-12 binders by the pie-plate method, helped improve both durability and fatigue cracking even after additional oxidative aging. The influence of production tolerances was also evaluated and determined to be more of an issue with FC-5 mixtures containing ARB-12 binder. When gradations ran toward the fine side of the production tolerance, researchers hypothesized that the residual crumb rubber in the ARB-12 binder limited the stone-on-stone contact of the FC-5 mixture, creating both durability (i.e., Cantabro loss) and rutting (i.e., HWTT) issues.

2.3.3.1. Experiments to Identify and Investigate Improvements to OGFC Mix Design Method

The Rutgers research team conducted a series of experiments to identify and investigate possible changes to the current OGFC mix design method with the objective of improving the field performance of these mixtures. The experiments targeted three areas:

- Improvements to the pie-plate method.
- Possible use of finer FC-5 mixtures.
- Influence of FDOT production tolerances.

Details of the experiments conducted by the researchers are given next.

Experiment 1: Evaluate the Pie-Plate Method

A field performance review of FC-5 mixtures placed on Florida highways as well as results from the Florida NCAT sections revealed the significance of the effective binder content as a predictor of field performance. The objective of the first experiment was to investigate whether the current pie-plate mix design method could be improved in two areas:

- Allow for aggregate absorption of the binder through a 2-hr volumetric conditioning.
- Use the binder selected for production to run the mix design in lieu of PG 67-22.

Table 2-7 presents the factor-level combinations for Experiment 1. The selected aggregates fall into two groups: granite and oolitic limestone. The aggregate blend for each type of material is shown in Table 2-78 which gives the job mix formula (JMF) from the FDOT database. The OBC in this table is for PG 67-22, in accordance with the existing FM 5-588 method.

Table 2-7. Factor-level Combinations for Experiment 1 (Bennert and Cooley 2014)

Factor	Levels
Aggregate	4 aggregates: 2 granites and 2 oolitic limestones
Gradation	1 gradation per aggregate
Binder	PG 76-22 and ARB-12
Binder Content	2 levels: optimum per JMF and 0.6% above optimum
Short-Term Oven Aging	2 levels: 0- and 2-hr conditioning using AASHTO R30

Table 2-8. Job Mix Formulas Used in Research Project (Bennert and Cooley 2014)

Sieve Size	Section 337 Gradation Band (percent passing)	Aggregate (percent passing)			
		Granite		Oolitic Limestone	
		Junction City	Martin Marietta	Titan America	White Rock Quarry
¾ inch (19 mm)	100	100.0	100.0	100.0	100.0
½ inch (12.5 mm)	85–100	97.2	95.4	89.8	86.2
⅜ inch (9.5 mm)	55–75	72.5	72.6	63.5	67.8
#4 (4.75 mm)	15–25	22.0	19.8	18.9	22.8
#8 (2.36 mm)	5–10	7.4	9.0	7.6	6.8
#16 (1.18 mm)		5.0	6.6	2.7	3.9
#30 (600 μm)		4.0	4.9	2.6	3.3
#50 (300 μm)		3.2	3.9	2.5	3.1
#100 (150 μm)		2.6	3.2	2.3	2.7
#200 (75 μm)	2–4	2.1	2.8	2.1	2.3
OBC (%)		5.9	5.7	7.0	6.6

Based on the test results, the Rutgers research team made the following recommendations:

- Volumetric conditioning prior to the pie-plate test is not recommended. The tests showed that draindown was occurring during the 2-hr conditioning, thus biasing the results.
- Using the binder selected for production (PG 76-22 or ARB-12) in the mix design is recommended. Using the appropriate binder type was found to improve the Cantabro abrasion loss performance at binder contents above what the pie-plate method would determine as excessive draindown. The research team explained that this result is due to the higher rotational viscosities of the ARB-12 (600 cP) and PG 76-22 (477 cP) binders relative to PG 67-22 (194 cP). Thus, better adhesion or lower draindown would occur using PG 76-22 or ARB-12.

Experiment 2: Evaluate Use of Finer FC-5 Mixtures

The research team investigated the use of a finer (9.5 mm NMAS) FC-5 mixture to check whether this finer mix would improve durability and fatigue resistance. Currently, FDOT uses a 12.5 mm NMAS gradation for FC-5 mixtures. Table 2-9 presents the factor-level combinations for Experiment 2, while Table 2-10 shows the 9.5 mm gradations the research team adopted based on the work done by Cooley et al. (2009).

Table 2-9. Factor-Level Combinations for Experiment 2 (Bennert and Cooley 2014)

Factor	Levels
Aggregate	2 aggregates: granite (Martin Marietta) and oolitic limestone (White Rock Quarries), the two most predominant aggregate sources
Gradation	2 gradations: 12.5 mm and 9.5 mm NMAS per aggregate
Binder	PG 76-22 and ARB-12
Binder Content	2 levels: optimum per JMF and 0.6% above optimum
Short-Term Oven Aging	2-hr conditioning using AASHTO R30
Long-Term Oven Aging	5 days at 85°C in accordance with AASHTO R30

Table 2-10. Gradations and Optimum Binder Content for 9.5 mm FC-5 Mixtures (Bennert and Cooley 2014)

Sieve Size	Percent Passing		
	Martin Marietta	White Rock Quarries	NCHRP Report 640 Gradation Band (Cooley et al. 2009)
¾ inch (19 mm)	100.0	100.0	
½ inch (12.5 mm)	100.0	100.0	100.0
⅜ inch (9.5 mm)	86.4	85.4	85–100
#4 (4.75 mm)	30.0	27.5	20–30
#8 (2.36 mm)	11.8	6.7	5–15
#16 (1.18 mm)	7.0	3.8	
#30 (600 μm)	5.1	3.1	
#50 (300 μm)	4.0	2.8	
#100 (150 μm)	3.3	2.4	
#200 (75 μm)	2.8	2.1	0–4
FM 5-588 OBC (%)	6.6	6.0	

The following tests were performed:

- Cantabro abrasion loss to assess the durability of FC-5 compacted specimens.
- Overlay Tester to assess the cracking potential.
- IDT strength at 10°C to assess cracking potential based on experience from previous FDOT projects.
- HWTT (AASHTO T 324) to assess rutting potential.

The performance tests showed that the 9.5 mm gradation improved the fatigue cracking performance of the FC-5 mixtures. However, the 12.5 mm NMAS mixtures outperformed the 9.5 mm mixtures in the HWTT. Because of the concern with the stability of the finer mix, and the lack of information on whether this finer gradation provides the necessary stone-on-stone contact to achieve stability, the research team did not recommend adopting the 9.5 mm gradation until additional work is done to verify that adequate stone-on-stone contact can be achieved with this mix.

Experiment 3: Evaluate the Influence of FDOT Production Tolerances

Section 337 of the FDOT specifications (2014c) specifies tolerances for quality control testing of FC-5 mixtures. Table 2-11 shows the tolerances that are used, which are based on the binder content, and the percent passing of the 9.5 mm, No. 4, and No. 8 sieve sizes. Table 2-12 shows the factor-level combinations for this experiment, while Table 2-13 and Table 2-14 show the different aggregate gradations used to investigate the effect of production tolerances on aggregate gradation. The Rutgers research team adjusted the gradation blends from the respective JMF to introduce deviations from target values that were still within the allowable tolerances. For the White Rock Quarries aggregate blend, the deviations were controlled by the 9.5 mm sieve, while for the Martin Marietta blend, the No.4 sieve controlled the deviations from target values. Not all possible combinations of the tolerances given in Table 2-11 were tested. The research team performed the same tests used in the previous experiment to evaluate the influence of production tolerances in Experiment 3.

Table 2-11. FDOT Section 337 FC-5 Master Production Range (FDOT 2014c)

Characteristic	Tolerance*
Binder content	Target ± 0.60
Percent passing 9.5 mm sieve	Target ± 7.50
Percent passing No. 4 sieve	Target ± 6.00
Percent passing No. 8 sieve	Target ± 3.50

* Tolerances for sample size of 1 from the verified mix design.

Table 2-12. Factor-Level Combinations for Experiment 3 (Bennert and Cooley 2014)

Factor	Levels
Aggregate	2 aggregates: granite (Martin Marietta) and Oolitic limestone (White Rock Quarries), the two most predominantly used aggregate sources
Gradation	3 gradations: JMF ± production tolerances
Binder	PG 76-22 and ARB-12
Binder Content	3 levels: optimum per JMF and ± 0.6% from optimum
Gradation size	12.5 mm NMAS
Short-term oven aging	2-hr conditioning using AASHTO R30

Table 2-13. Gradations and Binder Content for Testing FC-5 Mixtures: White Rock Quarries (Bennert and Cooley 2014)

Sieve Size	Percent Passing			Section 337 Production Tolerance
	(−) Tolerance	JMF	(+) Tolerance	
¾ inch (19 mm)	100.0	100.0	100.0	
½ inch (12.5 mm)	89.8	86.2	82.7	
⅜ inch (9.5 mm)	75.1	67.8	60.6	±7.50%
#4 (4.75 mm)	26.4	22.8	19.1	±6.00%
#8 (2.36 mm)	7.2	6.8	6.4	±3.50%
#16 (1.18 mm)	3.8	3.9	3.9	
#30 (600 μm)	3.2	3.3	3.5	
#50 (300 μm)	2.9	3.1	3.2	
#100 (150 μm)	2.6	2.7	2.8	
#200 (75 μm)	2.2	2.3	2.4	
Binder content (%)	6.0	6.6	7.2	±0.60

Table 2-14. Gradations and Binder Content for Testing FC-5 Mixtures: Martin Marietta (Bennert and Cooley 2014)

Sieve Size	Percent Passing			Section 337 Production Tolerance
	(−) Tolerance	JMF	(+) Tolerance	
¾ inch (19 mm)	100.0	100.0	100.0	
½ inch (12.5 mm)	86.3	95.4	94.7	
⅜ inch (9.5 mm)	76.6	72.6	69.2	±7.50%
#4 (4.75 mm)	25.6	19.8	13.9	±6.00%
#8 (2.36 mm)	9.7	9.0	6.7	±3.50%
#16 (1.18 mm)	7.0	6.6	5.0	
#30 (600 μm)	5.1	4.9	4.0	
#50 (300 μm)	3.9	3.9	3.4	
#100 (150 μm)	3.3	3.2	3.0	
#200 (75 μm)	2.8	2.8	2.6	
Binder content (%)	5.1	5.7	6.3	±0.60

The following observations were noted from this experiment:

- The Cantabro abrasion loss test results did not show as much sensitivity to deviations from JMF values for the White Rock Quarries FC-5 mixtures compared to the Martin Marietta mixtures, which showed a large increase in abrasion loss at 0.6 percent below OBC, and at the finer aggregate gradation.
- The results from the Overlay Tester did not appear to be significantly affected by gradation changes. However, the cracking resistance showed a decrease relative to the JMF performance for samples where the binder content was 0.6 percent below optimum. Conversely, the cracking resistance increased relative to JMF performance for samples prepared at 0.6 percent above OBC.
- The IDT strength was highest for specimens prepared at the JMF values (OBC and target gradation). At ±0.6 percent from OBC, and at the modified aggregate gradations, the IDT strengths decreased from the corresponding JMF values.
- Similar to the IDT strength test results, the number of cycles to reach 12.5 mm rutting in the HWTT was highest for those specimens prepared at the JMF values (binder content and gradation). For a given aggregate type, the PG 76-22 FC-5 mixtures showed better rutting resistance based on the HWTT compared to the ARB-12 mixtures. Between aggregate types, the samples prepared using the Martin Marietta aggregate showed less rutting resistance and greater sensitivity to deviations from JMF values.

In summary, test results from Experiment 3 showed that performance suffered when the binder decreased to the 0.6 percent lower tolerance. In addition, when the aggregate blend went finer, the ARB-12 mixtures dropped in performance, particularly the Martin Marietta mixtures. Knowing that residual crumb rubber particles still exist in the ARB-12 binder, the Rutgers research team noted the need to have sufficient void space between the aggregate particles to allow the crumb rubber to reside without pushing the aggregate skeleton apart. Since stone-on-stone contact was not verified using the voids in the coarse aggregate method, the research team believed it was likely that when the aggregate gradation moved toward the finer side of the production tolerance, FC-5 mixtures containing crumb rubber modified binders may have not achieved stone-on-stone contact, resulting in the instability shown during the HWTT.

2.3.3.2. Evaluate the Contribution of the Mixture Components on the Longevity and Performance of FC-5

The Rutgers research team examined the pavement management system (PMS) data on the Florida highway network to evaluate the field performance of pavement sections with FC-5 mixtures. A total of 16 sections were compiled from the seven Florida districts. The PMS cracking and raveling data showed that district location was not a direct influence on the overall durability performance of the FC-5 mixtures. In all cases, there were FC-5 sections that exhibited longer and shorter service lives. For example, District 4 had three FC-5 pavement sections; two of those sections, both on SR-91, had different levels of performance. The FC-5 placed between mileposts 0.552 to 8.506 lasted 9 years before it reached the terminal crack rating. However, milepost 26.338 to 29.335 was still rated as a 10 (no cracking present) at over 10 years of service life. Because of the possible influence of other factors, Rutgers did further analysis to explain the differences in reported field performance between FC-5 sections. Because no construction information was available, the analysis focused on the possible effects of traffic and mixture components. The researchers noted the following findings (Bennert and Cooley 2014):

- Among the variables that were investigated, the effective binder content showed the best correlation with the observed field performance, as illustrated in Figure 2-1. As the effective binder content increased, the fatigue life of the FC-5 section increased. The research team noted that the trend line asymptotes to around 6 percent, indicating that effective binder contents reaching this level would have superior fatigue cracking resistance.
- The estimated aggregate absorption and the estimated film thickness also showed some correlation with field performance, as illustrated in Figure 2-2 and Figure 2-3.
- Little to no correlation was found between traffic and FC-5 cracking performance (Figure 2-4), indicating that it may be possible to increase fatigue resistance of FC-5 mixtures through changes in materials and mixture properties.

In addition to looking at the pavement condition survey (PCS) data, the Rutgers team also conducted site visits of FC-5 pavement sections in Florida. These visits were made to develop a better understanding of the possible causes of pavement distresses reported on these pavements. Over 1,000 mi of Florida roadways were driven on these visits, with the majority of the pavements having an FC-5 wearing course. Along the way, Rutgers and FDOT personnel stopped at specific locations to make more detailed inspections. Table 2-15 summarizes the observations from the site visits.

The following observations were made (Bennert and Cooley 2014):

- Performance of FC-5 mixes was considered to be good.
- The most common distress was raveling of the wearing course. The most common form of raveling appeared to be the end-of-load variety that appears in a cyclical nature along the roadway. This type of raveling is most likely associated with some form of segregation and is considered to be construction related. The other form of raveling is one that develops across the pavement lane width, which is likely material related.
- Cracking was not a predominant distress observed within the FC-5 mixture. The vast majority of cracking appears to be reflective cracking from underlying joints.

- Flushing of the FC-5 layer was noticed on two projects along the Florida Turnpike. These sections were associated with long haul times during construction. The flushing was cyclical in nature and might be due to draindown during transportation of the mix.

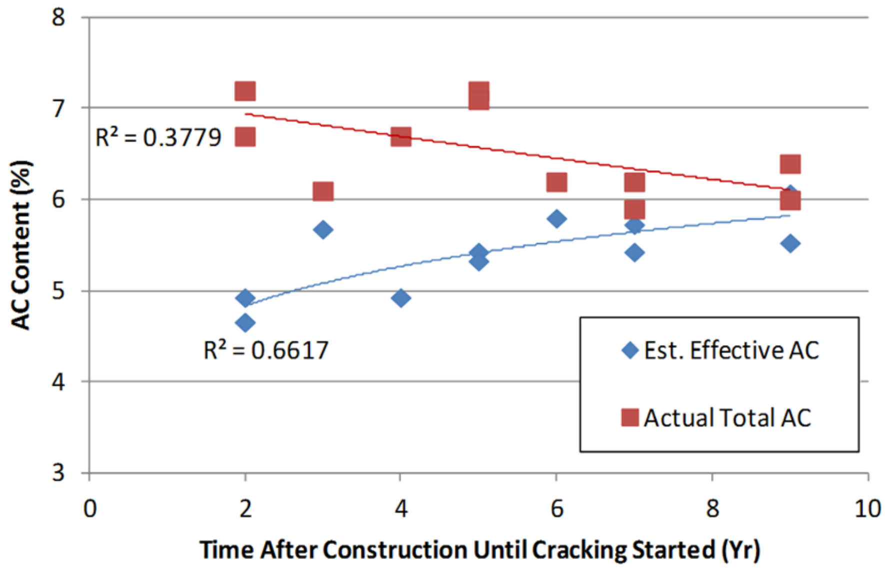

Figure 2-1. Binder content vs. time to cracking appearance (Bennert and Cooley 2014).

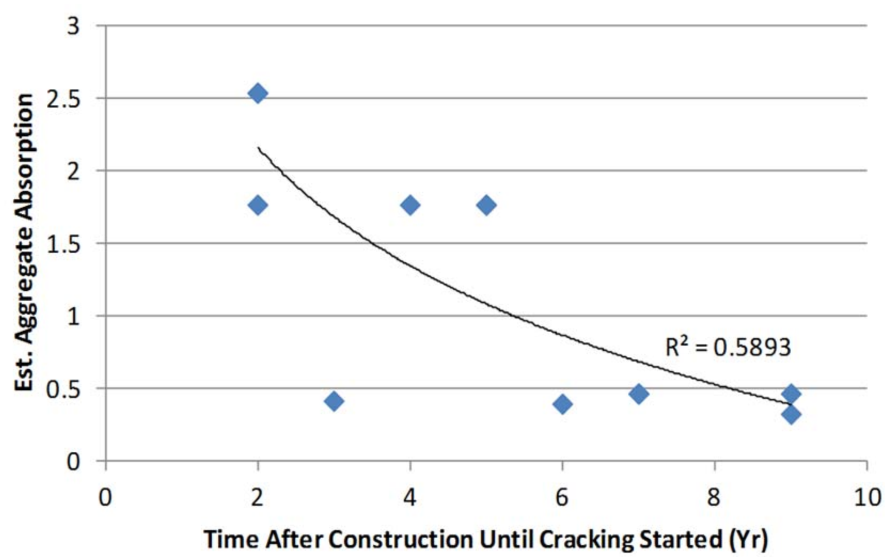

Figure 2-2. Aggregate absorption vs. time to cracking appearance (Bennert and Cooley 2014).

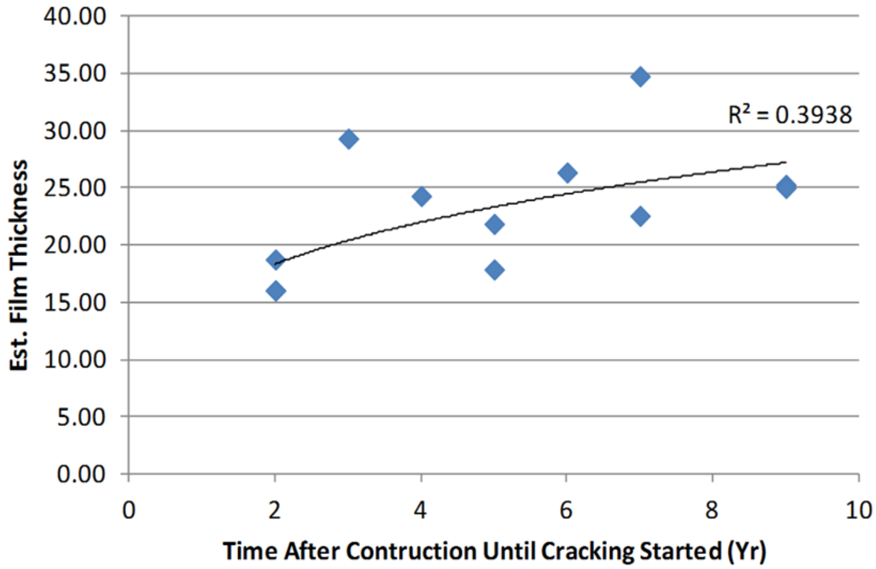

Figure 2-3. Binder film thickness vs. time to cracking appearance (Bennert and Cooley 2014).

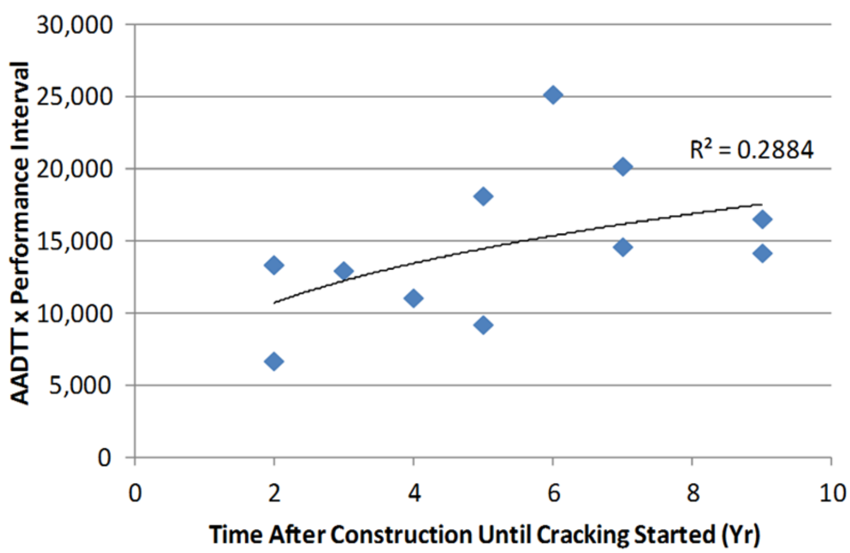

Figure 2-4. Cumulative truck traffic vs. time to cracking appearance (Bennert and Cooley 2014).

Table 2-15. Summary of Observations from Site Visits (Bennert and Cooley 2014)

Highway/ Interstate	Percent Location/Mile Posts	Distress Observed	Possible Causes
Hwy 20	West of Hawthorne	Raveling and longitudinal cracking	Low binder content
Hwy 441	South of Paynes Prairie	Raveling	Low binder content
I-75 (possible FC-2)	North of Lake City	Longitudinal cracking	Reflective construction joint
I-75 (possible FC-2)	454 to 455	Raveling	High mix production temperature
I-75 (possible FC-2)	461 to 462	Rutting, raveling, and cracking	Failure underlying layer
I-10	263	Longitudinal cracking	Underlying longitudinal joint
I-10	299 to 230	Transverse cracking	Reflected from underlying PCC pavement
I-75 (possible FC-2)	363 to 364	Longitudinal and transverse cracking, raveling	Unclear, possible issues in underlying layers
Florida Turnpike	133	Flushing and raveling	Long haul time during construction
I-75	30	Raveling	End-of-truck physical or thermal segregation
I-75	9	Flushing and raveling	Age/low binder content
Florida Turnpike	107	Flushing and raveling	Long haul time during construction

2.3.4. BDV25-820-1: Determination of the Optimum Binder Content of Open-Graded Friction Course (OGFC) Mixtures Using Digital Image Processing

The objective of this study was to improve the pie-plate method used to determine the OBC as part of the mix design of OGFC mixtures by eliminating the subjectivity involved during the visual inspection of the samples. Researchers from the University of South Florida proposed the use of digital imaging to improve the repeatability and accuracy of the FM 5-588 method, "Determining the Optimum Asphalt Binder Content of an Open-Graded Friction Course Mixture Using the Pie Plate Method." Researchers tested 19 different mix designs for a total of 120 granite and 108 oolitic limestone OGFC mixture samples. The development of the proposed image analysis process consisted of three steps (Gunaratne and Mejias de Pernia 2014):

1. Processing of images for noise removal.
2. Pattern classification to identify evaluation parameters (i.e., black pixels and connectivity of black pixels in the pie-plate images).
3. Statistical evaluation to determine the correlation between the evaluation parameters and the binder contents.

Researchers concluded that the percent area of black pixels in the pie plates and the binder content had a linear relationship, but with a significant amount of scatter. A slight improvement in scatter was observed when the connectivity of black pixels was compared against the binder content. Therefore, the percent black pixel area of the pie-plate images was not recommended as a stand-alone parameter for predicting the binder content of the pie plate. Rather, a combination of both percent black pixel area and connectivity of black pixels was suggested as the best evaluation parameter.

The results of this study, which was completed in 2015 included: (a) a perceptual image model based on specific imaging parameters which utilize human visual metrics that model human perceptive effects involved in estimating OBC, and (b) a Generalized Regression Neural Network that would discover the nonlinear relationship among the above imaging parameters.

2.3.5. BDV29-820-1: FC-5 Raveling Study

This recently completed project studied good and poor performing FC-5 pavement sections. This effort focused on the southeast portion of Florida since this is the area of the state that has had the most apparent problems with short-term raveling distress. Specifically, FDOT had a couple of high-visibility Interstate Highway projects in Palm Beach County that started raveling when they were just a few years old and had to be resurfaced in less than 7 years. Some of the possible causes of premature raveling that have been identified are:

- The coarser gradation of the limestone mixtures and the thickness at which these OGFC mixtures were placed (70 lb/yd^2) adversely impacted the texture, resulting in raveling.
- The absorptive nature of the limestone aggregate resulted in lower effective binder contents and more durability problems.
- The urbanized nature of paving in south Florida (Districts 4 and 6) resulted in longer haul times, piecemeal construction, poor construction practices, and poor oversight.

The State Materials Office (SMO) did a brief investigation and found that premature raveling was primarily related to poor construction practices (long haul times, tack problems, cold mix, thermal end-of-load segregation, etc.), and poor project oversight by FDOT during construction. However, SMO kept hearing complaints about how bad the OGFC pavements were performing, so FDOT sponsored a 1-year project with Florida International University (FIU) to do a records review of production and placement information on selected projects. The following tasks were proposed:

1. Conduct a field evaluation of projects in Districts 4 and 6 (five with good performance and five with poor performance) and provide the following summary for each project:
   a. Characterization of the extent of raveling.
   b. PCS performance data.
   c. Photographs of each project documenting the condition of the pavement.
2. Summarize the mix design information used on each project (mix designs for each of the projects provided by FDOT):
   a. Aggregate type.
   b. Gradation.
   c. Binder type.
   d. Optimum binder content.
   e. Locations where mix was placed.
   f. Other projects that have also used the same mix design, along with PCS performance information (provided by FDOT).
3. Review the production information from FDOT and provide the following:

   a. Summary of binder contents and gradation.
   b. Production temperatures.
   c. Haul distance and estimated haul time.
4. Review the construction records from FDOT and provide the following:
   a. Mix placement temperatures.
   b. Tack spread rates.
   c. Ambient air temperatures.
   d. Mix spread rates.
   e. Night or day paving.
   f. Correlation of date versus location of paving (lane and station).
5. Conduct interviews with project, district, and contractor personnel regarding the projects and summarize any noted problems or issues that occurred during construction.

FIU researchers conducted smartphone surveys of the projects identified by Districts 4 and 6 to quantify the amount of raveling on each project according to severity and extent. The surveys were conducted by mounting a smartphone to the windshield of a van vehicle and videotaping the road surface at highway speeds. Using a software application, the video was later reviewed to mark and classify the raveling area as low (6–10 percent stone loss), moderate (10–20 percent stone loss) or high (>20 percent stone loss) severity. The lane width was used to scale the image and quantify the area. In addition, PCS data, mix design, and quality control/quality assurance (QC/QA) data from the projects were compiled and submitted to FDOT. FDOT provided all three datasets to the Texas A&M Transportation Institute (TTI) as part of this literature review. Plots of the smartphone surveys and PCS data were generated and are shown in Appendix A. It should be noted that the smartphone surveys were performed on all lanes of a given project. However, the PCS data are given only for the continuous outermost or worst condition rated lane in each traffic direction. Therefore, the raveling data from the PCS database are for specific lanes on which cracking data are reported (i.e., the crack rating in the PCS dataset includes raveling).

Based on the raveling data collected by FIU, not much difference in raveling was observed between the good and poor performing projects. The average area of raveling on the good projects was 0.24 percent of the total area of lanes surveyed by FIU—the same as the average for the poor performing projects. Based on the PCS data since the last rehabilitation or resurfacing, not much differentiation was observed between the good and poor performing projects either. Only one project (SR-5/US-1) reached a deficient pavement condition rating of 6.4 within the current life cycle.

Based on FDOT's Flexible PCS Manual, when conducting PCS, raveling or loss of aggregate from the surface of the pavement for the rated sections is accumulated in the total percentage for Class III cracking. This total is added to the percentages for Class IB and Class II cracking, and then only the predominant type of cracking is coded. Raveling is coded in the rating form as follows:

1. Light—The aggregate and/or binder has begun to wear away but has not progressed significantly, with some loss of aggregate.
2. Moderate—The aggregate and/or binder has worn away and the surface texture is becoming rough and pitted. Loose particles generally exist. Loss of aggregate has progressed.

3. Severe—The aggregate and/or binder has worn away and the surface texture is very rough and pitted. Loss of aggregate is very noticeable.

Raveling is coded as percent of the roadway in four tiers: (a) 1–5 percent, (b) 6–25 percent, (c) 26–50 percent, and (d) 51+ percent. Raters code only the predominant severity level. Columns are left blank if the section has no raveling.

2.5. Numerical Modeling of Raveling in Asphalt Pavements

As previously mentioned, raveling is defined as the loss of aggregates at the surface of the pavement caused by repeated abrasion by traffic and often aggravated by the presence of moisture. The mechanism by which the aggregate particles are dislodged and expelled from the bulk of the mixture progresses rapidly in OGFC pavements; once it initiates, it can disintegrate the surface layer within months or even weeks (Huber 2000). As demonstrated from the works described in the previous sections, various materials (e.g., binder aging), mix designs (e.g., insufficient binder content), and construction factors (e.g., inadequate compaction) can promote cohesive failure within the binder or mastic and adhesive failure within the interfacial zone between the binder and the aggregate, which are the main causes driving the raveling degradation phenomenon (Mo et al. 2007; Shaowen and Shanshan 2011).

The necessity for identifying and better understanding the mechanisms associated with the initiation and progression of raveling in OGFC has motivated the development of numerical modeling efforts. These efforts have been mainly conducted by Delft University in the Netherlands, a country that, as was mentioned in the initial sections of this report, has more than 80 percent of the primary road networks surfaced with PA. Based on the necessity to gain a fundamental insight into OGFC performance and deterioration mechanisms, in 2006 the Road and Hydraulics Division of the Dutch Ministry of Transportation sponsored a series of fundamental research projects on OGFC behavior (Mo et al. 2007). The main results of some of these research efforts are presented in the following sections.

2.5.1. Finite Element Models

Table 2-16 presents a summary of the main two-dimensional (2D) and three-dimensional (3D) numerical works reported in the literature that have been developed to characterize raveling in OGFC. The first model of raveling in OGFC materials reported in the literature was developed in 2006 using the Computer Aided Pavement Analysis 3D (CAPA-3D) FE platform, which is an in-house FE software developed at Delft University (Mo et al. 2007). The goal of this research was to gain a better insight into the mechanics occurring within OGFC materials. It was expected that the results from this model were going to be useful in the development of new standards to obtain cost-effective, long-lasting, and low-maintenance OGFC pavements.

Table 2-16. Recent Numerical Studies of OGFC Materials

Reference	Modeling Approach	Objectives	Limitations*	Considered Raveling?
Mo et al. (2007) "Investigation into stress states in porous asphalt concrete on the basis of FE-modeling"	Mechanical finite element (2D)	Studied the mechanical response of an OGFC mixture at the micromechanical scale, emphasizing the causes of raveling and analyzing the stress concentration at the adhesive interface among materials.	The geometry of the microstructure was significantly simplified (aggregates were modeled as regular polygons). No actual deterioration processes at the interfaces were simulated. The impact of moisture on reducing raveling resistance was not considered.	Yes
Mo et al. (2008) "2D and 3D meso-scale finite element models for raveling analysis of porous asphalt concrete"	Mechanical finite element (2D and 3D)	Studied the mechanical response of OGFC mixtures, especially the response associated with the potential of the mixture to raveling.	The geometry of the microstructure was significantly simplified (aggregates were modeled as circles and spheres). No actual deterioration processes at the interfaces were simulated. The impact of moisture on reducing raveling resistance was not considered.	Yes
Huurman et al. (2010b) "Porous Asphalt ravelling in cold weather conditions"	Mechanical finite element (2D)	Studied the meso-mechanical response of the OGFC mixtures under low temperatures and high tire loads. An optimization tool was developed to understand strain and stress distributions on the OGFC mixes.	The geometry of the microstructure was significantly simplified (aggregates were modeled as circles). The impact of moisture on reducing raveling resistance was not considered.	Yes
Mo et al. (2010) "Investigation into material optimization and development for improved raveling resistant porous asphalt concrete"	Mechanical finite element (2D)	Conducted meso-mechanical simulations using a Lifetime Optimization Tool (LOT) to understand stress concentration under a moving tire and thermal loadings within OGFC materials. Considered adhesive elements between the aggregates and the mortar.	The geometry of the microstructure was significantly simplified (aggregates were modeled as circles of a unique size). The impact of moisture on reducing raveling resistance was not considered.	Yes

Table 2-16 (Continued). Recent Numerical Studies of OGFC Materials

Reference	Modeling Approach	Objectives	Limitations*	Considered Raveling?
Mo et al. (2011) "Bitumen–stone adhesive zone damage model for the meso-mechanical mixture design of raveling resistant porous asphalt concrete"	Mechanical finite element (2D)	Studied the meso-mechanical response of OGFC mixtures under tire loading, using an LOT. Considered the adhesive and cohesive failures as a cause of raveling, and evaluated the effect of aging, water, and type of stone on the OGFC durability.	The geometry of the microstructure was significantly simplified (aggregates were modeled as circles of a unique size). The adhesive zone was idealized as a system of two stone columns with a thin bitumen film between.	Yes
Mo et al. (2014) "Mortar fatigue model for meso-mechanistic mixture design of raveling resistant porous asphalt concrete"	Mechanical finite element (2D)	Used an LOT to transfer the mixture geometry, mortar viscoelastic response, and traffic loading into stresses or strains. The interpretation of these states was focused on the processes occurring at the adhesive zones. A practical mortar fatigue model based on the dissipated energy concept was developed to estimate the number of loading repetitions to raveling.	The geometry of the microstructure was significantly simplified (aggregates were modeled as circles of a unique size).	Yes

In order to achieve the research objectives, three meso-mechanical structural models of PFC were initially required:

- A 3D model of an idealized OGFC. This model required long computational times, which made it not practical (Mo et al. 2008).
- A 2D model of an idealized OGFC. This model was not costly in terms of computational time and provided new relevant information (Mo et al. 2007).
- A 2D model of scanned OGFC. This model represented and analyzed the response of OGFC at the meso-scale level.

The combination of the results from the first and the second model allowed the researchers to identify and understand the main limitations obtained from using 2D geometries of OGFC materials. The combination of the second and the third model gave insights into the effects of the idealizations made on the 2D model. The combination of the three models was expected to deliver a powerful tool to model the mechanical response of OGFC materials (Mo et al. 2007). As was mentioned above, the complexity of the problem forced the researchers to make significant simplifications. Even though these simplifications did not restrict the model to provide new and important information about the behavior of OGFC, they did limit the final scope of the work.

In general terms, the microstructure of OGFC was simplified to the following three phases, as illustrated in Figure 2-5; the relevant parameters of the model are listed in Table 2-17.

- Aggregate particles larger than 2 mm, represented by spherical 3D grains with an equivalent size.
- Mastic, a combination of binder and fine aggregates smaller than 2 mm.
- Air voids.

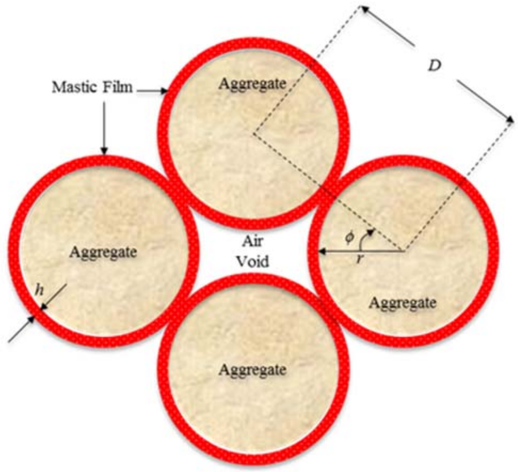

Figure 2-5. Idealized illustration of the 2D model (after Mo et al. 2007).

Table 2-17. Relevant Parameters for the 2D Model Presented in Figure 2-5.

No.	Parameter	Value
1	Diameter of particle (*d*)	9.6 mm
2	Radius of the aggregate particles (*r*)	4.8 mm
3	Distance between adjacent particles (*D*)	10.0–10.1 mm
4	Contact angle between aggregate particles (Φ)	40–50°
5	Thickness of the free mastic coating around the particles (*h*)	0.45–0.50 mm
6	Thickness of the mastic at the contact regions (*h*′)	0.005 mm
7	AV content	11–14%

The initial model of an OGFC was constructed by stacking several layers of circular aggregates, as shown in Figure 2-6. Coarse aggregate particles were homogeneously coated with a mastic film (i.e., combination of binder and fine aggregates smaller than 2 mm), whose thickness was determined using theoretical equations. The final thickness of the layer was 30 mm, which was defined after following a general accepted recommendation that stated that the final thickness of a regular HMA layer should be at least three times the NMAS of the mixture (Mo et al. 2007). At the upper parts of the surface, the grains were not coated with mastic, in concordance with real in-service or trafficked OGFC. The area of interest in this model was the upper middle part of the layer, where raveling is expected to occur.

The model was loaded using concentrated stresses on individual grains in order to simulate a moving wheel load. The load applied to the model represented a set of two 80 kN axle loads, which resulted in an average of 0.8 MPa vertical contact pressure on the OGFC. Two different driving speeds were considered in the model: high speed (22 m/s) and low speed (5.5 m/s). The model took into account some additional longitudinal (tangential) stresses produced by the driven wheel.

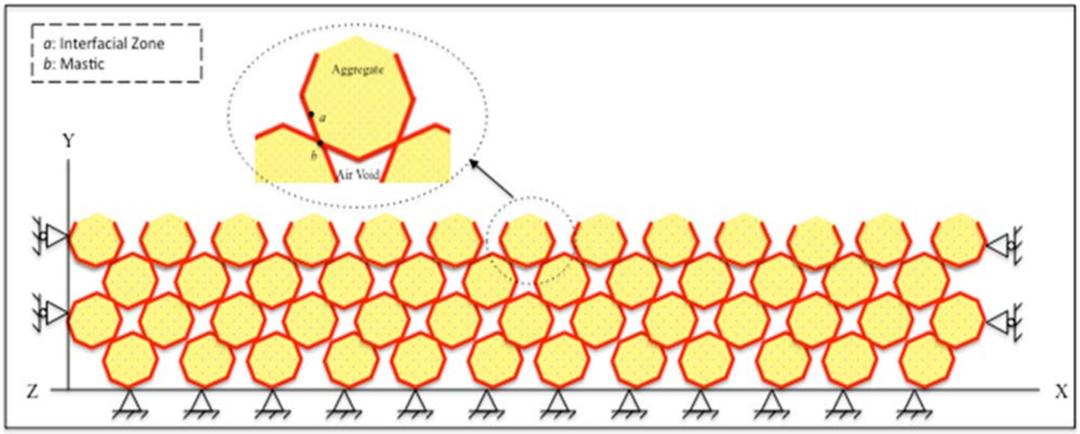

Figure 2-6. 2D model using circular particles covered by a constant mastic film (after Mo et al. 2007).

In terms of the mechanical response of the individual phases, the grains were modeled as linear elastic materials, with a modulus of $5x10^4$ MPa and a Poisson's ratio of 0.25; the mastic was modeled as a viscoelastic material. In addition, the stiffness of the interfacial zones between the mastic and the particle was obtained by a combination of the stiffness of both materials (in a 50-50 percent proportion). In terms of the material combinations, two different binders and mastics (unmodified and SBS modified) were considered in the study.

The objective of this FE model was to study the magnitude and location of the critical stresses that were developed in the system under the moving tire loads and the impact of the following parameters on those stresses:

- Type of binder, SBS modified vs. 70/100 penetration straight-run bitumen.
- Vehicle speed, 22 vs. 5.5 m/s.
- Binder content, 4.4 vs. 5.5 percent.
- Mastic film thickness, 0.45 vs. 0.5 mm.
- Degree of compaction, 99 vs. 101 percent.
- Void content of 12.6 percent
- Distance between particles, 10.1 vs. 10 mm.
- Contact angle between adjacent aggregates, 45 vs. 49 degrees.
- Temperature, 25 vs. 40°C.

Since raveling can be the result of adhesive failure (failure of the interfacial zone), cohesive failure (failure through the mastic), or a combination of both, the state of stresses at the interfacial zone and at the mastic were translated into a single quantity through the Mohr Coulomb and Von Mises criteria that indicate the overall material mechanical state.

The main results from this initial work showed that raveling might be mainly a low-temperature problem. The state of stresses obtained from the numerical simulations was compared with some experimental strength values reported in the literature by Frolov et al. (1983), from which it was concluded that the responses of the model were within a range of realistic values for the different cases studied.

The model described above corresponds to the initial phase of the projects DWW-25770 (Research Strategy Ravelling) and DWW-2923 (Life Optimization Tool for Porous Asphalt-LOT) sponsored by the Road and Hydraulic Engineering Institute of the Netherlands. Although this model represented an important advancement toward the understanding of the mechanics of failure in OGFC mixtures, it did not achieve all the objectives initially proposed by the researchers. As a consequence, in 2008 the same group of researchers worked on the development of a 3D model (also developed on the CAPA-3D software) whose principal objective was to improve the 2D model already developed by recognizing some of the main limitations that were observed in the initial model (Mo et al. 2008).

In this new study, tomography techniques were used to determine the real geometry of a typical OGFC mixture used on the main road networks of the Netherlands. Unfortunately, the computational cost of modeling the original geometry was very high, and all the simplifications and assumptions of the 2D model developed in 2007 were also applied to this new model.

The 3D model consisted of 30 particles located in two rows. The main particle of interest was the central one in the upper layer, which was surrounded with six particles at the top and supported by three particles at the bottom. Only the upper parts of the central seven particles were not surfaced with mortar, as shown in Figure 2-7. The other particles only played the role of a boundary condition and were simplified and modeled as viscoelastic ball bodies, which characterized the general response of stone-mortar combination. Furthermore, there was not a uniform coat thickness of mortar for each aggregate (Mo et al. 2008).

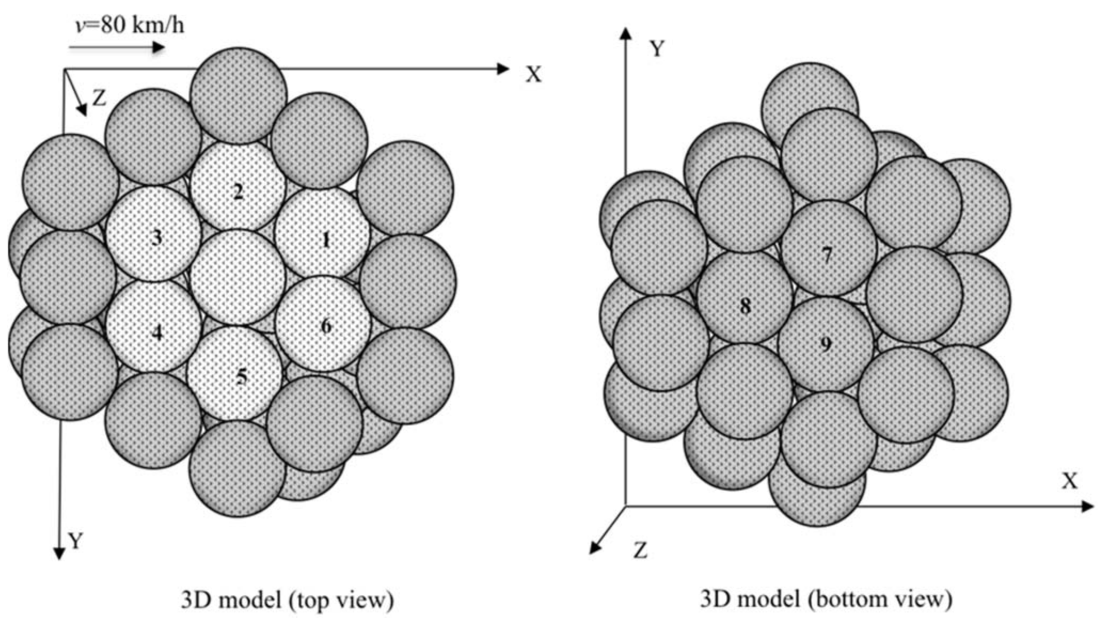

Figure 2-7. 3D meso-scale model (after Mo et al. 2008).

In order to compare the two models (2D and 3D), the aggregates were modeled as an elastic material with the same properties, and the mortar was modeled as a viscoelastic material with all the properties already defined in the previous work on CAPA-3D. In this way, the same groups of loads were applied to the system (moving tire loads). In addition to the 2D model already developed, two other cases were proposed and compared with each other:

- The 2D-1 (50 particles) model vs. the 2D-2 (38 particles) model, which was expected to give insight into the influence of particle packing. Figure 2-6 represents the 2D-1 model, and Figure 2-8 represents the 2D-2 model.
- The 2D-2 model vs. the 3D model without lateral loading (3D-1 model), which was used to study the effect of geometry between 2D and 3D models.
- The 3D model fully loaded in all the three directions (3D-2 model), which was expected to provide more acceptable information on stress conditions linked to raveling.

It is important to note that CAPA-3D is a pure 3D platform, so in order to develop a 2D model on this software, it was necessary to establish specific boundary conditions, as shown in Figure 2-6 and Figure 2-8.

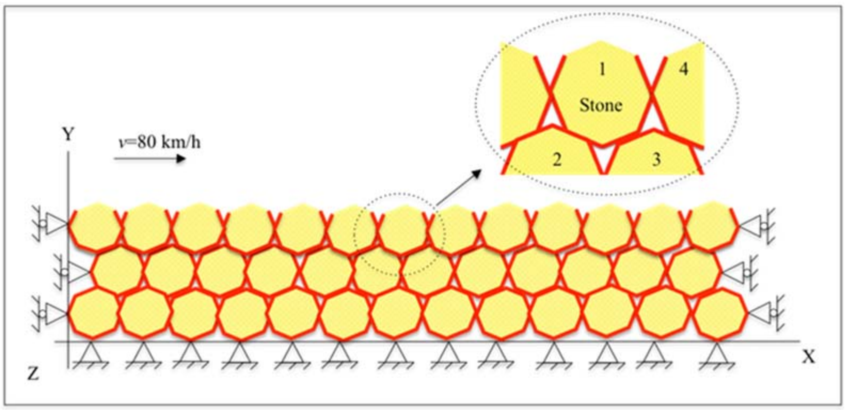

Figure 2-8. 2D-2 model representation (after Mo et al. 2008).

For comparison purposes, the six stress components of the 3D model were transformed into a single quantity. The state of stresses was represented using a similar approach as the one used for the 2D models (Mo et al. 2007) with the Mohr Coulomb and the Von Mises criteria. Unfortunately, the results obtained by the Von Mises criterion showed that the total stress presented by this indicator was significantly larger than the tensile strength of mortar, which made this indicator unacceptable. Therefore, only the Mohr Coulomb criterion was used to represent the total stress condition.

The results from this new model indicate that the second wheel (the driven wheel) generated higher stress states than the first wheel, which is in accordance to the results obtained from the initial model developed in 2007. At the same time, the results show that the state of stresses at the interfacial zone was similar to that in the mortar, a result that was expected due to the size of the contact region (i.e., the stress distribution could not vary significantly among its thickness direction; Mo et al. 2008). According to the authors, this result demonstrated that raveling resistance depends on the strength of the different phases, and especially on the fatigue behavior of the materials involved. However, since the measurements of the tensile strength of the interfacial zone were not representative of actual traffic loading, a damage accumulation model for binder-stone adhesion was developed based on time-stress history. In this case, the contact time of the wheel was set as 0.01 sec; thus, the required stress, σ_f, to fail the system was expected to be equal to or larger than 28 MPa. Therefore, the fatigue life of the mortar, N_f, was expressed as:

$$N_f = k\sigma^{-n}\mathrm{N_f} = \mathrm{k\sigma^{-n}N_f} = \mathrm{k\sigma^{-n}} \tag{2-1}$$

where k and n are material constants: $k = 5.2\text{x}10^6$ and $n = 4.8$. Unfortunately, when the fatigue life was estimated using some results obtained from the 3D-2 model, the result was unrealistic (i.e., 980 cycles to failure). This demonstrated that this model overestimated the stress conditions within the material.

Table 2-18 lists the conclusions from the two papers described above.

Table 2-18. Main Conclusions Obtained from the Modeling Works by Mo et al. (2007, 2008)

Reference	General Conclusions	Model-related Observations
Mo et al. (2007) "Investigation into stress states in porous asphalt concrete on the basis of FE-modeling"	• It was revealed that raveling OGFC is mainly a low-temperature problem. • It was determined that the interfacial zones are subjected to a combination of compressive and shear stresses. Tensile stresses were observed to remain small in all cases. Also, the high magnitude of the shear stresses that were quantified at the interfacial zones may exceed adhesive bonding strength between the aggregate and the mastic and cause adhesive failure leading to raveling. • It was shown that the stress levels in the mastic and at the interfacial zones decrease when the contact angle between the materials increases. According to the authors, this result suggests that the condition of the particle skeleton is more important than the type of bitumen used. Also, the obtained results showed that the modified bitumen only has a slightly positive effect on stress states compared to the unmodified binder (see next conclusion). • In terms of the impact of unmodified versus modified binder, it was found that modified binders reduced the stresses levels in the mastic and the interfacial zone at 25°C. At 40°C, the stresses in the mastic were strongly dependent on the type of binder. With the modified binder, the state of stresses was twice that observed in the unmodified binder case. • The modeling results also showed that the development of shear stresses was more complex in the interfacial zones, especially when a low-speed wheel loading was applied to the OGFC. • In terms of the stresses, at the interfacial zone, the maximum load condition was observed to be caused by a combination of a high shear condition and minor tensile stress.	• The responses of the model were logical in the different cases studied. This was corroborated after comparing the results with the experimental strength values reported by Frolov et al. (1983). This indicates that the 2D model developed is capable of providing valid stress states in the interfacial zones and in the mastic phase. • The authors recognized the limitations of the simplification made to the model. Nevertheless, it provided relevant insight that could be used in the development of better OGFC mixtures. • There was a lack of information about the strength of adhesive zones; the only information available is from 1983 and is very limited. • The model was expected to be improved by using image analysis techniques and developing a 3D model to investigate the impact of the 2D simplification.

Table 2-18 (Continued). Main Conclusions Obtained from the Modeling Works by Mo et al. (2007, 2008)

	• In terms of the binder content, an increase in this value resulted in a decrease in the stresses at the interfacial zone and in the mastic film. According to the authors, the reason for this situation could be that the contact area between the coarse aggregates increases with the increase of bitumen content. • When the temperature increased, the stresses in the mastic decreased for the two types of binder due to the viscoelastic response of the material. Meanwhile, stress levels at the interfacial zones increased with temperature, and that increase was stronger in the case of the modified binder.	•
Mo et al. (2008) "2D and 3D meso-scale finite element models for raveling analysis of porous asphalt concrete"	• Particle packing is one of the most important aspects when analyzing the mechanics of OGFC systems. • Von Mises stresses cannot be used as a failure indicator of OGFC systems because they overestimate the actual state of stresses. • The obtained stresses were so high that they were related to short fatigue lives, which is not in good agreement with the observations of the actual performance of OGFC in the field.	• The computational stresses on the 3D model were larger than the stresses on the 2D model; the difference could be 2.6–3.5 times into the interfacial zone and on the mortar bridge, respectively. • The current model assumed an idealized OGFC, which somehow limits the quality of the results. Working with other meso- or microstructural features that include aggregates of different sizes, shapes, textures, and packing geometries is recommended.

During this same period, a research group at Delft University also worked on the development of a meso-mechanistic tool (Lifetime Optimization Tool) that was designed to analyze some of the main causes of raveling (failure on stone-to-stone contact—Finite Element Modeling). The 2D idealized and 3D idealized models previously described are considered part of the pre-LOT phase of the project DWW-2923 (Huurman and Mo, 2007). As shown before, both models provided new, valuable results in terms of the mechanical response of the OGFC mixtures. However, one of the main limitations of these works was that they were developed in CAPA-3D, a computational tool that has the following restrictions:

- CAPA-3D is not a commercial platform, which means that it cannot be transferred to other groups external to Delft University.

- CAPA-3D does not allow the definition of rigid bodies and complex boundary conditions, so the definition of stones in CAPA-3D is associated with high computational costs.
- CAPA-3D is a pure 3D software and thus not able to reproduce 2D models; the 2D models developed were 3D models with specific boundary conditions that increased the overall computational cost.

For these reasons, it was decided to develop the mechanistic component of the LOT in Abaqus®, one of the most-used FE commercial software in the world (and selected for use in this project), which allowed for overcoming the main limitations faced with CAPA-3D. In these terms, the LOT combines the stress and strains obtained in the FE model with a damage accumulation model, based on the mortar fatigue behavior, which allows the prediction of the expected service life of a pavement structure. In 2007, an initial non-calibrated version of the LOT was finished, with the capability to translate the effect of moving traffic loadings, mixture geometry, and mortar response into stress and strain signals within the system, which could then be used to estimate the service life of the structure. In general terms, the LOT also allows for predicting the expected type of failure (adhesive or cohesive) and the number of load cycles that are required to cause that type of failure. Finally, the LOT was designed to provide information about which material component should be changed to achieve a better raveling resistance and a longer service life (Huurman and Mo 2007). Later, in 2009, the LOT was used to develop a mechanistic mixture design for OGFC; the results obtained from this work were validated with several full-scale raveling tests (Huurman et al. 2010a). As part of this project, the same models used by Huurman and Mo (2007) were used:

- A 2D idealized model with the geometry simplifications used in the 2D-1 model by Mo et al. (2007).
- A 3D idealized model with the geometry simplifications used in the 3D model of Mo et al. (2008).
- A 2D photo scan model based on a real OGFC cross-section (Nielsen 2006). In this model, the outlines of voids and aggregates were manually defined, and it was observed that it was difficult to differentiate between clogging dirt and the mortar phase, which is considered a potential source of error in the construction of the geometry of the model.

Only the 2D idealized model (Figure 2-9) was used as part of the LOT tool. The 3D idealized model and the 2D photo scan model were used to estimate the effects of the 2D simplification (Huurman and Mo 2007). These models were successfully validated, but no damage phenomena were studied (Huurman et al. 2010a).

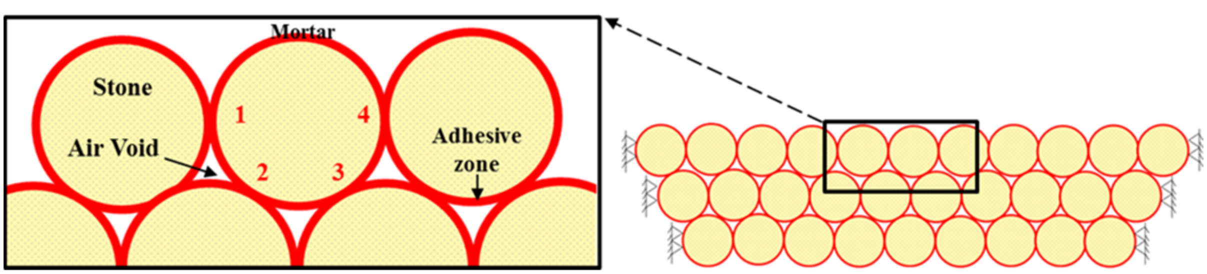

Figure 2-9. 2D idealized model (after Huurman et al. 2010a).

In 2009, the Netherlands was concerned with the detrimental effects that the winter period of 2008–2009 caused on pavements. As noted previously, aggressive raveling damages were observed in several main highway sections during those years, which caused a significant reduction in the overall network capability. At this point, the implementation of OGFC mixtures was questioned in the entire nation, and the research group at Deft decided to apply the LOT methodology to try to explain the main causes of raveling in cold weather conditions (Huurman et al. 2010b).

In order to do so, a representative case study was established, where a 50 kN wheel load was applied by a Goodyear 42R65 super single tire, generating a contact stress of 0.891 MPa. The wheel had a speed of 76.5 km/h, which means that the tire required 8 ms to pass over a certain selected point in the OGFC. The traffic was represented with a total of 10,000 equivalent 100 kN axles per day. Four different temperatures were simulated (−10, 0, +10, +20ºC), and an aged SBS modified mortar was considered in the model. In every simulation, three different load cases were studied:

- Forces introduced to the stones located at the surface of the pavement by passing tires.
- Deformations that follow from the deflection of the pavement as a whole.
- Stresses that might be introduced as a result of temperature variations.

Table 2-19 shows the principal properties of the representative case study. In this case, the objective was to obtain fundamental knowledge about the mechanism of failure associated with raveling, which required conducting a detailed study of the material properties such that new durable OGFC mixtures could be designed.

Table 2-19. Properties of the Representative Case Study (Huurman et al. 2010b)

Property	Value	Additional Information
Axle Load	50 kN	Applied by a Goodyear 425R65 super single tire
Contact Stress	0.891 MPa	
Speed	76.5 km/h	8 ms required to pass over certain point
Traffic	10,000 load repetitions	Standard axle: 100 kN
Temperature	−10, 0 ,+10, +20ºC	
Mortar	Long-term aged SBS modified	Response and fatigue properties from LOT project (Huurman and Mo 2007)
Thickness of the Adhesive Zone	10 µm	

The 2D idealized model (Figure 2-9) considered round spheres bounded together by mortar bridges. In general, the model consisted of three rows of aggregate particles enclosed by a mortar film. In this case, the aggregate particles were modeled as rigid bodies. The mortar closer to the middle zone of the model was of special interest, and it was counted with a finer element mesh. In this way, only the five particles closest to this area included a layer of thin elements representing adhesive zones (using the built-in cohesive zone element in Abaqus®). The main particle of interest was the central particle in the upper row, which had four contact areas with the surrounding materials.

For this model, a long-term aged SBS modifier was considered for the simulations. The fatigue properties were determined in the laboratory as part of the LOT project (Huurman and Mo 2007), and a Prony Series model was used to describe the mortar constitutive response. The adhesive zone stiffness was estimated based on the mortar stiffness and the adhesive zone thickness (i.e., 10 µm). It was shown that the main result of winter damage was a reduction in the relaxation potential of the aged mortar at low temperatures and a reduction in the adhesive zone performance at those temperatures.

Later that year, the same group of researchers, with the help of Wu and Molenaar, decided to use the LOT model and the representative case study already described (Mo et al. 2010) to conduct more research. As indicated earlier, cohesive failure at the mortar bridges might result in raveling. Thus, a mortar fatigue model was included in order to explain fatigue behavior of the mortar, and the model was based on the dissipated energy concept using the stress and strain signals already determined with the LOT model. The fatigue model used the following equation:

$$N_f = \left(\frac{W_{iitial-cycle}}{W_0}\right)^{-b} \tag{2-2}$$

Where:
b = a material constant.
W_o = a reference energy (MPa).
$W_{initial\text{-}cycle}$ = the dissipated energy per cycle in initial phase (MPa).

Since adhesive failure can also contribute to raveling, a damage model based on a linear damage accumulation rule combined with the Mohr Coulomb criterion failure was also developed:

$$\dot{D} = \left(\frac{\sigma_e}{\sigma_0}\right)^n for\ \sigma_e > 0, D = \dot{0}\ for\ \ \sigma_e < 0\ with\ \ \sigma_e = \sigma_n + \frac{|\tau|}{tg\emptyset} \tag{2-3}$$

Where:
$\dot{D}$ = the rate damage.
σe = the equivalent tensile stress (MPa).
σn = the normal stress (MPa) (− for compression and + for tension).
τ = the shear stress (MPa).
∅ = the internal friction angle (º).
t = time.

After analyzing the numerical results, researchers concluded that raveling could occur at both high and low temperatures (e.g., fracture or strength failure), and that the raveling resistance could be improved by changing mortar or bitumen properties (Mo et al. 2010). Table 2-20 summarizes the conclusions gained after analyzing the results obtained from the numerical simulations in this study. The DWW-2923 project is still under development. Since the last work described, the researchers have focused on improving the damage models to better predict the expected service life of OGFC mixtures (i.e., Mo et al. 2011, 2014); nevertheless, the main formulation of those works is still based on the same modeling principles and geometry as those used in the LOT.

Table 2-20. Conclusions from the Modeling Works by Huurman et al. (2010b) and Mo et al. (2010)

Reference	General Conclusions	Model-Related Observations
Huurman et al. (2010b) "Porous asphalt ravelling in cold weather conditions"	• The main cause of winter damage in OGFC is the reduction of the relaxation potential of aged mortars at low temperatures. • At high temperatures (i.e., +20ºC), the reduction in the strength of the adhesive zones makes the mixture susceptible to raveling. • Under hot conditions, raveling damages are less aggressive than under cold conditions. • The success of the performance of OGFC materials depends on the availability of the mortar to remain viscous at low temperatures with good adhesion to the aggregates, and on the capability of it to maintain its strength at high temperatures.	• The LOT is able to explain the aggressive raveling damage developed during the 2008–2009 winter in the Netherlands. • This was the first temperature validation made using the LOT. The results were compared to the experimental results previously obtained by Huurman et al. (2010a). • The LOT is able to explain low-temperature mixture performance.
Mo et al. (2010) "Investigation into material optimization and development for improved raveling resistant porous asphalt concrete"	• Raveling is a phenomenon that can occur in a wide range of temperatures. • Raveling is temperature dependent; it is critical at low and high temperatures. At intermediate temperatures, fatigue is the principal cause associated with raveling. • The deflection of the pavement under a mechanical load showed that the pavement structure has a significant influence on the raveling resistance. • Raveling resistance can be improved by changing mortar or binder properties. A binder with good relaxation properties showed optimal performance in terms of raveling resistance. • Adhesive failure was observed to be predominant at low temperatures, while cohesive failure was observed to be predominant at high temperatures.	• Meso-scale mechanical modeling in 2D seems to be a powerful tool for analyzing raveling effects in OGFC (Mo et al. 2010).

2.5.2. Other Numerical Models Used with OGFC

Raveling is not the only phenomenon of damage that has been studied in OGFC mixtures. Other relevant phenomena such as rutting or moisture damage have also been modeled and analyzed. For example, in 2009, a group of researchers from Shandong University were concerned about the damages related to moisture in OGFC (e.g., stripping, raveling, potholes, pumping, and map cracking; Cui et al. 2009). In order to understand this phenomenon, they developed a 3D model (using the FLAC3D software) to quantify the dynamic deflection, the dynamic pore water pressure, and the seepage force under a single vehicle load in OGFC. The results revealed the cause of the pumping phenomenon and the location of the maximum dynamic pressures (Cui et al. 2009; Cui 2010).

Some other groups have focused on understanding the micromechanical response of OGFC mixtures, such as Alvarez, Mahmoud, et al. (2010), who developed a Discrete Element Model based on image analysis techniques that allowed the quantitative determination of stone-on-stone contacts on OGFC mixtures. The authors verified that these contacts are the main characteristic required to achieve adequate resistance to raveling and permanent deformation in OGFC mixtures (Alvarez, Mahmoud, et al. 2010). Similarly, in 2013, the University of California undertook a full-scale test track experiment where the microstructure of the pavement was determined using X-ray computed tomography (CT; Coleri et al. 2013). After the application of accelerated loading cycles, changes in the air void structure and in the aggregate distributions were identified using image analysis and numerical techniques. The results suggested that the thickness of the underlying layers might also induce early rutting failures in these materials.

The study of the functionality of OGFC materials (i.e., permeability and noise reduction) has been another important topic of study. Authors like Raineiri et al. (2012) and Zhang et al. (2013) developed numerical models to simulate drainage characteristics in OGFC mixtures. The main objective of these models was to create a new design method (Raineiri et al. 2012) that provides an explicit solution for the maximum flow path length needed to avoid water exfiltration. Zhang et al. (2013) developed their model using a Finite Volume Method with a simplified geometry. The results showed that aggregate size is a relevant factor in the design of OGFC mixtures, and that controlling permeability is of great importance to assure adequate functionality (Zhang et al. 2013).

CHAPTER 3 . MATERIALS AND FIELD PERFORMANCE

3.1. Materials and Mixtures

The mixtures used in Task 3 included a combination of the following materials:

- Aggregates:
  - Granite—Martin Marietta Materials.
  - Limestone—White Rock Quarries.
- Binders:
  - Performance-graded SBS modified PG 76-22 (PMA).
  - Asphalt rubber PG 76-22 (ARB).

Details of the six mixtures are listed in Table 3-1. Mixtures 1 and 2 correspond to the good performing mixtures with respect to raveling with mix design IDs SPM 07-5654A by asphalt group and SP 05-3979A by community, respectively. These two mix designs are identical in terms of gradation, aggregate type, aggregate proportion, and mineral fiber, the only difference being the type of binder used. Mixture 3 corresponds to the poor performing mixture with respect to raveling with mix design ID SPM 05-3987B by APAC. This mixture is similar to mixture 1 with the difference that it does not include aggregate screenings. Mixture 4 corresponds to a modified version of mixture 3, employing the same aggregate gradation but different binder type. Granite aggregate is used in mixtures 5 and 6; mixture 6 is a modified version of mixture 5 that includes the same aggregate gradation but different binder type.

All mixtures included 0.4 percent mineral fiber by weight of the mixture to prevent binder draindown and an antistrip agent. The granite mixtures employed 1.0 percent hydrated lime by weight of aggregate, and the limestone mixtures employed 0.5 percent antistrip agent by weight of binder. The antistrip agent was blended with the binder at the terminal. All materials (aggregates, binders—with and without antistripping agent—and mineral fibers) were collected and shipped by FDOT.

The OBC determination was done by FDOT per its standard test method FM 5-588, "Determining the Optimum Asphalt Binder Content of an Open-Graded Friction Course Mixture Using the Pie Plate Method." The method consists of preparing 1,200 g aggregate batches including any fiber or hydrated lime as specified in the mix design, and mixing it with PG 67-22 binder at 5.3, 5.8, and 6.3 percent for granite mixtures, and 5.8, 6.3, and 6.8 percent for limestone mixtures. After mixing, the batches are transferred to the pie plate and left inside an oven at 160°C for 1 hr. After heating, the samples are removed from the oven and allowed to cool down. Then, the pie plates are inverted so the bottom can be inspected, as shown in Figure 3-1. The OBC is determined visually by assessing which batch displays sufficient bonding between the mixture and the bottom of the pie plate without evidence of excessive binder drainage. The selected OBC may be one of the trial contents or estimated based on visual assessment.

Table 3-1. Selected Mix Designs for the Proposed Research Plan

Sieve Size	FDOT FC-5 Specification Limits	Mixture # 1	2	3	4	5	6
19.0mm (3/4")	100%	100.0		100.0		100	
12.5mm (1/2")	85% - 100%	90.0		93.0		95.4	
9.5mm (3/8")	55% - 75%	66.0		69.0		72.6	
4.75mm (#4)	15% - 25%	24.0		23.0		19.8	
2.36mm (#8)	5% - 10%	10.0		9.0		9.0	
1.18mm (#16)	–	8.0		5.0		6.6	
600um (#30)	–	7.0		4.0		4.9	
300um (#50)	–	6.0		3.0		3.9	
150um (#100)	–	5.0		3.0		3.2	
75um (#200)	2% - 4%	3.5		3.0		2.8	
Aggregate Type/Producer		Limestone - White Rock Quarries				Granite – Martin Marietta	
Aggregate Proportion		50% S1-A, 45% S1-B, 5% Screenings		50% S1-A, 50% S1-B		83% S1-A, 11% S1-B, 5% Screenings	
Binder Type		PG 76-22 (PMA)	PG 76-22 (ARB)	PG 76-22 (PMA)	PG 76-22 (ARB)	PG 76-22 (PMA)	PG 76-22 (ARB)
Optimum Binder Content (%)		7.1		6.1		5.6	
Antistrip (%)		0.5 by wt. of binder				1.0 by wt. of aggregate	
Mineral Fiber (%)		0.4 by wt. of mix					

(a) (b) (c)

Figure 3-1. Example of the OBC visual determination method (FDOT 2014a); (a) insufficient asphalt content, (b) optimum asphalt content, (c) excessive asphalt content.

3.2. Field Projects

As previously mentioned, the good and poor performing mixtures with respect to raveling correspond to field projects on US-1 and I-75, respectively. The research team made site visits to these field projects to conduct a visual inspection, measure on-site permeability, and obtain cores. A forensic analysis was performed on the cores to determine the characteristics of the mixtures and help understand the observed field performance, as described next.

3.2.1. Field Project on I-75

This field project was located between Sheridan Dr. and Miramar Dr. The road has three travel lanes in each direction with a wide median strip. This section of the road is 6 to 8 years old, with a special use lane built in 2013. Soon after construction in 2013, FDOT reported severe raveling issues. The research team visited this field project in October 2015 to perform field drainability tests and obtain a set of field cores from the southbound outside lane near Exit 98. During the field visit, the pavement was under maintenance and rehabilitation with only the express lanes available for inspection. In general, the pavement appeared in poor condition, with visible delamination, potholes, and high severity and extent raveling, as shown in Figure 3-2.

Figure 3-2. Pavement distress observed on I-75 between Sheridan Dr. and Miramar Dr.

A field drainability test was performed at five locations about 60 m apart from each other; at each location, measurements on the wheel path and between the wheel paths (i.e., center of the lane) were done to assess the openness of the mixture. The principle of the drainability test is to measure the time required to discharge a given volume of water channeled into the pavement surface. The apparatus used for this purpose is a 150 mm diameter by 450 mm tall PVC tube with a clear pipette attached to the side to view the water level in the permeameter (Figure 3-3a). Plumber's putty is placed around the base of the PVC tube to create a watertight seal between the permeameter and the pavement (Figure 3-3b).

(a) **(b)**

Figure 3-3. Field drainability test: (a) schematic (TxDOT 2009), (b) field setup.

During the test, water is poured into the permeameter up to a level a few centimeters above the upper marking line on the pipette. Then, the time required for the water level to drop from the upper marking line to the lower marking line, which are 25.4 cm apart, is measured and recorded as the water flow value (WFV). Although the WFV cannot be considered a coefficient of permeability because the area and direction of flow during the test is not controlled, the rate of discharge is an indicator of the mixture's drainability. A maximum WFV at the time of construction is specified by some agencies to ensure adequate mixture drainability; for example, TxDOT prescribes a maximum of 20 sec.

The field drainability test results are presented in Table 3-2. The drainability measurements at the first two locations were performed following the procedure described previously. However, for the measurements at Locations 3 to 5, the rate of water discharge was so slow that instead of waiting for the water to reach the lower marking line, the drop in water level from the upper marking line achieved after 5 min was measured. In general, pavements with a WFV longer than 5 min are considered impermeable. Thus, the values reported in Table 3-2 show that the OGFC in this field section could be classified as impermeable. The variability in the results could be attributed to the differences in the surface texture of the pavement caused by the varying extent and severity of raveling; in some cases, the rough surface texture caused small gaps between the plumber's putty and the pavement, allowing water to runoff on the surface of the pavement rather than through it.

Table 3-2. Permeability Results for I-75 Field Project

Location	WFV (sec)	Water Drop (cm)	Rate of Discharge (m/day)
1 (wheel path)	591	25.4	37.1
1 (center of lane)	1176	25.4	18.7
2 (wheel path)	735	25.4	29.9
2 (center of lane)	300	7.6	21.9
3 (wheel path)	300	19.0	54.7
4 (wheel path)	300	1.5	4.3
5 (wheel path)	300	22.2	63.9
	Average		32.9

FDOT helped the research team obtain 150 mm diameter cores from the field project. The cores were several inches deep, including the OGFC surface layer of about 22 mm and several dense-graded under layers. A total of 10 cores were collected, five from the center of the lane and five from the right wheel path. All cores, except for a subset used in the Cantabro test (as noted below), were trimmed to eliminate the under layers. The cores were tested using the following standard laboratory test methods: ignition oven (AASHTO T 308), IDT strength test (AASHTO T 283), Cantabro loss test (AASHTO TP 108), and FDOT falling head permeameter test (FM 5-565). Two replicates from the center of the lane and two from the wheel path were used for the IDT test. The average results of all four replicates are shown in Table 3-3. After IDT, one replicate from the center of the lane and one replicate from the wheel path were tested in the ignition oven, and the average results are shown in Table 3-3. For Cantabro, the standard test method requires specimens 115 ± 5 mm thick, but since the thickness of the surface layer was only about 22 mm, specimens of both sizes (with and without the pavement under layers) were tested, as explained below. Only the average of the two thin replicate specimens is listed in Table 3-3. One replicate was employed in the permeameter test with a slight modification to the test setup, as detailed below, and the measured value is reported in Table 3-3.

Table 3-3. Laboratory Test Results for I-75 Field Cores

Laboratory Test	Test Parameter	Test Results
Ignition Oven	Binder Content (%)	4.6 (6.0 per mix design)
IDT Strength Test	IDT Strength (kPa)	921.0
Cantabro Loss Test	Abrasion Loss (%)	75.6 (22 mm specimens)
FDOT Falling Head Permeameter Test	Coefficient of Permeability (m/day)	25.2

The tested field cores had an average AV content of 19.2 percent measured via dimensional analysis. According to the ignition oven test results, the average binder content was 4.6 percent, which was 1.4 percent lower than the mix design OBC (i.e., 6.0 percent). The low binder content in the mix could be one of the primary reasons behind the raveling distress observed in the field. Figure 3-4 presents the aggregate gradations from the mix design and the one resulting after the ignition oven test. As illustrated, the gradation of the field cores was finer than the gradation specified in the mix design.

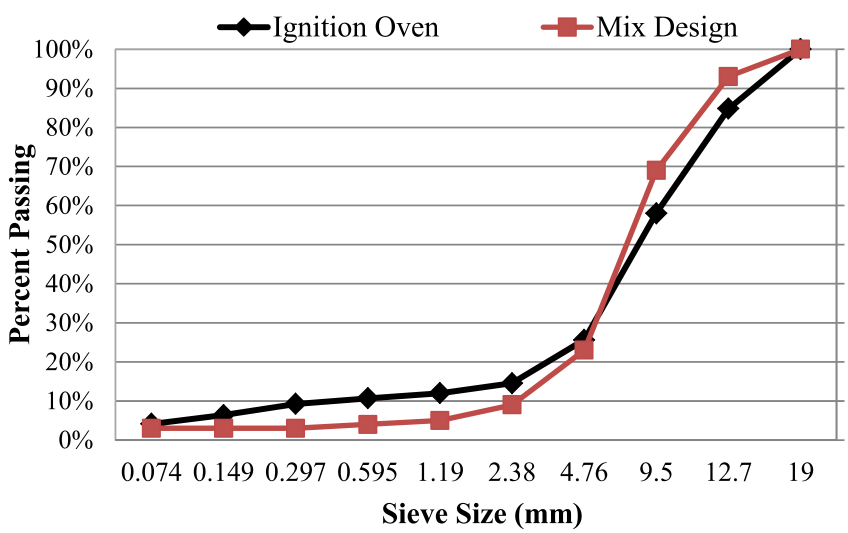

Figure 3-4. Aggregate gradations for the I-75 field project.

As previously mentioned, two sets of specimens were prepared for the Cantabro loss test; one set consisted of only the OGFC surface layer (approximately 22 mm thick), and the other consisted of the OGFC surface layer plus about 93 mm of the dense-graded under layers (approximately 115 mm thick in total, which is the standard Cantabro size), as shown in Figure 3-5. The idea was to have standard-size Cantabro specimens under the assumption that the OGFC layer was going to be the most susceptible during abrasion and any material loss would occur primarily in that layer.

During testing, the thin specimens (i.e., OGFC surface layer only) were not able to retain their integrity and disintegrated into several pieces, as shown in Figure 3-6. The weight of all individual pieces was considered as the final mass of the specimen for estimating the percent abrasion loss. Figure 3-7 presents a standard-size Cantabro specimen after testing (i.e., OGFC surface layer plus dense-graded under layers). As can be observed, the loss of material was more significant in the OGFC surface layer than in the dense-graded under layer. Regardless, material loss is still apparent in the under layers, especially at the bottom edge of the specimen. Since it was hard to quantify the loss from the surface layer and the under layers, these results were not reported in Table 3-3.

Figure 3-5. Specimens used for Cantabro loss test; OGFC surface layer only (left), OGFC surface layer plus dense-graded under layers (right).

Figure 3-6. OGFC surface layer specimen after Cantabro loss test.

Figure 3-7. OGFC surface layer plus dense-graded under layers specimen after Cantabro loss test.

The FDOT falling head permeameter test was performed in accordance with FM 5-565. In this test, saturated 150 mm diameter specimens are placed inside an apparatus that seals around the sides of the specimen (Figure 3-8). A fixed amount of water (500 ml) is then permitted to flow from a graduated cylinder through the specimen. The amount of time it takes (in seconds) for the water to flow through the specimen is recorded. The procedure is repeated until three recorded times fall within 4 percent of each other. The coefficient of permeability, k, is then calculated using Equation 3-1 and reported in whole units $\times 10^{-5}$ cm/s (FDOT 2014b). For comparison with standard values reported in the literature, this number was converted to m/day.

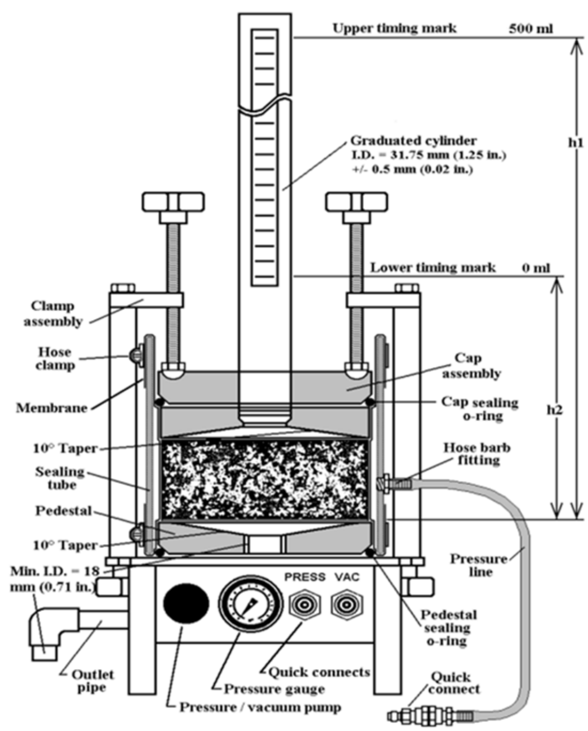

Figure 3-8. Schematic of FDOT falling head permeameter test (FDOT 2014b).

$$k = \frac{aL}{At} \ln \frac{h_1}{h_2} \times t_c \qquad (3\text{-}1)$$

Where:
a = inside cross-sectional area of the graduated cylinder, cm^2.
L = average thickness of the test specimen, cm.
A = average cross-sectional area of the test specimen, cm^2.
t = elapsed time between h_1 and h_2, sec.
h_1 = initial head across the test specimen, cm.
h_2 = final head across the test specimen, cm.
t_c = temperature correction for viscosity of water from 20°C standard.

A slight modification was done to the standard procedure given the fact that the rubber membrane was not able to seal the sides of the thin OGFC surface layer specimens when sitting on the equipment's pedestal. To address this issue, a 50 mm thick porous stone with a 18 mm hole drilled in the center to match the outlet pipe diameter was placed under the field cores during testing, as shown in Figure 3-9. This allowed for rising up the OGFC surface layer field core specimens, improving their contact area with the rubber membrane, and achieving a proper seal. The porous stone was saturated before being placed in the equipment and was tested without the field cores. The time required to drain 500 ml was 1.5 sec on average; therefore, the contribution of the porous stone was taken into account by subtracting 1.5 sec from the total time required to drain 500 ml from the combined porous stone plus field core specimen setup. The resulting coefficient of permeability is reported in Table 3-3. In agreement with the field permeameter evaluation, the coefficient of permeability was well under the recommended threshold for OGFC of 100 m/day.

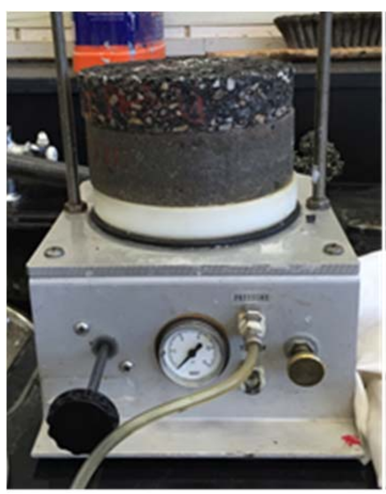

Figure 3-9. Modified falling head permeability setup with a 50 mm porous stone placed under the OGFC surface layer field core specimen.

Finally, one core was used for extraction and recovery per ASTM D5404. The PG of the extracted binder resulted in a high-temperature grade of more than 88°C, which exceeded the rheometer upper-temperature limit. The continuous low-temperature grade was −16.7.

3.2.2. Field Project on US-1

This field project was located on US-1 starting at St. Lucie Boulevard in Fort Pierce and extending approximately 2.5 mi toward the north. The field project had two lanes in each direction with a median strip and occasional crossover lanes. The original construction was completed in June 2006. The research team visited the field site in October 2015, performed field drainability tests, and obtained a set of field cores from the northbound outside lane near St. Lucie Boulevard (Figure 3-10). In general, the pavement was in a good condition; no major pavement distresses other than a small amount of raveling from the wheel path on the outside lanes were observed during the field visit.

Field drainability tests were performed at multiple locations on the wheel path and between the wheel paths (i.e., center of the lane) on the northbound outside lane, as shown in Figure 3-11. The drop in water level from the upper marking line achieved after 5 min was measured and is summarized in Table 3-4. Since none of the locations achieved a drop in water level of 25.4 cm in less than 5 min, the OGFC surface layer could be classified as impermeable. In some instances, the water runoff occurred on the surface of the pavement rather than through it.

Figure 3-10. Coring on US-1 on wheel path and between the wheel paths.

Figure 3-11. Field drainability testing on US-1.

Table 3-4. Permeability Results for US-1 Field Project

Location	WFV (sec)	Water Drop (cm)	Rate of Discharge (m/day)
1 (wheel path)	300	2.5	7.2
2 (center of lane)	300	3.8	10.9
3 (wheel path)	300	11.4	32.8
4 (center of lane)	300	12.1	34.8
5 (wheel path)	300	12.7	36.6
6 (center of lane)	300	24.1	69.4
7 (wheel path)	300	10.1	29.1
8 (center of lane)	300	20.3	58.5
	Average		34.9

As with the I-75 field project, FDOT helped the research team obtain ten 150 mm diameter field cores, five from the center of the lane and five from the right wheel path. The cores were several inches deep, including the OGFC surface layer of about 17 mm and several of the dense-graded under layers. All cores, except for a subset used in the Cantabro test (as noted below), were trimmed to eliminate the under layers. The cores were subjected to the same standard laboratory test methods: ignition oven (AASHTO T 308), IDT strength test (AASHTO T 283), Cantabro loss test (AASHTO TP 108), and FDOT falling head permeameter test (FM 5-565). Two replicates from the center of the lane and two from the wheel path were used for the IDT test, although three out of the four specimens were so thin that they were not able to stay centered in the frame during loading. Thus, the result of only one of the center-of-lane specimens is reported in Table 3-5. After the IDT test, one replicate from the center of the lane and one replicate from the wheel path were tested in the ignition oven, and the average results are shown in Table 3-5. For Cantabro and FDOT falling head permeameter tests, the same modifications used when testing the I-75 field cores were followed. For Cantabro, the average of the two replicate specimens 19 mm thick is listed in Table 3-5. One replicate was employed in the permeameter, and the measured value is reported in Table 3-5.

Table 3-5. Laboratory Test Results for US-1 Field Cores

Laboratory Test	Test Parameter	Test Results
Ignition Oven	Binder Content (%)	5.8 (7.1 per mix design)
IDT Strength Test	IDT Strength (kPa)	963.7
Cantabro Loss Test	Abrasion Loss (%)	55.2 (26 mm specimen)
FDOT Falling Head Permeameter Test	Coefficient of Permeability (m/day)	17.6

The field cores had an average AV content of 18.6 percent. According to the ignition oven test results, the average binder content was 5.8 percent, which was 1.3 percent lower than the mix design value (i.e., 7.1 percent). Figure 3-12 presents the aggregate gradation from the ignition oven test. As illustrated, the gradation of the field cores was finer than the gradation specified in the mix design.

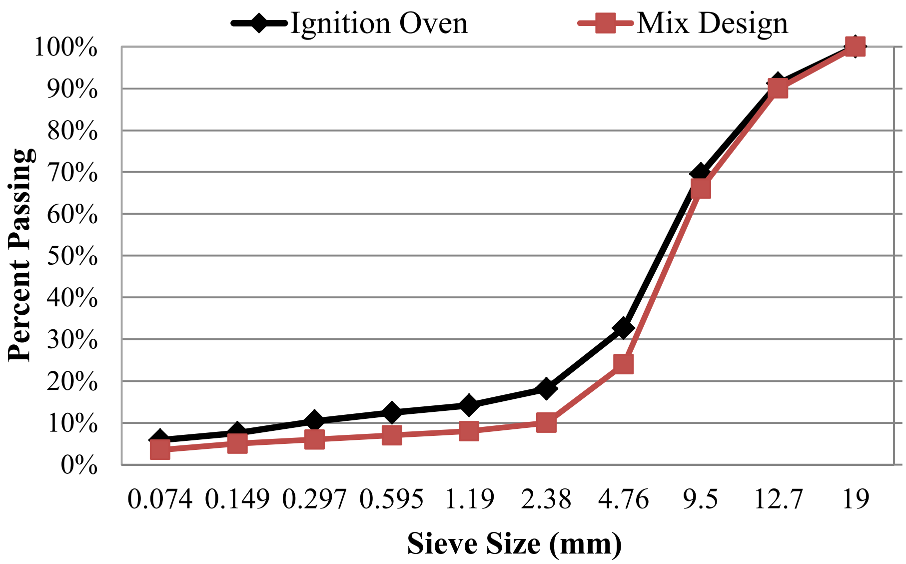

Figure 3-12. Aggregate gradations for the US-1 field project.

Finally, one core was used for extraction and recovery per ASTM D5404. The PG of the extracted binder resulted in a high-temperature grade of more than 88°C, which exceeded the rheometer upper-temperature limit. The continuous low-temperature grade was −18.0.

CHAPTER 4 . MATERIAL CHARACTERIZATION

A comprehensive characterization of the selected materials was performed by means of standardized and advanced testing methodologies. The results were used to understand the observed field performance and served as inputs to the numerical model detailed in Chapter 5. The methods and results obtained are detailed next.

4.1. Aggregate Properties

FDOT provided basic physical properties of the selected aggregates including bulk specific gravity, Los Angeles abrasion, water absorption, and insoluble residue through its Aggregate Analysis System database. These properties are summarized in Table 4-1. Only water absorption data were available for the granite aggregate, and the bulk specific gravity was estimated from a recently completed FDOT project that employed that material.

Table 4-1. Physical Properties of the Aggregates Provided by FDOT

Property	Limestone	Granite
Bulk Specific Gravity	2.420	2.600[a]
Los Angeles Abrasion	31.0	N/A[b]
Water Absorption	2.64	0.78
Insoluble Residue	15.7	N/A[b]

[a] Estimated from FDOT Project BDS15-977-01.
[b] Data not available in FDOT database.

Advanced aggregate tests, which are summarized in Table 4-2, were conducted to determine morphological and thermodynamic properties of the limestone and granite aggregates.

Table 4-2. Properties of the Aggregates Measured by TTI

<table>
<tr><th>Aggregate Property</th><th>Test Method/Apparatus</th><th>Test Standard</th><th>Test Parameter</th></tr>
<tr><td>Form</td><td rowspan="3">Aggregate Image Measurement System (AIMS)</td><td rowspan="3">AASHTO TP81 and AASHTO PP64</td><td rowspan="3">Form, Texture, and Angularity Indices</td></tr>
<tr><td>Texture</td></tr>
<tr><td>Angularity</td></tr>
<tr><td>Surface Free Energy (SFE)</td><td>Universal Sorption Device (USD)</td><td>Draft AASHTO standard</td><td>SFE components</td></tr>
</table>

4.1.1. Morphologic Characteristics

AIMS was used to provide quantitative values for the aggregate angularity, form, and texture. Figure 4-1 provides an illustration of these properties. Angularity refers to the sharpness of the edges of the aggregate, while form refers to the overall shape of the particle. Texture refers to the surface smoothness/roughness of the aggregate at a microscopic level, which does not affect the shape of the particle (Masad 2005). These properties have been shown to impact the structural performance and skid resistance of asphalt mixtures (Gates et al. 2011).

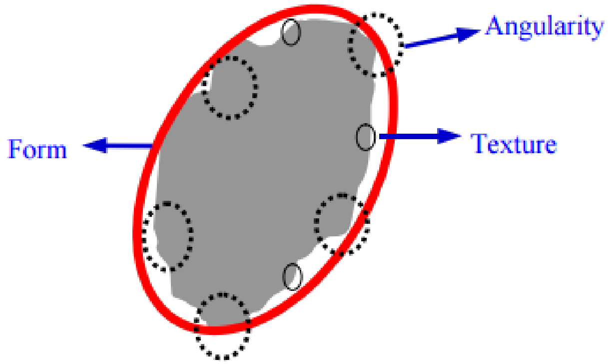

Figure 4-1. Illustration of aggregate morphological characteristics: angularity, form, and texture (Masad 2005).

AIMS is an automated, nondestructive, image-based system used to collect and analyze images of individual aggregate particles. The latest version of the equipment (i.e., AIMS2), shown in Figure 4-2, consists of a high-resolution camera, a variable magnification microscope, top and back lighting, and a rotating circular tray. Back lighting is used to create black-and-white images with the profile of the aggregate, from which the shape and angularity are measured; top lighting and variable magnification are used to capture grayscale images to perform texture estimates. A computer controls the image acquisition hardware and analyzes the data using special software that employs wavelet decomposition and a gradient-based method to analyze texture and angularity, respectively. Form analysis includes computing the shape factor and sphericity index, based on the length of the axis of the particle; the width and length are calculated by an eigenvalue decomposition method on the black-and-white profile projection, and depth is estimated with the microscope. The main advantages of the analysis methods are that they account for the effect of color variation on the surface of the aggregate, measure the form of the particle in all three dimensions, and significantly reduce the noise associated with image acquisition.

Figure 4-2. Second-generation Aggregate Image Measurement System—AIMS2 (Gates et al. 2011).

The aggregate sizes that can be analyzed using AIMS2 range from material retained on the No. 200 sieve (0.075 mm), up to 25 mm. Aggregates retained on the No. 4 sieve (4.75 mm) are considered coarse aggregates, while those passing the No. 4 sieve are considered fine aggregates. The system reports sphericity, angularity, flat-and-elongated ratio, and texture for coarse aggregates, but only angularity and 2D form for fine aggregates. Therefore, results for angularity, form, and texture were obtained for only the coarse portion of each aggregate type. Prior to testing, each aggregate was separated into groups by sieve size including 19.0 mm, 12.5 mm, and 4.75 mm. Once separated, the aggregates were washed over the No. 8 sieve (2.36 mm) to remove any surface dust and then allowed to oven dry overnight at 110°C. After cooling, individual aggregate particles were placed in plastic bags and stored at room temperature for testing.

For testing, individual aggregate particles were placed in the indentation of the circular trays, separating and distributing them evenly to allow the high-resolution camera to detect individual particles. Fifty particles are required for characterization of the coarse aggregate fractions. The circular tray was placed inside the chamber and closed to prevent outside light sources to affect the measurements. The tray rotated during measurement, positioning the aggregate particles in the back lighting and under the camera for imaging. The exact location of each particle was tracked to ensure that only particles that fell within the AIMS measurement specifications were included. A second scan was performed using the top lighting for height estimates, and a third scan captured the images used for texture evaluation. These three scans are needed for the coarse aggregate analysis.

Testing of the limestone and granite aggregates was conducted in a single day. AIMS2 analyzed the 50 particles from each aggregate size and output the distribution of values for each property as well as summary tables with a single value for angularity, sphericity, and texture based on the average for each parameter across the 50 particles analyzed for the group.

The software provided the results for each variable using predetermined indices as follows:

- Angularity: 1 (perfect circle) to 10,000:
  - 1 to 2100 is rounded.
  - 2100 to 3975 is moderate.
  - 3975 to 5400 is high.
  - 5400 to 10,000 is extremely angular.
- Sphericity: 0 to 1 (perfect sphere).
- Texture: 0 to 1000:
  - 0 to 200 is smooth.
  - 200 to 500 is moderate.
  - 500 to 750 is high.
  - 750 to 1000 is extreme.

The angularity, sphericity, and texture values for each aggregate size were then combined into a single value for each aggregate type. This was accomplished using Equation 4-1 by weighting the parameter value for each aggregate size based on the individual percent retained for that sieve size (as listed in the mix design) as a portion of the total coarse aggregate fraction (i.e., larger than the No. 4 sieve, or 4.75 mm). The final weighted averages for the three parameters for each aggregate type are shown in Table 4-3 and illustrated in Figure 4-3 with the scale of each parameter.

$$\frac{\sum(\%\ \mathrm{Ret.}_i \times \mathrm{Angularity}_i / \mathrm{Texture}_i / \mathrm{Sphericity}_i)}{\sum \%\ \mathrm{Retained}_{\mathrm{Coarse\ Agg.}}} \tag{4-1}$$

Table 4-3. Aggregate Angularity, Sphericity, and Texture Properties

Property	Limestone	Granite
Angularity	2,900.2	3,047.2
Sphericity	0.73	0.67
Texture	142.7	227.6

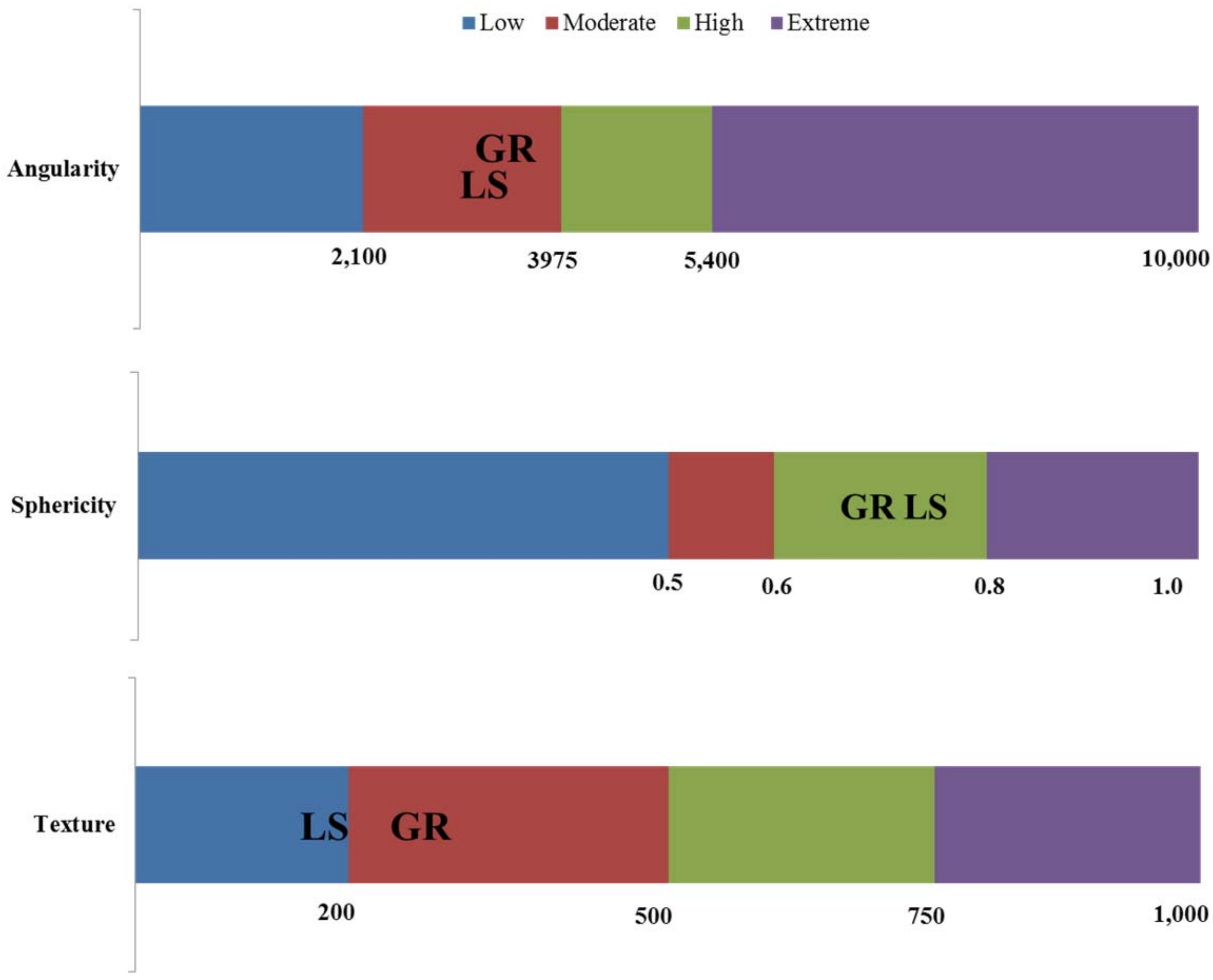

Figure 4-3. Aggregate morphological properties and scale (GR = granite aggregate; LS = limestone aggregate).

The limestone aggregate has moderate angularity, high sphericity, and low texture. The granite aggregate also has moderate angularity and high sphericity but high texture (though on the low end of the range). A comparison of the aggregate angularity, sphericity, and texture for the two aggregates reveals limited differences between the limestone and granite, though the higher texture value for granite may create a better interface for mechanical bonding between aggregate and binder in the asphalt mixtures.

4.1.2. Surface Free Energy

SFE is a fundamental thermodynamic material property commonly used to characterize aggregates. SFE is defined as the amount of work or energy required to create a new unit of surface of that material under vacuum conditions. When used to compute the work of adhesion, it is possible to determine the amount of energy or work required to separate two different materials in contact at their interface (i.e., the energy required to create a new unit of surface in each material or adhesion fracture). Thus, this thermodynamic quantity is an indicator of adhesion compatibility and resistance between different materials (e.g., binder and aggregate). This measure is ideal to quantify the resistance to raveling (i.e., the thermodynamic susceptibility of the aggregate-binder adhesive bond to be disrupted by the effect of mechanical loading and/or the presence of moisture) of various material combinations and determine which yields the highest adhesive bond with and without the presence of moisture.

The SFE components of each aggregate were determined by researchers at the University of Oklahoma using the USD, which operates under the principle of static vapor sorption. In the USD, an aggregate sample is introduced in an open container and suspended inside the testing chamber. The chamber is closed and subjected to vacuum. Then, a probe vapor is released and allowed to adsorb onto the surface of the aggregate until a predetermined vapor pressure is reached. A highly sensitive magnetic balance measures the amount of probe vapor that is adsorbed on the surface of the aggregate. Once the adsorption level reaches equilibrium, an additional amount of probe vapor is added until the next predetermined vapor pressure is achieved. This process is repeated 8 to 10 times at various predetermined vapor pressures. An isotherm is generated using the mass adsorbed at each vapor pressure for each of the probe vapors: water, methyl propyl ketone (MPK), and n-hexane. From the isotherm, the SFE components—which include the Lifshitz-van der Waals (LW) component, γ^{LW}; the Lewis acid component, γ^{+}; and the Lewis base component, γ^{-}—are determined. Details about the SFE calculations are included in Appendix B. The Branauer, Emmett, and Teller equation was used to estimate the specific surface area (SSA) of the aggregate from the adsorption isotherm for n-hexane (Little and Bhasin 2006). The resulting SFE components for the limestone and granite aggregates are presented in Table 4-4. Further analysis of these data, in combination with the binder SFE components, is presented in the next section.

Table 4-4. Surface Free Energy of the Aggregates

Aggregate Type	Surface Energy Components (ergs/cm^2)[a]				Specific Surface Area (m^2/g)
	γ^{Total}	γ^{LW}	γ^{+}	γ^{-}	
Limestone	90.2	49.0	1.9	221.4	0.55
Granite	515.2	51.9	86.7	619.3	0.35

[a] 1 erg = 1×10^{-7} J.

4.2. Binder Properties

The PMA and ARB binders were provided by FDOT in two conditions: neat (without any additives) and with a 0.5 percent (by weight of binder) liquid antistrip agent that was added at the terminal. Table 4-5 summarizes the tests executed to evaluate the binder properties. In addition, the PG of the binders was verified according to AASHTO M320.

Table 4-5. Measured Properties of the Binders

Binder Property	Test Method/Apparatus	Test Standard	Test Parameter
Stiffness before and after Rolling Thin Film Oven (RTFO) and Pressure Aging Vessel (PAV) Aging	Dynamic Shear Rheometer (DSR)	ASTM D7175	G* Phase Angle (δ) Master Curve Glover-Rowe (G-R)
SFE	Wilhelmy Plate (WP)	TTI Test Method	SFE Components

4.2.1. Rheological Characteristics

The continuous and rounded PG of the PMA and ARB binders with and without additives is listed in Table 4-6. Two replicates were measured at each temperature. All binders, except for ARB with liquid antistrip, resulted in a rounded PG grade of 76-22.

Table 4-6. PG of the Binders

Binder Type	Liquid Antistrip	PG Grade	
		Continuous	Rounded
PMA	No	81.9-24.4	76-22
ARB	No	80.8-22.5	76-22
PMA	Yes	81.9-26.7	76-22
ARB	Yes	79.2-28.0	76-28

To determine the response of each binder to aging, samples were run in the DSR in unaged, short-term aged (i.e., RTFO), and long-term aged (i.e., PAV) conditions. Two replicates were run for each test condition, and binder master curves were produced to determine binder susceptibility to aging. The two binder types, PMA and ARB, were tested using the DSR following ASTM 7175 with a modified frequency sweep method. The complex shear modulus, G*, and phase angle, δ, were measured at different temperatures and frequencies. Figure 4-4 provides an illustration of the testing conditions.

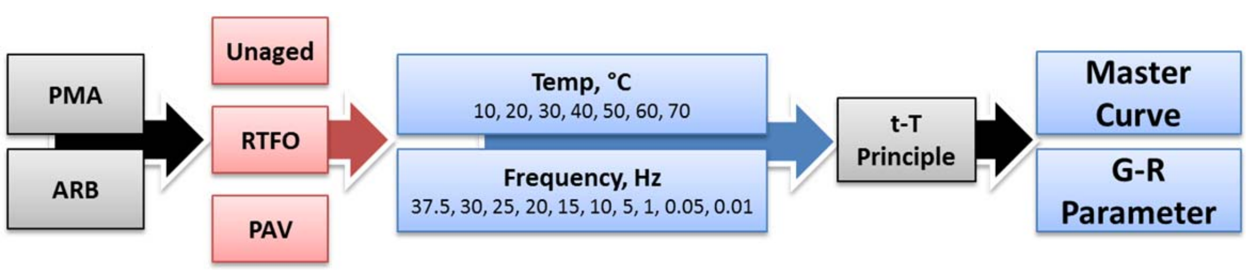

Figure 4-4. DSR testing methodology.

Using the time-temperature (t-T) superposition, raw test data from the DSR were shifted to a reference temperature of 20°C using a shift factor, a_T, applied to the loading frequency. This t-T adjusted frequency is referred to as the reduced frequency. The extended Christensen, Anderson, and Marastenau (CAM) model shown in Equation 4-2 was used to fit the data, and the Williams-

Landel-Ferry (WLF) model shown in Equation 4-3 was used to calculate the t-T shift factors (Kim et al. 2011).

$$|G^*| = G_g * \left(1 + \left(\frac{f_c}{f}\right)^k\right)^{-\frac{m_e}{k}} \tag{4-2}$$

Where:
G_g = maximum shear modulus or glass modulus, Pa.
f = reduced frequency, Hz.
f_c, m_e, k = fitting coefficients.

$$\log a_T = \frac{C_1(T-T_R)}{C_2+T-T_R} \tag{4-3}$$

Where:
T_R = reference temperature, °C (20°C for this experiment).
C_1, C_2 = fitting coefficients.

After applying the t-T superposition principle to shift the test data measured from 10°C through 70°C to the reference temperature, a binder stiffness master curve was produced. The master curve describes the time dependency of the binder, while the amount of shift required to create a smooth function reflects the temperature dependency of the material. A summary of the master curve fitting parameters is shown in Table 4-7.

Table 4-7. Binder Master Curve Coefficients and G-R Parameter

Binder Type	G*			a_T		G*	δ	G-R Parameter
	f_c	k	m_e	C_1	C_2	@ f = 0.005 rad/s		
PMA								
Unaged	385.3	0.23	0.74	−15.2	114.8	5.0E+04	85.5	307.2
RTFO	338.6	0.22	0.71	−15.6	115.8	8.0E+04	84.8	646.2
RFTO+PAV	85.4	0.17	0.64	−24.4	183.5	3.5E+05	79.1	12,799.4
ARB								
Unaged	659.3	0.2	0.75	−13.7	104.8	2.8E+04	84.6	243.0
RTFO	102.8	0.17	0.75	−15.6	112.2	8.4E+04	78.8	3,263.3
RFTO+PAV	64.6	0.14	0.64	−26.5	206.3	3.0E+05	74.7	21,409.0

The resulting master curves for both binders at multiple aging states are plotted in Figure 4-5. In the unaged state, both binders have parallel trendlines across the full spectrum of loading temperatures and frequencies, with the PMA binder being slightly stiffer than the ARB binder. Aging appears to minimally affect both binders at low temperatures or high reduced loading frequencies. The effect of aging is more pronounced at high temperatures or low reduced loading frequencies. Aging appears to affect the ARB more significantly at higher temperatures because the magnitude of the increase in complex shear modulus at intermediate and higher temperatures is greater for ARB than PMA from an unaged to RTFO state.

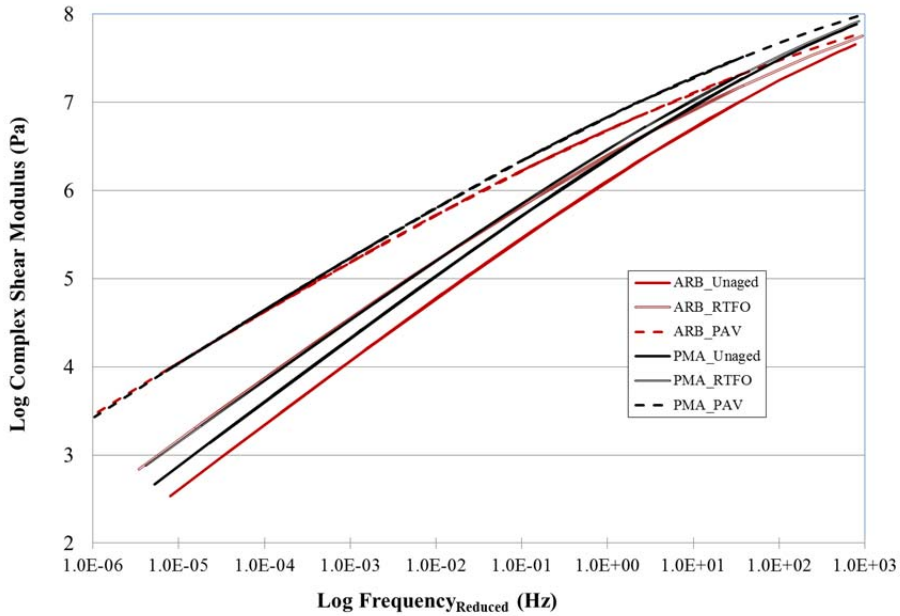

Figure 4-5. Master curves for PMA and ARB binders.

To better quantify the expected impact of aging on the two binder types, an additional parameter was examined. Glover et al. (2005) originally developed a single-point rheological parameter that provided a good predictor of binder resistance to failure due to oxidative hardening. Attained through DSR testing at 15°C and 0.005 rad/s, the parameter had excellent correlation with ductility and, most importantly, was found to be very reliable in predicting cracking performance with aging in the field. Rowe et al. (2014) modified the Glover parameter and attained the form of the G-R parameter shown in Equation 4-4.

$$\text{G-R Parameter} = \frac{G^{*}(\cos\delta)^{2}}{\sin\delta} \tag{4-4}$$

In comparisons with cracking in the field, Rowe et al. (2014) showed that the onset of early raveling could be predicted with G-R parameter values ≥ 180 kPa and that significant cracking occurred with a G-R parameter value ≥ 450 kPa. This range of values for the G-R parameter, between 180 kPa and 450 kPa, is considered the binder damage zone.

The G-R parameters for each binder type and aging state were estimated from the master curves and are listed in Table 4-7 and plotted in Figure 4-6 on a Black Space diagram. The Black Space diagram shows G* and δ on a single graph, which is useful to visualize the effect of aging on the rheological properties of the binder. The binder damage zone is also plotted on the Black Space diagram, representing the previously described G-R parameter thresholds of 180 kPa and 450 kPa. Binders that fall below this zone are not expected to experience cracking.

As binder ages, it becomes stiffer and thus more prone to fracture. This behavior manifests as an increase in G* and a decrease in δ as the binder becomes less ductile. DSR testing confirmed this expectation, as shown in Figure 4-6, where the G-R parameter shifts up and to the left as the PMA and ARB binders age. From the Black Space diagram, it is clear that neither binder is susceptible to failure due to oxidative hardening and that ARB ages more rapidly than PMA.

Indeed, the G-R parameter for ARB after RTFO aging was 13 times higher as compared to the unaged value, while PMA only experienced a twofold increase in the G-R parameter after the same short-term aging. This finding indicates that the ARB binder could be more susceptible to aging during plant production as compared to the PMA binder. Based on the PAV data points, the effect of long-term aging was also more pronounced for ARB than for PMA. Overall, it can be said that the ARB binder appears to be more susceptible to aging as compared to the PMA binder.

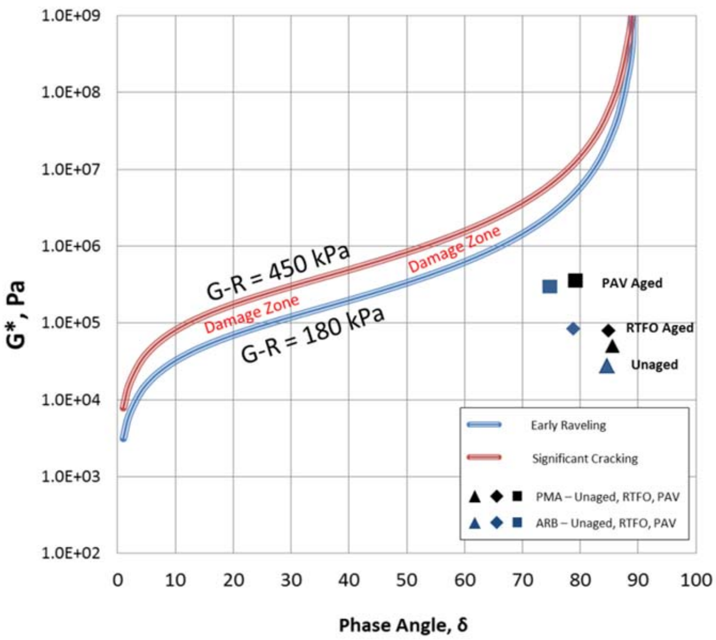

Figure 4-6. G-R parameters in Black Space diagram for PMA and ARB binders.

4.2.2. Surface Free Energy

SFE components of each binder type (PMA and ARB) were evaluated in unaged, RTFO, and PAV conditions. In addition, filler samples were tested in the WP. In the case of limestone, the filler samples included material passing the No. 200 sieve (no mineral fiber), and in the case of granite, the filler samples included the material passing the No. 200 sieve and lime (1 percent by replacement of the material passing the No. 200 sieve). The proportion of filler to the total weight of the filler sample (i.e., filler plus binder) was 47 percent. The filler samples were prepared by warming up a premeasured amount of binder in an aluminum tin and adding to that a premeasured amount of filler that had also been warmed up to the same temperature in an oven. The mixing was done manually using a wood stick. Once thoroughly mixed, the material was used to prepare the WP and DSR specimens.

The WP apparatus is based on equilibrium of kinetic forces and uses thin glass slides uniformly coated with binder that are submersed in liquids of known properties (i.e., reference liquids). A dynamic contact angle analyzer was used to measure the contact angles of each binder and filler sample (Figure 4-7a). During testing, the coated glass slides were suspended from a highly accurate balance inside the testing equipment. Then, the coated glass slide was immersed and further withdrawn at a very slow and constant speed from a container filled with the reference liquid, as shown in Figure 4-7b. The contact angle was calculated using a relationship between the weight of the slide in air and its weight as it was being submerged, the SFE of the reference liquid, and the geometry of the slide. The average contact angles measured after immersing the coated glass slides in five reference liquids were used to determine the SFE components (γ^{LW}, γ^{+}, and γ^{-}) for each binder type and condition. The reference liquids used were (a) distilled water, (b) glycerol, (c) ethylene glycol, (d) formamide, and (e) diiodomethane.

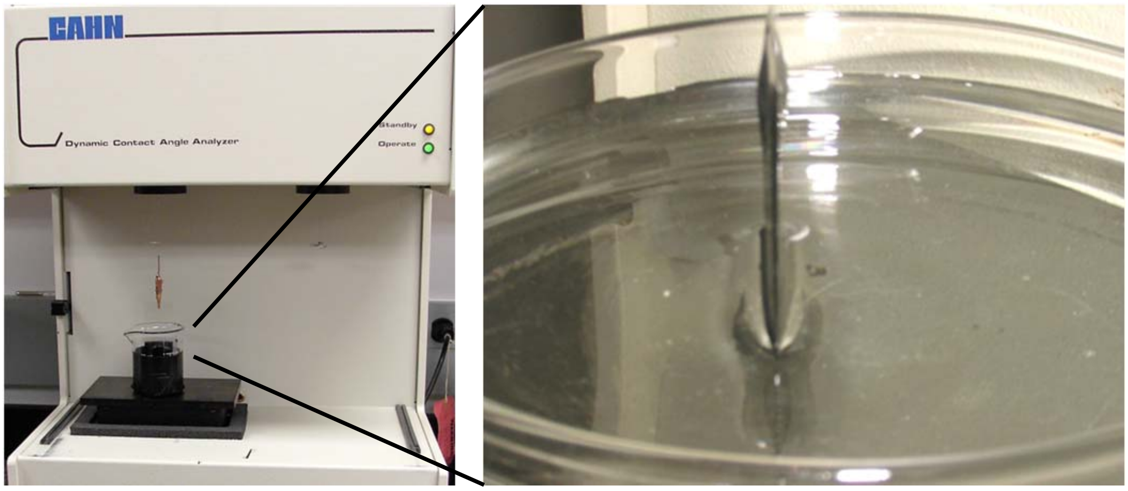

(a) (b)

Figure 4-7. Wilhelmy Plate: (a) dynamic contact angle analyzer equipment, (b) coated thin glass slide submerged in reference liquid.

This procedure required a number of replicate measurements to generate repeatable results. Particular care was given to producing coated glass slides of consistent thickness. This was found to reduce the variability of contact angle measurements between slides, requiring fewer replicates and improving the precision of the data. Once the contact angle data were acquired, the Young-Dupree equation (Equation 4-5) was used to calculate the SFE components of each binder sample. Equation 4-5 shows the relationship between the work of adhesion, WLS (from Equation B-2 in Appendix B); the measured contact angle, θ; and the SFE components of both the reference liquids and the binder or filler material (Little and Bhasin 2006).

$$W_{LS} = \gamma_L(1 + \cos\theta) = 2\sqrt{\gamma_S{}^{LW}\gamma_L{}^{LW}} + 2\sqrt{\gamma_S{}^{+}\gamma_L{}^{-}} + 2\sqrt{\gamma_S{}^{-}\gamma_L{}^{+}} \qquad (4\text{-}5)$$

In Equation 4-5, the total SFE (γ_L) and the three SFE components (γ^{LW}, γ^{+}, and γ^{-}) for the reference liquids are known, and the contact angle is measured using the WP. The unknowns are the SFE components of the solid, namely the binder or filler samples. By using the measured contact angles resulting from submersing the coated glass slides in the reference liquids, a system of equations can be solved for the unknowns. The resulting SFE components for the PMA and ARB binders at each aging condition are summarized in Table 4-8.

The value of total SFE for each binder ranged from 12.2 to 22.2 ergs/cm^2, which is at the low range as compared to typical results for other binders (i.e., 15 to 45 ergs/cm^2 [Little and Bhasin 2006]). The LW component was the most significant contributor to the surface energy of the binders with a range from 7.5 to 22.2 ergs/cm^2. The acid component for all binders was very small, ranging from 0.0 to 2.6 ergs/cm^2. The base component for all binders was small as well, ranging from 2.1 to 8.6 ergs/cm^2.

Table 4-8. Surface Free Energy of the Binders

Binder Type	Aging Condition	Surface Energy Components (ergs/cm²)[a]			
		γ^{Total}	γ^{LW}	γ^{+}	γ^{-}
PMA	Unaged	16.42	12.53	0.44	8.61
	RTFO	12.16	7.48	2.64	2.08
	RTFO + PAV	18.25	16.58	0.28	2.45
ARB	Unaged	22.21	22.21	0.00	3.43
	RTFO	21.90	21.90	0.00	5.29
	RTFO + PAV	20.94	19.98	0.05	4.83

[a] 1 erg = 1×10^{-7} J.

Using the aggregate and binder SFE data, combinations of aggregate and binder (with and without aging) were used to generate values for the thermodynamic adhesion, debonding, and cohesion potential at the aggregate-binder interface. Equations B-2 through B-5 found in Appendix B were used to calculate the following: W_{AB}, the work of adhesion; $W_{\mathrm{ABW}}^{\mathrm{wet}}$, the work of debonding or the reduction of surface free energy when water displaces the binder at the aggregate-binder interface; and W_{BB}, the work of cohesion of the binder. The results are shown in Figure 4-8.

For an aggregate to be durable and resistant to moisture damage, the work of adhesion between the aggregate and binder, W_{AB}, should be as high as possible. Similarly, the work of cohesion, W_{BB}, should be as high as possible to improve the durability of the binder. Conversely, a higher magnitude of $W_{\mathrm{ABW}}^{\mathrm{wet}}$, the work of debonding, indicates a high thermodynamic potential for water to replace the binder at the aggregate-binder interface; therefore, it is desirable that this quantity be as small as possible to reduce moisture susceptibility. Figure 4-8a shows that the aggregate-binder interface has a greater work of adhesion for granite than for limestone across all binder aging conditions. Thus, it would require more work to displace binder from the granite surface than from the limestone surface. However, Figure 4-8b shows that the average magnitude of the work of debonding at the aggregate-binder interface is greater for GR than for LS. This indicates that water has a greater affinity for granite as compared to limestone, and thus it would be more thermodynamically favorable to displace the binder from the granite than the limestone aggregate. Figure 4-8c indicates that the ARB binder has a slightly higher work of cohesion than the PMA binder does, indicating that ARB may be less moisture susceptible.

To further evaluate the aggregate-binder interaction, the energy parameters ER_1, ER_2, $ER_1 \times SSA$, and $ER_2 \times SSA$ were calculated using Equations B-6 through B-9 listed in Appendix B. These parameters are summarized in Table 4-9. The relevance of including SSA of the aggregate in the energy calculations is to acknowledge that the work of adhesion or debonding occurs over the entire surface of the aggregate. Higher SSA values usually correlate with high microtexture and a better bonding ability with the binder. The limestone+PMA combination had the highest $ER_1 \times SSA$ and $ER_2 \times SSA$ values for all aging conditions, which is desired, while the granite+ARB combination had the lowest values. Based on this comparative approach, a limestone PMA would yield the least moisture-susceptible asphalt mixtures, while the granite ARB combination would produce a mixture with higher moisture susceptibility. In addition, the combinations with PMA binder seem to be less moisture susceptible than their ARB counterparts for each aggregate type. Finally, it is interesting to note that based on the energy parameters, the moisture susceptibility rankings do not appear to be influenced by aging.

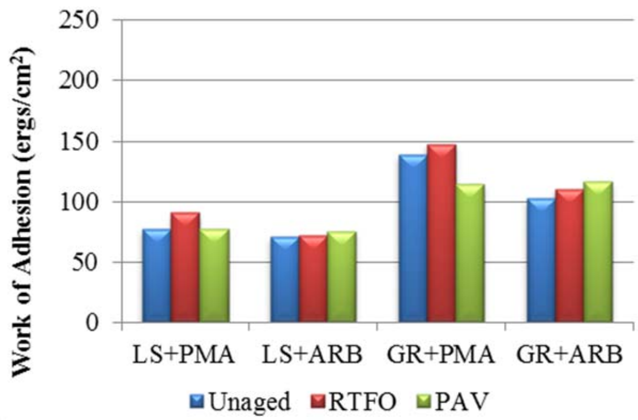

(a)

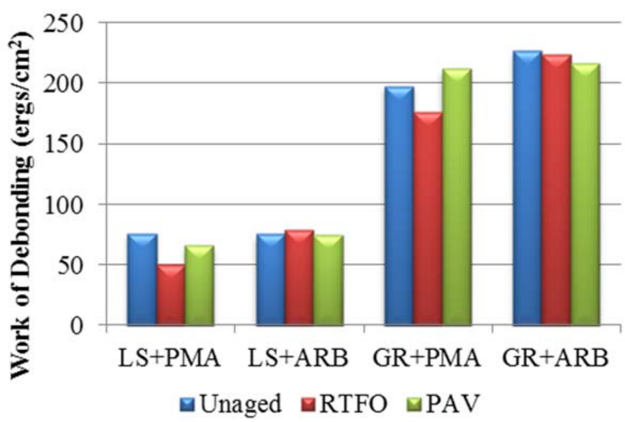

(b)

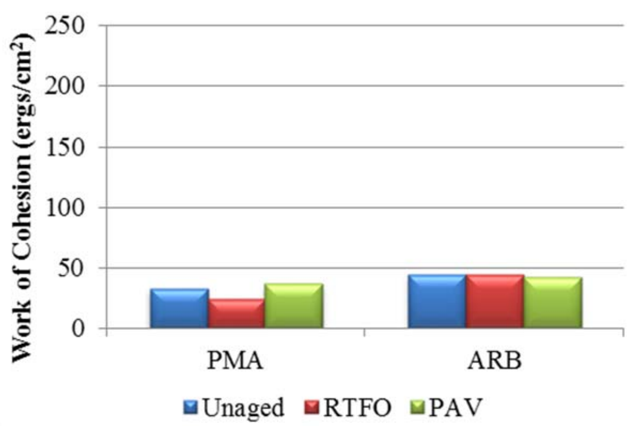

(c)

Figure 4-8. Thermodynamic potential of the aggregate-binder interface: (a) adhesion, (b) debonding, (c) cohesion (GR = granite aggregate; LS = limestone aggregate).

Table 4-9. Energy Parameters for the Aggregate-Binder Combinations

Aggregate-Binder Combination	Aging Condition	ER_1	ER_2	ER_1×SSA	ER_2×SSA
Limestone + PMA	Unaged	1.02	0.59	0.56	0.32
	RTFO	1.82	1.33	1.00	0.73
	PAV	1.17	0.62	0.64	0.34
Limestone + ARB	Unaged	0.94	0.36	0.52	0.20
	RTFO	0.91	0.36	0.50	0.20
	PAV	1.01	0.45	0.55	0.25
Granite + PMA	Unaged	0.70	0.54	0.25	0.19
	RTFO	0.83	0.70	0.30	0.25
	PAV	0.54	0.37	0.19	0.13
Granite + ARB	Unaged	0.45	0.26	0.16	0.09
	RTFO	0.49	0.30	0.17	0.11
	PAV	0.54	0.35	0.19	0.12

CHAPTER 5 . MIXTURE CHARACTERIZATION

Besides the characterization of the aggregates and binders, laboratory mixture specimens were prepared as described in this section. The objective was to evaluate the moisture susceptibility of the mixtures listed in Table 3-1 to (a) determine if a correlation exists between laboratory and field performance, and (b) provide additional input to the numerical model explained in the next chapter. Table 5-1 summarizes the tests conducted on the laboratory mixture specimens.

Table 5-1. Measured Properties of the Asphalt Mixtures

Mixture Property	Test Method/ Apparatus	Test Standard	Test Parameter	Specimen Height (mm)
Air voids	Dimensional analysis	ASTM D3203	Total percent air voids	–
Permeability	FDOT falling head permeameter	FM 5-565	Coefficient of permeability	115
Indirect tensile strength[a]	MTS	ASTM D6931	IDT strength and TSR	75
Cantabro[a]	Los Angeles abrasion without spheres	AASHTO TP 108	Percent abrasion loss	115
Rutting and stripping	HWTT	AASHTO T 324	Rut depth with load cycles and load cycles to stripping number	62

[a] Test performed before and after moisture conditioning.

5.1. Washed Sieve Analysis

The first step in producing the asphalt mixture specimens was to adjust the proportion of the aggregates in order to meet the job mix formula prescribed in the mix design. Limestone and granite aggregates were provided by FDOT in 5-gal buckets from the original quarries. Initially, FDOT recommended batching aggregates from each stockpile at the percentages prescribed in the job mix formula, but when FDOT performed the pie-plate analysis to estimate the OBC of the mixtures, it was determined that the current gradation of the individual aggregate stockpiles did not match the ones noted in the mix design. Therefore, all aggregates received from FDOT were oven dried at 110°C for 24 hr, allowed to cool, and separated into individual sieve sizes.

A washed sieve analysis was then conducted according to ASTM C117 to account for the fines in the aggregates. Two 2,500 g samples were batched according to the job mix formula. Both samples were covered with water and agitated to bring the fines into suspension. Then, the water was poured over a pair of nested sieves (the No. 16 sieve [1.18 mm] on top and the No. 200 sieve [75 µm] on bottom). This rinse process was repeated until the agitated water was clear, indicating most of the fines had been rinsed from the aggregates and the portion larger than the No. 200 sieve had been collected on that sieve. The remaining material from the bowl and the material retained on the two sieves were combined and dried to determine the percent of material passing the No. 200 sieve.

The iterative process of washed sieve analysis continued until the differences between the target gradation noted in the job mix formula of the mix design and the gradation after the washed sieve analysis were within 1 percent for particle sizes larger than the No. 4 sieve (4.75 mm) and within 0.5 percent for particles smaller than the No. 4 sieve (4.75 mm). Table 5-2 shows the results of the washed sieve analysis compared with the job mix formula prescribed in the mix design. The resulting washed gradations were used to batch all laboratory mixture specimens for testing.

Table 5-2. Washed Sieve Analysis Results

Sieve Size	Mixtures 1 & 2		Mixtures 3 & 4		Mixtures 5 & 6	
	Original	**Washed**	**Original**	**Washed**	**Original**	**Washed**
19.0 mm (3/4″)	100.0	100.0	100.0	100.0	100.0	100.0
12.5 mm (1/2″)	90.0	88.8	95.4	92.7	95.4	95.2
9.5 mm (3/8″)	66.0	64.0	72.6	69.4	72.6	72.9
4.75 mm (No. 4)	24.0	19.0	19.8	22.0	19.8	16.8
2.36 mm (No. 8)	10.0	5.6	9.0	8.7	9.0	8.7
1.18 mm (No. 16)	8.0	4.4	6.6	4.7	6.6	6.4
600 µm (No. 30)	7.0	4.2	4.9	3.6	4.9	4.6
300 µm (No. 50)	6.0	4.2	3.9	2.5	3.9	3.7
150 µm (No. 100)	5.0	4.2	3.2	2.5	3.2	2.9
75 µm (No. 200)	3.5	2.8	2.8	2.5	2.8	2.5

5.2. Volumetrics

Having determined the adjusted aggregate gradation from the washed sieve analysis and with the OBC for each mixture provided by FDOT, researchers were ready to combine the mixture components. First, theoretical maximum specific gravity, G_{mm}, was determined for all asphalt mixtures. Previous experience with PFC mixtures suggested the high OBC and high viscosity of the modified binders would prohibit following ASTM D2041 to determine G_{mm} (Alvarez et al. 2009). It was suggested that reproducible results could not be achieved due to the inability to separate the aggregate particles after mixing and loss of binder from excessive draindown. A trial batch was produced, and it was determined that draindown was not an issue for these mixtures (likely due to the addition of mineral fiber) and that, with particular care and effort, mixture clumps could be separated sufficiently. Therefore, the procedure outlined in ASTM D2041 was used to determine G_{mm} for each asphalt mixture at the OBC provided by FDOT (Table 3-1). Initially, two 2,500 g replicates were used to determine G_{mm} for each asphalt mixture, but additional replicates were eventually added for mixtures 2, 5, and 6 to verify the results.

The target AV content for all specimens was 20 ± 2 percent. The bulk specific gravity, G_{mb}, and the AV content for each compacted sample were determined by dimensional analysis using Equation 5-1.

$$G_{\text{mb-dimensional}} = \frac{\frac{W}{V_{tot}}}{\rho_w} \tag{5-1}$$

Where:
W = weight of the specimen in air, g.

V_{tot} = volume of the specimen, cm^3.
ρ_w = density of water, g/cm^3.

The volume of the specimen was measured with the following process: the average height was determined from four height measurements taken with digital calipers at quarter intervals around the circumference of the specimen, and the average diameter was determined with digital calipers using two top-diameter measurements and two bottom-diameter measurements. The compacted specimen was considered to be a cylinder and was calculated using Equation 5-2.

$$V_{tot} = \frac{\pi \cdot d^2 \cdot h}{4} \quad (5\text{-}2)$$

Where:
d = average measured diameter of the specimen, cm.
h = average measured height of the specimen, cm.

G_{mm} and $G_{mb\text{-}dimensional}$ were then used to estimate the volumetric properties of each compacted specimen, with Equation 5-3 being utilized to calculate air voids.

$$\text{Total AV content} = 100 \times \left(1 - \frac{G_{mb}}{G_{mm}}\right) \ (\%) \quad (5\text{-}3)$$

5.3. Specimen Fabrication

Given the previously determined G_{mm} for each mixture and because dimensional analysis was required to calculate air voids, it was necessary to compact specimens to a specific G_{mb} to achieve the target air voids of 20 ± 2 percent. This value of G_{mb} was based on the weight of asphalt mixture placed in the mold, the diameter of the mold, and the final height of the specimen after compaction. However, as previous research (Alvarez et al. 2009) and laboratory experience noted, compacted OGFC specimens tend to expand in the vertical direction after extraction from the SGC. In addition, the high AV content can cause some specimens to crumble if not confined after extraction. To prevent this, all compacted specimens were extracted into, and subsequently cooled overnight in, a 150 mm diameter PVC pipe that was used as a mold. The PVC pipe was removed after the specimen cooled for 24 hr.

To determine a repeatable specimen fabrication protocol, multiple test specimens were compacted and measured. It was determined that compacted specimens expanded about 1.0 mm in the vertical direction after extraction. Smaller-height specimens (< 80 mm) grew more than larger-height specimens (115 mm). It was also found that although the SGC mold was 150 mm, the extracted specimen diameter averaged 150.6 mm. Therefore, when calculating the weight of asphalt mixture to place in the mold to achieve 20 ± 2 percent AV, each specimen was assumed to have a diameter of 150.6 mm, and the compaction height input into the SGC was 1.0 mm to 1.5 mm below the target height to allow for vertical expansion.

Compacted specimens were prepared for testing using AASHTO R30. The mixing and compaction temperature prescribed by FDOT was 160°C. The aggregates were batched according to the washed sieve analysis results and dried overnight at the mixing temperature. When hydrated lime was used (i.e., mixtures 5 and 6), it was added to the aggregate batch and dried overnight. After drying, and before adding the binder to the aggregate batch, the mineral fiber was added at 0.4 percent by weight of mixture. Before compaction, the asphalt mixture was STOA for 2 hr at 160°C. To prevent over-aging, when multiple asphalt mixture specimens were prepared on the same day, mixing and STOA times were staggered to allow for the compaction of one mixture while the others were aging. This was especially crucial when compacting specimens for mixtures 5 and 6 due to the high number of gyrations needed to achieve the target specimen height.

The SGC was used to compact all specimens at a compaction angle of 1.25 degrees and a compaction pressure of 600 kPa. As previously discussed, compacted specimens were extruded directly into 6-inch PVC pipes for cooling. The PVC pipes were cut along one side to allow them to expand and accept the compacted specimen without disturbing it. Once extruded, the pipe was closed and sealed with duct tape to contain the compacted specimen. When mixture 1 was compacted, it was noted that it was impossible to achieve the required height necessary for the HWTT test (i.e., 62 mm) while meeting the desired AV content. Thus, for all mixtures, HWTT specimens were compacted to a height of 75 mm and then trimmed to the required 62 mm.

Mixtures 5 and 6 proved to be especially difficult to compact. Several specimens from mixtures 5 and 6 were prepared based on volumetric properties and allowed to compact to 300–500 gyrations. Despite the high number of gyrations, these specimens exceeded the required height by an average of 2.5 mm and the target air voids by about 2 percent. Thus, specimens for these two mixtures were compacted 10 mm taller than required and trimmed to meet each specific test height requirement. Additionally, for mixtures 5 and 6, a maximum of 250 gyrations was set for compaction. Only two out of the 38 compacted specimens from mixtures 5 and 6 required fewer than the prescribed maximum number of gyrations.

There were several compacted specimens that required trimming either as prescribed for the permeability test or, as discussed above, to meet the target AV requirement. For the permeability test, FDOT standard test method FM 5-565 requires that the top and bottom of each compacted specimen be trimmed by a thickness equal to the NMAS (FDOT 2014b). All specimens were trimmed using a diamond-tipped saw blade with a water cooling system. Trimmed specimens were then rinsed to remove debris generated during the trimming process, air dried for 48–72 hr, and further dried using the CoreDry device to remove excess moisture.

In total, 114 compacted specimens were prepared for testing. Volumetrics were determined using dimensional analysis between 24–72 hr after specimen compaction. Samples that were not immediately subjected to performance testing after cooling to testing temperatures were stored in a temperature-controlled room set at 20°C. All compacted specimens were tested within 2 to 3 weeks after fabrication. The results of specimen fabrication and air void calculations for each mixture are summarized in Table 5-3.

Table 5-3. Specimen Volumetric and Fabrication Characteristics

Mixture	Height (mm)	Test	Replicates	G_{mm}	Average		
					G_{mb}	Air Voids (%)	Gyrations (#)
1	115	Cantabro Loss	6	2.308	1.835	20.5	45
	77[a]	Permeability	3		1.835	20.5	25
	75	IDT	6		1.826	20.9	79
	62[b]	HWTT	4		1.839	20.3	52
2	115	Cantabro Loss	6	2.296	1.837	20.0	32
	77[a]	Permeability	3		1.848	19.5	18
	75	IDT	6		1.823	20.6	95
	62[b]	HWTT	4		1.857	19.1	49
3	115	Cantabro Loss	6	2.319	1.860	19.8	92
	90[a]	Permeability	3		1.848	20.3	41
	75	IDT	6		1.846	20.4	170
	62[b]	HWTT	4		1.874	19.2	170
4	115	Cantabro Loss	6	2.342	1.871	20.1	78
	90[a]	Permeability	3		1.874	20.0	45
	75	IDT	6		1.860	20.6	167
	62[b]	HWTT	4		1.892	19.2	146
5	115	Cantabro Loss	6	2.434	1.935	20.5	250[d]
	90[a]	Permeability	3		1.979	18.7	245[d]
	75[c]	IDT	6		1.918	21.2	250[d]
	62[c]	HWTT	4		1.913	21.4	250[d]
6	115	Cantabro Loss	6	2.448	1.956	20.1	250[d]
	90[a]	Permeability	3		1.983	19.0	283[d]
	75[c]	IDT	6		1.946	20.5	250[d]
	62[c]	HWTT	4		1.934	21.0	250[d]

[a] AV for permeability specimens measured after trimming NMAS from top and bottom.
[b] AV for HWTT specimens measured after trimming to test specimen size.
[c] All mixture 5 and 6 specimens had to be trimmed to achieve target AV.
[d] The maximum number of gyrations for mixtures 5 and 6 was set to 250.

5.4. Moisture Conditioning

To assess the moisture susceptibility of the asphalt mixtures, the IDT strength and Cantabro tests were performed on laboratory specimens before and after conditioning following AASHTO T 283 and using the moisture induced stress tester (MIST) device according to ASTM D7870, “Standard Practice for Moisture Conditioning Compacted Asphalt Mixture Specimens by Using Hydrostatic Pore Pressure.” Certain deviations from the standards were done, as noted in the following paragraphs.

AASHTO PP 77-14, “Standard Practice for Materials Selection and Mixture Design of Permeable Friction Courses (PFCs),” recommends evaluating the moisture susceptibility following AASHTO T 283 using one freeze/thaw cycle and subjecting the specimens to 87.8 kPa of vacuum for 10 min without regard to the degree of saturation achieved by the specimen. The standard prescribes compacting the specimens with 50 SGC gyrations to target AV content between 18 and 22 percent. The actual number of gyrations used to achieve the prescribed target AV content is listed in Table 5-3. The minimum TSR requirement noted in the standard is 0.7.

Moisture conditioning in the MIST device (Figure 5-1a) subjects a specimen to high temperatures and exerts a cyclic pore pressure within the asphalt mixture structure (Figure 5-1b) by inflating and deflating a bladder located at the bottom of the device. This allows rapid moisture damage conditioning similar to that occurring over time under traffic loading at service temperatures. Figure 5-1c shows a schematic of the MIST device loaded with two specimens, as recommended by the equipment’s manufacturer and done in this project. During testing, compacted specimens were placed inside the MIST chamber. Then, water was added to fill the chamber and submerge the compacted specimens. Further, the top of the device was screwed in place and water was added to an overflow device to ensure the chamber was completely filled with water. The device then heated and maintained the water at 60°C. The unit pressurized itself to 276 kPa using a bladder at the bottom of the chamber. When the set temperature and pressure were achieved, the device cycled the pressure to condition the specimen.

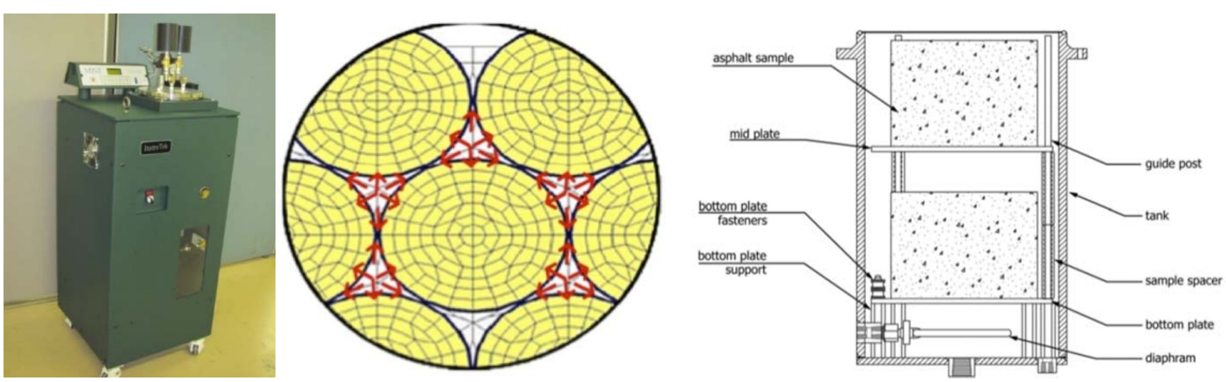

(a) (b) (c)

Figure 5-1. Moisture Induced Stress Tester: (a) equipment; (b) schematic of pore pressure; (c) typical setup using two specimens (ASTM 2013).

Previous studies have shown that MIST can provide accelerated moisture conditioning and is a viable alternative to AASHTO T 283 (Chen and Huang 2008; Schram 2012; Zofka et al. 2014; Weldegiorgis and Tarefder 2015). Based on the research team’s previous experience, the recommended 3,500 cycles by ASTM D7870 are too severe for some OGFC specimens, causing them to crumble. Thus, the selected test parameters were 1,000 cycles, 40 psi pressure, and a water temperature of 60°C. After MIST conditioning, the specimens were transferred to a water bath at 25°C and left undisturbed for 1 hr before air drying for 48–72 hr. Excess moisture was then removed with the CoreDry device according to ASTM D7227.

5.5. Performance Tests

One nondestructive test (i.e., permeability) and three destructive tests (i.e., Cantabro, IDT strength, and HWTT) were used to assess the performance of the asphalt mixtures.

5.5.1. Permeability

Permeability was measured using the FDOT falling head permeameter test according to FM 5-565. Three replicates were tested and the average results were reported for each mixture. Prior to testing, the laboratory specimens were allowed to saturate overnight in water. Then, to ensure an adequate seal around the perimeter of the specimen, a layer of petroleum jelly was applied to the perimeter, as shown in Figure 5-2. Once placed inside the permeameter, pressure was applied at 69 kPa to the rubber membrane surrounding the specimen to achieve a watertight seal. This process guaranteed that water was only traveling from the top to the bottom of the specimen and not draining through its sides. To ensure the specimen remained saturated, water was continuously circulated through the specimen for 2 to 3 min.

Figure 5-2. Permeability specimen sealed with petroleum jelly.

times until the error between measurements was less than 4 percent. During testing, after continuously circulating water through the specimen for 2 to 3 min, the differences in time measurements were always less than 2 percent. The average permeability values for the three replicates along with the average number of SGC gyrations for all mixtures are presented in Figure 5-3. The minimum recommended permeability of 100 m/day per AASHTO PP 77-14 is also shown in Figure 5-3 for reference, but the measured values for all mixtures were well below this threshold.

Results show that mixture 1 was the most permeable and mixture 5 was the least permeable. A statistical analysis of variance (ANOVA) with a significance level of $\alpha = 0.05$ found that aggregate type, gradation, and the number of gyrations significantly affected permeability. Details of the statistical analysis are presented in Appendix C. It is important to note that mixtures 5 and 6 required an average of 264 gyrations to meet the target AV requirement, as opposed to 32 gyrations required by the specimens belonging to mixtures 1 through 4. It is likely that due to the significantly higher number of gyrations, the specimens belonging to mixtures 5 and 6 had smaller and less interconnected AVs and even some aggregate fractures. Therefore, there appeared to be a stronger correlation between permeability and compaction effort as opposed to aggregate gradation.

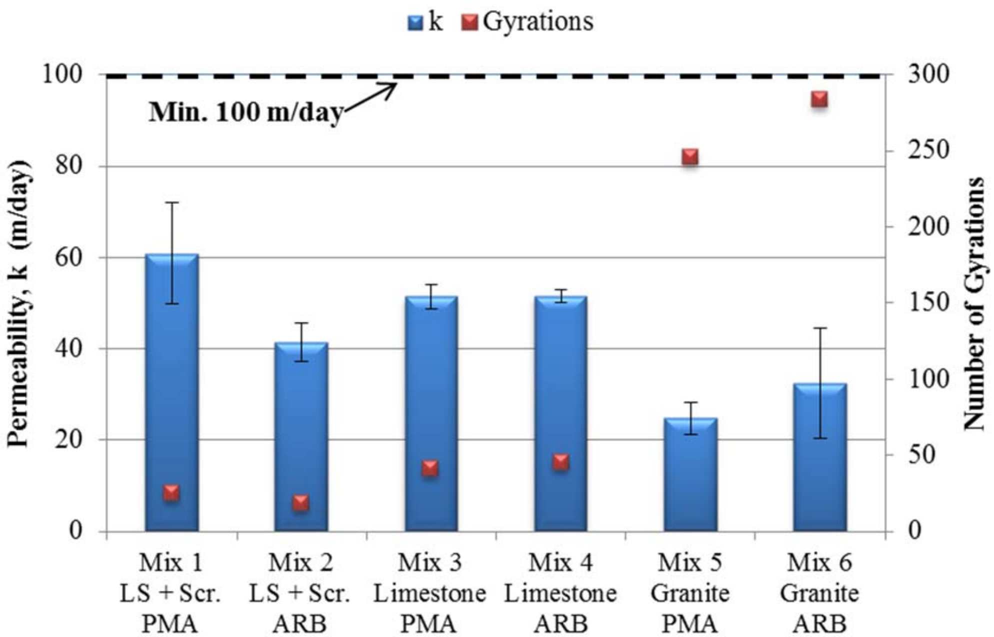

Figure 5-3. Average permeability and number of gyrations for all mixtures.

5.5.2. Cantabro

The Cantabro abrasion loss test has been recommended by several researchers as one of the best tests to assess the durability of OGFC mixtures (Kandhal 2002; Alvarez et al. 2010; Watson et al. 2003). The standard method followed to conduct the test was AASHTO TP 108, which prescribes placing 115 mm height specimens inside the Los Angeles abrasion drum without the metal spheres. The specimen is allowed to rotate freely inside the drum at a rate of 30–33 revolutions per minute for 300 revolutions. The test is performed at room temperature. Afterwards, the specimen is extracted from the drum, any loose material is discarded, and the ratio of the final specimen weight to the initial specimen weight is calculated and reported as the abrasion loss. Figure 5-4 shows a visual comparison of specimens before and after testing. For the moisture-conditioned specimens, the ratio of the average conditioned Cantabro abrasion loss to the average unconditioned Cantabro abrasion loss was also calculated. Three replicates per mixture type and condition were tested.

Figure 5-4. Cantabro abrasion loss specimens before and after testing.

The graph in Figure 5-5 provides a comparison of Cantabro abrasion loss before and after moisture conditioning per MIST and AASHTO T 283. A statistical ANOVA with a significance level of $\alpha = 0.05$ showed that in dry condition, mixture 1 and 2 performed better than mixtures 3 through 6, and that mixture 2 outperformed all other mixtures. Mixture 3 was the least durable in dry condition, with an average loss of 15.4 percent. Moisture conditioning was not a statistically significant factor, meaning that the conditioning protocols did not impact the outcome of the Cantabro loss test. When comparing Cantabro abrasion loss for the PMA and ARB binders, the statistical analysis showed significant differences, with mixtures employing ARB binder being more durable than their PMA equivalents.

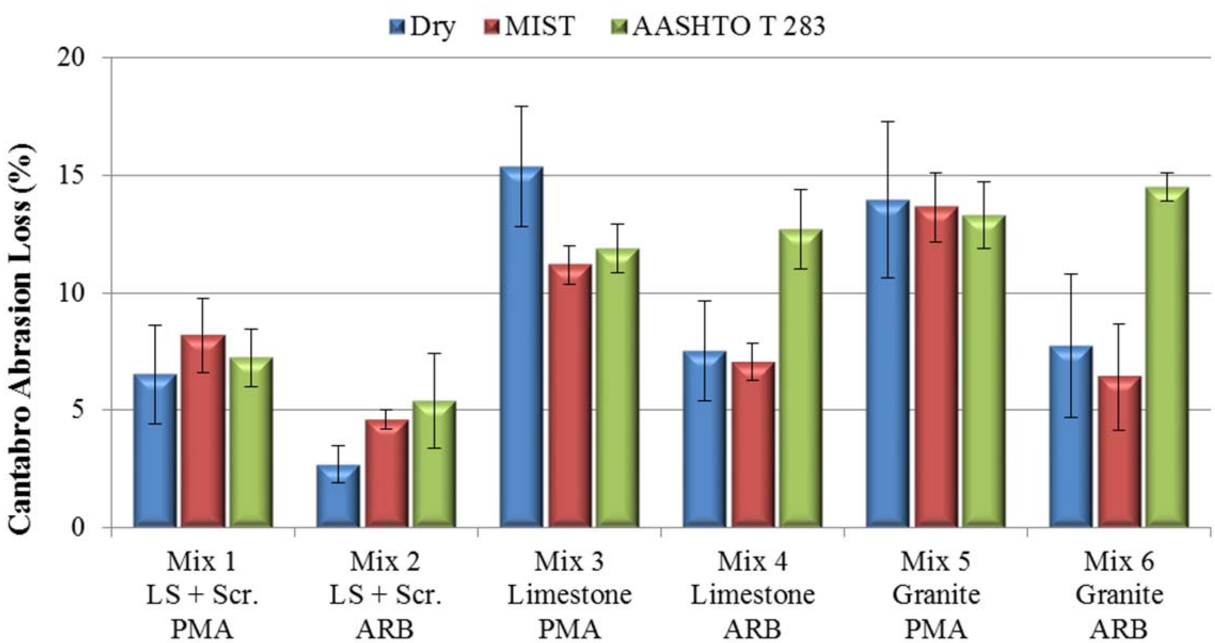

Figure 5-5. Cantabro abrasion loss results for all mixtures.

For the dry specimens, the PMA average Cantabro loss was 12 percent, while for the ARB mixtures, it was only 6 percent. Similarly, for the MIST-conditioned specimens, the average loss was 11 percent for the PMA mixtures and 6 percent for the ARB mixtures. The specimens conditioned following AASHTO T 283 showed a different trend, with an equivalent average percent loss for the PMA and ARB mixtures of about 11 percent. Additionally, aggregate type statistically influenced the Cantabro abrasion loss results, with the limestone mixtures showing better durability, on average, as compared to the granite mixtures. Complete details of the statistical analysis are provided in Appendix C.

5.5.3. IDT Strength

ASTM D6931 is the standard test method followed to perform the IDT strength of unconditioned and moisture-conditioned specimens. Three replicates were tested for each mixture type and condition. The test consists of placing the 150 mm diameter, 75 mm thick specimens on their side in the loading frame and applying a vertical load at a rate of 50 mm per minute until failure. The maximum load is recorded, and the IDT strength is calculated according to Equation 5-4. The ratio of the average conditioned IDT strength to the average unconditioned IDT strength provides the TSR of the asphalt mixture. The test was performed at room temperature.

$$S_t = \frac{2000 \times P}{\pi \times H \times D} \tag{5-4}$$

Where:
S_t = IDT strength, kPa.
P = maximum load, N.
H = specimen height immediately before test, mm.
D = specimen diameter, mm.

During testing, the maximum load was achieved quickly (on average 6 sec) and with very little deformation (on average 3.5 percent maximum strain). Figure 5-6 shows a specimen from mixture 6 after failure with 4 percent strain.

Figure 5-6. Laboratory specimen from mixture 6 after IDT strength test failure.

The average IDT strength values and TSR are presented in Figure 5-7 and Figure 5-8, respectively. In terms of dry IDT strength, the results revealed that the limestone mixtures were stronger than the granite mixtures, with mixture 3 having the highest average IDT strength and mixture 6 the lowest.

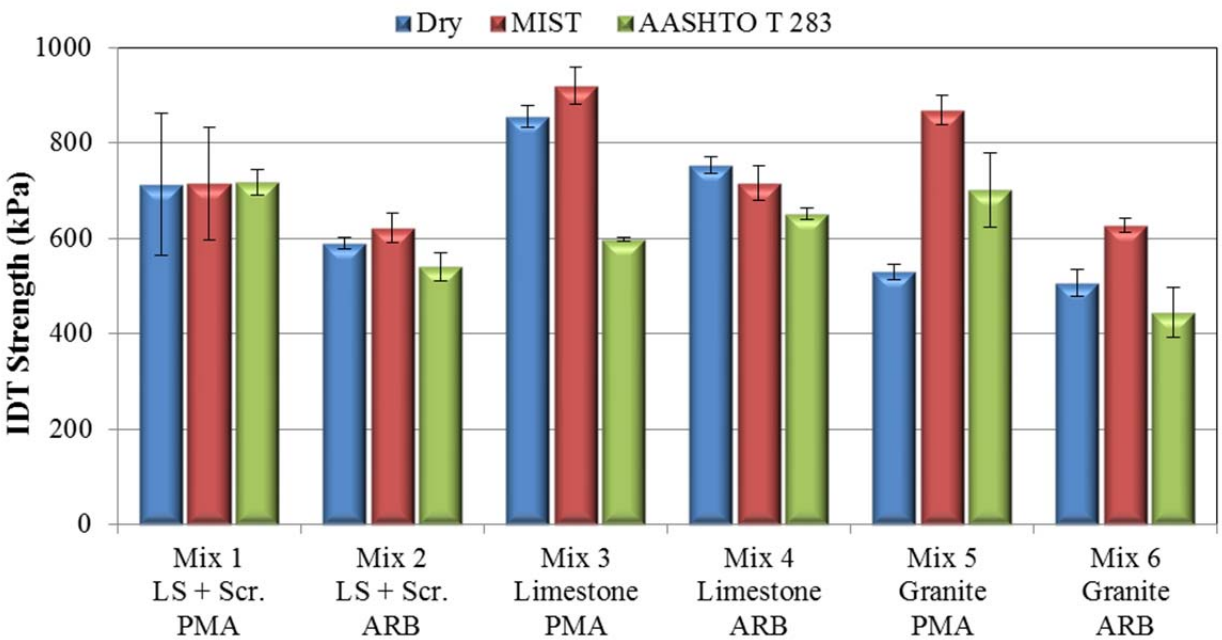

Figure 5-7. IDT strength results for all mixtures.

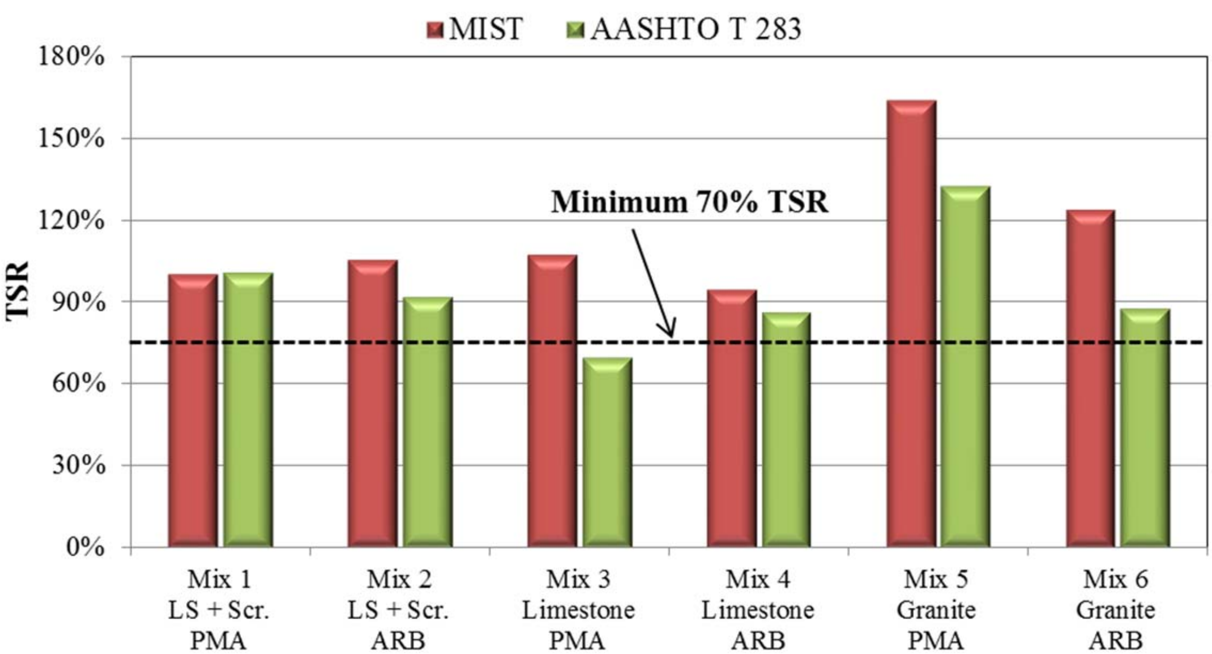

Figure 5-8. Tensile strength ratio for all mixtures.

With regard to moisture conditioning, the majority of the mixtures had a TSR near or above 100 percent, suggesting an equal or better IDT strength after conditioning, which is contrary to expected behavior. A statistical ANOVA at a significance level of $\alpha = 0.05$ with gradation, binder, and conditioning as main effects and all possible two-way effects between them showed that MIST conditioning affected mixtures 5 and 6 but did not significantly affect the IDT strength for mixtures 1–4. The effect was positive, though, with an increase in IDT strength after conditioning, as indicated before. Conditioning per AASHTO T 283 had a significant effect on mixtures 3 and 5, with a decrease in IDT strength for mixture 3 but an increase for mixture 5. The only mixture with a TSR below the recommended threshold of 0.70 was mixture 3 after moisture conditioning per AASHTO T 283. Complete details of the statistical analysis are provided in Appendix C.

To investigate the effect of changing the MIST conditioning parameters, a small study was run on mixture 5. Results of this study are summarized in Table 5-4. ASTM 7870 recommends testing of MIST-conditioned specimens within 6 hr of completing the conditioning protocol. That procedure was not followed due to the interest in having dry specimens for the IDT strength and Cantabro loss tests. Two additional specimens were conditioned in the MIST, one with the same parameters used before (i.e., 1,000 cycles, 40 psi pressure, and a water temperature of 60°C), and the other with 5,000 cycles, 40 psi pressure, and a water temperature of 60°C. Both specimens were tested immediately after the 2-hr conditioning at 25°C instead of letting them air dry for 48–72 hr and further using the CoreDry to remove remaining moisture, as done with the other specimens.

Table 5-4. MIST Conditioning Parameters Experiment

Conditioning	IDT (kPa)	TSR (%)
Unconditioned	529	–
MIST 1000 cycles + 72 hr air dry	868	164
MIST 1000 cycles + wet	602	114
MIST 5000 cycles + wet	562	106

The results of the small study showed that testing without drying the specimens greatly reduced IDT strength as compared to drying the specimens prior to testing. In addition, the larger number of MIST cycles (i.e., 5,000) resulted in a significantly lower IDT strength as compared to the specimens subjected to the 1,000 MIST cycles. However, all three MIST-conditioned specimens still had TSR values above 100 percent, indicating that the specimens were not negatively affected by the moisture conditioning. These OGFC mixtures demonstrated outstanding moisture resistance in the laboratory, and further research is needed to investigate adequate moisture conditioning protocols for these types of mixtures.

5.5.4. Hamburg Wheel Tracking Test

AASHTO T 324 was the standard test method used to conduct the HWTT. This test is widely used to predict the moisture susceptibility and rutting resistance of asphalt mixtures. Two compacted specimens are placed in a 50°C water bath below a steel wheel. There are two wheels per test apparatus, so four specimens can be tested at once, producing two test replicates, as shown in Figure 5-9. The wheels are lowered and the specimens are allowed to condition for 30 min in the water bath. Then, the wheels roll over the paired specimens at a rate of 52 passes per minute until 20,000 passes are reached or the rut depth at the center point exceeds 0.5 inch (12.5 mm).

Figure 5-9. HWTT test setup.

Figure 5-10 shows the three stages a specimen typically experiences as it is loaded in the HWTT. The first stage, known as the post-compaction or consolidation stage, occurs rapidly at the onset of loading. The second stage—or creep phase—follows, and its duration depends on the quality of the asphalt mixture being tested. The third stage is when the asphalt mixture experiences damage due to stripping. In addition to the traditional output of rut depth versus load cycle, a novel analysis method developed by Yin et al. (2014) was used in this project. The method consists of fitting a curve to the HWTT data and identifying the inflection point of the curve, that is, where the negative curvature of the creep phase changes to a positive curvature during the stripping phase, as shown in Figure 5-11. This point is labeled the stripping number (SN), and the number of load cycles at which the SN occurs (LC_{SN}) is an indicator of the quality of the mixture. A lower LC_{SN} represents an asphalt mixture that is more prone to stripping and thus is more susceptible to moisture damage (Yin et al. 2014).

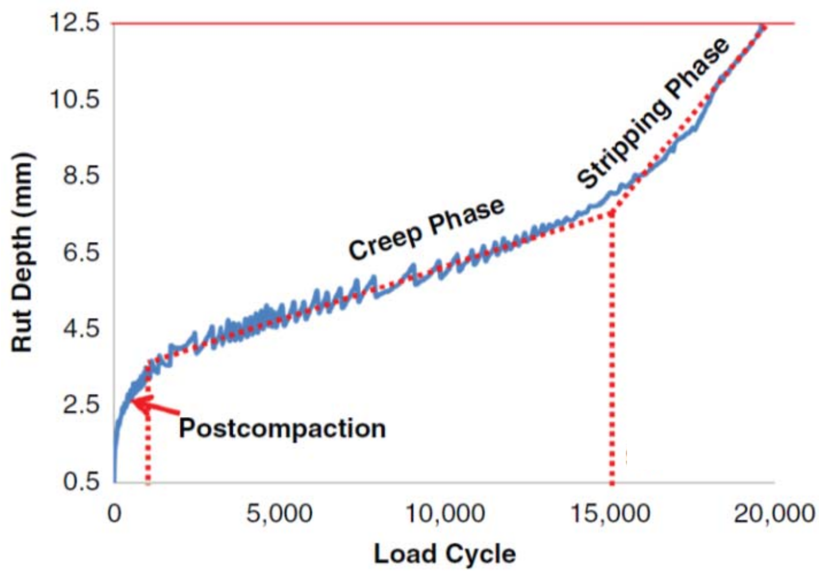

Figure 5-10. Typical HWTT deformation stages (Yin et al. 2014).

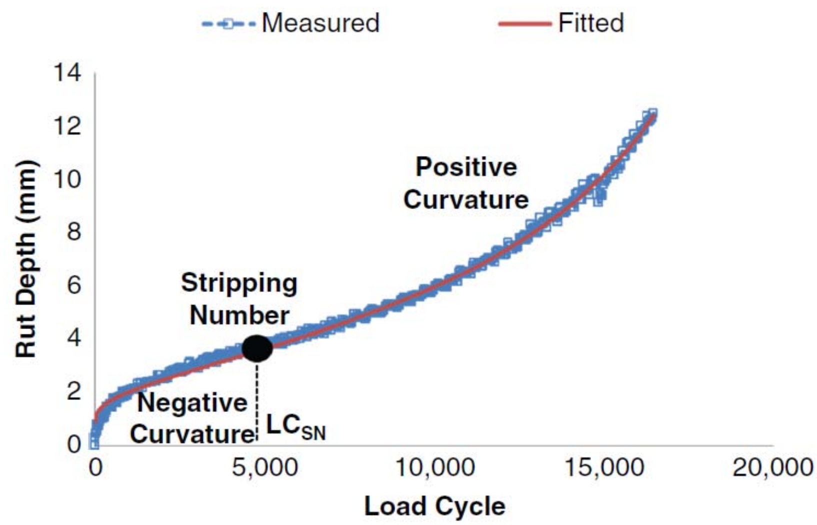

Figure 5-11. HWTT novel analysis method (Yin et al. 2014).

The measured rut depth for the six mixtures when plotted versus load cycles showed all specimens had a two-phase behavior (i.e., post-compaction and creep phase), meaning that none of the asphalt mixtures experienced stripping during testing. This hindered the possibility of using the novel HWTT analysis methodology described above. The average maximum rut depth at the center point of the specimens, calculated using the left and right wheels, was used as an output parameter and is shown in Figure 5-12. Results showed that none of the mixtures reached 12.5 mm after 20,000 load cycles.

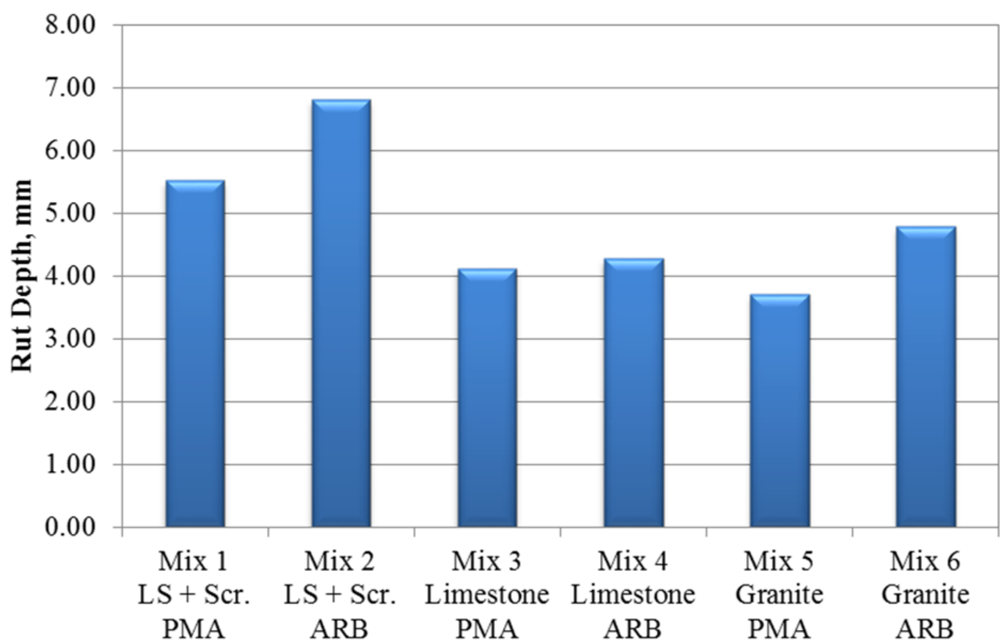

Figure 5-12. Average HWTT rut depths for all mixtures.

A statistical ANOVA with a significance level of α = 0.05 with gradation, binder, and wheel (i.e., left and right wheel) as main effects and gradation/binder as a two-way interaction effect was conducted. The results revealed that aggregate type and binder type were not statistically significant with regard to rut depth. Further, it was determined that mixtures 1 and 2 were the most susceptible to rutting, while mixtures 3–6 were not different statistically. Complete details of the statistical analysis are provided in Appendix C.

5.5.5. Summary

Table 5-5 provides a summary of all laboratory tests used in this project, their desired outcome as a value or range of values, and an explanation of the effect that result has on the component or the asphalt mixture.

Table 5-5. Desired Properties for Moisture-Resistant Mixtures

Test	Desired Result	Effect
AIMS	High angularity	Better mechanical bonding
	High texture	
	Low sphericity	
G-R Parameter	< 180 kPa	Less likelihood of cracking or raveling
SFE	High Energy Ratio values	More work required for water to displace the binder
IDT	High TSR	Less susceptible to moisture damage
Cantabro	Low abrasion loss	More durable
HWTT	Low rut depth	Better rutting resistance
	High or no SN	Less susceptible to moisture damage
Permeability	High k-value	Faster water drainability

Based on the properties shown in Table 5-5, Table 5-6 and Table 5-7 summarize the results from both observational and statistical analyses of the material and mixture characterization. A review of the summary data shows variability between the best performer from each test and the proposed moisture sensitivity of the corresponding asphalt mixture. The component material test results in Table 5-6 indicate that an asphalt mixture made with PMA binder would be less moisture susceptible. An examination of the performance test results in Table 5-7 shows significant variability in the outcome. The best performer in the IDT test, mixture 3, was the worst performer in the Cantabro abrasion loss test. In addition, PMA asphalt mixtures outperformed ARB asphalt mixtures in the IDT test, but the opposite was true for the Cantabro abrasion loss test, where ARB outperformed PMA. The HWTT results would appear to have some correlation with the IDT data in terms of which gradations performed better than others, but the HWTT actually revealed that none of the asphalt mixtures was moisture susceptible.

Table 5-6. Summary of Material Characterization

Test	Component	Best Performer	Corresponding Mixture	Explanation
AIMS	Aggregate	Granite	5, 6	Higher texture, better mechanical bonding
G-R Parameter	Binder	PMA	1, 3, 5	Slower progression of the G-R parameter toward the damage zone
SFE	Aggregate-Binder Interface	Limestone+PMA	1, 3	Least moisture susceptible combination

Table 5-7. Summary of Mixture Characterization

Test	Aggregate	Gradation [a]		Binder		Mixture		Moisture Conditioning
		Best	Worst	Best	Worst	Best	Worst	
Permeability	Granite	A/B	C	N.S.[b]		1	5/6	N/A[c]
Cantabro	Limestone	A	B/C	ARB	PMA	2	3	Not significant
IDT Strength	Limestone	B	A/C	PMA	ARB	3	6	Significant
HWTT	N.S.	B/C	A	N.S.[b]		3/4/5	1/2	N/A[c]

[a] Gradation A: Limestone + Scr. (mixtures 1/2); Gradation B: Limestone (mixtures 3/4); Gradation C: Granite (mixtures 5/6).
[b] N.S.: not significant.
[c] N/A: not applicable.

The results of the component material and mixture characterization were compared with the field performance of mixtures 1, 2, and 3. As a recap, the good performing mixtures that exhibited little to no raveling in the field were mixtures 1 and 2. These asphalt mixtures were made with the finer limestone Gradation A, and both PMA (mixture 1) and ARB (mixture 2) binders. Mixture 3 was made of limestone as well but used the coarser Gradation B. In addition, mixture 3 used ARB binder. From the component material tests, the G-R parameter and SFE both identified PMA as a better performer and could be considered as adequate tools to identify materials with good resistance to moisture damage.

When studying the outcomes of the mixture characterization, a good correlation between the Cantabro abrasion loss and field performance was established. The Cantabro test results revealed that mixtures 1 and 2 were superior performers and that mixture 3 was the least durable. This was the only performance test, from the ones included in this project, that correlated well with field observations.

CHAPTER 6 . FINITE ELEMENT MODELING

After finalizing the on-site and experimental activities, a 2D FE model was developed to complement the acquired knowledge about the mechanisms associated with raveling in OGFC. The power of currently available numerical approaches, like the FE model discussed herein, is that they are versatile tools that permit activities that are not practical or even possible to pursue in the laboratory, such as the evaluation of the impact of multiple traffic and environmental conditions on the behavior of road materials

The numerical model, that was developed in the commercial FE software Abaqus®, and compared to existing models, accounts for novel factors like realistic geometries of the microstructures of OGFC and coupled mechanical-moisture formulations. These novel characteristics permitted a comprehensive evaluation of the impact of several internal and external factors on raising the chances for raveling distresses in OGFC. The following sections present a detailed description of the different components of the model, the modeling methodology, and a corresponding analysis of results.

6.1. Previous numerical works on raveling in OGFC materials

The literature review showed that there are limited published works on this topic, and that most of them have been conducted at the Delft University of Technology (the Netherlands) under the guidance of Professor Molenaar. Table 2-16 summarized these models, which constitute a significant contribution in the understanding of this phenomenon. Based on this information, it was possible to identify the influence of different parameters in the potential initiation and development of raveling in OGFC. Table 6-1 summarizes these parameters and explains the relative importance of each one of them in promoting raveling. This previous knowledge was used as a starting point in the design of the modeling methodology for this project.

Table 6-1. Relevant Parameters in Promoting Raveling Based on Previous Numerical Modeling Efforts

Parameters	Importance in Promoting Raveling	Reference
Geometry	**Low.** Three different models (two models with idealized circular [2D] and spherical [3D] geometries for the aggregates, and a simplified 2D model with a more realistic geometry), with the same material properties that were exposed to identical loading conditions, produced similar results (using the LOT tool).	Huurman and Mo (2007)
Diameter of particles	**High.** Due to the idealized geometry in the models (i.e., horizontal arrays of circular aggregates coated with mastic in contact with each other), the total AV of the mixture's microstructure depends on the diameter of the aggregates, the central distance between particles (i.e., on the mastic film thickness), and the contact angle. As expected, AV was observed to strongly impact the mechanical response of the mixture.	Mo et al. (2007)
Mastic film thickness (binder content)		
AV content		
Central distance between particles		
Contact angle of adjacent aggregates—condition of particle skeleton—particle packing	**High.** The numerical results showed that an increase in the contact angle at the interfacial zones (aggregates and mastic) is useful to reduce stress concentrations.	Mo et al. (2007)
	High. Particle packing was the most significant factor affecting the magnitude of the stresses at the interfacial areas (3D model).	Mo et al. (2008)
Binder type	**Medium.** In an initial model, the differences and/or benefits of using modified binder or unmodified binder were not observed to be significant.	Mo et al. (2007)
	High. New models corroborated that the type of binder influences the adhesive and cohesive resistances of the mixture, which are crucial in preventing raveling.	Mo et al. (2008, 2010, 2011, 2014); Huurman and Mo (2007)
Tire surface loading—load cases	**Medium.** The type of loading and the vehicle-pavement interaction characteristics were observed to be important factors that partially define raveling susceptibility.	Huurman et al. (2010a)
Temperature	**Medium-low.** The results of the simulations suggested that raveling does not only occur under low temperatures—as suggested in some initial studies—but that it also occurs under high temperatures.	Huurman et al. (2010b); Mo et al. (2010)
Presence of water	**Medium.** The impact of moisture was accounted for by changing the mechanical properties of the mastic. The numerical results showed an increase in the magnitude of the stresses within the skeleton of the mixture in these cases, but this parameter was not observed to be as relevant as other features of the mixture.	Mo et al. (2011, 2013);

6.2. Modeling Methodology

In order to accomplish the objectives of this task, a three-step methodology was used, as illustrated in Figure 6-1, and described next:

1. Characterization of the mechanical properties of the constitutive phases of the mixtures and identification of other relevant information regarding the materials.
2. Numerical implementation of the model:
   a. Definition of the OGFC geometries to be modeled.
   b. Definition of the properties of the materials (input parameters).
   c. Definition of the mechanical loading conditions.
   d. Definition of other external conditions applied to the structure.
   e. Numerical simulations.
3. Development of a methodology to process and analyze the data to obtain the main conclusions and recommendations from the numerical simulations.

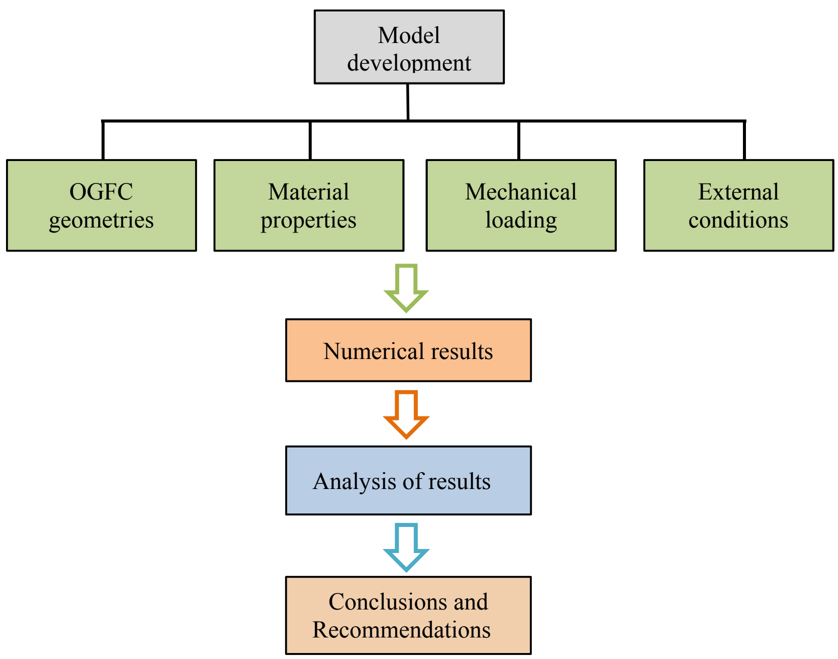

Figure 6-1. Modeling methodology.

The first stage, which included the results from the characterization of the different materials and mixtures evaluated, provided vital input information for the proposed models. Indeed, the information related to materials and mixture properties (e.g., gradation, AV content, binder content, internal skeleton and geometry of the mixture, etc.) constituted what has been defined as the *internal parameters* of the model. Besides these parameters, several values of traffic loading and speed as well as different weather conditions (e.g., temperature, moisture diffusion, structural capacity of the pavement underneath the OGFC) were also considered as part of the modeling strategy. The set of parameters that depend on issues different from the mixtures themselves were defined as the *external parameters* of the model. Once all these parameters were defined, the models were implemented in Abaqus®, and a load simulating the pass of a wheel over the surface of a pavement with a specific OGFC was conducted.

Table 6-2 presents a comparison between the different internal and external parameters that have been evaluated in previous numerical works and the parameters that were considered in this project. As observed, the modeling simulations in this project included comprehensive sets of parameters in comparison to those considered in previous works.

Not all the parameters were evaluated or modified in each simulation. In fact, the process consisted of modifying only one parameter per simulation, with the objective of identifying the relative effect of such parameter in the mechanical response of the mixture. Thus, for example, this work included some simulations where the mixture was not affected by moisture (dry condition), others where the mixture was subjected to moisture diffusion processes (wet condition), some others where the wheel load passed over the OGFC faster or slower, etc. The matrix that contained all the simulation cases was selected such that the results were useful to evaluate the impact of each variable on the macro- and micromechanical responses of the OGFC layer.

In terms of the numerical results, one advantage of FE simulations is that they permit researchers to quantify the mechanical response of any component of the model at any desired moment (i.e., simulation time). In this project, however, this advantage became a challenge due to the volume of information that needed to be analyzed in order to obtain valid conclusions on the expected durability of the OGFC. Based on this, a rigorous methodology to process and analyze the data was especially developed. This methodology used energy dissipation principles and probabilistic theory to identify the conditions and/or factors that threaten the durability of these mixtures.

One important assumption made in this project was that the contact between aggregates within the OGFC is a mastic-mastic contact. Mastic is herein defined as the combination of binder and aggregate filler. Due to the typical gradations used in the fabrication of OGFC mixtures, it is more realistic to assume that every aggregate is coated by a thin film of mastic than by a thin film of pure binder. Therefore, when two aggregates are in contact, the mastics that are coating those aggregates are the materials that are interacting, as illustrated in Figure 6-2. Thus, in this project, the OGFC asphalt mixtures were assumed to be composed of three constitutive phases: (a) aggregates, (b) mastic, and (c) air voids. In terms of the durability of the mixture, raveling susceptibility is considered to be related to the failure potential of any stone-on-stone contact (i.e., a mastic-mastic contact). Thus, the cohesive failure of the mastic was assumed to be the main cause of raveling in this type of mixture. It should be clarified that adhesive failure (i.e., loss of interaction or separation at the interface between mastic and aggregate) could also be a relevant source of raveling in OGFC. However, since the model considered the interaction between mastic materials and not pure binders, the adhesion properties between the different types of aggregates and binders was somehow indirectly accounted for by this material in the simulations. More details of this assumption and other relevant characteristics of the model are presented in the following sections.

Table 6-2. Parameters Evaluated on Existing Models of Raveling

Model	Parameters									
	Geometry		Air voids	Mastic film thickness	Binders	Loads	Types of aggregate	Moisture effects	Pore pressure	Layer thickness
	Idealized	Realistic								
Mo et al. (2007)	X			X	X	X				
Mo et al. (2008)	X		X	X	X	X				
Huurman et al. (2010b)	X				X	X				
Mo et al. (2010)	X				X	X				
Mo et al. (2011)	X				X	X	X	X (not directly)		
Mo et al. (2014)	X				X	X	X	X (not directly)		
Current Model		**X**	**X**	**X**	**X**	**X**	**X**	**X (directly)**	**X**	**X**

Figure 6-2. Stone-on-Stone contacts used in the numerical models.

6.3. Material Properties

6.3.1. Aggregates

The two types of aggregates used in the experimental portion of the project (i.e., GR and LS) were also employed in the numerical simulations. In terms of their mechanical response, aggregates were considered linear elastic materials, with the material properties shown in Table 6-3 (Rummel 1991).

Table 6-3. Aggregate Properties

ID	Aggregate Type	Description	*E* (MPa)	ν (-)
GR	Granite	Martin Marietta Materials	50,000	0.3
LS	Limestone	White Rock Quarries	27,000	0.3

6.3.2. Mastics

The master curves of the two types of binders used in the study (i.e., PMA and ARB, both with antistripping agents and classified as PG76-22) were determined through DSR testing and presented previously as part of the experimental characterization of materials. However, the FE model assumes that the aggregates in the mixture are coated by mastics and not by pure binder. Therefore, the rheological properties of the mastics were required as input parameters for the models. Consequently, the master curves of all the combinations of binders and filler types (Table 6-4) were experimentally determined.

Table 6-4. Tests Conducted on Mastics

Filler Type	Antistrip (%)	DSR Master Curves	SFE (WP)
PMA + LS filler	0.5	X	X
ARB + LS filler	0.5	X	X
PMA + GR filler	1.0	X	X
ARB + GR filler	1.0	X	X

The mastics were fabricated using a filler/binder volume ratio of 0.33. This value is commonly used in the experimental characterization of mastic materials in the literature (Alvarez et al. 2012). In addition, as noted in Table 6-4, all the analyzed mastics contained antistripping agents. Figure 6-3 presents the master curves obtained at a reference temperature of 30ºC for the four mastics, which is the average temperature of the OGFC in the numerical simulations. Besides the linear viscoelastic properties, the SFE properties of all the mastics were also determined using the WP method. As will be explained in later sections, this thermodynamic property of the mastics was a crucial parameter in this work since it is associated with the cohesive failure potential at stone-on-stone or mastic-mastic contacts (i.e., raveling potential).

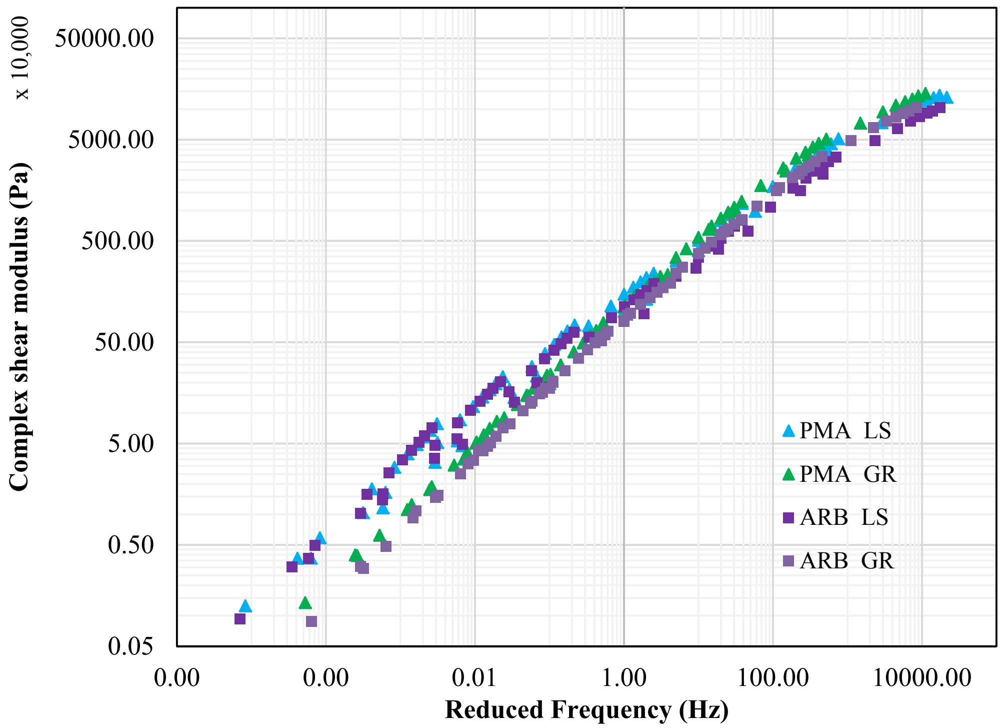

Figure 6-3. Master curves of mastics (T_R = 30ºC).

The information extracted from each master curve was used to include the linear viscoelastic material properties of the mastics in Abaqus®. In order to do so, a Prony Series representing the relaxation modulus of the material at 30ºC was obtained for each material by transforming the data from the frequency domain (i.e., master curves) to the time domain (i.e., relaxation modulus). The Prony Series used as input in Abaqus® is normalized with respect to the instantaneous shear modulus, as expressed by the following equations.

$$g(t) = 1 - \sum_{i=1}^{n} g_i(1 - e^{-\frac{t}{\rho}}) \quad (6\text{-}1)$$

Where:
$g(t)$ = the normalized shear relaxation modulus of the material with respect to the instantaneous shear modulus (G_0).
ρ_i = one of the two main sets of parameters of a typical Prony Series.
g_i = the Prony Series parameter G_i divided by the instantaneous shear modulus (i.e., $g_i = \frac{G_i}{G_0}$).

Also, Equation 6-1 produces the following relationship between the instantaneous shear modulus, G_0, the infinite or long-term shear modulus, G, and the Prony Series parameter, G_i:

$$G_0 = G_\infty + \sum_{i=1}^{n} G_i \tag{6-2}$$

An example of the Prony Series parameters characterizing the constitutive response of the mastic composed by PMA binder with antistripping and LS filler are presented in Table 6-5 and illustrated in Figure 6-4. Similar parameters were obtained for all other mastics.

Table 6-5. Prony Series Parameters of the Mastic LS/PMA+LS

i	G_i (Pa)	g_i (-)	ρ_i (Pa)
1	7.57E+07	0.47200	0.00001
2	6.09E+07	0.38049	0.0001
3	1.72E+07	0.10760	0.001
4	4.78E+06	0.02986	0.01
5	1.06E+06	0.00663	0.1
6	2.71E+05	0.00170	1
7	9.18E+04	0.00057	10
8	2.61E+04	0.00016	100
9	3.50E+03	0.00002	1000
10	3.50E+03	0.00002	10000
G_0 (Pa)	1.60E+08		
E_0 (MPa)	448.33		
ν(-)	0.4		

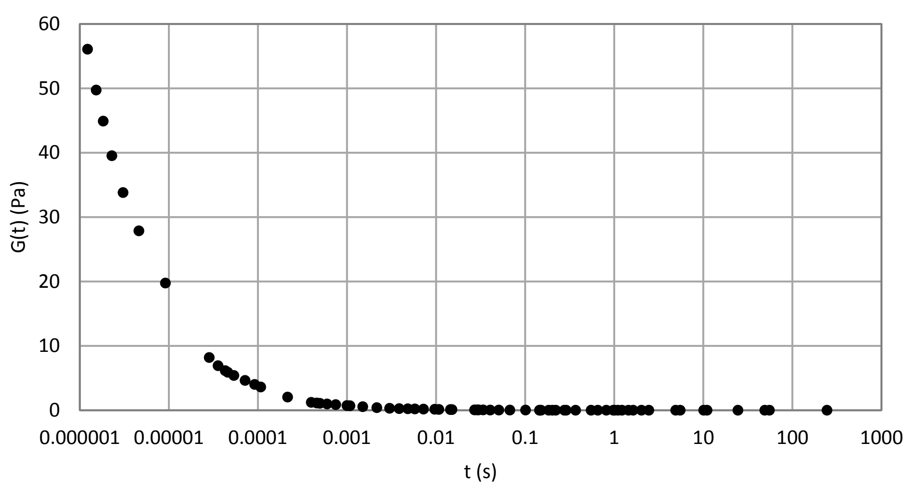

Figure 6-4. Relaxation curve for the (PG 76-22 PMA+AS)+LS filler.

Finally, Table 6-6 presents the cohesive bond energy obtained from the SFE components of the mastics. The cohesive bond energy, also called work of cohesion, corresponds to twice the total value of the SFE of the material. Since this quantity represents the amount of energy required to create two new surfaces of the material in vacuum condition (i.e., to create a crack in the material), it can be used to characterize the theoretical fracture resistance of the mastic-mastic contacts located between aggregates in each mixture. In the presence of moisture, however, this resistance is reduced due to the deleterious effects that water produces on both the rheological properties of the binder and the adhesive resistance between the binder and the solid fillers. As a simplification, however, the thermodynamic potential of moisture to disrupt the binder-aggregate bond (i.e., adhesive bond in the presence of moisture) listed in Table 6-6 is used as an indirect measurement of the impact of moisture on the fracture resistance of the mastic-mastic contacts.

Table 6-6. Cohesive Bond Energy of Mastics in Dry Condition and Adhesive Bond Energy of Binders in the Presence of Moisture

Mastic/ Binder	Cohesive—Dry (J/m^2)	Adhesive with Granite—Wet (J/m^2)	Adhesive with Limestone—Wet (J/m^2)
PMA-LS	43.91	−345.49	−91.82
PMA-GR	47.83	−327.47	−74.83
ARB-LS	29.27	−324.16	−43.75
ARB-GR	31.23	−359.55	−60.41

6.4. OGFC Microstructures Characterization

Taking into account that the geometry of the OGFC mixtures and the properties of their constitutive phases are fundamental input data for the numerical model, different types of OGFC mixtures were fabricated in the Integrated Laboratory of Civil Engineering (Department of Civil and Environmental Engineering) at Universidad de los Andes. Mixtures 2 and 5, whose characteristics were listed in Table 3-1, were prepared using the SGC.

The objective of preparing these specimens was to obtain information of the internal geometry of the microstructure of these mixtures. This information constituted the geometry of the OGFC for the FE models. The mixtures were fabricated using different materials than those used in the experimental portion of the project, but with aggregates with similar origin and morphological properties. The mixtures were used exclusively to obtain typical microstructural geometries of the OGFC (i.e., the mixtures were not tested in the lab). In total, four specimens were prepared, as follows:

- **Specimen 1:** Gradation of mixture 5, OBC of 5.6 percent, AV of 20 percent.
- **Specimen 2:** Gradation of mixture 2, OBC of 6.5 percent, AV of 20 percent.
- **Specimen 3:** Gradation of mixture 2, OBC of 6.5 percent, AV of 25 percent.
- **Specimen 4:** Gradation of mixture 5, OBC of 5.6 percent, AV of 25 percent.

There were two specimens per mixture, each with a different AV content. The four specimens were scanned using X-ray CT techniques. Specifically, the images of the internal structure of the specimens were captured using an i-CAT MV FLX computerized axial tomographer with a resolution of 3200 x 2600 pixels. The obtained images were processed using the ImageJ software and AutoCAD. Figure 6-5 presents the scanning process and a typical 3D reconstruction of one of the mixtures using image analysis.

(a) (b) (c)

Figure 6-5. X-ray CT: (a) compacted mixture, (b) scanning process, and (c) 3D reconstruction of the mixture through image processing techniques.

The image analysis procedures permitted researchers to characterize the properties of the internal structure of the mixture, such as gradation, AV content, average aggregate orientation and amount, and length of stone-on-stone contacts. This, in turn, made it possible to identify rectangular fractions of images with 2 cm height and 11.82 cm width that complied with the required target gradation and AV content previously described, as observed in Figure 6-6. These rectangular images were chosen as the OGFC microstructure geometry that was used in the construction of the FE models. A summary of the methodologies used for the characterization of the four specimens is presented next, as well as properties of the selected microstructures used in the FE models.

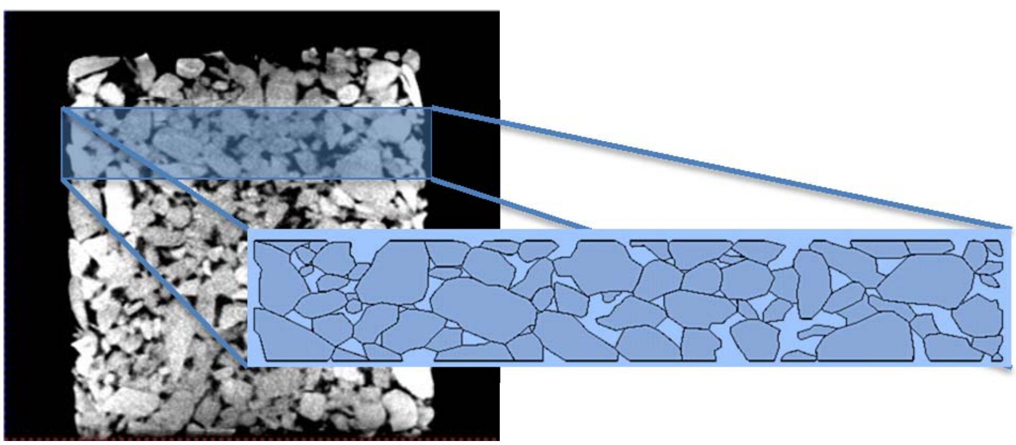

Figure 6-6. Extraction of a segment of an OGFC image Used in the FE models.

AutoCAD 2014 was used to determine the gradation of a specific 2D image of a mixture. In order to do so, the image was converted into a vector image, where the aggregates were represented by polygons. This information was then used to quantify the area and perimeter of each aggregate, the AV content of the sample, and other relevant information of the microstructure. Specifically, the gradation of the 2D OGFC section was determined after conducting a frequency distribution analysis of the areas of all particles. Figure 6-7 illustrates the process used to obtain the area of each aggregate.

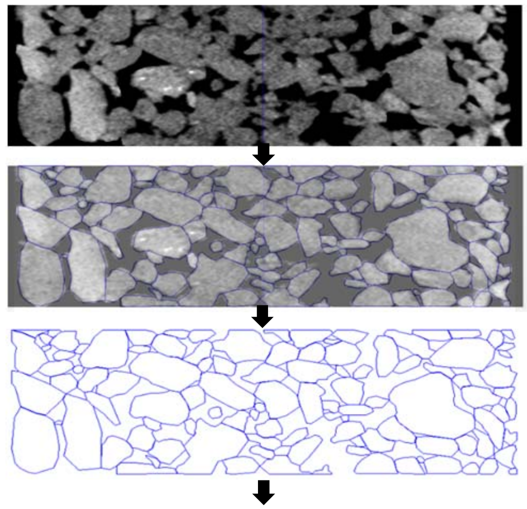

No. of the Aggregate	Aggregate	Area of the Aggregate (mm^2)
1		98.68

Figure 6-7. Quantification of the gradation of a 2D section of the OGFC mixture.

To define the orientation distribution of the aggregates, the angle between the longest line along each aggregate and a horizontal line was quantified. The longest line in a vector image is defined as the highest distance between the two farthest points on the contour or perimeter of the particle. This definition of aggregate orientation restricts the resulting values to the −90-degree to 90-degree range. The results of the orientation of all aggregates were used to define the frequency distribution within the OGFC section. Figure 6-8 depicts the process used to obtain the orientation of one aggregate particle.

As detailed in the literature review chapter, stone-on-stone contact in OGFC materials ensures proper resistance to raveling and permanent deformation. Therefore, the determination of stone-on-stone contact characteristics of the selected sections used in the FE model was of special interest in this project. For each selected OGFC section, two different parameters were quantified: (a) the number of contacts of each aggregate; and (b) the contact length of each aggregate, expressed as the percentage of the perimeter of the aggregate that was in contact with another aggregate. In this process, it was assumed that two particles were in contact if the distance between the edges of the aggregates in the image was less than 0.2 mm. Figure 6-9 illustrates the total number of contacts for each aggregate in a full 2D section obtained for one of the specimens, and Figure 6-10 presents the definition of the stone-on-stone contact length between a pair of aggregates, as well as the procedure used to determine this parameter.

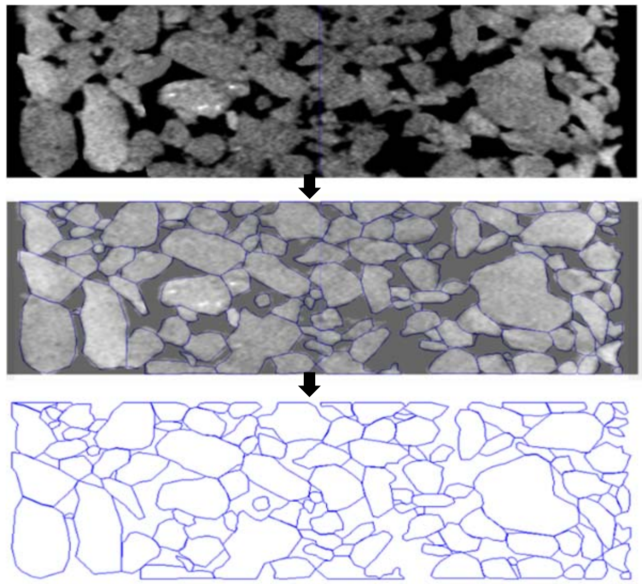

No. of the aggregate	Illustration of the Orientation	Orientation (Degrees)
1	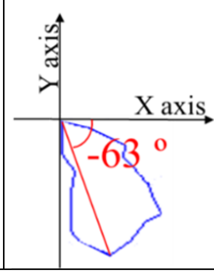	−63

Figure 6-8. Quantification of the aggregate orientation in a 2D section of the OGFC mixture.

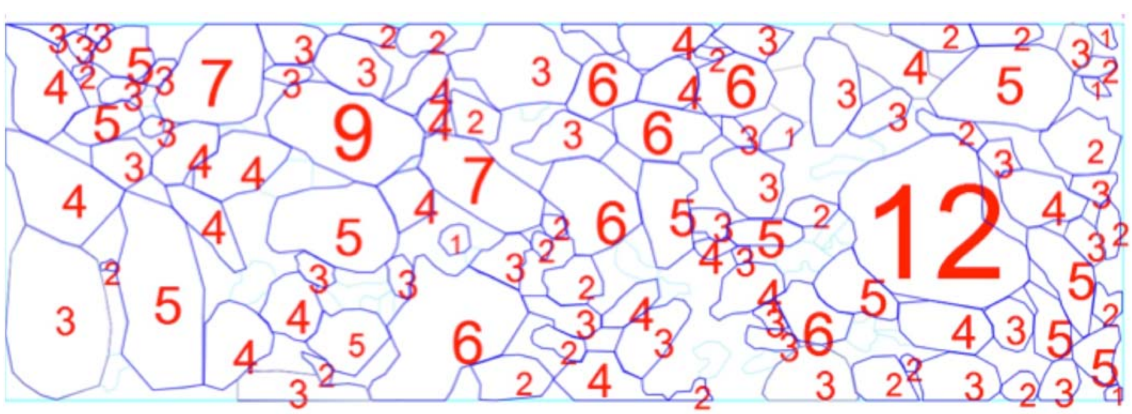

Figure 6-9. Number of contact points for each aggregate.

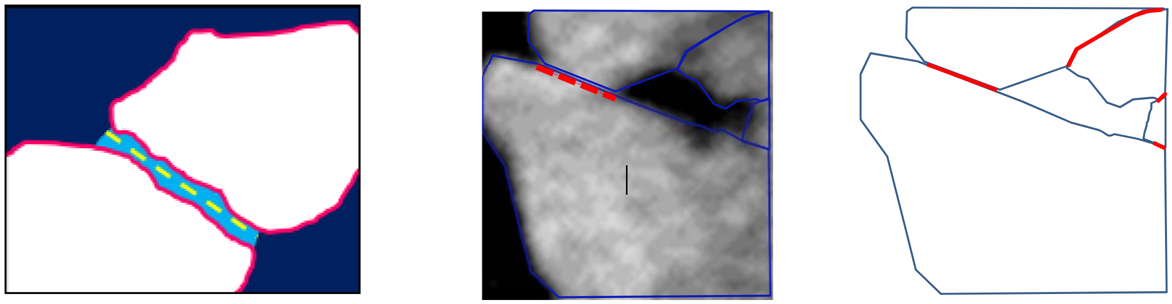

Figure 6-10. Contact length between two aggregates.

The results of each one of the characteristics of the selected OGFC sections obtained from each specimen are summarized next. The criteria for the selection of a specific section included a target AV value of the mixture (20 or 25 percent) and a gradation similar to the one specified for the mixture.

Table 6-7. Estimation of Aggregate Gradation of the Selected OGFC Sections of Each Specimen

Aggregate Gradation | **Aggregate Gradation Curve (red: specification; blue: selected OGFC section)**

Specimen 1

Sieve Size	Percent Passing (FDOT)	Percent Passing (image analysis)
3/4" (19.0 mm)	**100.0**	**100.0**
1/2" (12.5 mm)	**95.4**	**93.6**
3/8" (9.5 mm)	**72.6**	**64.8**
#4 (4.75 mm)	**19.8**	**33.6**
#8 (2.36 mm)	**9.0**	**20.80**
#16 (1.18 mm)	**6.6**	**8.8**
#30 (600 µm)	**4.9**	–
#50 (300 µm)	**3.9**	–
#100 (150 µm)	**3.2**	–
#200 (75 µm)	**2.8**	–

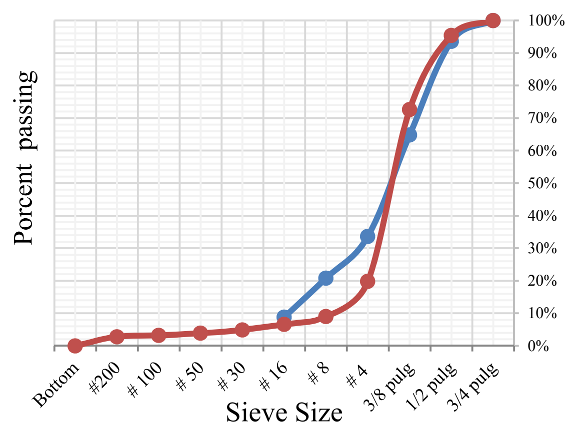

Specimen 2

Sieve size	Percent Passing (FDOT)	Percent Passing (image analysis)
3/4" (19.0 mm)	**100.0**	**100.0**
1/2" (12.5 mm)	**90.0**	**90.2**
3/8" (9.5 mm)	**66.0**	**51.6**
#4 (4.75 mm)	**24.0**	**38.2**
#8 (2.36 mm)	**10.0**	**27.5**
#16 (1.18 mm)	**8.0**	**16.7**
#30 (600 µm)	**7.0**	–
#50 (300 µm)	**6.0**	–
#100 (150 µm)	**5.0**	–
#200 (75 µm)	**3.5**	–

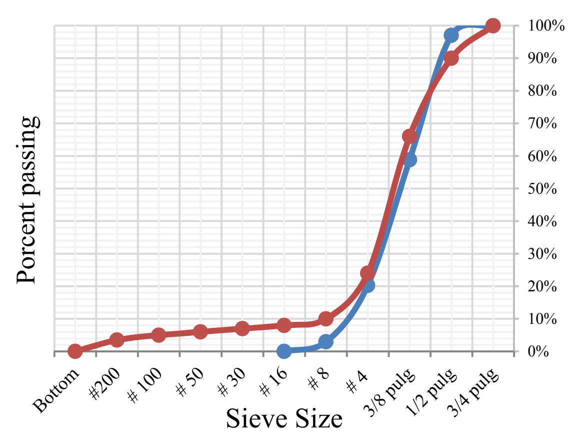

Table 6-7 (Continued). Estimation of Aggregate Gradation of the Selected OGFC Sections of Each Specimen

Specimen 3

Sieve size	Percent Passing (FDOT)	Percent Passing (image analysis)
3/4" (19.0 mm)	**100.0**	**100.0**
1/2" (12.5 mm)	**90.0**	**91.2**
3/8" (9.5 mm)	**66.0**	**47.4**
#4 (4.75 mm)	**24.0**	**34.3**
#8 (2.36 mm)	**10.0**	**24.8**
#16 (1.18 mm)	**8.0**	**15.33**
#30 (600 µm)	**7.0**	–
#50 (300 µm)	**6.0**	–
#100 (150 µm)	**5.0**	–
#200 (75 µm)	**3.5**	–

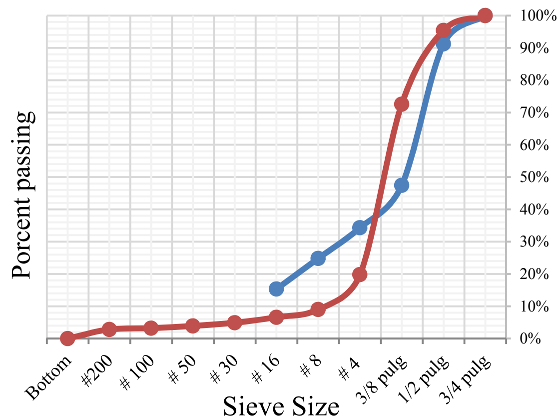

Specimen 4

Sieve Size	Percent Passing (FDOT)	Percent Passing (image analysis)
3/4" (19.0 mm)	**100.0**	**100.0**
11/2" (12.5 mm)	**95.4**	**91.3**
3/8" (9.5 mm)	**72.6**	**49.3**
#4 (4.75 mm)	**19.8**	**15.9**
#8 (2.36 mm)	**9.0**	–
#16 (1.18 mm)	**6.6**	–
#30 (600 µm)	**4.9**	–
#50 (300 µm)	**3.9**	–
#100 (150 µm)	**3.2**	–
#200 (75 µm)	**2.8**	–

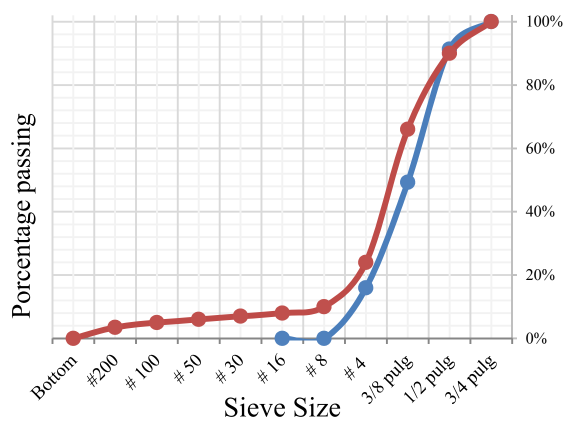

Data in Table 6-7 show that the image analysis process did not provide information on particles with an area smaller than 0.28 mm^2, which was a consequence of the resolution of the tomographer. Despite these limitations, the results show that the analysis provided a good indication of the actual gradation of the mixtures. Furthermore, the similarities between the target gradation and the actual gradation (i.e., mean square error lower than 9 percent in all cases) validated the use of the selected sections for the FE model.

Figure 6-11 summarizes the results of aggregate orientation of each OGFC section. This figure presents both the longest distance of each aggregate and the angle orientation distribution of those lines.

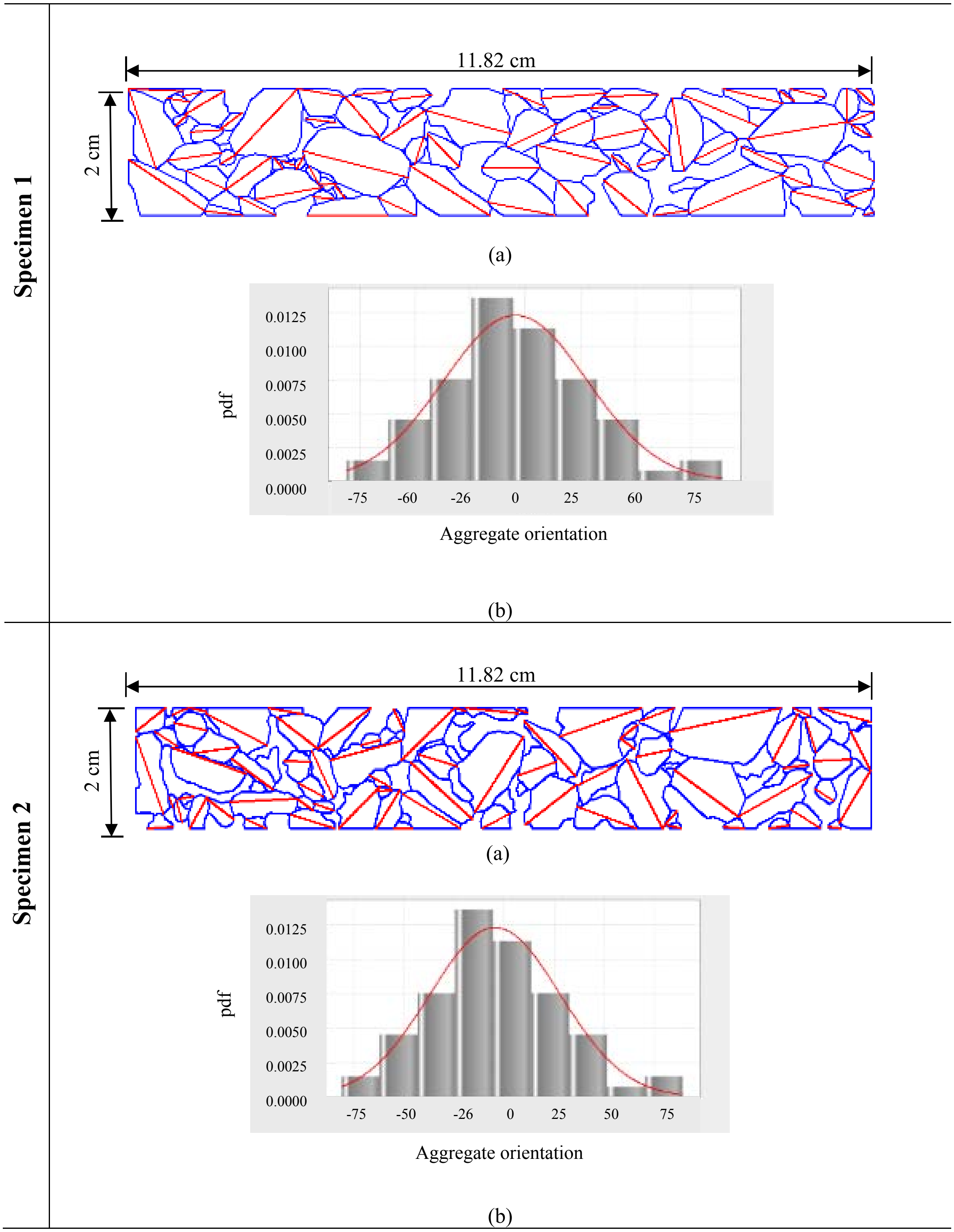

Figure 6-11. Aggregate orientation of the selected OGFC sections of each specimen: (a) lines used to define aggregate orientation, (b) aggregate orientation frequency distribution and corresponding probability density function (pdf).

Specimen 3

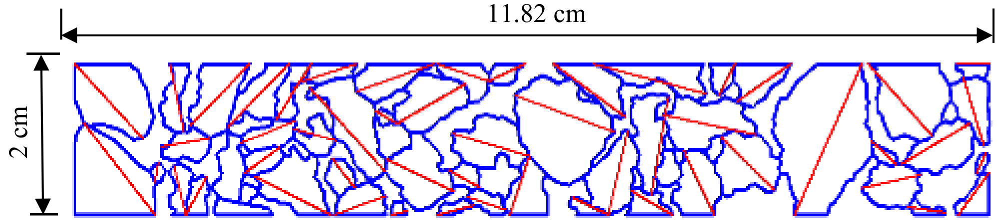

(a)

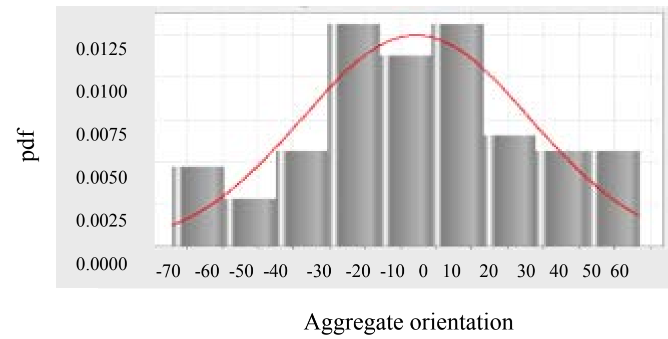

(b)

Specimen 4

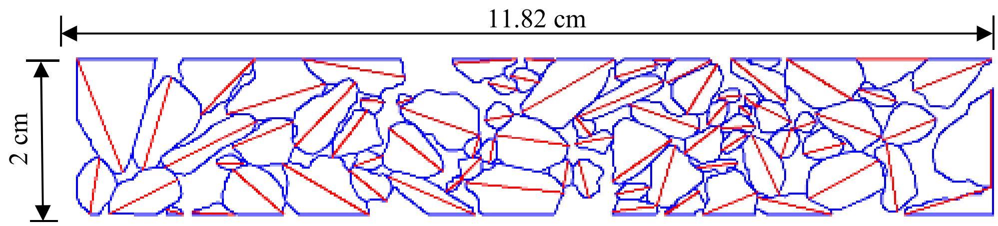

(a)

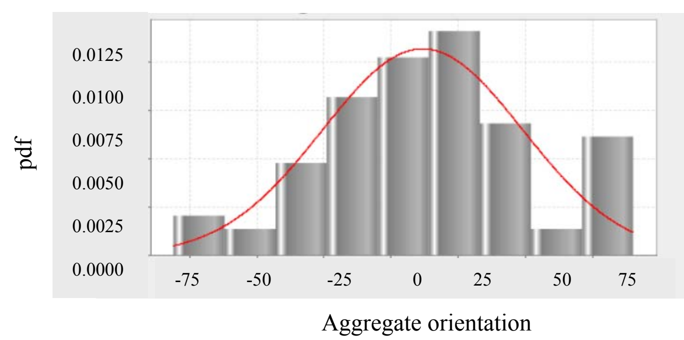

(b)

Figure 6-11 (Continued). Aggregate orientation of the selected OGFC sections of each specimen: (a) lines used to define aggregate orientation, (b) aggregate orientation frequency distribution and corresponding probability density function (pdf).

Table 6-8 lists the corresponding probability density function (pdf) presenting the best fit for the aggregate orientation distributions.

Table 6-8. pdf of Aggregate Orientation

Sample	Total Particles Analyzed	Pdf Distributions	Parameters
Specimen 1	70	Normal	$\mu = -4.52^o$ $\sigma = 32.42^o$
Specimen 2	59	Normal	$\mu = -5.63^o$ $\sigma = 31.86^o$
Specimen 3	56	Normal	$\mu = -9.55^o$ $\sigma = 37.87^o$
Specimen 4	77	Normal	$\mu = -11.71$ $\sigma = 37.30^o$

The results of the aggregate orientation analysis show that the particles had a preferred horizontal orientation, which is a well-known consequence of both aggregate form and compaction processes. Also, it is observed that mixtures with larger AV content (25 percent) had larger mean values of aggregate orientation angles than did mixtures with a smaller AV amount.

Finally, in terms of the stone-on-stone contact properties of the OGFC microstructures, both the number of contacts per aggregate and the percentage of the perimeter of each aggregate in contact with another aggregate were computed. Figure 6-12 presents the number of contacts per aggregate as well as the corresponding pdfs.

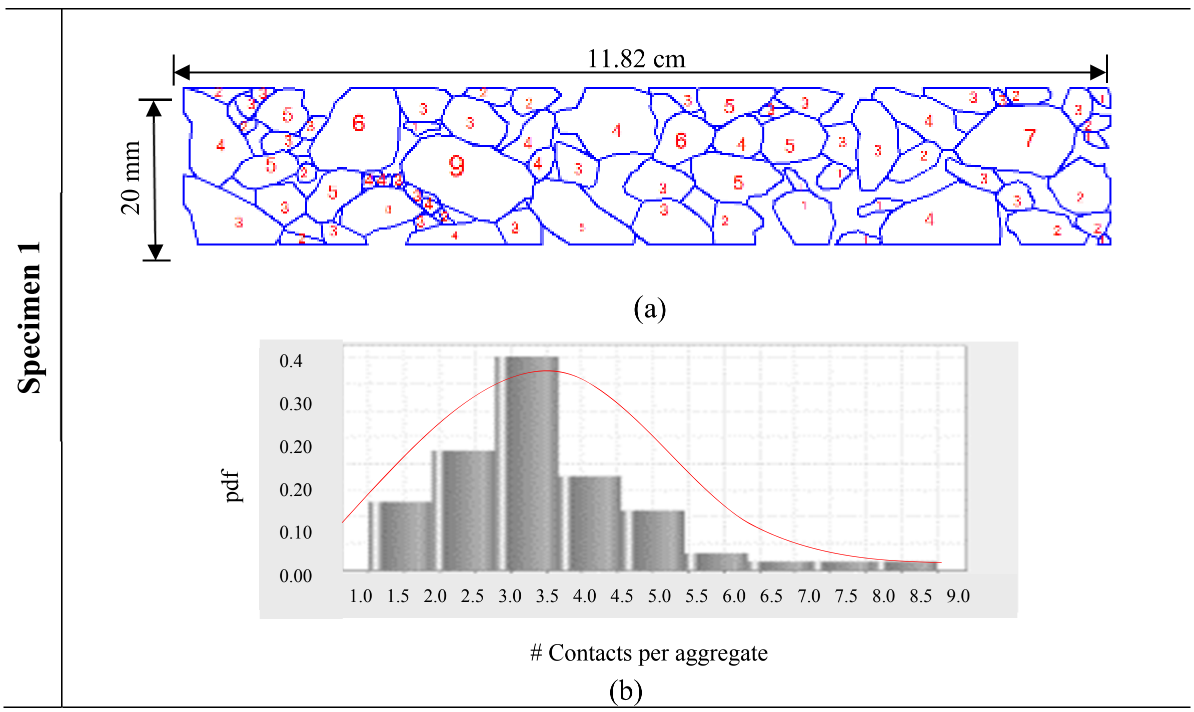

Figure 6-12. Aggregate contacts of the selected OGFC sections of each specimen: (a) number of contacts, (b) frequency distribution and corresponding probability density function (pdf).

Specimen 2

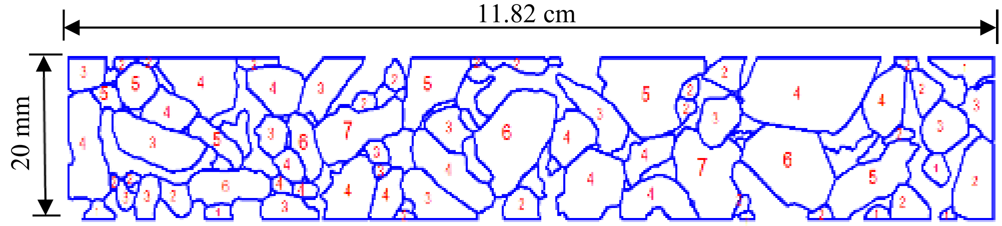

(a)

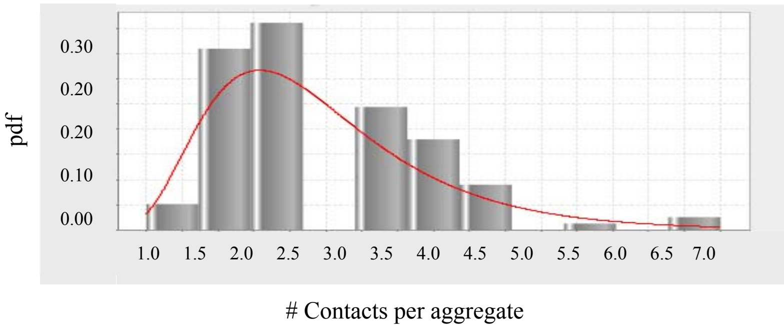

(b)

Specimen 3

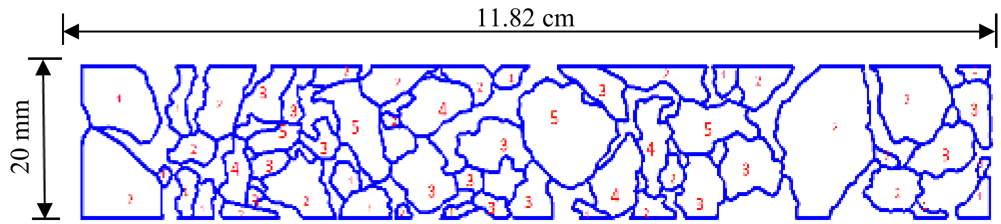

(a)

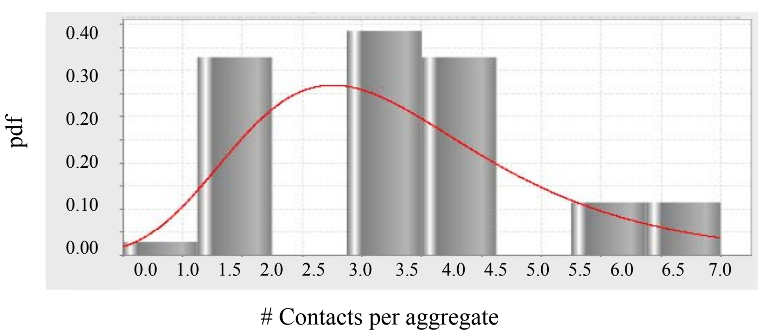

(b)

Figure 6-12 (Continued). Aggregate contacts of the selected OGFC sections of each specimen: (a) number of contacts, (b) frequency distribution and corresponding probability density function (pdf).

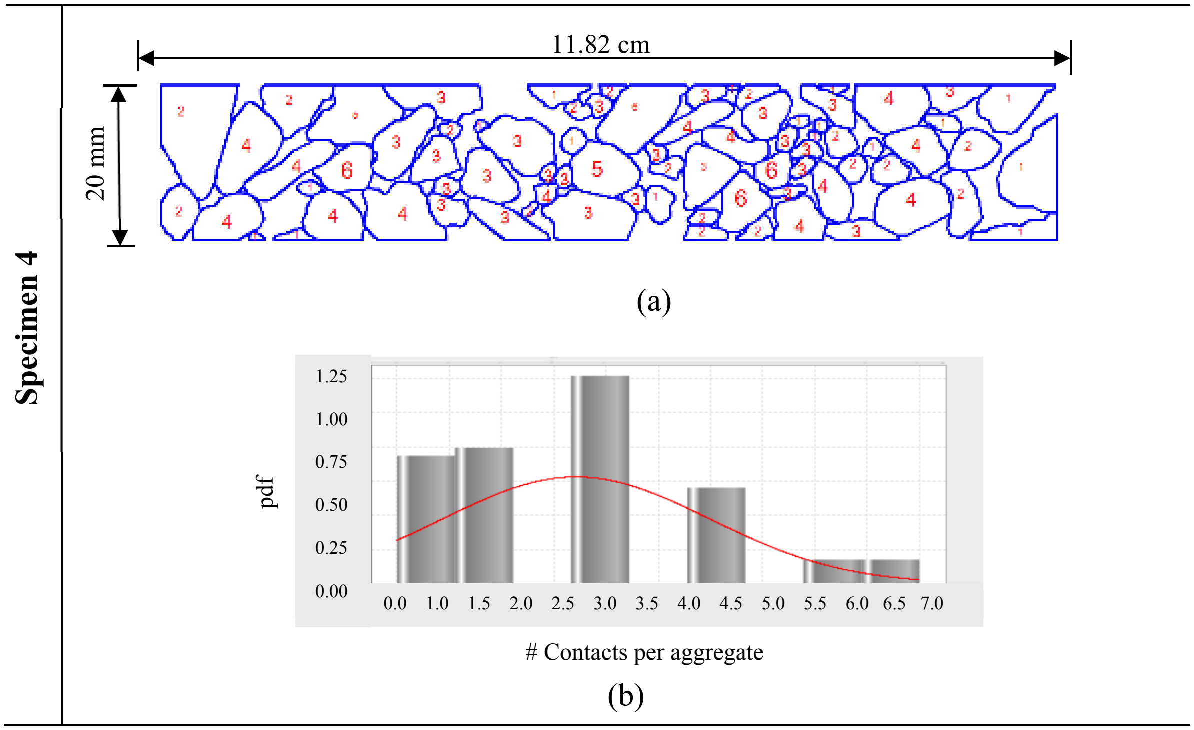

Figure 6-12 (Continued). Aggregate contacts of the selected OGFC sections of each specimen: (a) number of contacts, (b) frequency distribution and corresponding probability density function (pdf).

Table 6-9 summarizes the pdfs presenting the best fit for the number of contacts per aggregate.

Table 6-9. pdfs of Aggregate Contacts

Specimen	Total Particles Analyzed	pdf Distribution	Parameters	Other Statistics
Specimen 1	70	Gamma	$\alpha = 4.25$ $\lambda = 1.32$	$\mu = 3.23$ $\sigma = 1.58$
Specimen 2	59	Gamma	$\alpha = 5.38$ $\lambda = 1.59$	$\mu = 3.39$ $\sigma = 1.44$
Specimen 3	56	Normal	$\mu = 2.32$ $\sigma = 1.20$	$\mu = 2.32$ $\sigma = 1.20$
Specimen 4	77	Weibull	$\alpha = 2.27$ $\lambda = 0.33$	$\mu = 2.71$ $\sigma = 1.28$

The analysis showed that the mean number of contacts for the specimens having 20 percent AV was three, while the mean number of contacts for specimens having 25 percent AV was only two, a result that suggests that higher compaction levels increased the number of contacts among aggregates, as expected.

Finally, Figure 6-13 presents the contact length and the pdfs of the percent of the perimeter of each aggregate that was in contact with other aggregates.

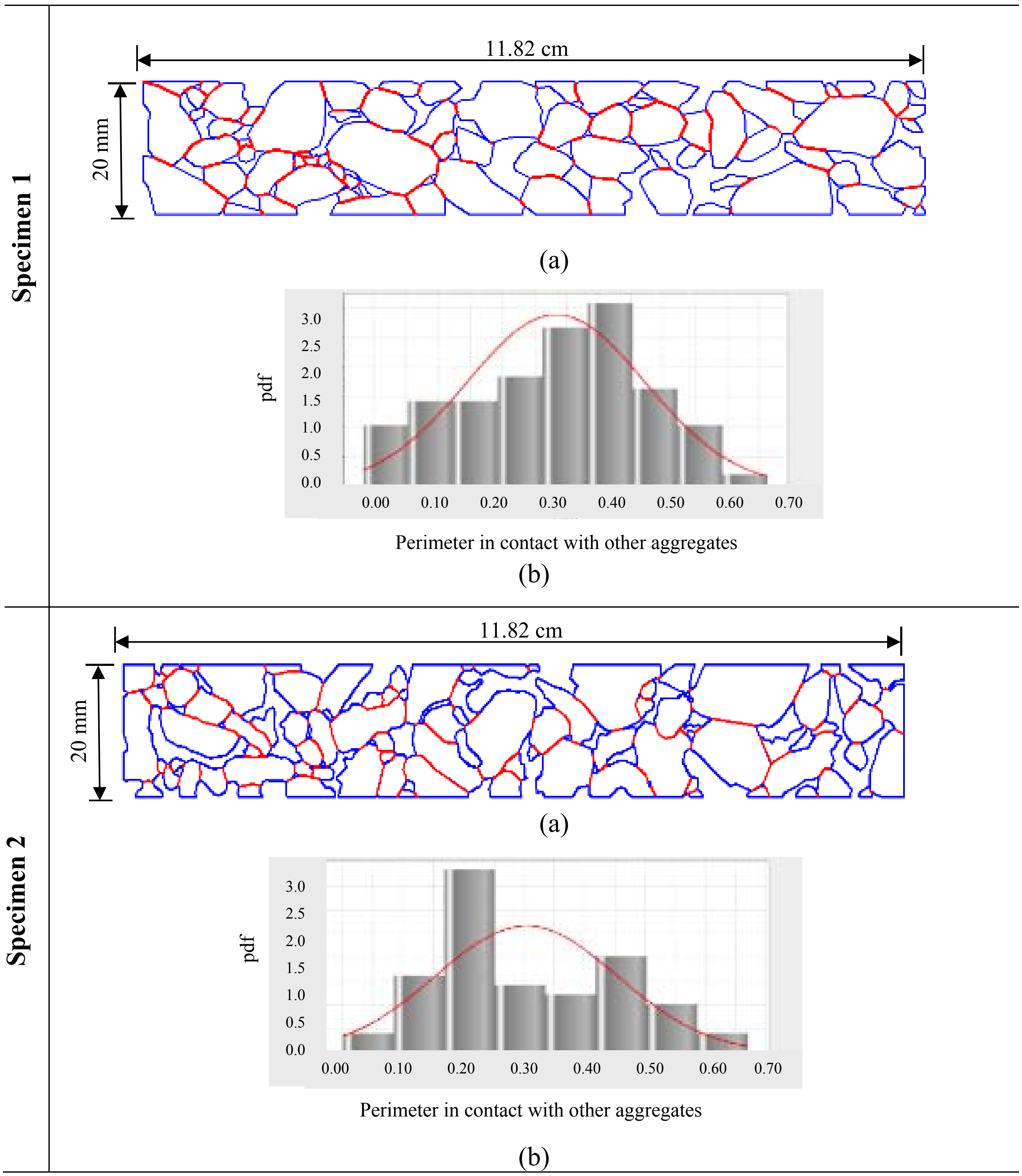

Figure 6-13. Aggregate perimeter in contact with other aggregates of the selected OGFC sections of each specimen: (a) stone-on-stone (mastic-mastic) contacts, (b) frequency distribution and corresponding probability density function (pdf).

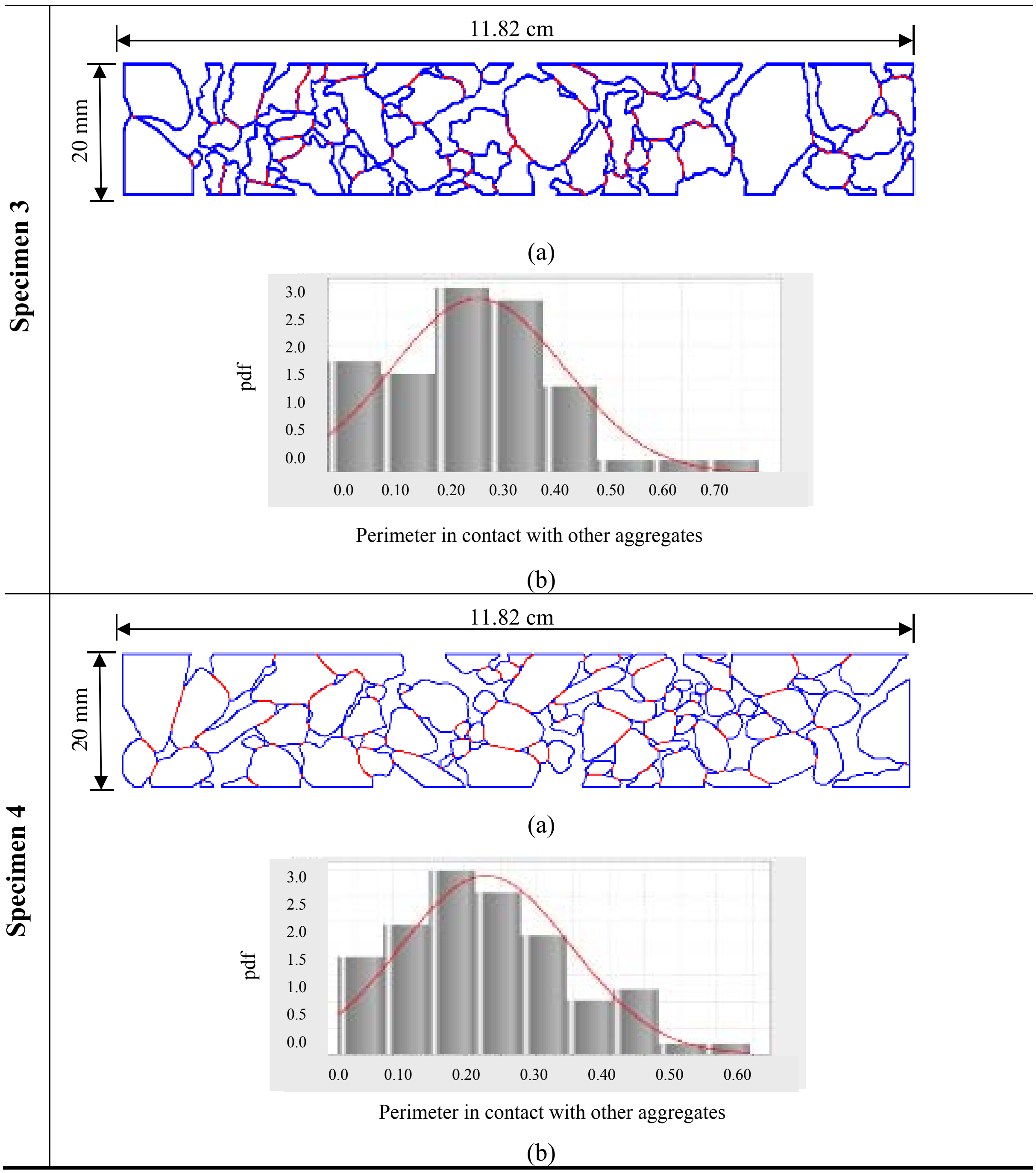

Figure 6-13 (Continued). Aggregate perimeter in contact with other aggregates of the selected OGFC sections of each specimen: (a) stone-on-stone (mastic-mastic) contacts, (b) frequency distribution and corresponding probability density function (pdf).

The pdf results showed that the two samples fabricated with 20 percent AV had a higher percentage of the perimeter of each aggregate in contact with other aggregates as compared to mixtures with higher AV content. These results, presented in Table 6-10, are in good agreement with the previous analysis of the number of contacts per aggregate.

Table 6-10. pdfs of Percentage of Aggregate Perimeter in Contact with Other Aggregates

Sample	Total particles analyzed	pdf distribution	Parameters
Specimen 1	70	Normal	μ = 33.33% σ = 13.88%
Specimen 2	59	Normal	μ = 35.40% σ = 14.98%
Specimen 3	56	Normal	μ = 25.59% σ = 14.40%
Specimen 4	77	Normal	μ= 22.98% σ = 11.82%

6.5. FE Modeling

As was stated above, the input parameters to the 2D FE model in Abaqus® consisted of the results obtained from the material characterization stage and the experimental work used to generate valid geometries of the mixtures. The OGFC mixtures in the model were exposed to different internal and external conditions, as illustrated in Figure 6-14. A total of 82 simulations were conducted to measure the influence of the internal and external variables in the susceptibility of the mixtures to raveling.

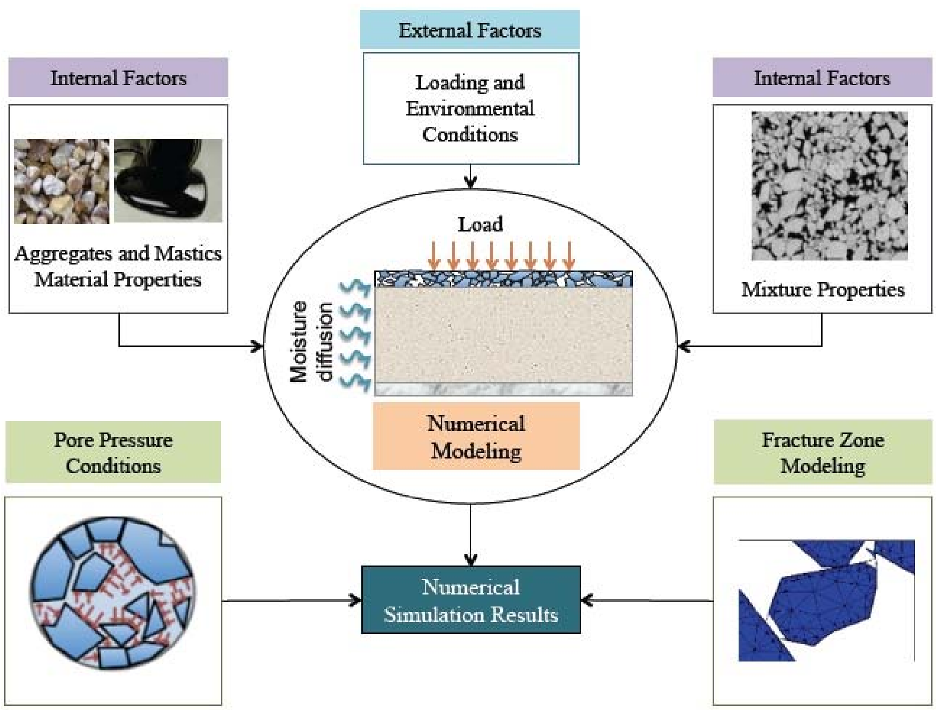

Figure 6-14. Numerical model overall methodology.

The model simulations were divided into two parts:

- The performance of the pavement models using the six OGFC mixtures that were characterized in the experimental portion of this project.

- The performance of two base models that consisted of mixtures 2 and 5 with 20 percent AV. The base models are herein defined as two typical cases with average external conditions and with internal structures corresponding to two commonly used mixtures. After conducting the simulations with the two base models, the following internal and external factors were evaluated, and the corresponding results were compared to those of the base models:
  - **Internal factors:** material combinations, OGFC binder content or AC (percent), OGFC total AV content (percent), and OGFC layer thickness.
  - **External factors:** pavement structure beneath the OGFC, OGFC temperature, load magnitude, load speed, longitudinal forces, moisture diffusion.

Additionally, simulations to evaluate the impact of pore pressure on the potential initiation of cracking processes at stone-on-stone contacts, as well as fracture simulations using cohesive zone modeling (CZM) in aged OGFC in those contact areas, were conducted.

Thus, the mechanical performance of the six OGFC mixtures under study was evaluated, followed by the simulation cases on the two base models. The base models were subjected to the listed internal and external conditions to analyze the influence of each parameter in raveling susceptibility.

6.5.1. Pavement Structure Geometry for the FE Models

The pavement model consisted of three main layers: (a) an OGFC, (b) an equivalent base layer, and (c) a typical subgrade. The OGFC layer was composed of three phases—(a) aggregates, (b) mastic, and (c) air voids—while the equivalent base and the subgrade were assumed to be continuum materials. The equivalent layer represented all other layers existing in the pavement structure between the OGFC and the subgrade. This simplification permitted researchers to reduce the computational time of the simulations and focus on the localized phenomena occurring within the OGFC. In this work, the equivalent base layer was composed by a linear elastic material with an equivalent linear elastic modulus (E) of 520 MPa and a Poisson's ratio, ν, of 0.35, while the subgrade was composed of a linear elastic material with an elastic modulus (E) of 100 MPa and a Poisson's ratio, ν, of 0.45.

The OGFC layers were fabricated using the rectangular sections described in the section on OGFC microstructure characterization. Figure 6-15 presents the modeled asphalt pavement, which had an OGFC layer 2 cm thick, an equivalent rectangular base of 59 x 60 cm, and a rectangular subgrade of 59 x 40 cm. These thicknesses were defined based on typical OGFC used in Florida and, in the case of the equivalent base layer, using a thickness equivalent procedure on a common pavement structure used in Florida (FDOT 2008). In terms of the boundary conditions, the bottom of the model was restrained to move or rotate in any direction, and the sides of the model were restrained to displace in the horizontal direction, enabling the whole model to represent a transverse section of a typical flexible pavement with an OGFC layer.

The resolution of the images obtained from X-ray CT permitted researchers to obtain a clear identification of the aggregate particles but not of the mastic that coated those aggregates. Therefore, each aggregate in the model was coated with a thin mastic film. As observed in Figure 6-15, the model assumed that the mastic film thickness was the same for all aggregates. Thus, based on the binder content, or AC, of the mixture, the mastic film thickness changed between 10 and 20 μm. For this calculation, all aggregates were simplified as spheres of different sizes depending on the gradation of the mixture. With this information, the total surface area of all aggregates was computed, so the effective binder volume was divided by the total surface area in order to estimate the mastic film thickness.

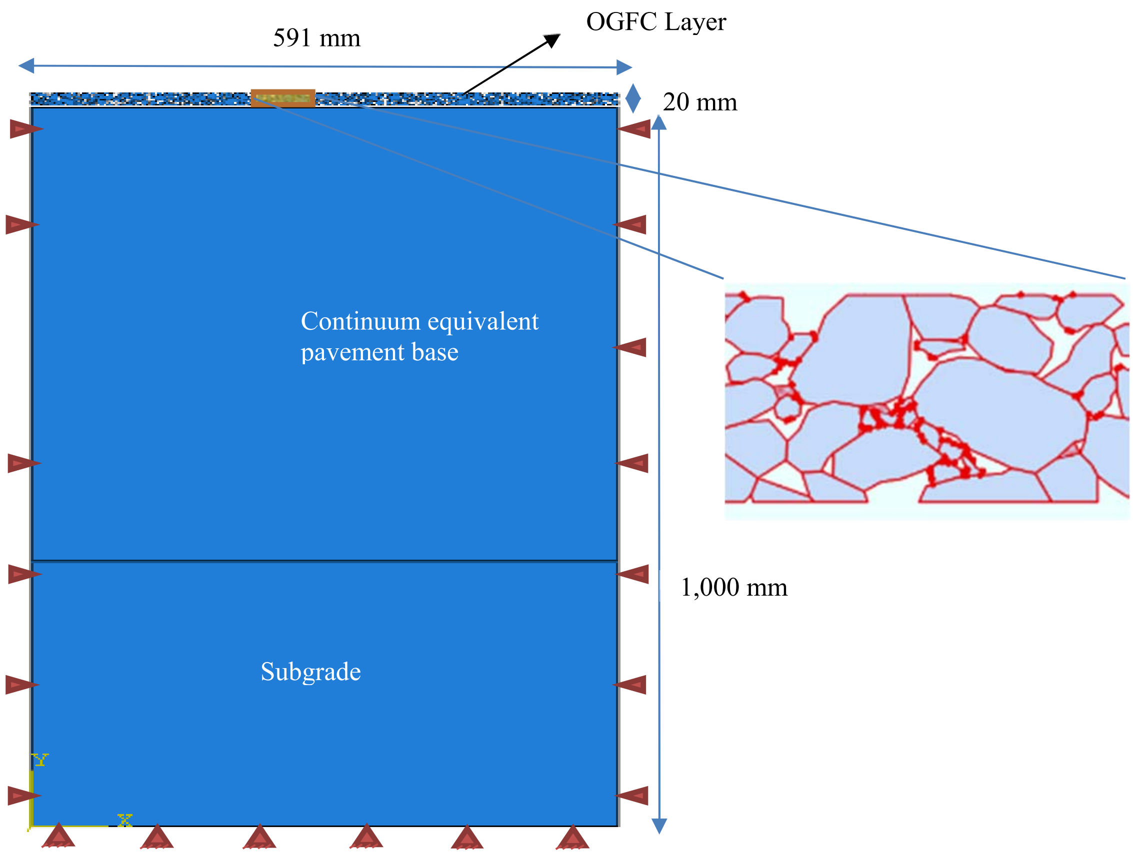

Figure 6-15. Geometry of the Abaqus® FE model.

6.5.2. Mechanical Loading

The base models were subjected to the action of a circular moving wheel that corresponded to half of a single-single axle load of 49.7 kN. This value was identified to be a typical loading magnitude in highways in Florida, according to three different load control stations (Figure 6-16; LTPP 2015). The tire-pavement interaction was assumed to have a pressure contact (q) of 0.88 MPa, which resulted in a contact radio (a) of 9.5 cm. This wheel ran over the structure at a speed of 55 mph[1] (88.5 km/h). In addition to this case, two other load magnitudes (66.6–83.7 kN) and two other speed conditions (48–113 km/h) were evaluated.

[1] 55 mph is the minimum velocity recommended by FDOT.

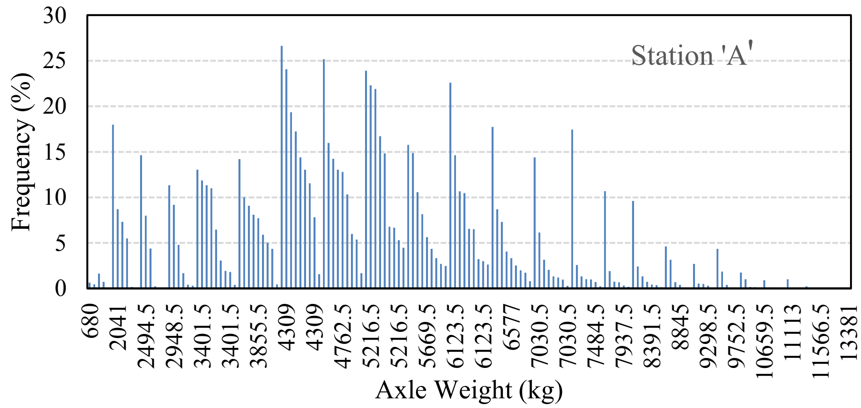

Figure 6-16. A Florida load spectra 2011 (LTPP 2015).

In terms of the horizontal loading that was developed at the contact between the wheel and the surface of the OGFC layer, as established by Milne et al. (2004) in numerical FE models of pavements subjected to free rolling tires, the maximum longitudinal force (F_x) in the displacement direction was around 30 percent of the maximum vertical force (F_v), and the resistance to rolling was around 2.5 percent F_v. The exact value of the maximum vertical stress depended on the tire weight and on the specific dynamics of the problem. Besides this case, the models also considered another condition in which the vehicle was braking, which implied that the longitudinal load was around 78 percent F_v.

Figure 6-17 presents some initial results obtained for one of the base models. These internal stress distributions changed as a function of the several different variables that were included as part of the analysis. In this particular case, the model corresponded to a wheel of 24.8 kN that ran over the pavement at a speed of 88.5 km/h, when the OGFC had a mean temperature value of 30°C.

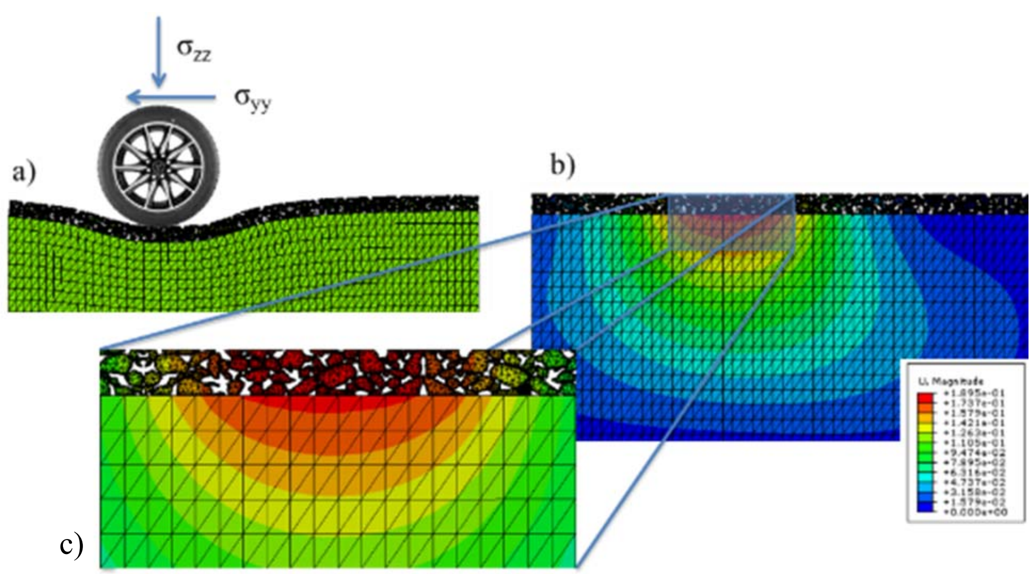

Figure 6-17. Base model illustration: (a) Moving wheel, (b) deformation in the vertical direction (deformation scale factor: 1.0), (c) deformation at the surface (deformation scale factor: 200).

6.5.3. Temperature

To determine the pavement surface temperature, the LTPPBind (2015) software was used. The software allows for computing the temperature at the interior of a pavement located at specific coordinates at several depths. Figure 6-18 shows the results from the Miami Beach weather station at a depth of 25 mm, which is the minimum permitted depth in the software. The maximum air temperature reported in this zone was 32.4ºC, which is related to a temperature of 50ºC at 25 mm from the surface of the pavement. Although the actual thickness of the layer was smaller than 25 mm, and this model is for regular dense-graded HMA (i.e., the actual temperature for the OGFC could be different), this value was considered a good indicator of what could be the temperature in the OGFC surface layer. Furthermore, an FE numerical model of temperature diffusion on an actual 20 mm OGFC was applied using the air temperature from that station, and the maximum values of temperatures obtained within the mastic material were also similar. Therefore, three temperatures were modeled: (a) high pavement temperature: 50ºC; (b) mean pavement temperature: 30ºC (base cases); and (c) low pavement temperature: 9.7≈10ºC.

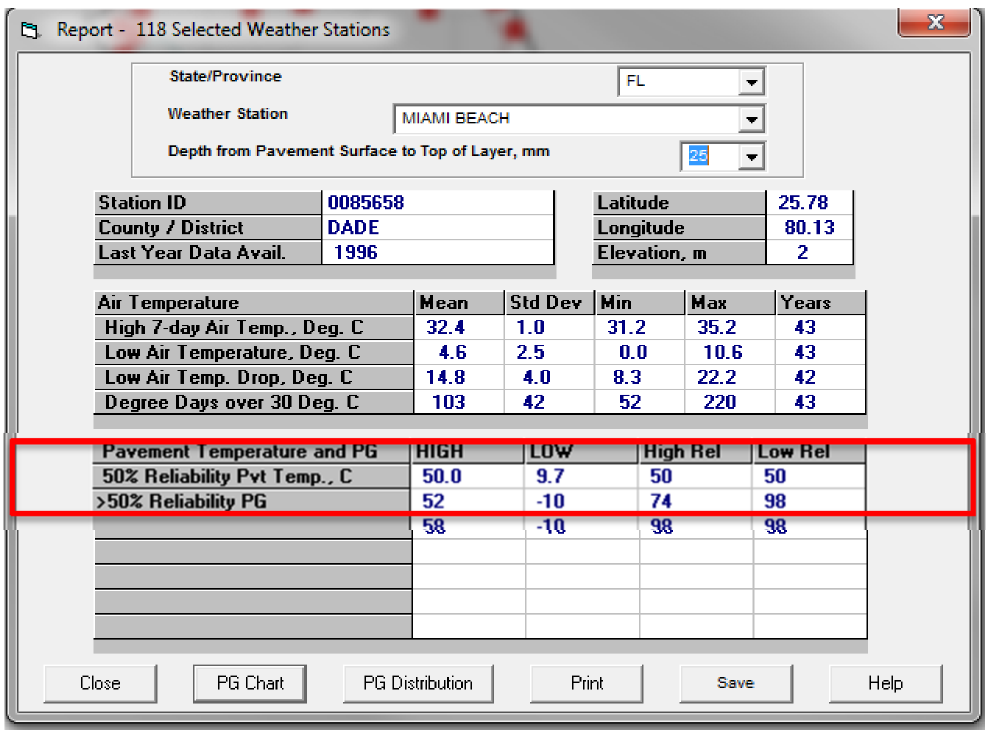

Figure 6-18. Pavement temperatures at a depth of 25 mm from the surface of the pavement.

6.5.4. Moisture Diffusion and Pore Pressure

Moisture diffusion is believed to be an important factor promoting raveling in OGFC mixtures. For this reason, all the material combinations (e.g., aggregate/mastic) were evaluated under different levels of relative humidity (RH). In order to do so, the mixtures were exposed to a 1-month moisture diffusion process that consisted of applying a constant extreme value of RH of 100 percent on the top of the OGFC, as observed in Figure 6-19.

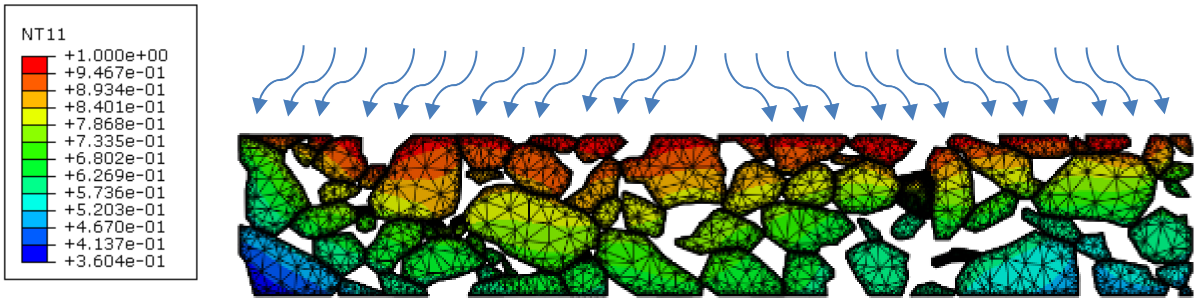

Figure 6-19. Moisture diffusion in an OGFC mixture with gradation type 4 and material combination GR/PMA+LS Filler (note: NT11 is the normalized moisture content; a value of 1.0 represents a saturated condition).

After this conditioning process, the load wheel was applied to the pavement. In these coupled simulations, the rheological properties of the mastics coating the aggregates were modified as a function of the amount of RH at each specific location. In order to do so, the instantaneous modulus of the relaxation curves of the mastics, E_0, which affects all the parameters of the Prony Series, were made dependent of the amount of moisture as follows (Hernández 2013):

$$E_{0wet} = E_{0dry} * RH\ factor \tag{6-3}$$

$$RH\ factor\ (-) = e^{0.27843(u-7)} \tag{6-4}$$

$$RH\ factor\ (-) = e^{0.27843(u-7)} \tag{6-5}$$

$$RH\ (\%) = 10^{2-\left(10^{u-6.502}\right)} \tag{6-6}$$

Where u is suction in pF, which is another form to express RH (Equation 6-6). Thus, the factor by which the instantaneous modulus is modified as a function of RH (Equation 6-3) is given in Figure 6-20.

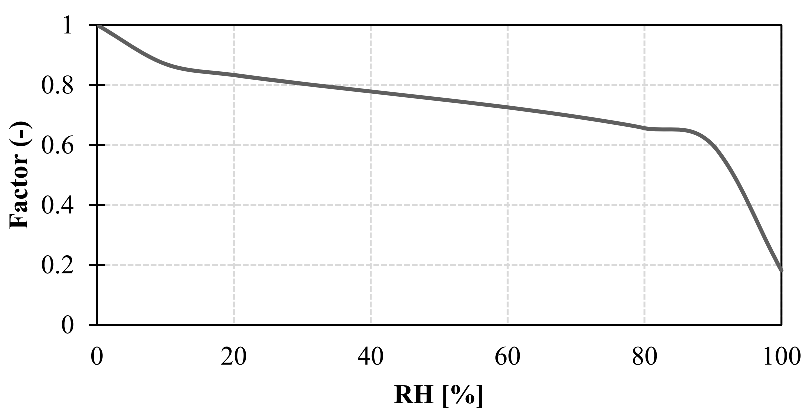

Figure 6-20. RH factor used to modify the linear viscoelastic material properties of the mastics as a function of moisture content.

Table 6-11 shows the different moisture diffusion coefficients used for each constitutive phase, while Figure 6-21 shows the change in the instantaneous axial modulus (E_0) of the mastic PMA+LS filler at 30ºC under different levels of RH.

Table 6-11. Moisture Diffusion Coefficients

Material	Diffusion Coefficient (mm^2/s)	Reference
PMA	3.088x10^{-06}	Kringos et al. (2008)
ARB-12	4.00x10^{-08}	Kringos et al. (2008)
Granite	2.44x10^{-04}	Caro et al. (2010)
Limestone	2.40x10^{-04}	Arambula et al. (2010)

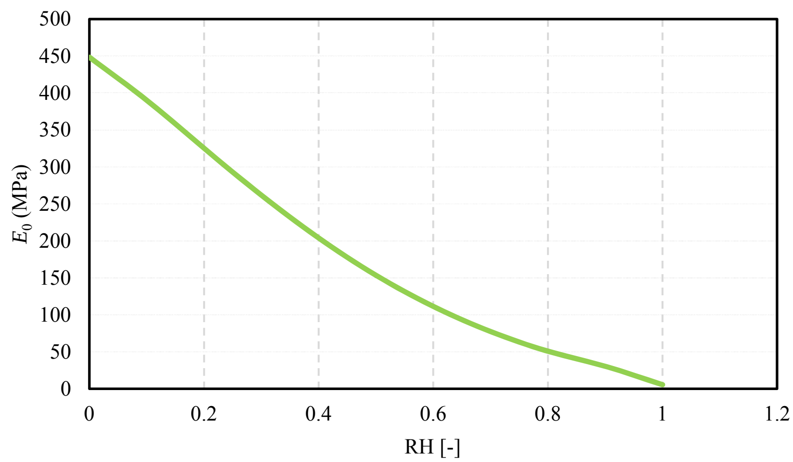

Figure 6-21. Instantaneous modulus of the material combination PMA+ LS Filler for different RH values.

Another potential deleterious effect of moisture in the generation of raveling was analyzed through the effects of pore pressure. In this case, however, a simplified FE model was used. The model consisted on a small OGFC section with several aggregates and the additional localization of stresses and strains developed at the mastic-mastic contacts with the presence of pore pressure. Pore pressure was studied in two states: under a drained saturated condition (i.e., water is flowing within the OGFC) and under an undrained saturated condition (i.e., water is trapped within the OGFC due to, for example, clogging).

6.5.5. AV Content and OGFC Thickness

In order to analyze the impact of the AV content and the OGFC thickness layer, six different models were considered, as presented in Figure 6-22. Mixture 2 and mixture 5, which corresponded to Base Models 1 and 2, were evaluated with two values of AV—20 and 25 percent—and mixture 5 (Base Model 1) was also evaluated with an OGFC layer thickness of 4 cm.

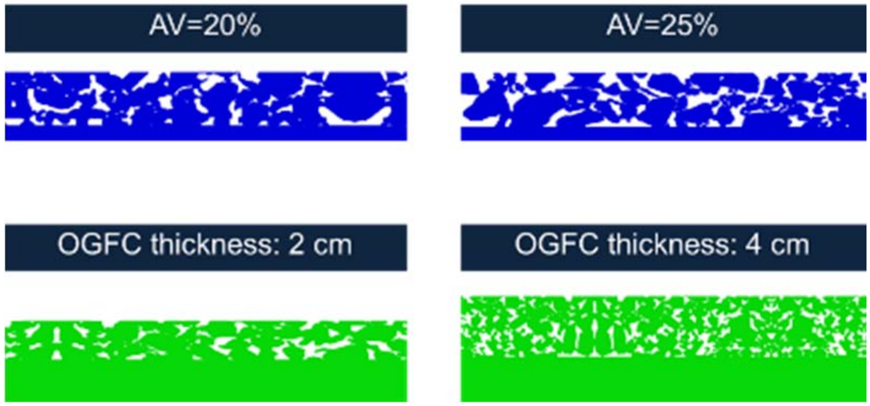

Figure 6-22. AV content and OGFC thickness.

6.5.6. Fracture within the OGFC

The FE models previously described provided an indication of raveling through the magnitudes of the stresses and strains developed at the stone-on-stone (mastic-on-mastic) contacts. However, none of those models represented actual cohesive fracture or equivalent raveling initiation. In order to verify the results obtained from the simulations, the CZM technique was used to simulate fracture. Models able to simulate fracture initiation and progression processes in FE are usually numerically unstable and time consuming (i.e., approximately 12 hr per model, in this study). For this reason, only two simulations were conducted with this fracture model, which corresponded to Base Models 1 and 2.

The CZM technique assumes that there exists a process zone in front of the crack tip that supports a certain level of traction. However, when the material reaches its maximum tensile strength in any of the classical modes of fracture (Mode I, II, or III), such level of resistance starts decreasing due to the stresses that are being developed near the crack tip, to the point where the material cannot support any more load, the element physically disappears, and the crack propagates. At this point, the process zone displaces, promoting the evolution of the cracking process. The energy required for this process to initiate corresponds to the critical fracture energy of the material. In this work, that energy was estimated based on the experimental measurements conducted to determine the SFE of the different mastics, as presented in previous sections. The cohesive elements were located at the interface between aggregate contacts, representing the stone-on-stone contact zones.

In this work, a traction separation law that assumes a linear elastic behavior before damage initiation was selected. After damage initiation, the traction separation law follows an exponential decay that symbolizes the softening process occurring in the material. Figure 6-23 presents the location of the cohesive elements and the traction separation law selected, while Figure 6-24 illustrates the initiation and propagation of cracks within one OGFC model. A main result of this model is the time required for fracture to initiate and the amount of elements that fail with time during the pass of the wheel.

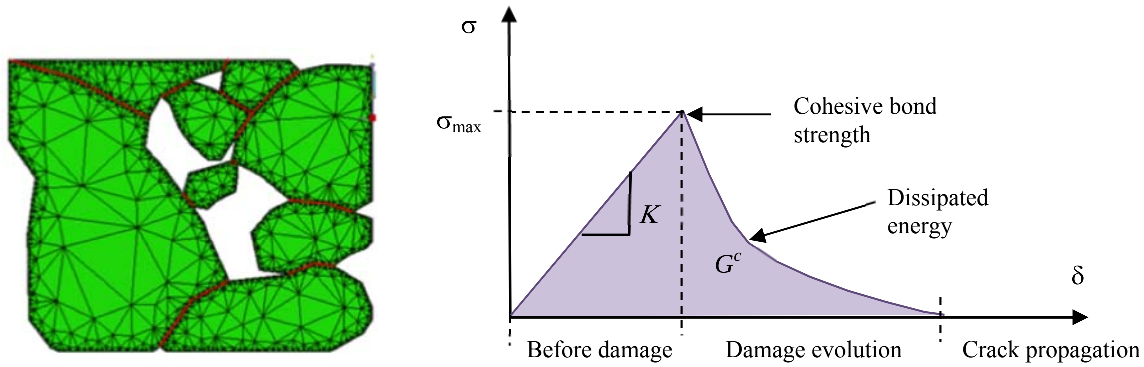

(a) **(b)**

Figure 6-23- Cohesive zones: (a) location, and (b) constitutive behavior.

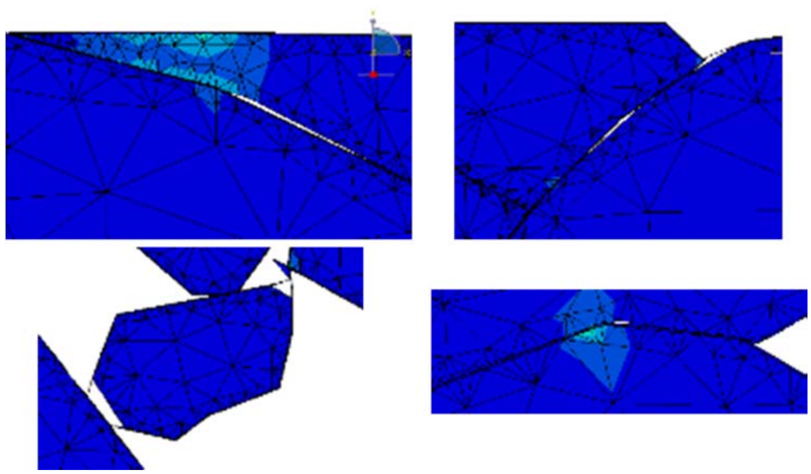

Figure 6-24. Crack propagation within the OGFC.

Since cohesive fracture due to raveling is more probable when the material becomes more brittle after a certain time in service (e.g., due to oxidative hardening), the simulations were conducted using rheological properties of the mastics in a state that simulates long-term aging. For this reason, information on the rheological properties of the binders in a PAV state were used to estimate the changes in properties of the mastics, and the Prony Series of each mastic was modified accordingly.

6.5.7. Summary of the Internal and External Parameters

Table 6-12 presents the values of the different parameters considered in the FE simulations.

Table 6-12. Internal and External Parameters Considered in the FE Model

Internal Parameters	Properties
Materials (Aggregate/Mastic)	**GR/PMA+GR**, GR/ARB+GR, LS/PMA+LS, and **LS/ARB+LS**
Equivalent Base (MPa)	400, **520**, and 645
Subgrade (MPa)	50, **100**, and 150
AC (%)	4.1, **5.6**, and **7.1**
AV (%)	**20** and 25
OGFC Layer Thickness (cm)	**2** and 4
External Parameters	**Properties**
Temperature (°C)	10, **30**, and 50
Vertical Load Magnitude (kN)	**24.8**, 66.7, and 83.7
Vertical Load Radius (cm)	**9.5**, 11, and 12
Longitudinal Force Magnitude (kN)	**0.62**, 7.45, and 19.38
Load Speed (km/h)	48, **88.5**, and 113
Moisture Diffusion	1 month of moisture conditioning under an RH condition of 100%
Aging	CZM implementation
Pore Pressure	Analysis of pore pressure effects under critical saturated undrained conditions

Note: Bold and underlined parameters correspond to the ones used in Base Models 1 and 2. Base Model 1 had GR/PMA+GR and 5.6 percent OBC; Base Model 2 had LS/ARB+LS and 7.1 percent OBC.

6.6. Data Analysis Methodology

After the FE simulations were conducted, it was necessary to define a strategy to analyze the results, with the objective to determine the raveling susceptibility of the OGFC mixture under multiple conditions.

FE models directly provided the horizontal, vertical, and shear stresses (σ) and strains (ε) for each finite element through time. However, since raveling was expected to occur at stone-on-stone contact areas, it was not necessary to analyze the mechanical response of any constitutive phase outside these zones. In Base Model 1, this rationale allowed researchers to evaluate the mechanical response of only 2,900 finite elements, which corresponded to the total elements existing at contact areas, instead of evaluating the total 30,000 mastic elements. Figure 6-25 presents the OGFC with the total mastic elements and the contact mastic elements that were considered in the analysis.

An algorithm was developed to extract the information of the horizontal, vertical, and shear stresses and strains at the mastic elements located at the contact areas. As an example, Figure 6-26 presents the horizontal strains of all the elements (i.e., each curve corresponds to one finite element) located in a contact zone through time, for a simulation conducted on Base Model 1 for mixture 5. From this information, an envelope of the maximum horizontal strains through time was obtained, as observed in Figure 6-27. These data permitted researchers to identify the elements that presented the maximum stresses and strains in the global directions (i.e., horizontal, vertical, and shear) as illustrated in Figure 6-28.

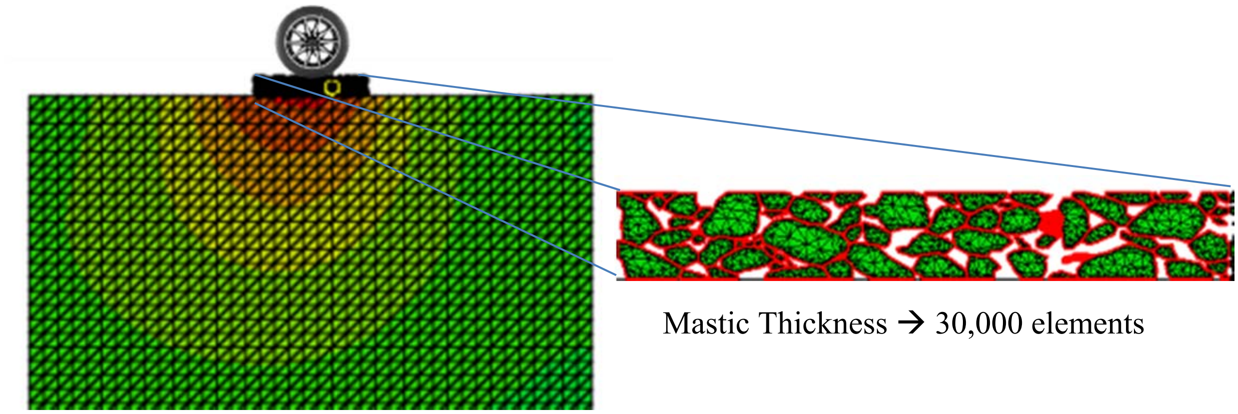

(a)

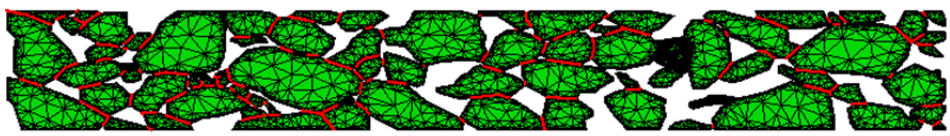

(b)

Figure 6-25. Finite elements: (a) OGFC zone of analysis and detail of the total mastic elements, (b) mastic elements in contact areas.

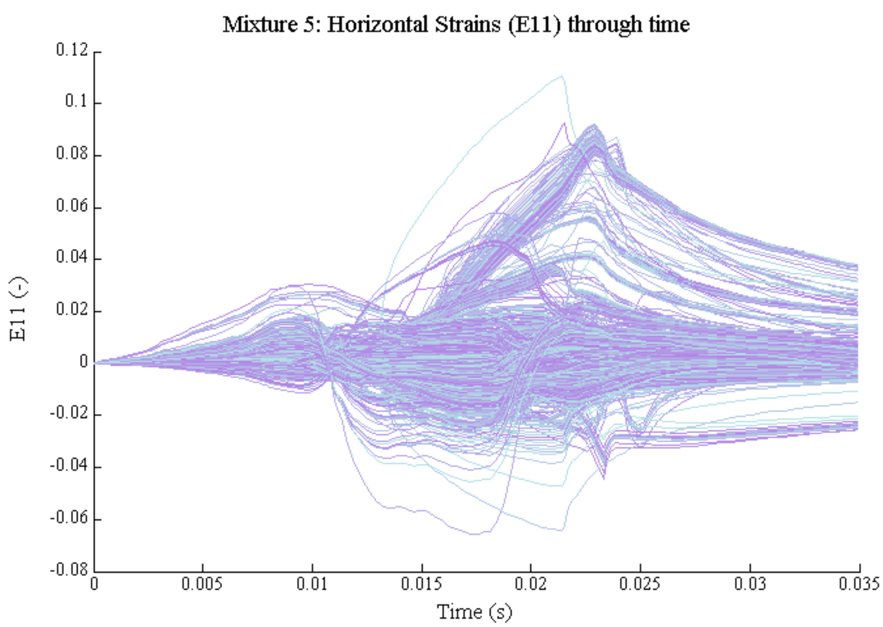

Figure 6-26. Horizontal strains through time on Base Model 1 (mixture 5).

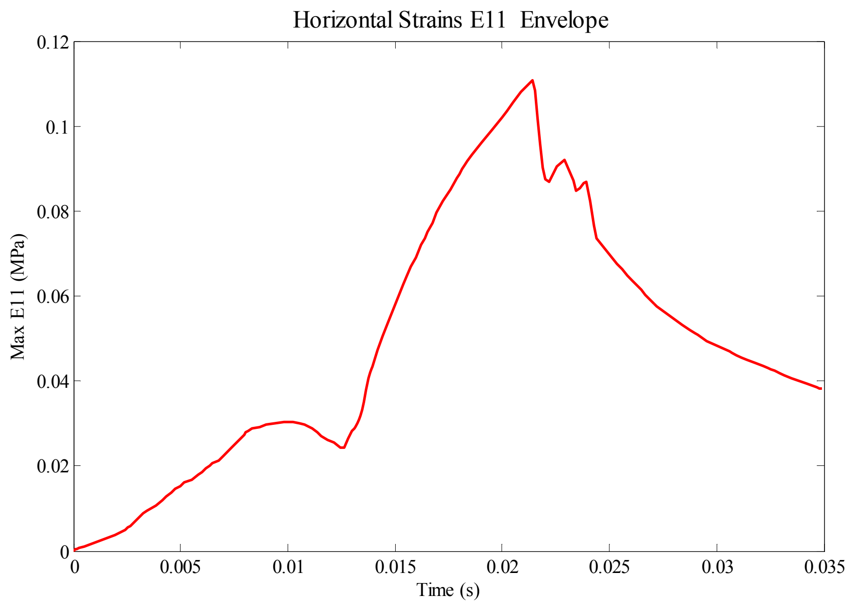

Figure 6-27. Envelope of maximum horizontal strains through time (mixture 5).

Although knowing the magnitude and location at which the maximum strains and stresses occurred provided researchers with new and interesting information about the localization of stress-strain conditions in the model (Figure 6-28), it did not provide fundamental information about raveling susceptibility because the global coordinates did not correspond to the directions or coordinates of the two expected main modes of failure (Mode I or opening mode, and Mode II or shear mode), which are responsible for the actual fracture of a stone-on-stone contact. This situation is illustrated in Figure 6-29.

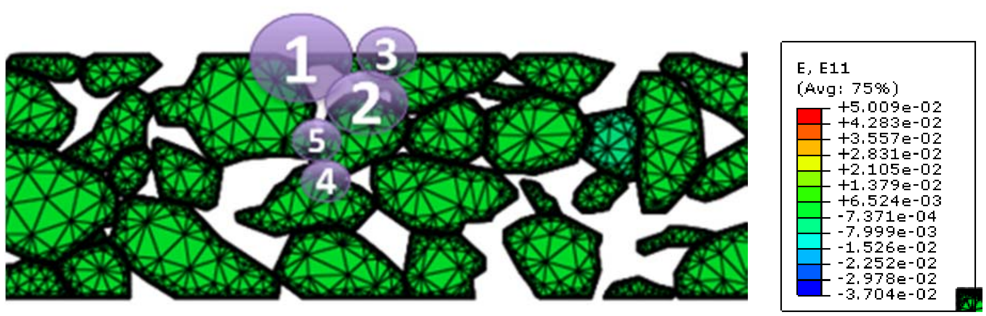

Figure 6-28. Maximum strain locations (Base Model 1).

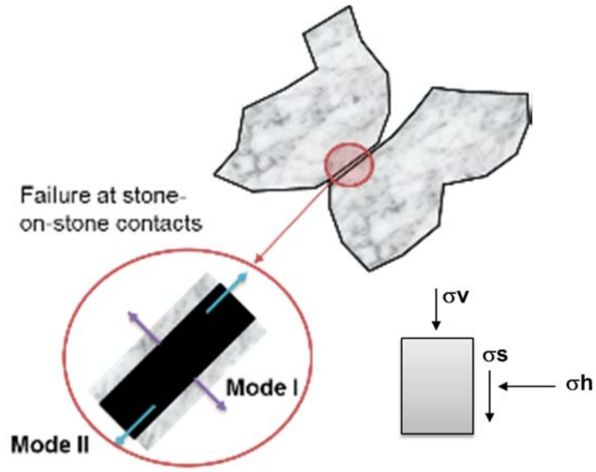

Figure 6-29. Fracture modes I and II in a stone-on-stone contact.

In order to account for the actual potential modes of failure that could generate raveling, the maximum tensile and shear stresses and strains were computed for each element using the Mohr's circle (Figure 6-30). Thus, the maximum tensile stress and strain within each contact element were related to Mode I of failure, while the maximum shear stress and strain within each contact element were related to Mode II of failure.

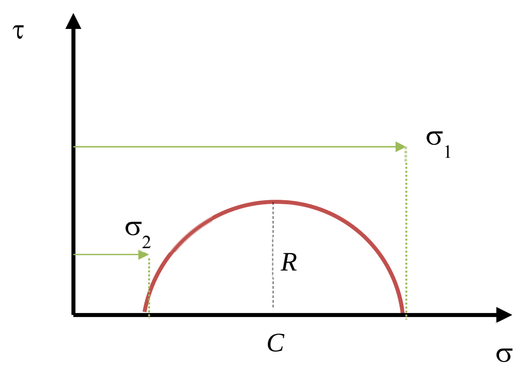

Figure 6-30. Mohr's circle (principal stresses: σ_1 and σ_2).

Based on the state of stresses in the Mohr's circle, the center and the radius were computed with the following equations:

$$\boldsymbol{Center}: \boldsymbol{\sigma_{avg}} = \frac{\boldsymbol{\sigma_h + \sigma_v}}{\boldsymbol{2}} \tag{6-7}$$

$$Radius: R = \sqrt{\left(\frac{\sigma_h + \sigma_v}{2}\right)^2 + \tau^2} \tag{6-8}$$

$$\sigma_1 = \sigma_{avg} + R \tag{6-9}$$

$$\sigma_2 = \sigma_{avg} - R \tag{6-10}$$

Where:
σ_h, σ_v, and τ = the horizontal, vertical, and shear stresses, respectively.
σ_1 and σ_2 = the principal stresses of the element.

Therefore, the maximum tensile stress, σ_1, was related to Mode I of failure, while the maximum shear stress, or τ_{max}, that corresponded to the radius (*R*) of the Mohr's circle was related to Mode II of failure. A similar procedure was conducted to obtain the maximum tensile and shear strains within each contact element.

After computing the maximum tensile and shear stresses and strains at each mastic element in the contact zones, it was necessary to define a mechanical parameter to evaluate the overall mechanical response of the OGFC. Since raveling is a problem where both stresses and strains are equally relevant (due, among other things, to the fact that the problem is considering viscoelastic materials at intermediate temperatures), it was convenient to use the *dissipated energy* of the mastic elements as part of the raveling susceptibility criterion. The dissipated energy was computed as the area within the curve of the maximum tensile (Mode I) and shear (Mode II) stresses and strains. Figure 6-31 illustrates a typical maximum tensile stress vs. maximum tensile curve, as well as the corresponding dissipated energy, for Mode I of failure. Notice that since this is a stress and strain curve and not a force-displacement curve, the dissipated energy has units of J/m^3 and not directly of Joules.

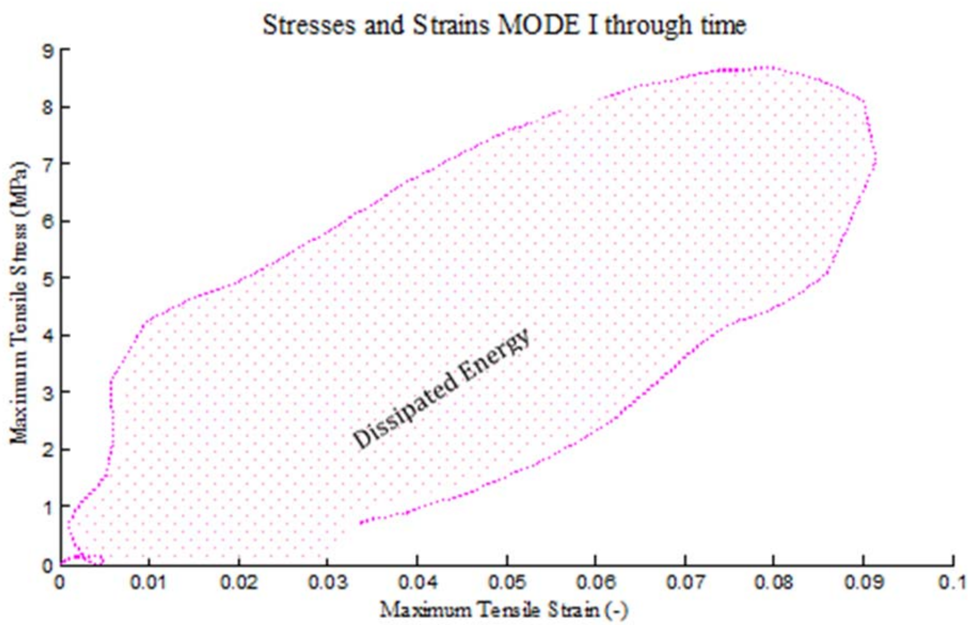

Figure 6-31. Dissipated energy per element for Mode I of failure.

6.6.1. Raveling Index (R.I.)

The total dissipated energy of the mastic contact element provided crucial information regarding the mechanical response of the OGFC subjected to different conditions. However, it did not provide direct information on the raveling potential of each mixture because the relevant factors include not only the magnitude of the dissipated energy, but also the actual energy that is required to produce fracture. For example, one OGFC could have dissipated 100 J/m^3 of energy after one mechanical simulation, while another OGFC mixture, subjected to the same external conditions, could have dissipated 50 J/m^3. If the fracture toughness of the first mixture is 200 J/m^3 and the fracture toughness of the other mixture is 52 J/m^3, the second mixture is more prone to fracture or raveling, even when the total dissipated energy is lower in comparison to the first one.

Therefore, information regarding the energy required to produce fracture in the different OGFC mixtures was required. Since there are not standardized fracture experiments on mastics that could easily provide this information, the cohesive bond energy computed based on the SFE of the mastics was used for this purpose. Thus, the R.I. for all the cases that did not include the presence of moisture (i.e., dry cases) was defined as:

$$R.I._{dry} = \frac{Dissipated\ energy\left(\frac{J}{m^3}\right)}{Cohesive\ bond\ energy_{dry}\left(\frac{J}{m^2}\right)} \tag{6-11}$$

In this way, larger R.I.$_{dry}$ values (i.e., larger ratio values between the dissipated energy and the cohesive bond energy) indicated that the mixture was more susceptible to raveling. Please note that, as demonstrated by Masad et al. (2010), the theoretical work of adhesion (i.e., adhesive bond energy) computed through SFE measurements is several orders of magnitude smaller than the actual work of adhesion (or critical facture energy) measured for any material in the laboratory. This means that the R.I. can never be 1.0 or close to 1.0 for any mixture (the dissipated energy will never be equal to the energy required to fracture). Furthermore, both quantities have different units, which means that R.I. should be understood only as a parameter or a scalar that can be related to the potential to fracture. Consequently, the sole purpose of this index is to provide valid comparative analyses of the failure susceptibility of different mastic-mastic contacts based on the fact that higher values always represent a higher probability of a material to crack.

In the simulations where moisture was present, a different indicator was required. In these cases, the following R.I. was proposed:

$$R.I._{wet} = \frac{Dissipated\ Energy\left(\frac{J}{m^3}\right)}{Cohesive\ bond\ energy_{reduced}\left(\frac{J}{m^2}\right)} \tag{6-12}$$

This index considers the impact of moisture on the resistance of the mastics to fracture. The factor by which the cohesive bond energy is reduced was related to the propensity of the filler particles and binder interfaces to be affected by the presence of moisture within the mastic materials (i.e., adhesive bond energy). As explained in previous sections of this report, there is a thermodynamic favorable tendency of moisture to affect the interface between these two materials, which results in a negative value of the adhesive bond energy. Thus, the reduction factor used to represent the impact of moisture on the cohesive bond energy of each mastic was related to this adhesive quantity. In order to do so, researchers assumed that the cohesive bond strength of the mastic with the highest susceptibility to moisture damage was reduced by 20 percent (a value related to a typical minimum acceptable value for dense mixtures in the AASHTO T 283 test), and the cohesive bonds of all other mastics were reduced in a smaller proportion depending on their adhesive bond energy, as shown in Table 6-13. Thus, once again, larger R.I.$_{wet}$ values indicated a higher propensity of a material to failure at the contact zones (i.e., to raveling).

Table 6-13. Reduced Cohesive Bond Energy

Mastic	Adhesive Bond Wet Conditions (J/m^2)	Reduction Factor	Dry Cohesive Bond Energy (J/m^2)	Reduced Cohesive Bond Energy (J/m^2)
ARB+GR	−359.55	20.00%	47.83	38.27
PMA+GR	−327.47	17.97%	31.23	25.62
PMA+LS	−91.82	3.04%	29.27	28.38
ARB+LS	−43.75	2.77%	43.91	42.70

Note that the use of the R.I. was not necessary in the simulations that included CZM since in those cases, fracture actually occurred within the model. In those simulations, the number of contacts presenting fracture through time was considered an evaluation parameter to compare raveling effects.

6.7. Analysis of Results

The initial part of the analysis studied the global mechanical performance of the six FDOT mixtures evaluated in this project, while the second part focused on evaluating the performance of the mixtures selected as base models and the impact of the changes in the response of those mixtures when affected by the internal and external factors summarized in Table 6-12.

6.7.1. Mechanical Response of the OGFC

Six mixtures were evaluated according to the standard load conditions presented in Table 6-12 (q = 0.88 MPa, a = 9.5 cm, v = 88.5 km/h). These OGFC mixtures corresponded to the mixtures experimentally evaluated in previous tasks. In order to provide a proper framework to better understand the data analysis presented in this section, the basic information of these mixtures is presented again in Table 6-14.

Table 6-14. Asphalt Mixture Description

Mixture	Field Performance	Aggregate Type	Asphalt Type	OBC (%)	Antistrip (%)
1	Good	LS	PMA	7.1	0.5
2	Good	LS	ARB	7.1	0.5
3	Poor	LS	PMA	6.1	0.5
4	N/A	LS	ARB	6.1	0.5
5	N/A	GR	PMA	5.6	1.0
6	N/A	GR	ARB	5.6	1.0

Based on the description of the gradation of the mixtures presented in previous sections, it can be concluded that there were three different gradations, corresponding to (a) mixtures 1 and 2, (b) mixtures 3 and 4, and (c) mixtures 5 and 6. For this reason, three basic geometries were used to model all mixtures. As previously mentioned, the rectangular microstructures representing these gradations with a total AV content of 20 percent were used in the FE model. All particles were considered uniformly coated with mastic, and the mastic thickness varied depending on OBC, amount of binder absorbed by the aggregates, and gradation. Table 6-15 lists the mastic thickness corresponding to each mixture.

Table 6-15. Mastic Thickness in the FE Models for the Six FDOT Mixtures

Mixture	Mastic thickness (μm)
1 & 2	17
3 & 4	10
5 & 6	15

After conducting the numerical simulations, researchers computed the R.I.$_{dry}$ values for the six mixtures by applying Equation 6-11, after obtaining the dissipated energy on both modes of failure. The maximum R.I.$_{dry}$ values reported among all contact elements within the mixture are presented in Figure 6-32 for Mode I and Mode II of failure. Based on these results, researchers concluded that the predominant failure mode of these mixtures as a consequence of the action of traffic was Mode I. Figure 6-32 also shows that mixture 3 had the highest R.I.$_{dry}$, which suggested that this mixture could develop raveling at a contact element with a higher probability; this finding is in good agreement with reported field performance. Mixtures 5 and 6, in contrast, both fabricated with GR aggregates, presented the lowest R.I.$_{dry}$ values, which indicated a smaller propensity to fracture at stone-on-stone contacts.

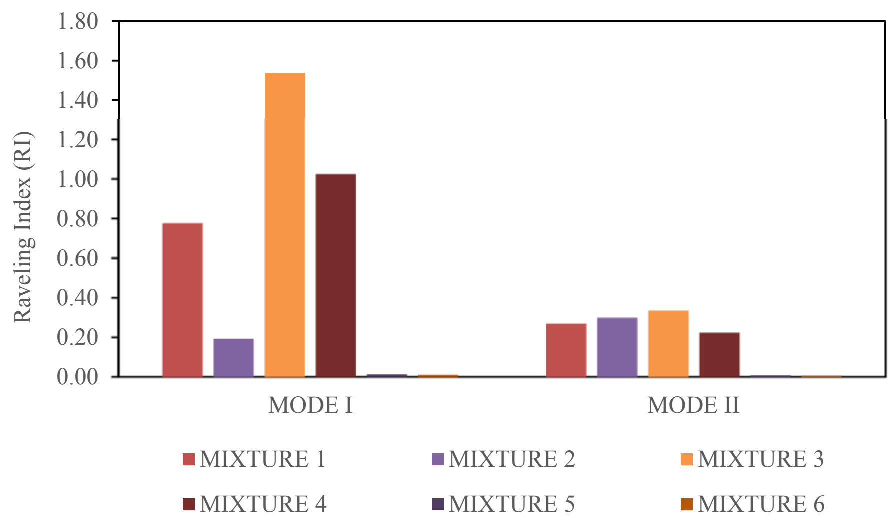

Figure 6-32 Maximum R.I.$_{dry}$ at mastic contact elements among mixtures.

Nevertheless, a maximum R.I. $_{dry}$ value does not necessarily represent the overall response of the mixture since they only provide information on the contact mastic element with the largest probability to failure. Therefore, in order to conduct a better evaluation of the overall propensity of each mixture to raveling, the processed mechanical results (i.e., R.I.$_{dry}$ for Mode I and Mode II) were adjusted to a pdf with a confidence level of 95 percent. Figure 6-33 illustrates one of those probability distribution curves, which in this case corresponded to the R.I.$_{dry}$ value for Mode I of failure of mixture 5.

Since raveling is a fracture-related phenomenon, it constitutes a classical problem of extreme values. In other words, the evaluation of raveling susceptibility should not focus on the mean values of the probability distributions but on the characteristics of the tail of those distributions. This implies that only elements with high values of $R.I._{dry}$ are considered relevant. For the analysis, it was determined that $R.I._{dry}$ values larger than 5.0×10^{-3} for Mode I and Mode II, which properly captured the tail of all the pdf distributions, were appropriate to characterize raveling susceptibility. This selected threshold of $R.I._{dry}$ guaranteed a confident pdf analysis by having at least 40 elements in this range for all mixtures. Researchers calculated the pdf of the tails of $R.I._{dry}$ pdfs of all mixtures; in other words, the probability distribution of the $R.I._{dry}$ values larger than 5.0×10^{-3} were computed. Figure 6-34 illustrates the pdf of the tail of the distribution presented in Figure 6-33. Notice that these new pdfs contained information only on the stone-on-stone contact elements within an OGFC mixture that presented stress-strain localization and, therefore, could be considered susceptible to separation, which permitted researchers to conduct a comprehensive evaluation of the propensity of the mixture to undergo raveling.

To account for the dispersion of the $R.I._{dry}$ data, which were also relevant since they provided information on the uncertainty of the occurrence of raveling, the mean plus one standard deviation ($\mu+\sigma$) of the selected values of $R.I._{dry}$, which were obtained from the pdf curves of the tails of the $R.I._{dry}$ distributions, were computed, as presented in Table 6-16 and Figure 6-35. This quantity, which captured the overall propensity of the mastic contact elements to fracture, is considered an excellent parameter to rank the mixtures.

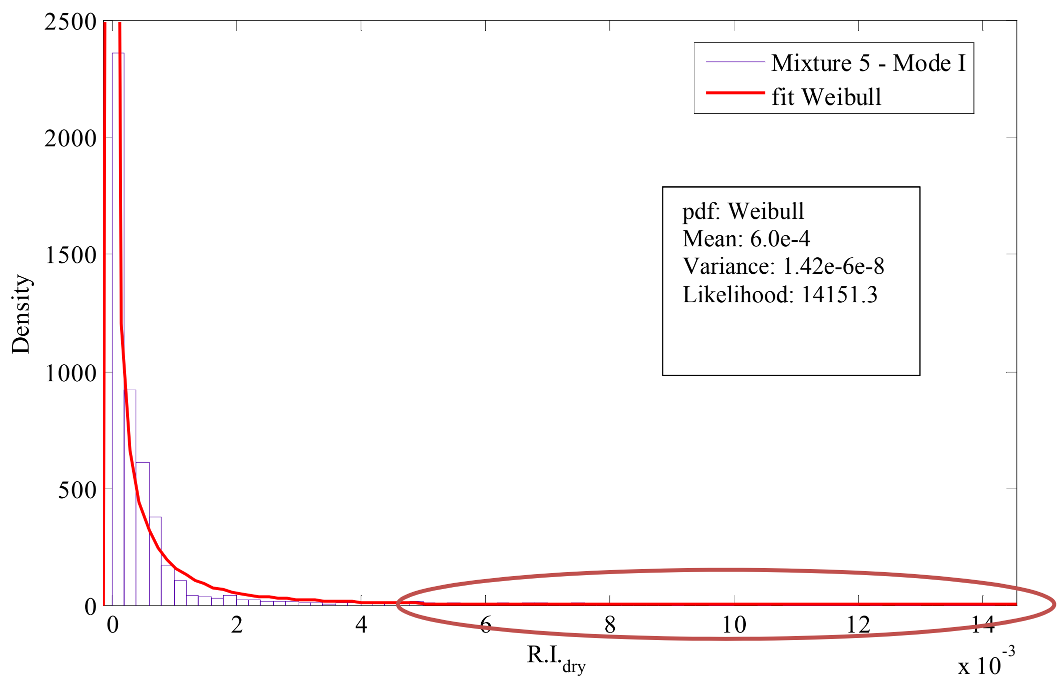

Figure 6-33. Adjustment of the $R.I._{dry}$ probability distribution for mixture 5.

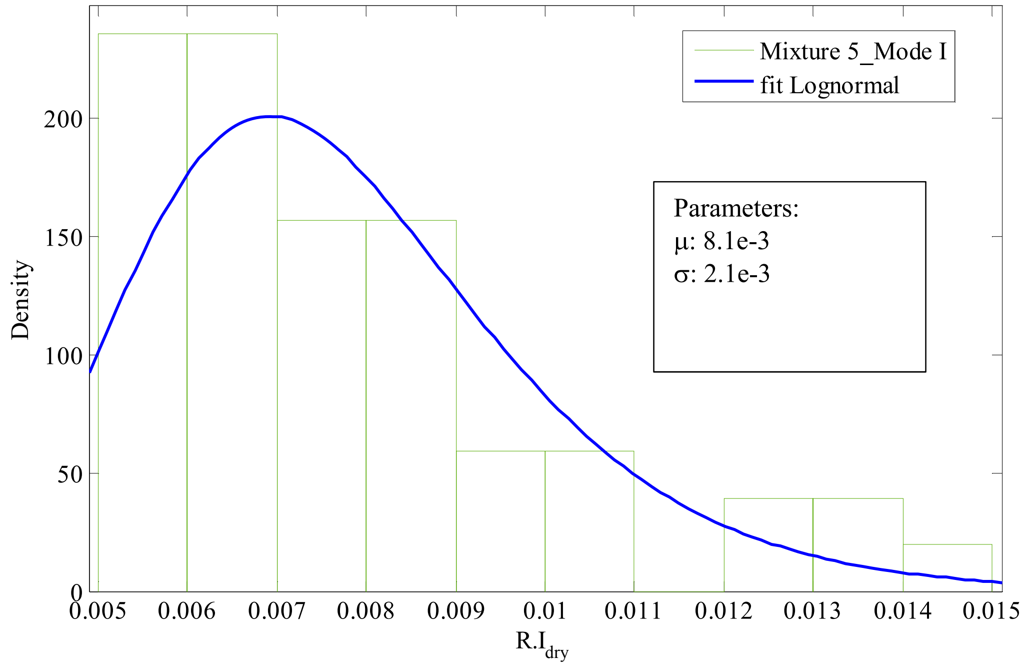

Figure 6-34. pdf of high R.I.$_{dry}$ values for mixture 5.

Table 6-16. pdf Parameters for Mode I—Mixture Analysis

Mixture	pdf	Mode I		Mode II	
		Mean (μ)	Std. Deviation (σ)	Mean (μ)	Std. Deviation (σ)
1	Log normal	04.02×10^{-2}	07.60×10^{-2}	01.58×10^{-2}	2.91×10^{-2}
2	Log logistic	02.90×10^{-2}	03.25×10^{-2}	02.27×10^{-2}	4.23×10^{-2}
3	Log normal	04.30×10^{-2}	09.13×10^{-2}	01.58×10^{-2}	2.26×10^{-2}
4	Log normal	03.48×10^{-2}	06.16×10^{-2}	01.28×10^{-2}	1.74×10^{-2}
5	Log normal	08.11×10^{-3}	02.10×10^{-3}	05.53×10^{-3}	08.81×10^{-3}
6	Log normal	04.63×10^{-3}	01.90×10^{-3}	02.40×10^{-3}	05.43×10^{-4}

Since the R.I.$_{dry}$ parameters for Mode I were, on average, 70 percent higher than those for Mode II, researchers estimated that Mode I constituted the main mechanisms of raveling in OGFC. Thus, Table 6-17 presents the ranking of the raveling susceptibility of all mixtures based on the mean plus one deviation standard (μ+σ) of the large R.I.$_{dry}$ values for Mode I, and the normalized results relative to the maximum of those values (i.e., raveling parameters divided by the maximum value). Table 6-17 suggests that, in dry condition, mixture 6 is the least susceptible to raveling, while mixture 3 is the most susceptible, with a difference of 99.8 percent in their raveling susceptibility parameter. It should be pointed out that mixtures 1 and 2, which reported a good performance in the field, presented medium-high and low-medium levels of raveling susceptibility, respectively, in the simulations. Also, in the FE simulations, all mixtures were subjected to identical external conditions, but the differences in those conditions in reality could explain why, even with relatively close values of raveling parameters, mixtures 1 and 3 performed differently in terms of raveling in the field. Additionally, it is interesting to notice that mixture 2 showed the same susceptibility to raveling for Mode I and Mode II, which is a special behavior in comparison to all other mixtures.

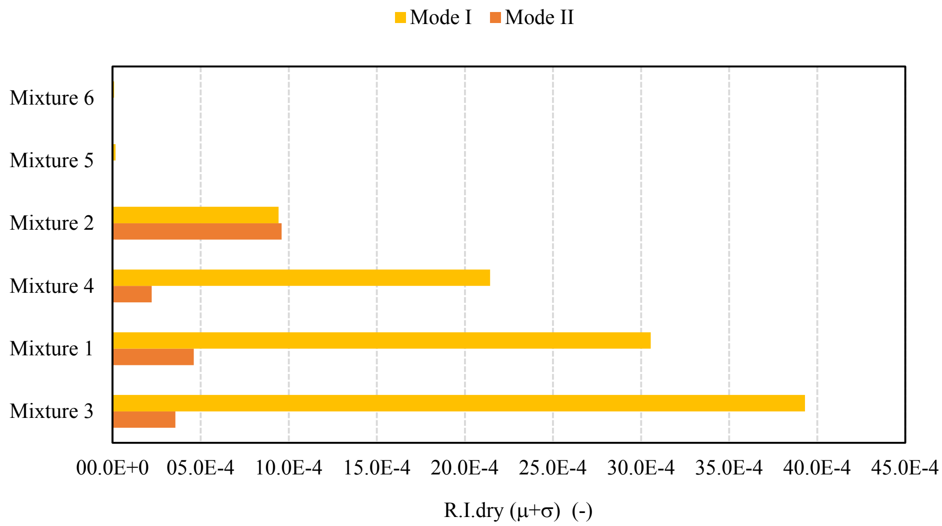

Figure 6-35. Raveling susceptibility for all mixtures.

Table 6-17. Influence of Type of Mixture Raveling Susceptibility—Ranking

	Mode I					
	Mixture 6	**Mixture 5**	**Mixture 2**	**Mixture 4**	**Mixture 1**	**Mixture 3**
R.I.$_{dry}$>5x10^{-3} (μ+σ)	08.81E-06	17.03E-06	09.42x10^{-4}	21.43x10^{-4}	30.55x10^{-4}	39.30x10^{-4}
Normalized R.I.$_{dry}$>5x10^{-3} (μ+σ)	0.002	0.004	0.240	0.545	0.777	1.000
	Higher raveling susceptibility					

6.7.2. Impact of Internal and External Conditions on Raveling

As explained previously, OGFC geometries corresponding to the gradation of mixtures 2 and 5 were selected as base models. These mixtures were subjected to different conditions in the FE models to quantify the effect of internal (constitutive materials, OBC, AV, and OGFC thickness) and external (temperature, load magnitude, wheel speed, longitudinal force, pavement structure, moisture diffusion and CZM, and pore pressure) variables on their raveling susceptibility. Table 6-18 summarizes the initial conditions of the base models. Only one variable of the base models was changed in each simulation, which permitted researchers to make an accurate evaluation of its impact on the raveling susceptibility of the mixture. The following sections present the results on the impact of each internal or external condition.

Table 6-18. Base Model Properties

Parameter	Base Model 1	Base Model 2
Mixture Type	5	2
Aggregate Type	Granite (50,000 MPa)	Limestone (27,000 MPa)
Binder Type	PMA	ARB
OBC (%)	5.6	7.1
Mastic Thickness	15 μm	17 μm
AV	20%	20%
Pavement Temperature (ºC)	30	30
Load Speed	88.5 km/h	88.5 km/h
Axle Type	Single-single	Single-single
Load Magnitude	49.7 kN	49.7 kN
Load Radius	9.5 cm	9.5 cm
PFC Thickness	2 cm	2 cm
Equivalent Base	520 MPa	520 MPa
	Medium	Medium
Subgrade	100 MPa	100 MPa
Moisture Diffusion	No	No
Cohesive Zones	No	No

6.7.2.1. Impact of the Type of Materials (Internal Condition)

The versatility of the FE model is that it allows evaluating of mixtures that were not experimentally characterized. In this case, only the material properties of the base models were changed, while the other properties remained constant (Table 6-18). Table 6-19 summarizes the material combinations considered in the simulations under dry conditions.

Table 6-19. Materials Code

Aggregate	Mastic	Material Code (Aggregate/Mastic)
GR	PMA+GR	GR/PMA+GR
GR	ARB+GR	GR/ARB+GR
LS	PMA+LS	LS/PMA+LS
LS	ARB+LS	LS/ARB+LS

In order to estimate the raveling susceptibility of the mixtures, the same probabilistic analysis as the one described in the previous sections was done. That is, the pdfs of the $R.I._{dry}$ values larger than $5x10^{-3}$ were computed, and the quantity ($\mu+\sigma$) of those distributions was used to rank the mixtures.

Table 6-20 and Table 6-21 present the parameters of the pdfs obtained for each material combination, for each failure mode, and for each one of the two base models. To complement this information, Figure 6-36 and Figure 6-37 present the mean ($\mu+\sigma$) of the selected $R.I._{dry}$ values for each material combination.

Table 6-20. pdf Parameters for Mode 1—Material Combinations, Base Model 1

Material Code	pdf	Mode I		Mode II	
		Mean (μ)	Std. Deviation (σ)	Mean (μ)	Std. Deviation (σ)
GR/PMA+GR	Log normal	81.09×10^{-4}	21.00×10^{-4}	62.03×10^{-4}	08.81×10^{-4}
LS/PMA+LS	Log normal	68.71×10^{-4}	32.24×10^{-4}	33.45×10^{-4}	09.21×10^{-4}
GR/ARB+GR	Log normal	46.33×10^{-4}	19.01×10^{-4}	30.34×10^{-4}	05.43×10^{-4}
LS/ARB+LS	Log normal	70.98×10^{-4}	39.60×10^{-4}	36.26×10^{-4}	08.89×10^{-4}

Table 6-21. pdf Parameters for Mode I—Material Combinations, Base Model 2

Material	pdf	Mode I		Mode II	
		Mean (μ)	Std. Deviation (σ)	Mean (μ)	Std. Deviation (σ)
GR/PMA+GR	Log normal	03.61×10^{-2}	04.08×10^{-2}	02.84×10^{-2}	04.17×10^{-2}
LS/PMA+LS	Log normal	03.64×10^{-2}	05.77×10^{-2}	02.44×10^{-2}	04.05×10^{-2}
GR/ARB+GR	Log normal	02.07×10^{-2}	02.52×10^{-2}	01.70×10^{-2}	02.73×10^{-2}
LS/ARB+LS	Log normal	02.99×10^{-2}	04.48×10^{-2}	02.27×10^{-2}	04.23×10^{-2}

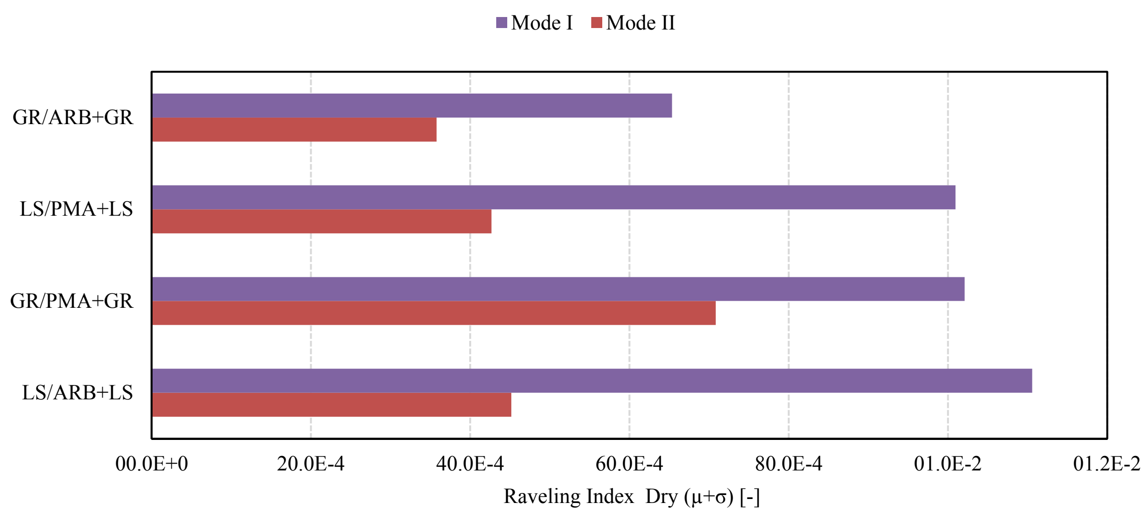

Figure 6-36. Susceptibility of different material combinations to raveling—Base Model 1.

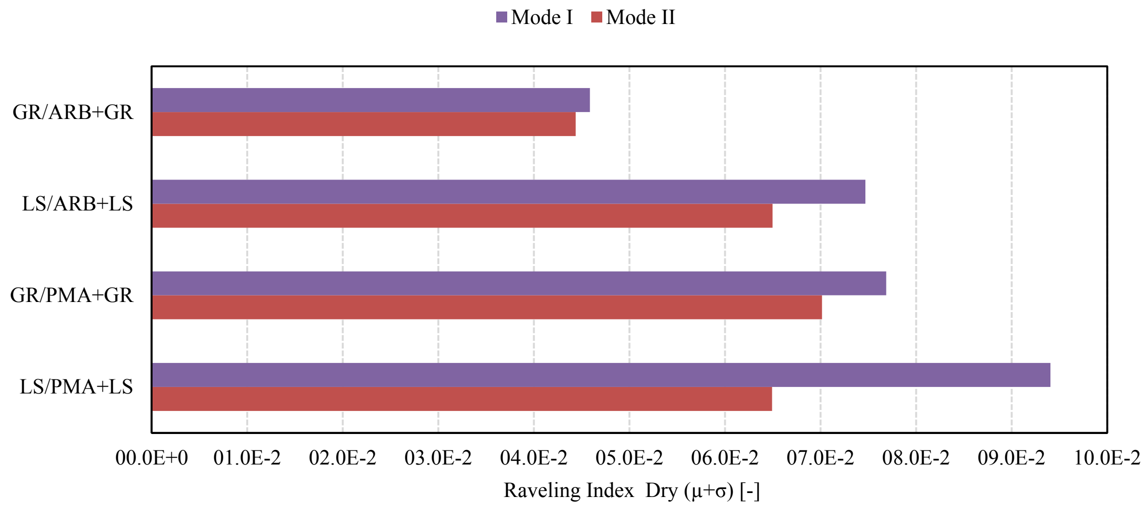

Figure 6-37. Susceptibility of different material combinations to raveling—Base Model 2.

The results showed that the material combination GR/ARB+GR seemed to be the least susceptible to raveling for both base models, while the material combination LS/ARB+LS was the most susceptible to raveling in Base Model 1, and LS/PMA+LS in Base Model 2. Once again, Mode I was the predominant mode of failure (in Base Model 1, the values for Mode I were approximately 51 percent larger than those for Mode II, and in Base Model 2, the values for Mode I were 14 percent larger than those for Mode II).

The material combinations presenting the larger raveling parameters (i.e., LS/ARB+LS for Base Model 1 and LS/PMA+LS for Base Model 2) were used to rank the raveling susceptibility of the mixtures. Therefore, all the raveling parameters were divided by the values of those two material combinations. Table 6-22 presents the results, which corroborated that the material combination GR/ARB+GR was the least susceptible mixture to raveling in both models. The difference between the least and the most susceptible material combination was approximately 55 percent, showing the high sensitivity of this parameter on the mechanical performance of the mixtures. The results also illustrate the interesting impact of aggregate gradation and mastic film thickness since, based on data in Table 6-22, the raveling parameters for Base Model 2 were approximately seven times higher than the parameters obtained for Base Model 1.

Table 6-22. Influence of Material Combination on Raveling Susceptibility—Ranking

Mode I					
Base Model 1	**Material**	GR/ARB+GR	LS/PMA+LS	GR/PMA+GR	LS/ARB+LS
	R.I.$_{dry}$>5x10^{-3} (μ+σ)	65.34x10^{-4}	01.01x10^{-2}	01.02x10^{-2}	01.11x10^{-2}
	Normalized R.I.$_{dry}$>5x10^{-3} (μ+σ)	0.59	0.91	0.92	1.00
		Higher raveling susceptibility			
Base Model 2	**Material**	GR/ARB+GR	LS/ARB+LS	GR/PMA+GR	LS/PMA+LS
	R.I.$_{dry}$>5x10^{-3} (μ+σ)	04.59x10^{-2}	07.47x10^{-2}	07.69x10^{-2}	09.41x10^{-2}
	Normalized R.I.$_{dry}$>5x10^{-3} (μ+σ)	0.49	0.79	0.82	1.00
		Higher raveling susceptibility			

6.7.2.2. Impact of Binder Content (Internal Condition)

OBC is one of the most sensitive parameters when it comes to OGFC mixture design. In this case, three different ACs were evaluated in the base models, and since both models had different gradations, the mastic thicknesses were not the same in these cases. Table 6-23 summarizes the selected AC values and the corresponding mastic thickness for each base model.

Table 6-23. AC Values Evaluated

Binder Content	**Mastic Thickness (μm)**	
	Base Model 1	**Base Model 2**
4.1%	11	10
5.6%	15	13
7.1%	19	17

Table 6-24 and Table 6-25 present the parameters of the pfds obtained for the R.I.$_{dry}$ values larger than 5x10^{-3}, and Figure 6-38 and Figure 6-39 list the corresponding (μ+σ) parameters that permitted researchers to compare the raveling susceptibility of the mixture.

Table 6-24. pdf Parameters—AC, Base Model 1

AC	**pdf**	**Mode I**		**Mode II**	
		Mean (μ)	**Std. Deviation (σ)**	**Mean (μ)**	**Std. Deviation (σ)**
4.1%	Log normal	78.71x10^{-4}	28.34x10^{-4}	60.79x10^{-4}	17.25x10^{-4}
5.6%	Log normal	81.09x10^{-4}	21.00x10^{-4}	55.38x10^{-4}	08.81x10^{-4}
7.1%	Log normal	01.15x10^{-2}	74.83x10^{-4}	01.22x10^{-2}	47.73x10^{-4}

Table 6-25. pdf Parameters—AC, Base Model 2

AC	pdf	Mode I		Mode II	
		Mean (μ)	Std. Deviation (σ)	Mean (μ)	Std. Deviation (σ)
4.1%	Log normal	04.73×10^{-2}	07.00×10^{-2}	02.60×10^{-2}	03.01×10^{-2}
5.6%	Log normal	04.32×10^{-2}	06.09×10^{-2}	02.33×10^{-2}	03.83×10^{-4}
7.1%	Log normal	02.99×10^{-2}	21.15×10^{-2}	02.27×10^{-2}	20.56×10^{-2}

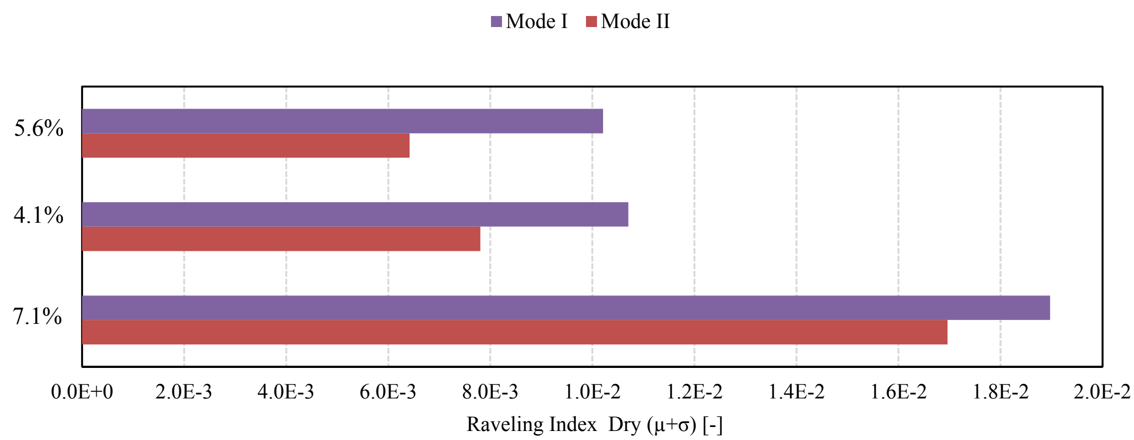

Figure 6-38. Effect of AC on the susceptibility to raveling of OGFC—Base Model 1.

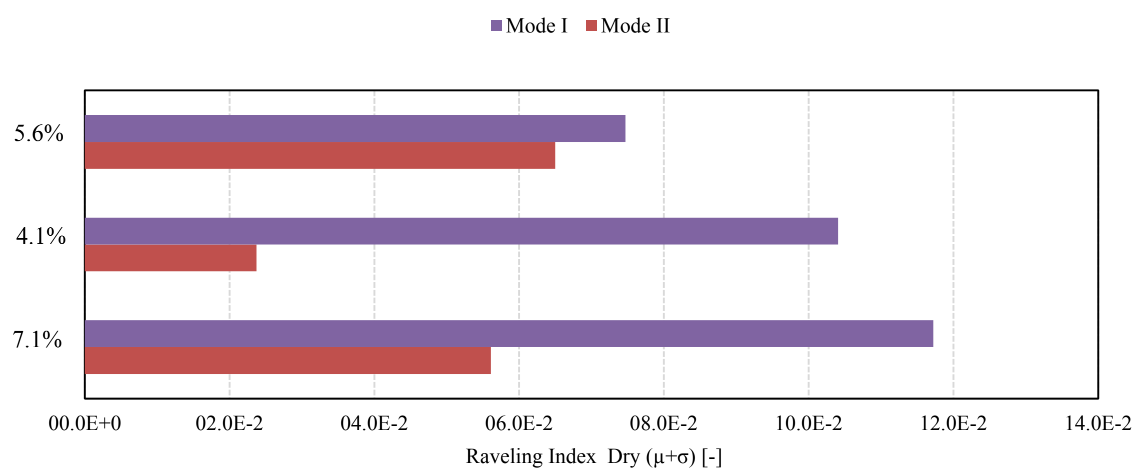

Figure 6-39. Effect of AC on the susceptibility to raveling of OGFC—Base Model 2.

The results showed that mixtures with an AC of 5.6 percent presented the smallest susceptibility to raveling, while AC of 7.1 percent resulted in the most susceptible raveling condition. This last value was selected as a control parameter in order to normalize and compare the results between models, and the results are summarized in Table 6-26. It is interesting to note that Base Model 1 presented the lowest susceptibility to raveling with the AC value of 5.6 percent, which corresponded to the OBC for mixture 5. In other words, it seems that the OBC in this mixture was the one that optimized its durability. On the other hand, Base Model 2, which represented mixture 2, had a design OBC of 7.1 percent, which resulted in an unfavorable case for raveling resistance. As a first hypothesis, researchers believed that this finding could explain the higher raveling susceptibility that was observed for Base Model 2 in the cases studied. The results suggest that the AC content used in mixture 2 may not be the optimum in terms of durability. Therefore, mixtures with larger AC values as compared to the OBC could be equally or even more susceptible to raveling as compared to mixtures with lower AC values than the OBC.

Table 6-26. Influence of AC on Raveling Susceptibility—Ranking

Mode I				
Base Model 1	**AC (%)**	**5.6%**	**4.1%**	**7.1%**
	R.I.$_{dry}$>5x10^{-3} (μ+σ)	01.02x10^{-2}	01.07x10^{-2}	01.90x10^{-2}
	Normalized R.I.$_{dry}$>5x10^{-3} (μ+σ)	0.54	0.56	1.00
		Higher raveling susceptibility		
Base Model 2	**AC (%)**	**5.6%**	**4.1%**	**7.1%**
	R.I.$_{dry}$>5x10^{-3} (μ+σ)	07.47x10^{-2}	10.41x10^{-2}	11.72x10^{-2}
	Normalized R.I.$_{dry}$>5x10^{-3} (μ+σ)	0.64	0.89	1.00
		Higher raveling susceptibility		

6.7.2.3. Impact of the Total Air Void Content (Internal Condition)

Field compaction is a main concern with OGFC; recent studies have observed that this quantity is not controlled during construction. With the purpose of evaluating the effect of having a higher AV content than the target AV (i.e., poor compaction), two new geometries of the mixtures complying with the desired gradation but with an AV of 25 percent were evaluated. The pdf parameters of the R.I.$_{dry}$ values larger than 5.0x10^{-3} are presented in Table 6-27 and Table 6-28. Figure 6-40 and Figure 6-41 present the (μ+σ) values from those pdf functions.

Table 6-27. pdf Parameters—AV Content, Base Model 1

AV	pdf	Mode I		Mode II	
		Mean (μ)	**Std. Deviation (σ)**	**Mean (μ)**	**Std. Deviation (σ)**
20	Log normal	81.09x10^{-4}	21.00x10^{-4}	55.38x10^{-4}	08.81x10^{-4}
25	Log normal	02.52x10^{-2}	03.05x10^{-2}	02.12x10^{-2}	02.90x10^{-2}

Table 6-28. pdf Parameters—AV Content, Base Model 2

AV	pdf	Mode I		Mode II	
		Mean (μ)	**Std. Deviation (σ)**	**Mean (μ)**	**Std. Deviation (σ)**
20	Log normal	02.99x10^{-2}	04.48x10^{-2}	02.27x10^{-2}	04.23x10^{-2}
25	Log normal	09.74x10^{-2}	09.34x10^{-2}	09.89x10^{-2}	06.58x10^{-2}

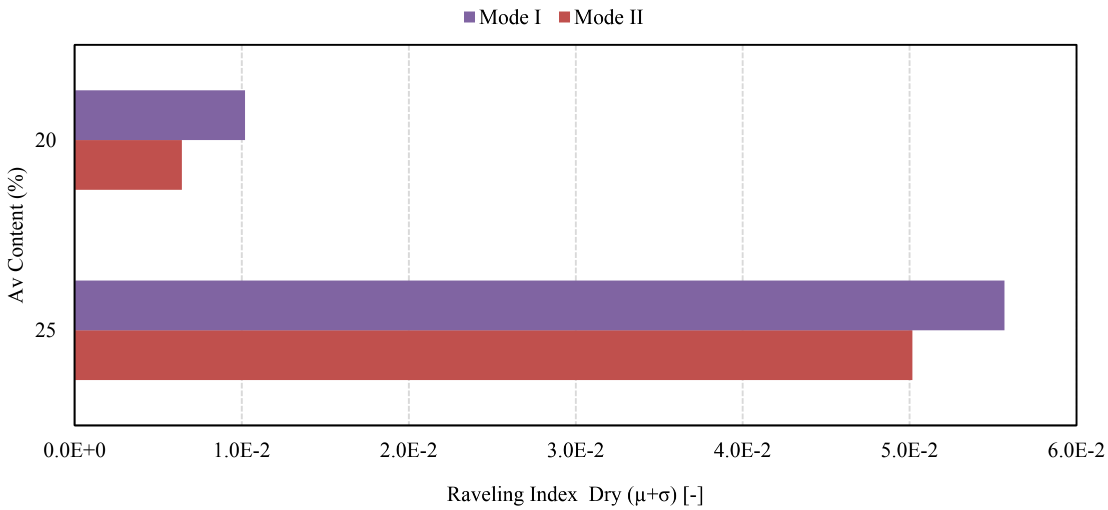

Figure 6-40. Effect of AV on the susceptibility to raveling of OGFC—Base Model 1.

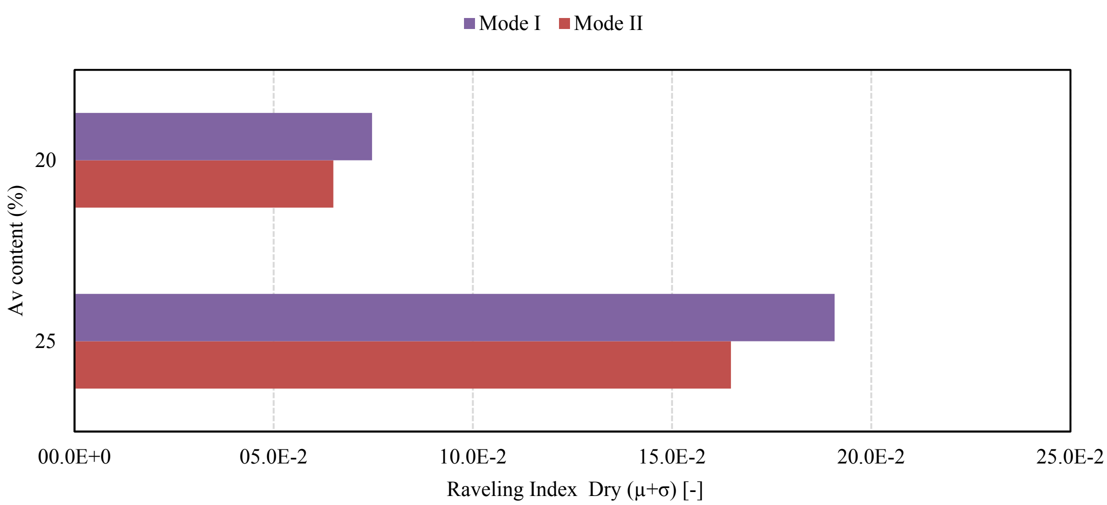

Figure 6-41. Effect of AV on the susceptibility to raveling of OGFC—Base Model 2.

Table 6-29 presents the raveling susceptibility of the models normalized to the case with the highest damage potential. In this case, the most susceptible mixture corresponded to that with an AV content of 25 percent. Meanwhile, the models with 20 percent AV had a raveling susceptibility of 0.18 and 0.39 for Base Models 1 and 2, respectively. These results show that a strict control of the AV content during construction is critical to assure the durability of the mixture since an increase of 5 percent in the AV values generated an increase of 61 percent and 82 percent in the susceptibility of the mixture to undergo raveling. This finding could be explained by the fact that, as determined during the characterization of the OGFC microstructures, an increase in 5 percent in the AV content affected the quality of the skeleton of the mixture, reducing the average number of contacts per aggregate from three to two. Compared to the previous factors evaluated, AV appears to be crucial in affecting the durability of OGFC.

Table 6-29. Influence of AV on Raveling Susceptibility—Ranking

Mode I			
Base Model 1	**AV content (%)**	**20**	**25**
	R.I.$_{dry}$>5x10^{-3} (μ+σ)	01.02x10^{-2}	05.57x10^{-2}
	Normalized R.I.$_{dry}$>5x10^{-3} (μ+σ)	0.18	1.00
		Higher raveling susceptibility	
Base Model 2	**AV content (%)**	20	25
	R.I.$_{dry}$>5x10^{-3} (μ+σ)	07.47x10^{-2}	19.08x10^{-2}
	Normalized R.I.$_{dry}$>5x10^{-3} (μ+σ)	0.39	1.00
		Higher raveling susceptibility	

6.7.2.4. Impact of OGFC Layer Thickness (Internal Condition)

Based on information received from FDOT, the OGFC layers in the state have a typical thickness of 20 mm. This section describes the evaluation of Base Model 1 using OGFC layers with thickness values of 20 cm and 40 mm. The pdf of the R.I.$_{dry}$ values larger than 5x10^{-3} are presented in Table 6-30, while Figure 6-42 presents the (μ+σ) of those two pdf distributions.

Table 6-30. pdf Parameters—Layer Thickness, Base Model 1

OGFC Thickness	pdf	Mode I		Mode II	
		Mean (μ)	Std. Deviation (σ)	Mean (μ)	Std. Deviation (σ)
20 mm	Log normal	07.92x10^{-4}	02.65x10^{-4}	04.10x10^{-4}	01.11x10^{-4}
40 mm	Log normal	14.15x10^{-4}	12.95x10^{-4}	08.76x10^{-4}	08.49x10^{-4}

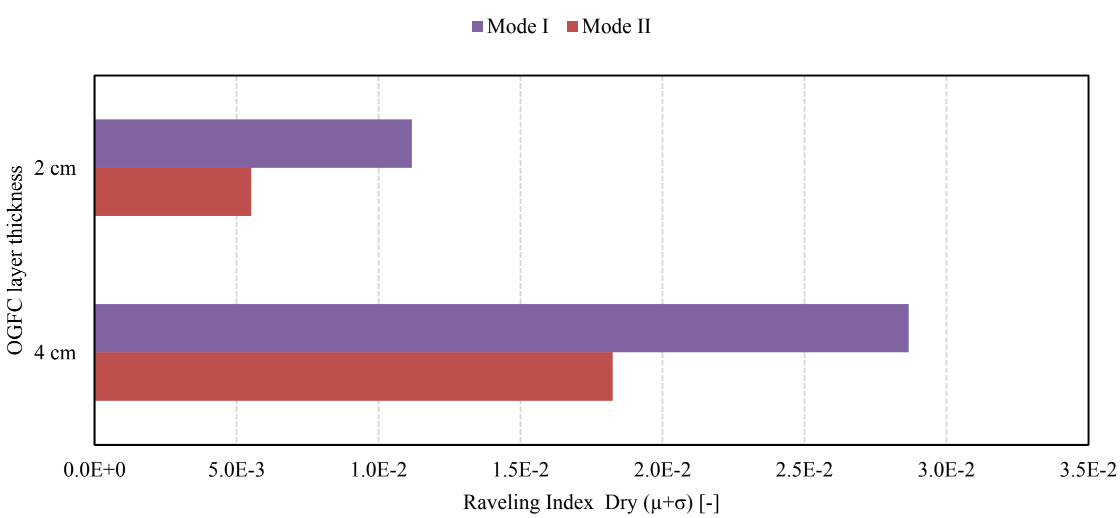

Figure 6-42. Effect of OGFC thickness on the susceptibility to raveling—Base Model 1.

The results showed that the model with an OGFC layer of 40 mm exceeded the values from the 20 mm OGFC layer by 61 percent, suggesting a larger susceptibility to develop raveling, which is also observed in Table 6-31.

Table 6-31. Influence of OGFC Thickness on Raveling Susceptibility—Ranking

Mode I		
AV content (%)	**20 mm**	**40 mm**
R.I.$_{dry}$>5x10^{-3} (μ+σ)	1.12x10^{-2}	2.87x10^{-2}
Normalized R.I.$_{dry}$>5x10^{-3} (μ+σ)	0.39	1.00
	Higher raveling susceptibility →	

The results obtained for the model with an OGFC thickness of 40 mm could be partially attributed to the specific stone-on-stone characteristics of the selected microstructure. Figure 6-43 presents the Mises stress state in global coordinates, in Mpa, in which it is easy to identify several stress paths within the mixture. This figure shows that the mixture presents a localization of stresses at the middle bottom part of the mixture (stress values higher than 47 MPa, while the average stress values in the overall model are near 2 MPa). This stress concentration could be a consequence of the spatial distribution of the aggregates. According to the microstructure characterization conducted for mixture 5, the percentage of perimeter of the aggregates that was in contact with other aggregates follows a normal distribution with a mean value of 33 percent and a standard deviation of 13.88 percent. In this particular geometry, it was found that the percentage of aggregate perimeter in contact with other aggregates was more than one standard deviation smaller than that mean value, which produced a very unfavorable condition of the mixture to support loads. In this sense, the results from these simulations are not conclusive. Therefore, it would be important to corroborate the results presented herein with other models of the same mixture and thickness but with more representative aggregate skeletons.

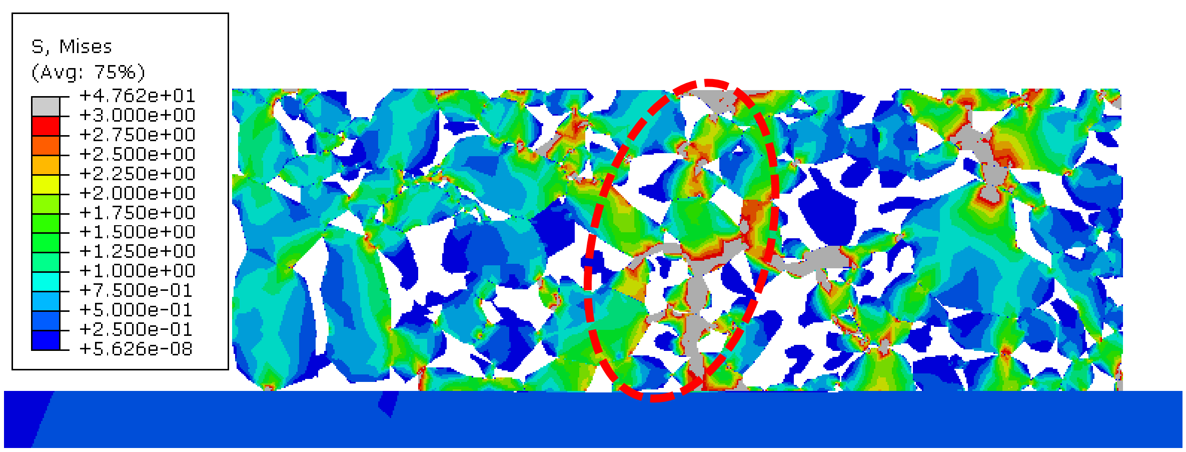

Figure 6-43. Mises stress state for 40 mm width OGFC layer (in MPa).

6.7.2.5. Impact of Temperature (External Condition)

To evaluate the effect of the temperature of the OGFC on the susceptibility of the mixture to raveling, three different values were considered in the two base models: high (50ºC), medium (30ºC), and low (10ºC). The impact of temperature in the mechanical performance of the mixture is caused by the changes occurring in the linear viscoelastic material properties of the mastics (i.e., change in the Prony Series of these materials). When temperature changes, the resistance to failure of a viscoelastic material also changes. Therefore, it would be incorrect to compute the $R.I._{dry}$ (Equation 6-11) using a unique value for the same cohesive bond energy. Thus, the results of the impact of temperature on the cohesive strength of the fine aggregate materials reported by Kim et al. (2005) and Kim and Lutiff (2008) were used to make the cohesive bond energy of the mastics in the base models dependent on temperature. Table 6-32 presents the cohesive bond energy as a function of temperature used in computation of $R.I._{dry}$.

Table 6-32. Cohesive Bond Energy as a Function of Temperature

Temperature (ºC)	Cohesive Bond Energy (J/m^2)	
	Base Model 1	Base Model 2
10	455.2	348.6
30	330.4	253.0
50	205.6	157.5

The parameters for the pdfs that provided the best fit for the $R.I._{dry}$ values larger than $5x10^{-3}$, as well as the corresponding values of ($\mu+\sigma$) for those distributions, are summarized in Table 6-33 and Table 6-34, and in Figure 6-44 and Figure 6-45. As observed in these figures, for the first time, Mode II of failure was more probable to occur at 10ºC than Mode I, in both base models. This was also the most probable mode of failure at 50ºC for Base Model 2. The difference between these raveling parameters between the two modes of failure was near 40 percent for the cases at 10ºC and 75 percent for the case at 50ºC (Figure 6-44 and Figure 6-45).

Table 6-33. pdf Parameters—Temperature Analysis, Base Model 1

Temperature (°C)	pdf	Mode I		Mode II	
		Mean (μ)	Std. Deviation (σ)	Mean (μ)	Std. Deviation (σ)
10	Log normal	$12.22x10^{-4}$	$01.05x10^{-4}$	$16.78x10^{-4}$	$01.56x10^{-4}$
30	Log normal	$81.09x10^{-4}$	$21.00x10^{-4}$	$05.23x10^{-4}$	$08.81x10^{-4}$
50	Log normal	$03.89x10^{-2}$	$06.61x10^{-2}$	$16.78x10^{-4}$	$01.31x10^{-2}$

Table 6-34. pdf Parameters—Temperature Analysis, Base Model 2

Temperature (°C)	pdf	Mode I		Mode II	
		Mean (μ)	Std. Deviation (σ)	Mean (μ)	Std. Deviation (σ)
10	Log normal	$56.08x10^{-4}$	$21.62x10^{-4}$	$77.24x10^{-4}$	$63.19x10^{-4}$
30	Log normal	$02.99x10^{-2}$	$04.48x10^{-2}$	$02.27x10^{-2}$	$04.23x10^{-2}$
50	Log normal	$04.05x10^{-2}$	$10.26x10^{-2}$	$04.69x10^{-2}$	$16.63x10^{-2}$

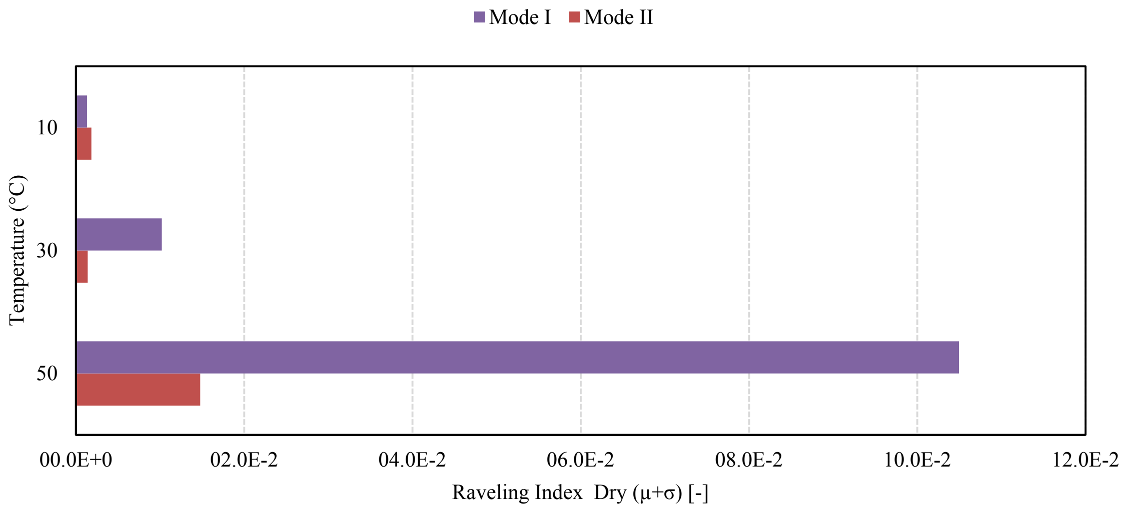

Figure 6-44. Effect of temperature on the susceptibility to raveling of OGFC—Base Model 1.

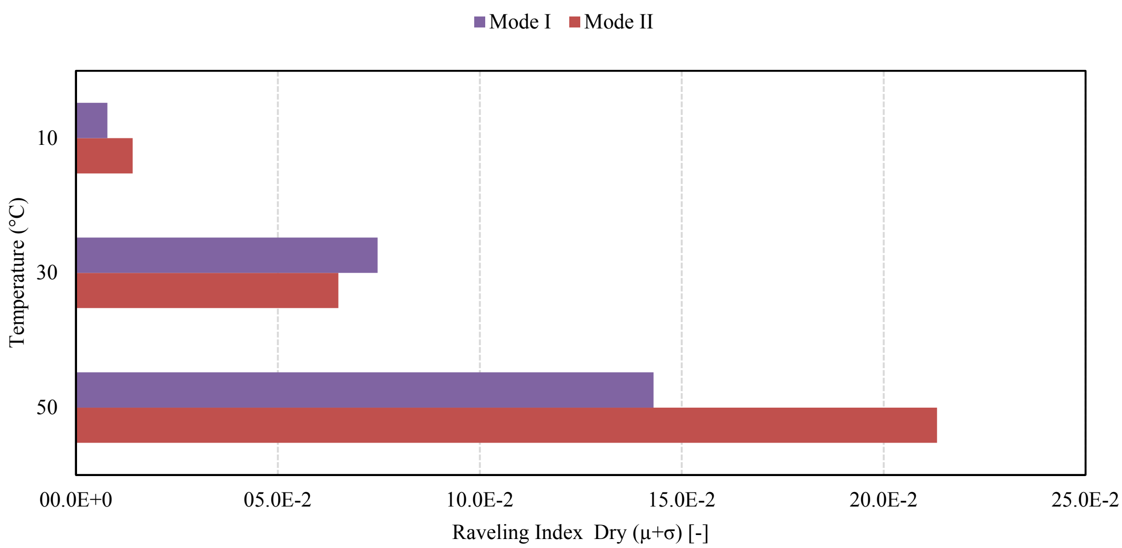

Figure 6-45. Effect of temperature on the susceptibility to raveling of OGFC—Base Model 2.

Table 6-35 shows the ranking of raveling susceptibility as a function of the temperature of the OGFC mixture for Mode I of failure. Temperatures between 10ºC and 30ºC were considered intermediate values and, as a result, their mechanical response and raveling susceptibility results were similar. In contrast, at 50ºC, this parameter became critical, showing differences with respect to the mean values of R.I.$_{dry}$ at 10°C and 50°C of 97 percent, suggesting that there is a significant increase in raveling susceptibility at higher temperatures. It is noteworthy that at very low temperatures, which were not analyzed in this project, when the material becomes stiffer and more brittle, the susceptibility to raveling will be critical, as reported by the published works summarized in the literature review chapter.

Table 6-35. Influence of Temperature on Raveling Susceptibility—Ranking Mode I

Mode I				
Base Model 1	**Temperature (ºC)**	**10**	**30**	**50**
	R.I.$_{dry}$>5x10^{-3} (μ+σ)	$13.27x10^{-4}$	$01.02x10^{-2}$	$10.49x10^{-2}$
	Normalized R.I.$_{dry}$>5x10^{-3} (μ+σ)	0.01	0.10	1.00
		Higher raveling susceptibility		
Base Model 2	**Material**	**10**	**30**	**50**
	R.I.$_{dry}$>5x10^{-3} (μ+σ)	$77.70x10^{-4}$	$07.47x10^{-2}$	$14.30x10^{-2}$
	Normalized R.I.$_{dry}$>5x10^{-3} (μ+σ)	0.05	0.52	1.00
		Higher raveling susceptibility		

Since Mode II seemed to be the most probable mode of failure in Base Model 2, Table 6-36 presents the ranking of the most susceptible parameters according to this mode of failure. These results show that a temperature of 50ºC in the mixture was the most unfavorable situation for Base Model 2. In fact, the difference in the raveling potential between the mixture with a temperature of 10ºC and a temperature of 50ºC was as high as 93 percent.

Table 6-36. Influence of Temperature on Raveling Susceptibility—Ranking Mode II

Mode II				
Base Model 1	**Temperature (ºC)**	**30**	**10**	**50**
	R.I.$_{dry}$>5x10^{-3} (μ+σ)	$14.05x^{-4}$	$18.34x10^{-4}$	$01.48x10^{-2}$
	Normalized R.I.$_{dry}$>5x10^{-3} (μ+σ)	0.10	0.12	1.00
		Higher raveling susceptibility		
Base Model 2	**Material**	**10**	**30**	**50**
	R.I.$_{dry}$>5x10^{-3} (μ+σ)	$01.40x10^{-2}$	$06.50x10^{-2}$	$21.32x10^{-2}$
	Normalized R.I.$_{dry}$>5x10^{-3} (μ+σ)	0.07	0.30	1.00
		Higher raveling susceptibility		

6.7.2.6. Load Conditions (External Condition)

The axle load spectrum obtained from the LTPP database can be described by a normal distribution with mean 47.7 kN and a standard deviation of 16.9 kN. With the purpose of covering this spectrum, three different cases were evaluated, as shown in Table 6-37. It is important to note that this spectrum corresponded to a single-single axle load, and the model only represented one wheel running over the structure at 55.8 km/h, which implies that data in Table 6-37 correspond to half of the total axle load.

Table 6-37. Load Magnitude Cases Evaluated

Load case	Vertical load kN	Contact pressure (q) MPa	Radio cm	Longitudinal force kN (2.5% vertical load)
μ	24.9	0.88	9.5	0.621
μ+σ	33.3	0.88	11	0.833
μ+2σ	41.8	0.88	12	1.046

Table 6-38 and Table 6-39 present the pdf parameters of the relevant R.I.$_{dry}$ values, and Figure 6-46 and Figure 6-47 illustrate the raveling parameter (μ+σ) obtained from those pdf distributions. The results show that there was good agreement between the results of the two base models since both cases presented an increase in the susceptibility to raveling with an increase in the load magnitude, as expected. Nevertheless, it was observed that Base Model 2 presented a larger potential to raveling in comparison to Base Model 1, similar to all previous cases.

Table 6-38. pdf Parameters—Load Analysis, Base Model 1

Load Case	pdf	Mode I		Mode II	
		Mean (μ)	Std. Deviation (σ)	Mean (μ)	Std. Deviation (σ)
μ	Log normal	81.09×10^{-4}	21.00×10^{-4}	55.38×10^{-4}	08.81×10^{-4}
μ+σ	Log normal	97.12×10^{-4}	37.93×10^{-4}	64.06×10^{-4}	08.14×10^{-4}
μ+2σ	Log normal	01.01×10^{-2}	42.49×10^{-4}	64.87×10^{-4}	08.33×10^{-4}

Table 6-39. pdf Parameters—Load Analysis, Base Model 2

Load Case	pdf	Mode I		Mode II	
		Mean (μ)	Std. Deviation (σ)	Mean (μ)	Std. Deviation (σ)
μ	Log normal	51.95×10^{-4}	77.66×10^{-4}	39.38×10^{-4}	73.39×10^{-4}
μ+σ	Log normal	01.43×10^{-2}	99.21×10^{-4}	01.19×10^{-2}	95.74×10^{-4}
μ+2σ	Log normal	01.43×10^{-2}	01.04×10^{-2}	01.24×10^{-2}	01.03×10^{-2}

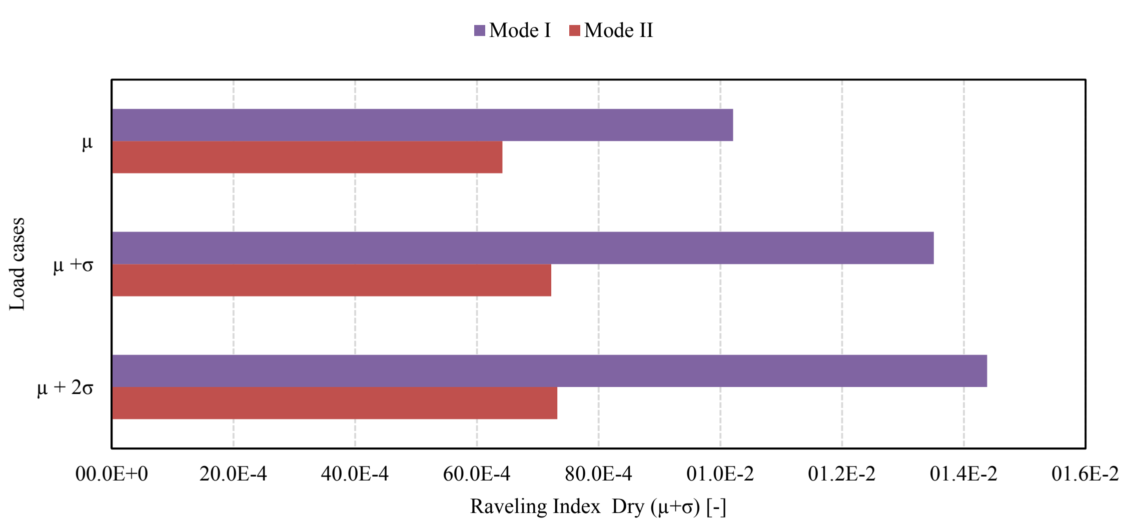

Figure 6-46. Effect of load magnitude on the susceptibility to raveling of OGFC—Base Model 1.

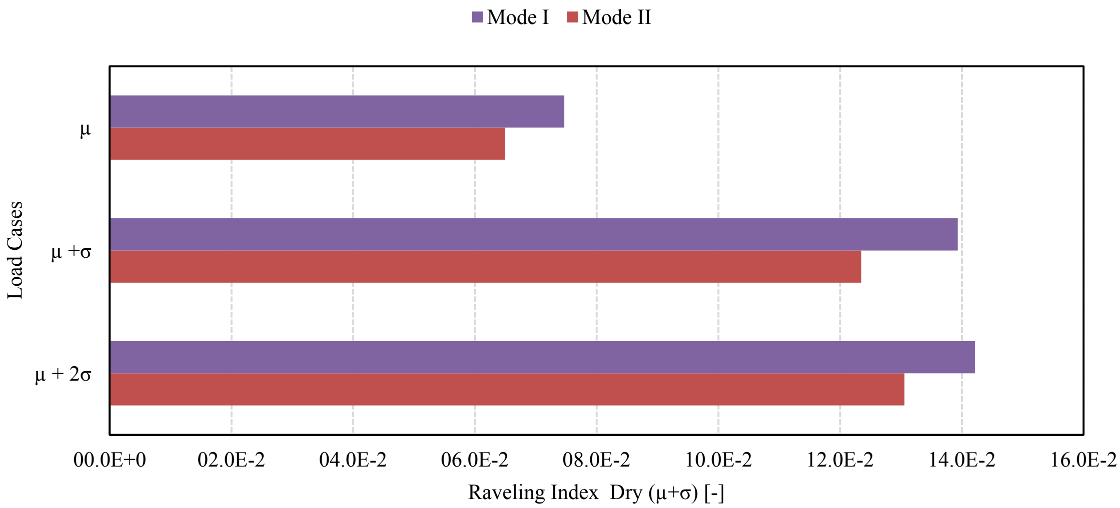

Figure 6-47. Effect of load magnitude on the susceptibility to raveling of OGFC—Base Model 2.

Table 6-40 presents the raveling susceptibility rank for the different cases, from which it can be observed that although in both models the Mode I of failure was more probable to occur, the difference between the two modes was smaller in Base Model 2. In addition, the susceptibility to raveling was similar in the mean and high load cases (near 3 percent difference), and it was 23 to 46 percent smaller for the low load magnitude, which suggests an intermediate sensitivity of this parameter in the durability of the mixture.

Table 6-40. Influence of Load Magnitude on Raveling Susceptibility—Ranking

	Mode I			
Base Model 1	**Load Magnitude**	μ	μ+σ	μ+2σ
	R.I.$_{dry}$>5x10^{-3} (μ+σ)	01.02x10^{-2}	01.35x10^{-2}	01.44x10^{-2}
	Normalized R.I.$_{dry}$>5x10^{-3} (μ+σ)	0.71	0.94	1.00
		Higher raveling susceptibility →		
Base Model 2	**Load Magnitude**	μ	μ+σ	μ+2σ
	R.I.$_{dry}$>5x10^{-3} (μ+σ)	07.47x10^{-2}	13.93x10^{-2}	14.21x10^{-2}
	Normalized R.I.$_{dry}$>5x10^{-3} (μ+σ)	0.53	0.98	1.00
		Higher raveling susceptibility →		

6.7.2.7. Influence of Traffic Speed (External Condition)

Even though current specifications require OGFC to be placed only on high-speed facilities, the variable "traffic speed" was included as part of the analysis with the objective of better identifying the mechanisms associated with raveling processes. Therefore, the effect of traffic speed was measured in three different cases:

- Low speed: 48 km/h.

- Recommended speed: 88.50 km/h.
- Maximum allowable speed: 113 km/h.

The pdf distribution parameters of the relevant R.I.$_{dry}$ values are summarized in Table 6-41 and Table 6-42, and Figure 6-48 and Figure 6-49 present the ($\mu+\sigma$) values of those probabilistic distributions. The results indicate that OGFCs are more susceptible to raveling when the vehicles circulate at a lower speed. Once again, Mode I of failure was more significant in both cases, with a difference of 40 percent with respect to Mode II in Base Model 1 and 13 percent in Base Model 2. The only exception was the case of a speed of 48 km/h in Base Model 2, where the most probable mode of failure was Mode II. Another interesting result was that the values obtained in Base Model 2 were one order of magnitude larger than the results for Base Model 1, indicating, once again, the strong impact of the gradation, geometry, and mastic film thickness of the OGFC mixture.

Table 6-41. pdf Parameters—Traffic Speed Analysis, Base Model 1

Speed	pdf	Mode I		Mode II	
		Mean (μ)	Std. Deviation (σ)	Mean (μ)	Std. Deviation (σ)
48 km/h	Log normal	01.05×10^{-2}	49.68×10^{-4}	63.68×10^{-4}	07.91×10^{-4}
88.5 km/h	Log normal	81.09×10^{-4}	21.00×10^{-4}	55.38×10^{-4}	08.81×10^{-4}
113 km/h	Log normal	50.35×10^{-4}	20.97×10^{-4}	40.83×10^{-4}	10.91×10^{-4}

Table 6-42. pdf Parameters Mode I—Traffic Speed Analysis Base Model 2

Speed	pdf	Mode I		Mode II	
		Mean (μ)	Std. Deviation (σ)	Mean (μ)	Std. Deviation (σ)
48 km/h	Log normal	03.36×10^{-2}	05.45×10^{-2}	03.34×10^{-2}	05.83×10^{-2}
88.5 km/h	Log normal	02.99×10^{-2}	04.48×10^{-2}	02.27×10^{-2}	04.23×10^{-2}
113 km/h	Log normal	02.87×10^{-2}	04.08×10^{-2}	02.30×10^{-2}	03.69×10^{-2}

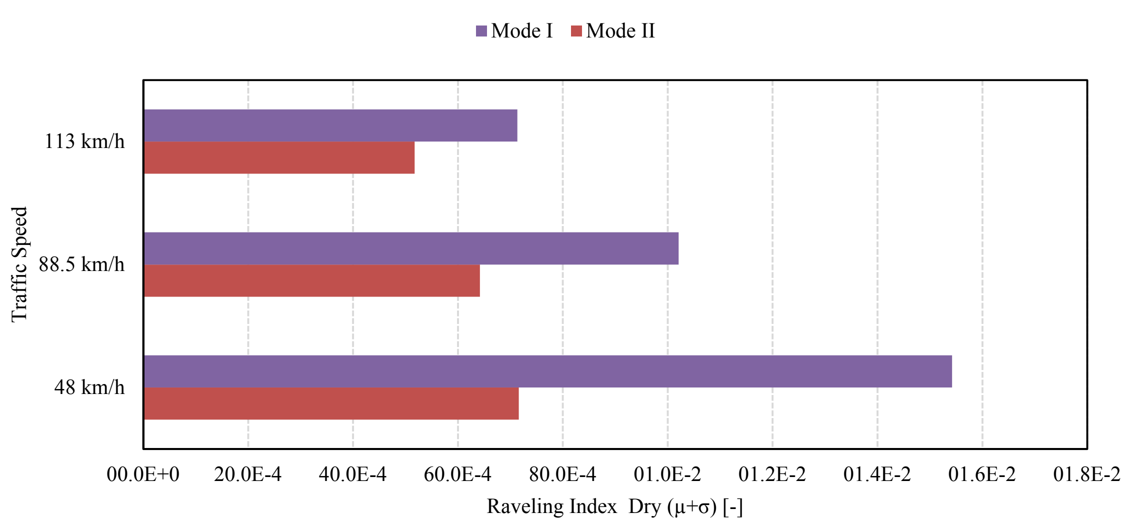

Figure 6-48. Effect of traffic speed on the susceptibility to raveling of OGFC—Base Model 1.

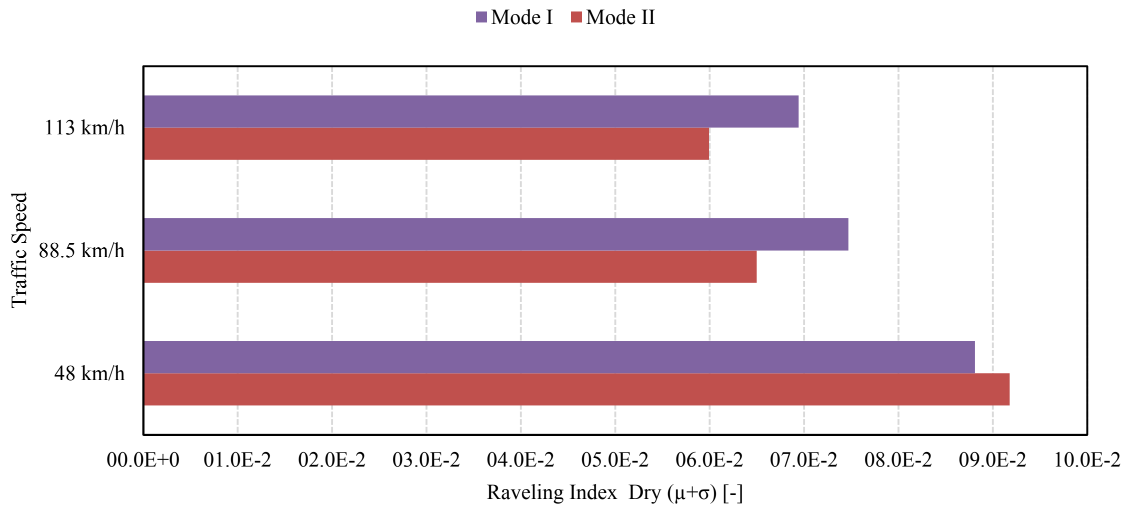

Figure 6-49. Effect of traffic speed on the susceptibility to raveling of OGFC—Base Model 2.

Table 6-43 presents the raveling susceptibility of the mixtures with respect to the maximum (μ+σ) values obtained from the probabilistic analysis. As mentioned previously, OGFC mixtures seem to be less probable to develop raveling when the vehicles circulate at high speeds (e.g., 113 km/h), which seems to justify the fact that these mixtures are used on high-speed roads (although other considerations regarding functionality of the layer are also vital in this decision). The difference in raveling potential between this case and the one with the mean traffic speed was near 6 percent for Base Model 2 and 20 percent for Base Model 1. Despite the fact that the raveling susceptibility in Base Model 1 was lower than in Base Model 2, the first model was more sensitive to any change in traffic speed.

Table 6-43. Influence of Traffic Speed on Raveling Susceptibility—Ranking

Mode I				
Base Model 1	**Traffic speed**	113 km/h	88.5 km/h	48 km/h
	R.I.$_{dry}$>5x10^{-3} (μ+σ)	71.32x10^{-4}	01.02x10^{-2}	01.54x10^{-2}
	Normalized R.I.$_{dry}$>5x10^{-3} (μ+σ)	0.46	0.66	1.00
		Higher raveling susceptibility →		
Base Model 2	**Traffic speed**	113 km/h	88.5 km/h	48 km/h
	R.I.$_{dry}$>5x10^{-3} (μ+σ)	06.94x10^{-2}	07.47x10^{-2}	08.81x10^{-2}
	Normalized R.I.$_{dry}$>5x10^{-3} (μ+σ)	0.79	0.85	1.00
		Higher raveling susceptibility →		

<u>6.7.2.8. Influence of Longitudinal Forces, or *Fx* (External Condition)</u>

When a wheel runs over a pavement structure, several forces appear at the pavement-vehicle interface. For simplification, only two types of forces were evaluated: (a) the vertical force, which results from the axle weight; and (b) the longitudinal force, F_x, or friction force, which is usually a percentage of the vertical force (Figure 6-50).

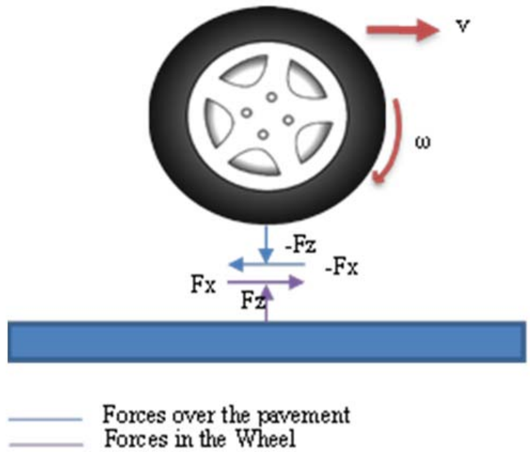

Figure 6-50. Forces produced by pavement-vehicle interaction.

Both base models included a vertical force per wheel of 24.8 kN, and the longitudinal forces changed as indicated in Table 6-44. In this table, the rolling friction force corresponds to the minimum possible F_x and represents a wheel running over the pavement, the maximum rolling friction force simulates the longitudinal force when the pavement is assumed as a deformable body, and the kinematic friction force corresponds to the longitudinal force when a car brakes over the pavement (i.e., when the wheel stops spinning and, as a result, the longitudinal force increases).

Table 6-44. Longitudinal Forces (F_x) Conditions

Longitudinal Force	F_x	Reference
Rolling friction force	2.5% F_v = 0.62 kN	Milne et al. (2004)
Maximum rolling friction force	30% F_v = 7.40 kN	Milne et al. (2004)
Kinematic friction force	78% F_v = 19.38 kN	Tang et al. (2013)

The results of the pdf fittings for the sets of relevant R.I.$_{dry}$ values are summarized in Table 6-45, Table 6-46, Figure 6-51, and Figure 6-52. These results show that OGFC mixtures presented a larger susceptibility to raveling when the longitudinal force corresponded to the kinematic friction force (i.e., when the car was braking). As observed in Table 6-47, the raveling susceptibility between the maximum friction rolling force and the kinematic force was 51 percent in Base Model 1 and 27 percent in Base Model 2. It can also be observed that, similar to the previous cases, Base Model 2 was more susceptible to raveling, although the differences in R.I.$_{dry}$ with respect to the different longitudinal forces in this case were not as notorious as in Base Model 1.

Table 6-45. pdf Parameters—Longitudinal Force (*Fx*), Base Model 1

F_x	pdf	Mode I		Mode II	
		Mean (μ)	Std. Deviation (σ)	Mean (μ)	Std. Deviation (σ)
0.62 kN	Log normal	$81.09\text{x}10^{-4}$	$21.00\text{x}10^{-4}$	$55.38\text{x}10^{-4}$	$17.49\text{x}10^{-8}$
7.40 kN	Log normal	$01.14\text{x}10^{-2}$	$62.25\text{x}10^{-4}$	$66.15\text{x}10^{-4}$	$51.84\text{x}10^{-8}$
19.38 kN	Log normal	$01.48\text{x}10^{-2}$	$02.09\text{x}10^{-2}$	$01.25\text{x}10^{-2}$	$01.74\text{x}10^{-6}$

Table 6-46. pdf Parameters Mode I—Longitudinal Force (*Fx*), Base Model 2

F_x	pdf	Mode I		Mode II	
		Mean (μ)	Std. Deviation (σ)	Mean (μ)	Std. Deviation (σ)
0.62 kN	Log normal	$02.99\text{x}10^{-2}$	$04.48\text{x}10^{-2}$	$02.27\text{x}10^{-2}$	$04.23\text{x}10^{-2}$
7.40 kN	Log normal	$03.24\text{x}10^{-2}$	$04.58\text{x}10^{-2}$	$02.24\text{x}10^{-2}$	$02.84\text{x}10^{-2}$
19.38 kN	Log normal	$06.79\text{x}10^{-2}$	$03.33\text{x}10^{-2}$	$04.33\text{x}10^{-2}$	$01.58\text{x}10^{-2}$

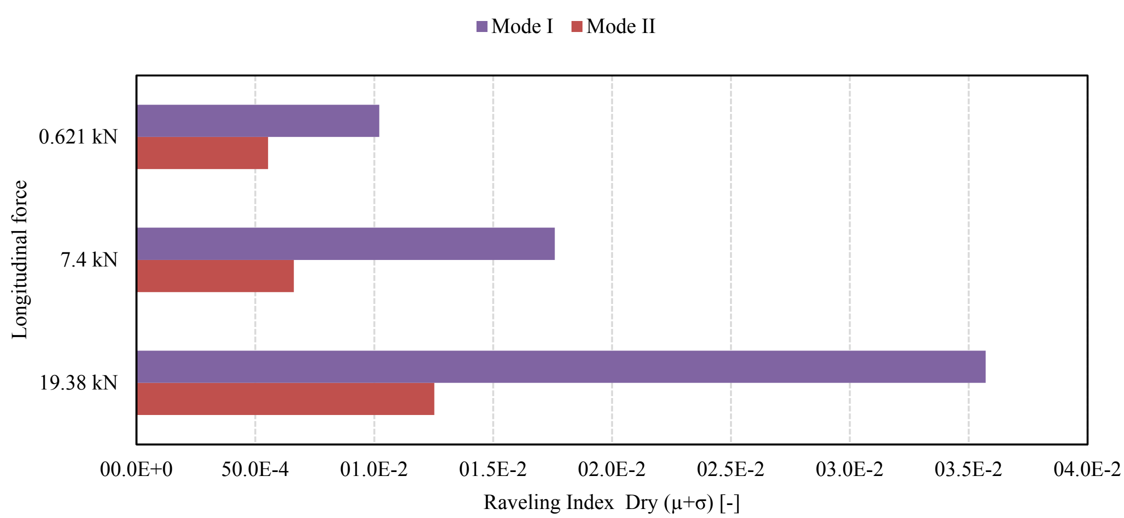

Figure 6-51. Effect of the longitudinal force on the susceptibility to raveling of OGFC—Base Model 1.

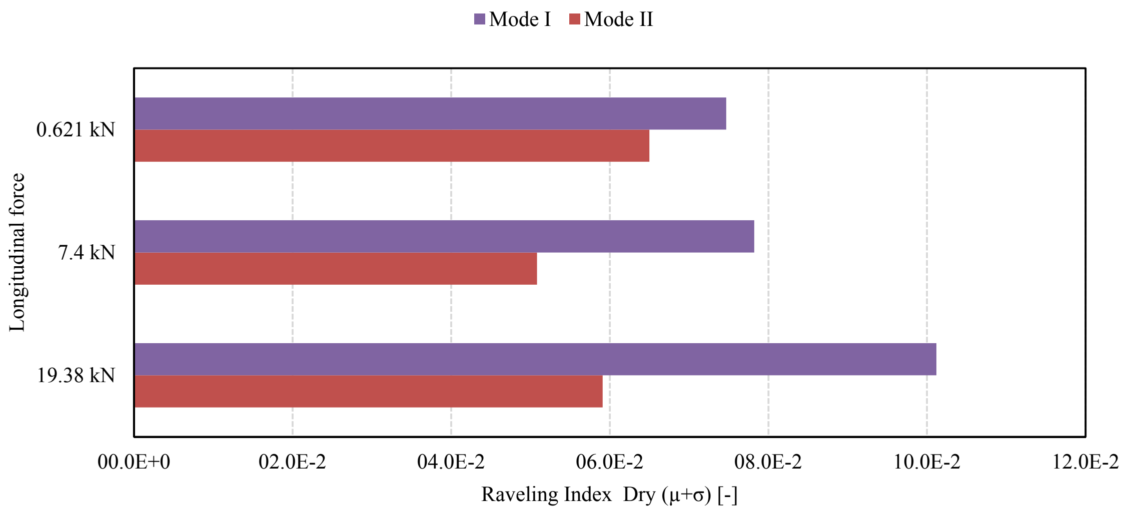

Figure 6-52. Effect of the longitudinal force on the susceptibility to raveling of OGFC—Base Model 2.

Table 6-47. Influence of Longitudinal Force on Raveling Susceptibility—Ranking

Mode I				
Base Model 1	F_x	0.621 kN	7.4 kN	19.38 kN
	R.I.$_{dry}$>5x10^{-3} (μ+σ)	01.02x10^{-2}	01.76x10^{-2}	03.57x10^{-2}
	Normalized R.I.$_{dry}$>5x10^{-3} (μ+σ)	0.29	0.49	1.00
		Higher raveling susceptibility →		
Base Model 2	F_x	0.621 kN	7.4 kN	19.38 kN
	R.I.$_{dry}$>5x10^{-3} (μ+σ)	7.47x10^{-2}	7.82x10^{-2}	1.01x10^{-1}
	Normalized R.I.$_{dry}$>5x10^{-3} (μ+σ)	0.74	0.77	1.00
		Higher raveling susceptibility →		

6.7.2.9. Impact of the Pavement Structural Capability (External Condition)

The pavement structural capability refers to the mechanical capacity of the equivalent base layer and the subgrade located bellow the OGFC layer. Besides the standard base model, two other cases were evaluated—a strong and a weak pavement structure—as shown in Table 6-48.

Table 6-48. Pavement Structures Evaluated

Structure Type	Equivalent Base (MPa)	Subgrade (MPa)
Weak	400	50
Medium (base case)	520	100
Strong	645	150

Following the same procedure as the previous cases, the pdf of the R.I.$_{dry}$ values higher than 5x10^{-3} was obtained, as summarized in Table 6-49 and Table 6-50, and with this information, the raveling parameters (μ+σ) for these distributions were computed, as observed in Figure 6-53 and Figure 6-54.

Table 6-49. pdf Parameters—Pavement Structural Capacity, Base Model 1

Pavement Structure	pdf	Mode I		Mode II	
		Mean (μ)	Std. Deviation (σ)	Mean (μ)	Std. Deviation (σ)
Weak	Log normal	77.58×10^{-4}	19.79×10^{-4}	54.60×10^{-4}	08.84×10^{-4}
Medium	Log normal	81.09×10^{-4}	21.00×10^{-4}	55.38×10^{-4}	08.81×10^{-4}
Strong	Log normal	82.87×10^{-4}	21.53×10^{-4}	55.33×10^{-4}	09.05×10^{-4}

Table 6-50. pdf Parameters—Pavement Structural Capacity, Base Model 2

Pavement Structure	pdf	Mode I		Mode II	
		Mean (μ)	Std. Deviation (σ)	Mean (μ)	Std. Deviation (σ)
Weak	Log normal	03.20×10^{-2}	04.82×10^{-2}	02.23×10^{-2}	04.20×10^{-2}
Medium	Log normal	02.99×10^{-2}	04.48×10^{-2}	02.27×10^{-2}	04.23×10^{-2}
Strong	Log normal	02.91×10^{-2}	04.27×10^{-2}	02.30×10^{-2}	04.26×10^{-2}

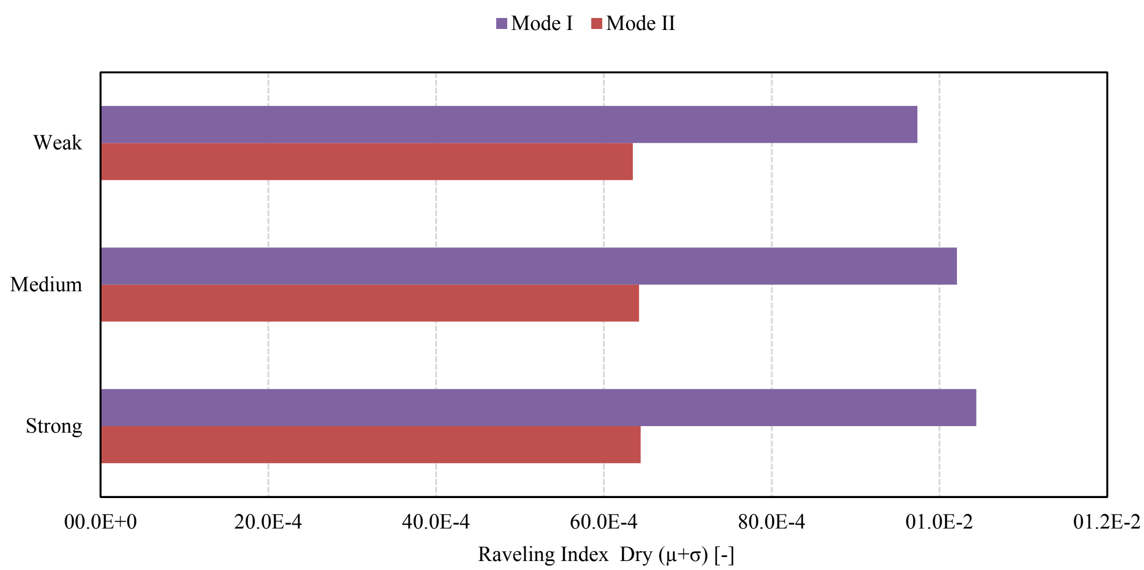

Figure 6-53. Effect of the structural capacity of the pavement on the susceptibility to raveling of OGFC—Base Model 1.

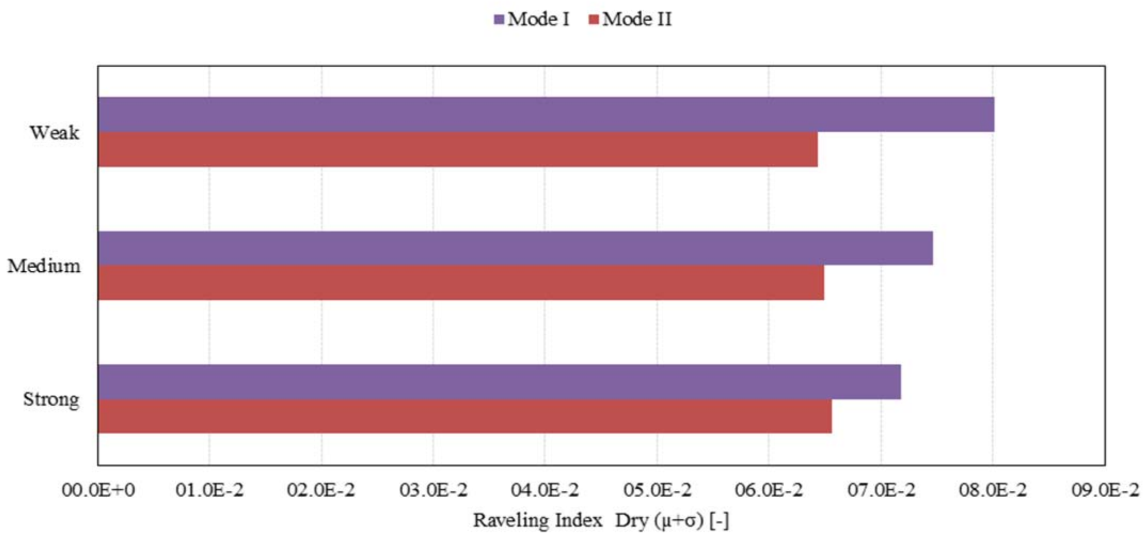

Figure 6-54. Effect of the structural capacity of the pavement on the susceptibility to raveling of OGFC—Base Model 2.

The first interesting conclusion of these results is that compared to the other parameters analyzed, the structural capacity of the pavement beneath the OGFC had a small influence on the raveling susceptibly of the mixture. In addition, the results were not consistent for the two base models. In Base Model 1, the raveling parameter was larger when the OGFC was located over a strong pavement structure, while the opposite occurred in Base Model 2. Nevertheless, as mentioned before, this result is not of concern since the characteristics of the pavement structure do not seem to be a critical factor in the susceptibility to raveling of these mixtures. This finding was verified when ranking the three cases, after normalizing the raveling parameters with respect to the maximum (Table 6-51). Researchers concluded that the difference between the cases presenting the highest and the smallest susceptibility to raveling was around 8.5 percent. Since the pdfs used as part of these analyses were obtained with a 95 percent confidence level, this difference was near the fitting error and therefore was not significant.

Table 6-51. Influence of the Pavement Structural Capacity on Raveling Susceptibility—Ranking

		Mode I		
Base Model 1	**Pavement Structural Capacity**	**Weak**	**Medium**	**Strong**
	R.I.$_{dry}$>5x10^{-3} (μ+σ)	9.74x10^{-3}	1.02x10^{-2}	1.04x10^{-2}
	Normalized R.I.$_{dry}$>5x10^{-3} (μ+σ)	0.93	0.98	1.00
		Higher raveling susceptibility →		
Base Model 2	**Pavement Structural Capacity**	**Strong**	**Medium**	**Weak**
	R.I.$_{dry}$>5x10^{-3} (μ+σ)	7.18x10^{-2}	7.47x10^{-2}	8.02x10^{-2}
	Normalized R.I.$_{dry}$>5x10^{-3} (μ+σ)	0.90	0.93	1.00
		Higher raveling susceptibility →		

6.7.2.10. Influence of Moisture (External Condition)

The exposure of asphalt mixtures to moisture, in any state (liquid or vapor), reduces the structural capability of those materials. This condition, known as moisture damage, is believed to be an important factor in increasing the susceptibility of an OGFC mixture to raveling. In this case, all the material combinations presented in Table 6-19 were evaluated by subjecting the pavement to the moving wheel after exposing the OGFC to 1-month moisture diffusion at a critical condition (RH: 100 percent).

For the moisture-related simulations, the $R.I._{wet}$ was evaluated as follows:

$$R.I._{wet} = \frac{Dissipated\ energy}{Cohesive\ bond\ energy_{reduced}} \quad (6\text{-}13)$$

After verifying the results from the maximum $R.I._{wet}$ values, those higher than $9.0x10^{-3}$ were adjusted to a probabilistic distribution, similar to what was done in the dry simulations for the $R.I._{dry}$ values larger than $5x10^{-3}$. Table 6-52 and Table 6-53 present the pdf fitting parameters of these cases, and Figure 6-55 and Figure 6-56 present the mean plus one standard deviation values of this parameter.

Table 6-52. pdf Parameters—Wet Conditions, Base Model 1

Material	pdf	Mode I		Mode II	
		Mean (μ)	Std. Deviation (σ)	Mean (μ)	Std. Deviation (σ)
GR/ARB+GR	Log normal	$7.71x10^{-3}$	$8.04x10^{-3}$	$4.07x10^{-3}$	$2.82x10^{-3}$
LS/ARB+LS	Log normal	$3.66x10^{-2}$	$2.16x10^{-2}$	$1.72x10^{-2}$	$5.35x10^{-3}$
GR/PMA+GR	Log normal	$1.75x10^{-2}$	$1.80x10^{-2}$	$8.99x10^{-3}$	$5.53x10^{-3}$
LS/PMA+LS	Log normal	$5.75x10^{-2}$	$8.86x10^{-2}$	$2.90x10^{-2}$	$2.55x10^{-2}$

Table 6-53. pdf Parameters—Wet Conditions, Base Model 2

Material	pdf	Mode I		Mode II	
		Mean (μ)	Std. Deviation (σ)	Mean (μ)	Std. Deviation (σ)
GR/ARB+GR	Log normal	$2.70x10^{-2}$	$6.37x10^{-2}$	$1.97x10^{-2}$	$5.29x10^{-2}$
LS/ARB+LS	Log normal	$5.98x10^{-2}$	$5.49x10^{-2}$	$8.87x10^{-2}$	$1.33x10^{-1}$
GR/PMA+GR	Log normal	$6.31x10^{-2}$	$1.57x10^{-1}$	$3.86x10^{-2}$	$9.09x10^{-2}$
LS/PMA+LS	Log normal	$1.64x10^{-1}$	$4.48x10^{-1}$	$1.23x10^{-1}$	$4.31x10^{-1}$

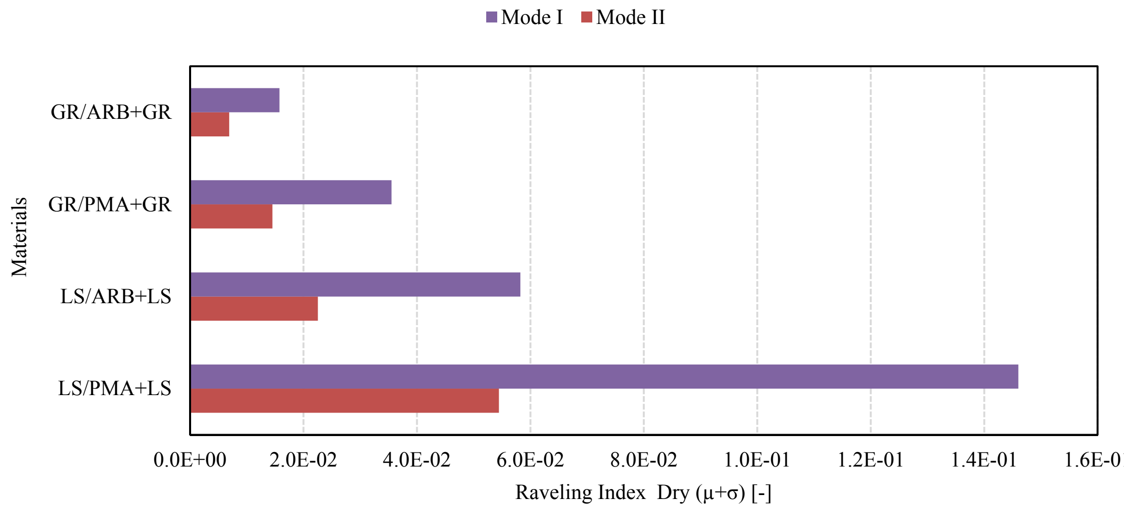

Figure 6-55. Effect of moisture on the susceptibility to raveling of OGFC—Base Model 1.

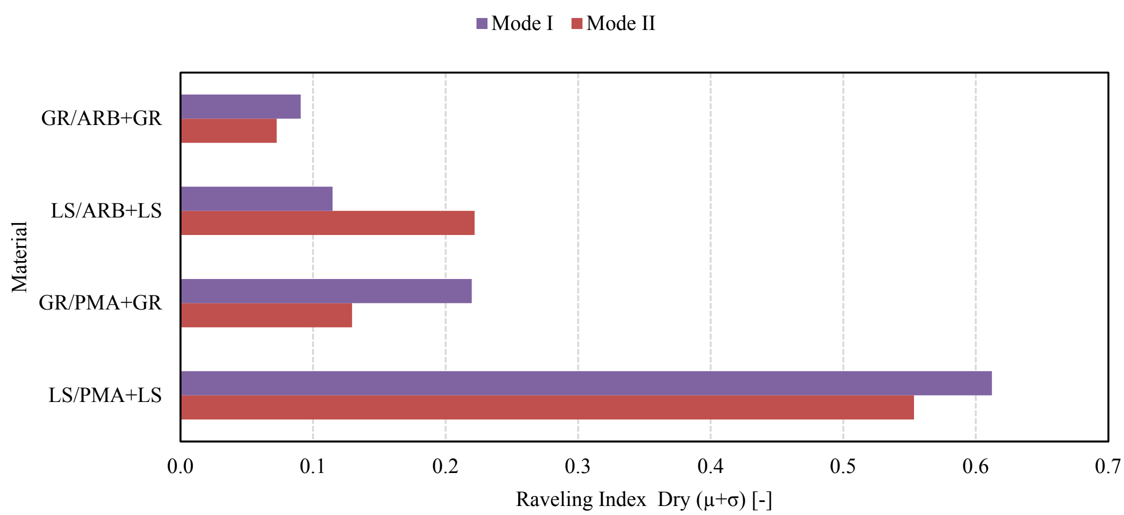

Figure 6-56. Effect of moisture on the susceptibility to raveling of OGFC—Base Model 2.

The results, which are summarized in Table 6-54, show that the most susceptible material to raveling was LS/PMA+LS. In both base models, this material combination presented a difference of up to 89 percent with respect to the material combination GR/ARB+GR, which was the least susceptible mixture to raveling under moisture conditions. The results also suggest that the susceptibility to raveling in these cases did not depend only on the moisture damage susceptibility of the material but mostly on the mechanical response of the mixture. According to the SFE measurement, the material combination LS/PMA+LS was 3.5 times less susceptible to moisture damage in comparison to the combinations GR/ARB+GR and GR/PMA+GR. However, the material combination LS/PMA+LS had one of the lowest cohesive bond energies in dry conditions and is the base parameter that has been used to evaluate the mechanical performance of the mixture. This finding led researchers to qualify LS/PMA+LS as the material combination that presented the highest susceptibility to raveling. Finally, the results show that in both base models, the most probable mode of failure was Mode I, with the exception of the material combination LS/ARB+LS in Base Model 2, which seemed to be more prone to crack through Mode II, placing this material combination as the second more susceptible to raveling in these simulations.

Table 6-54. Influence of Moisture Diffusion on Raveling Susceptibility—Ranking

Mode I					
Base Model 1	**Material**	**GR/ARB+GR**	**GR/PMA+GR**	**LS/ARB+LS**	**LS/PMA+LS**
	R.I.$_{wet}$>9x10^{-3} (μ+σ)	0.02	0.04	0.06	0.15
	Normalized R.I.$_{wet}$>9x10^{-3} (μ+σ)	0.11	0.24	0.40	1.00
		Higher raveling susceptibility →			
Base Model 2	**Material**	**GR/ARB+GR**	**LS/ARB+LS**	**GR/PMA+GR**	**LS/PMA+LS**
	R.I.$_{wet}$>9x10^{-3} (μ+σ)	0.09	0.11	0.22	0.61
	Normalized R.I.$_{wet}$>9x10^{-3} (μ+σ)	0.15	0.19	0.36	1.00
		Higher raveling susceptibility →			

Two main conclusions can be obtained when comparing these results with the results of the simulations of the same material combinations in dry conditions: (a) the sensitivity of the combination of materials to raveling increases in wet conditions (i.e., a maximum difference of 89 percent in the raveling susceptibility in the wet cases compared to a maximum difference of 41 percent in the raveling susceptibility in the dry cases); and (b) the least and the most susceptible material combinations for raveling (i.e., GR/ARB+GR and LS/PMA+LS, respectively) are the same in both dry and wet cases.

6.7.3. Modeling Fracture in OGFC Materials (CZM Approach)

As explained before, the CZM technique was used to conduct simulations in which the mastic-mastic contacts had the capacity to break or crack. In these cases, and taking into account that cohesive fracture is more probable to occur when the material becomes more brittle, the simulations in the base models were conducted using the rheological properties of the mastics under a long-term aging condition (i.e., PAV). Figure 6-57 presents the master curves for mastic ARB+LS and PMA+GR in PAV conditions. As observed, the master curves of the aged mastics presented higher complex moduli than the unaged cases, as expected.

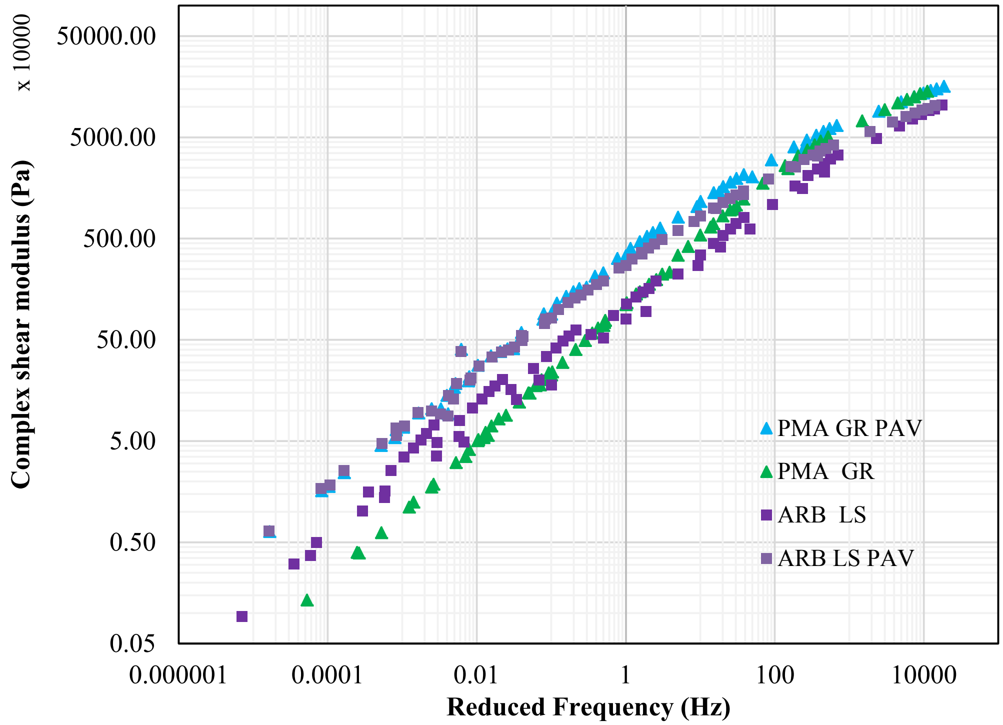

Figure 6-57. Master curves for mastics in PAV state (T_R = 30°C).

As explained before, in this case, the elements in contact between the aggregates were replaced by cohesive elements, using the traction separation law illustrated in Figure 6-23. These elements required the following input parameters to define their constitutive response: (a) the instantaneous modulus of the mastic, E_0; (b) the maximum tensile strength of the material, $\sigma_{\tau max}$; and (c) the total critical energy released rate, G^c. The instantaneous mastic modulus was obtained from the viscoelastic material properties of the mastics, the tensile strength of the materials was obtained after scaling the results for fine asphalt mixtures from data reported by Kim et al. (2005, 2008) to the mastics evaluated, and the critical energy released rate was estimated for each mastic based on the SFE results after assuming that the problem was isotropic (i.e., the same fracture properties for both modes of failure). The parameters used in the model are summarized in Table 6-55.

Table 6-55. Parameter for the Traction Separation Law of the Cohesive Zone Elements

Mastic	E_0 (MPa)	σ_{max} (MPa)	Dissipated Energy G^c (N/mm)
ARB-LS	382.04	0.63	$6.96\text{x}10^{-04}$
PMA-GR	811.65	0.66	$4.16\text{x}10^{-04}$

Due to the differences in the geometries of both models, Base Model 1 had a total of 2938 cohesive elements, while Base Model 2 had 3895. After running the simulations, researchers observed that 35 and 33 percent of the cohesive elements in Base Models 1 and 2 failed, respectively. An example of the failure occurring in the cohesive elements can be observed in Figure 6-58, where the Mises stress distribution of the system is presented for both models.

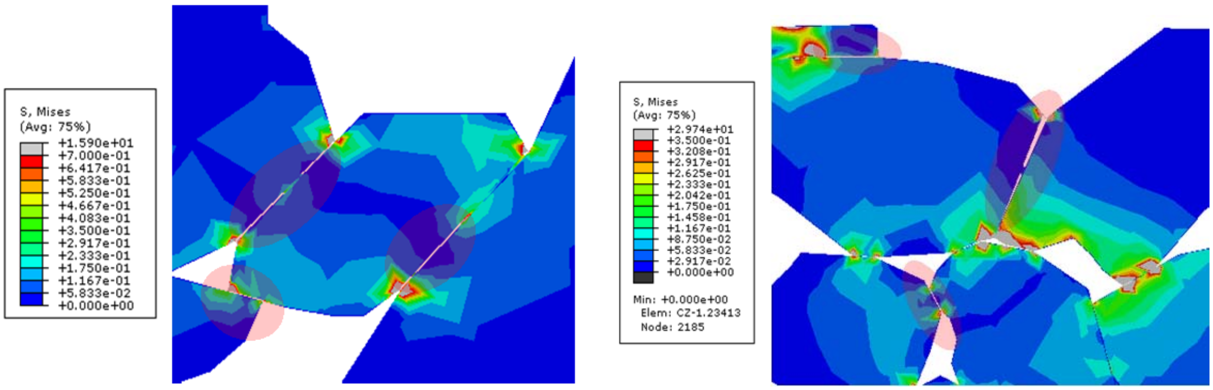

(a) (b)

Figure 6-58. Fractured cohesive elements: (a) Base Model 1, (b) Base Model 2.

In order to determine the model that is more prone to raveling under the unfavorable long-term aging conditions considered, the number of cohesive elements that were failing through time was quantified, and the results are presented in Figure 6-59.

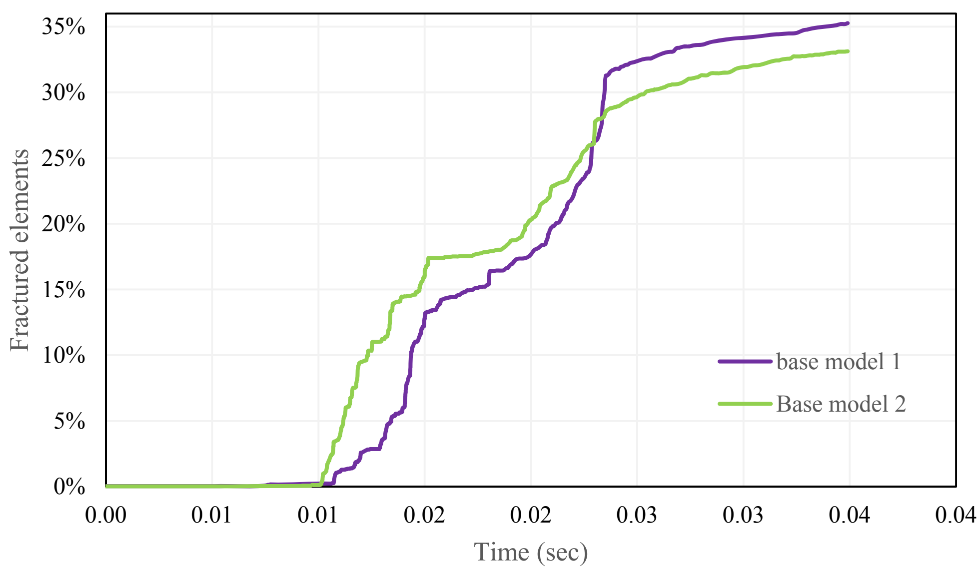

Figure 6-59. Percentage of cohesive elements that failed through time.

Regardless that Base Model 1 presented 2 percent more failed elements at the end of the simulation, Figure 6-59 shows that Base Model 2 had a tendency to have more failed elements for a longer time (i.e., 0.01–0.025 sec), insinuating a slightly higher susceptibility to raveling. However, the results showed that in the long term, both models (i.e., both mixtures) behaved similarly, and that the propensity to raveling under aged conditions was comparable between the two OGFCs. There are two reasons that could explain this finding: (a) the SFE of the PAV binders was more similar for both materials than the SFE values of the materials in the unaged case, and (b) the master curves of both materials in the PAV condition were also closer than in the unaged case. These two conditions make the mechanical response of the two mixtures more similar than the response in the unaged case. Therefore, even though during all previous simulations it was observed that Base Model 2 (LS/ARB+LS) was more susceptible to raveling than Base Model 1 (GR/PMA+GR), this difference in susceptibility tended to decrease with an increase in oxidation. It should be stated, however, that this result does not mean that the raveling susceptibility of a mixture decreases with time, since it has been proved that the probability of raveling increases with the service life of any OGFC. The results suggest only that the differences of raveling susceptibility among different mixtures decreases with time. This observation, in turn, suggests that it is critical to control raveling in the initial phase of service life of the mixtures (i.e., by controlling construction quality, etc.) since under those conditions, this distress is very sensitive to the selected materials for the mixture.

6.7.4. Pore Pressure

As explained in previous sections, pore pressure is considered an aggressive mechanism associated with moisture damage. Pore pressure is generated within the structure of a porous media as a result of the dynamic application of loading when the material is under saturated conditions. The presence of this additional pressure impacts the mechanical response of the material, to the point that it can cause the initiation of micro-cracks. In the case of OGFC, it is believed that pore pressure could increment the localized stresses and strains at the stone-on-stone contact zones, also increasing the chances of raveling.

In order to evaluate the impact of pore pressure on the mechanical response of OGFC, researchers developed a simplified FE model, the geometry of which is illustrated in Figure 6-60. In the model, all the aggregates were coated with a mastic film of 15 μm, which corresponded to the condition of Base Model 1.

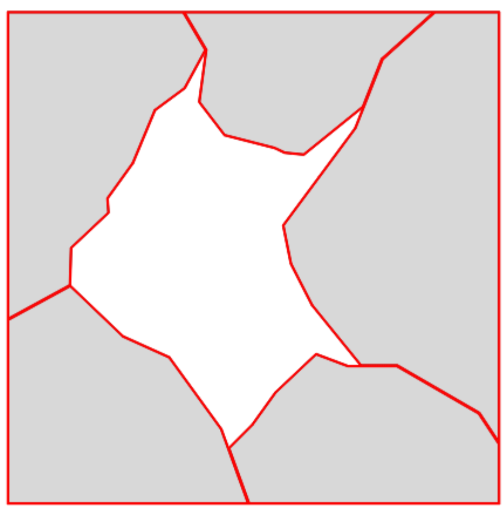

Figure 6-60. Geometry used to study the impact of pore pressure.

Four cases were evaluated by varying the combination of materials (i.e., aggregates—GR or LS—and type of mastic—GR/ARB+GR, GR/PMA+GR, LS/ARB+LS, and LS/PMA+LS). Similar to the previous FE models, the aggregates were considered linear elastic materials, with the same material properties as before.

In order to evaluate the additional impact of pore pressure on the stress and strain concentration at the mastic-mastic contact areas, pressure was applied to the surfaces of the particles that were in the perimeter of the central air void, as observed in Figure 6-61. This condition simulated the impact of pore pressure within the OGFC microstructure. The results from this simulation provided the *additional* energy that was being dissipated at the mastic contacts due to the pass of a vehicle when the mixture was under water-saturated conditions. Two different values of pore pressure were considered: 50 kPa and 5 kPa. The first value represented a typical saturated undrained condition within a composite pore structure with cementitious properties. This case corresponded to a worst-case scenario, in which it was assumed that water reached the microstructure and, due to a deficiency in the drainage system in the layer (e.g., clogging), it did not flow outside the microstructure. The second value represented a more favorable condition in which saturation occurred under drained conditions (i.e., expected conditions in OGFC). Reference values of pore pressure for drained and undrained conditions on soils can be found elsewhere (Mitchell and Soga 2005).

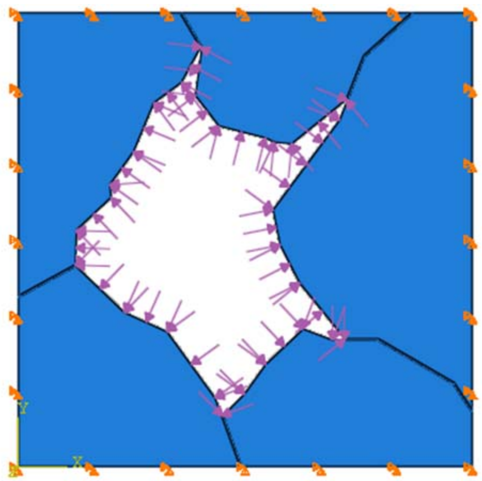

Figure 6-61. Pore pressure condition within the model.

Figure 6-62 presents the overall stress distribution for one case study. Similar to the previous simulations, the maximum tensile and shear stresses and strains were obtained for all the elements at the mastic-mastic contact areas, which were used to compute the maximum dissipated energies and the R.I.$_{dry}$ parameters for each case.

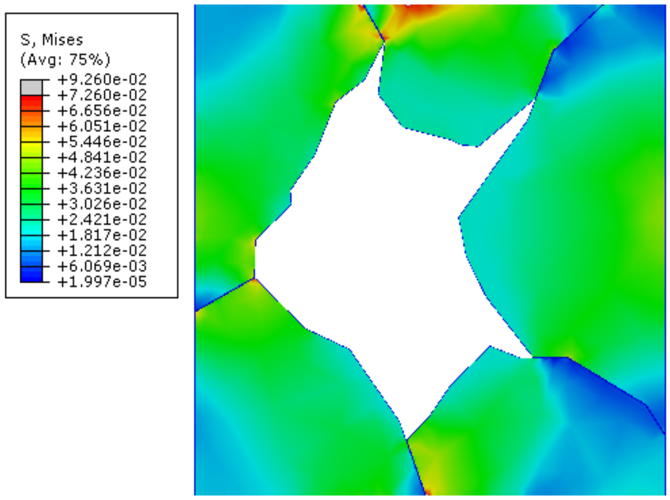

Figure 6-62. Mises stress distribution in the model (in Mpa).

Table 6-56 and Table 6-57 present the parameters for the best-fit pdf distributions of the larger R.I.$_{dry}$ values corresponding to all the material combinations and the two saturated conditions (drained and undrained), while Figure 6-63 and Figure 6-64 illustrate the corresponding (μ+σ) values of those pdf distributions.

Table 6-56. pdf Parameters—Drained Conditions (5 kPa)

Material	pdf	Mode I		Mode II	
		Mean (μ)	Std. Deviation (σ)	Mean (μ)	Std. Deviation (σ)
GR/ARB+GR	Log normal	$1.96\text{x}10^{-9}$	$1.28\text{x}10^{-9}$	$1.51\text{x}10^{-9}$	$2.46\text{x}10^{-10}$
LS/ARB+LS	Log normal	$1.77\text{x}10^{-9}$	$1.05\text{x}10^{-9}$	$1.43\text{x}10^{-9}$	$3.53\text{x}10^{-10}$
GR/PMA+GR	Log normal	$2.70\text{x}10^{-9}$	$1.42\text{x}10^{-9}$	$2.17\text{x}10^{-9}$	$3.01\text{x}10^{-10}$
LS/PMA+LS	Log normal	$2.81\text{x}10^{-9}$	$2.02\text{x}10^{-9}$	$1.58\text{x}10^{-9}$	$2.44\text{x}10^{-10}$

Table 6-57. pdf Parameters—Undrained Conditions (50 kPa)

		Mode I		Mode II	
Material	pdf	Mean (μ)	Std. Deviation (σ)	Mean (μ)	Std. Deviation (σ)
GR/ARB+GR	Log normal	$1.96\text{x}10^{-7}$	$1.28\text{x}10^{-7}$	$1.51\text{x}10^{-7}$	$2.46\text{x}10^{-8}$
LS/ARB+LS	Normal	$1.81\text{x}10^{-7}$	$1.47\text{x}10^{-7}$	$1.42\text{x}10^{-7}$	$3.35\text{x}10^{-8}$
GR/PMA+GR	Log normal	$3.11\text{x}10^{-7}$	$2.23\text{x}10^{-7}$	$1.75\text{x}10^{-7}$	$2.70\text{x}10^{-8}$
LS/PMA+LS	Normal	$2.44\text{x}10^{-7}$	$4.42\text{x}10^{-8}$	$1.95\text{x}10^{-7}$	$2.79\text{x}10^{-8}$

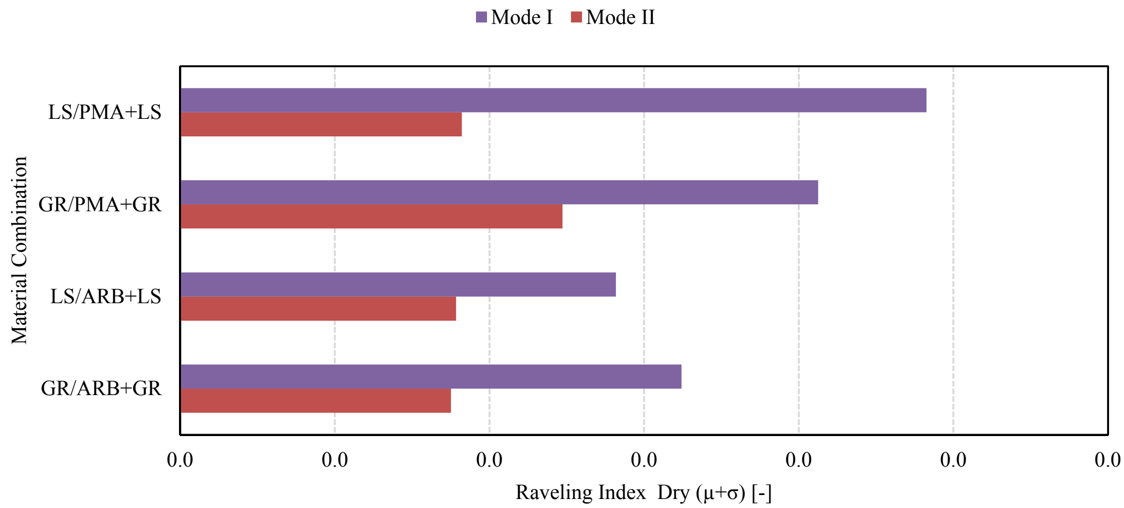

Figure 6-63. Effect of pore pressure on the susceptibility to raveling of OGFC—drained case.

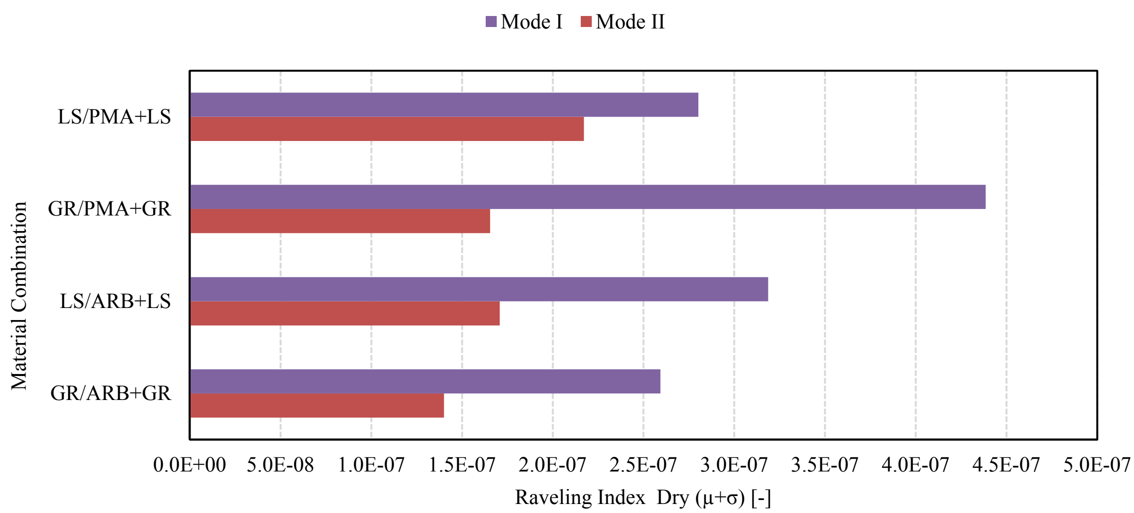

Figure 6-64. Effect of pore pressure on the susceptibility to raveling of OGFC—undrained case.

Several observations were extracted from these results. First, when comparing the magnitude of the raveling parameters to those obtained in the dry material simulations, researchers observed that pore pressure could increase raveling susceptibility by 0.01 percent in the saturated undrained condition and 0.0001 percent in the saturated drained condition. This range value was not relevant, suggesting that pore pressure is not a critical factor affecting the durability of the mixture, although it also demonstrated that a saturated undrained condition within the mixture is 100 times more adverse than a saturated drained condition. Thus, guaranteeing a proper functionality of the mixture (i.e., proper permeability properties, prevention of clogging) could help prevent durability issues. The results also showed that the material that presented the highest susceptibility to the effects of pore pressure was the GR/PMA+GR, while the mixture GR/ARB+GR was the least susceptible to this condition.

It is important to mention that in these simulations, the dry or original viscoelastic properties of the mastic were used as input parameters. However, if water is present within the mixture, pore pressure probably occurs when the mastic materials are under wet conditions. In this case, the rheological properties of the mixtures are less favorable, implying that in a more realistic simulation, the additional energy dissipated by the contact elements would be much higher. In those cases, the contribution of pore pressure to raveling might not be negligible.

6.7.5. Summary of Results

In all analyses, the sensitivity of each individual parameter in promoting the development of raveling was studied. However, it was also important to identify which parameters were a real hazard to the durability of the mixtures. Therefore, researchers identified the parameters with the highest and lowest influence on the development of raveling (i.e., [μ+σ] of R.I.$_{dry}$>5x10^{-3}). This information could help inform decisions about which factors should be controlled to extend the service life of OGFC layers.

To conduct such an analysis, researchers compared the maximum raveling parameters (i.e., [μ+σ] of R.I.$_{dry}$>5x10^{-3}) for the predominant Mode I of failure obtained from each set of simulations, as listed in Table 6-58. Figure 6-65 illustrates the same data as Table 6-58 but for an easier interpretation. It is important to note that Table 6-58 does not include the results of the moisture diffusion simulations. This omission is due to the fact that since a different evaluation index was used in these cases, it was not possible to compare the results with those obtained from all other simulations. Also, since the results of the impact of the OGFC thickness were not conclusive, they were included in the table but were not included as part of the analysis.

Table 6-58. Maximum R.I.$_{dry}$ (μ+σ)

Base Model 1				Base Model 2		
Parameter	**Condition**	**R.I.$_{dry}$ (μ+σ)**		**Parameter**	**Condition**	**R.I.$_{dry}$ (μ+σ)**
Temperature[a]	High	0.105	**Higher raveling susceptibility**	Air Void	High	0.191
Air Void	High	0.056		Temperature	High	0.143
Longitudinal Force	High	0.036		Load Magnitude	High	0.142
OGFC Layer Thickness[b]	4 cm	0.029		Binder Content	Too low or too high	0.117
Binder Content	Too low or too high	0.019		Longitudinal Force	High	0.101
Traffic Speed	Low	0.015		Material Combination	LS/PMA +LS	0.094
Load Magnitude	High	0.014		Traffic Speed	Low	0.088
Material Combination	LS/ARB +LS	0.011		Pavement Structure	Weak	0.080
Pavement Structure	Strong	0.010				

[a] Temperature lower than 10ºC were not considered. For low temperatures the raveling susceptibility is expected to increase, as has been demonstrated by previous numerical works (refer to the Literature Review chapter for details).
[b] Results were not conclusive; further analysis is needed.

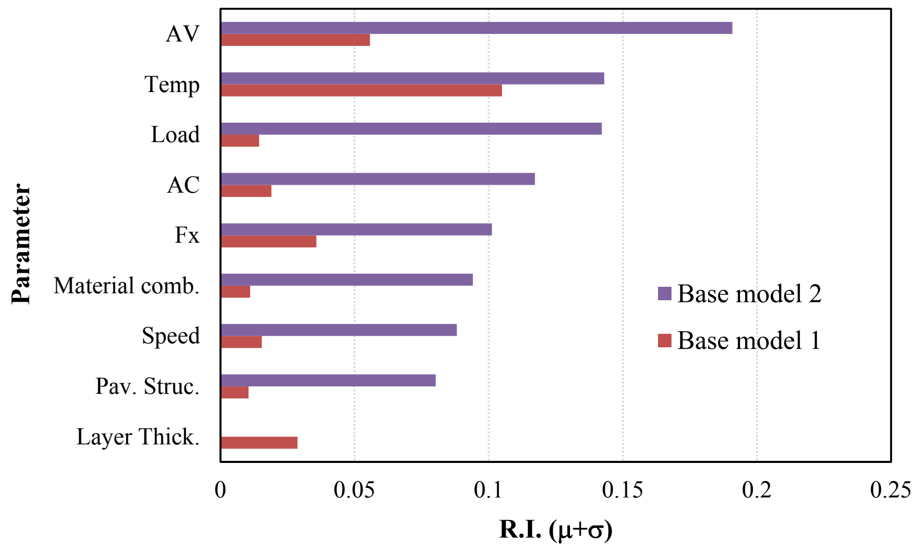

Figure 6-65. Parameters with the highest influence on raveling.

Based on these results, the top 5 factors that raised the chances for raveling in each base model are shown in Table 6-59:

Table 6-59. Top Five Most Relevant Factors that Promoted Raveling

Ranking	Most critical parameters	
	Base model 1	Base model 2
1	High temperature[a]	High air voids
2	High air voids	High temperature
3	High longitudinal force	High load magnitude
4	Too low or too high	Too low or too high
5	Low traffic speed	High longitudinal force

[a] Temperature lower than 10ºC were not considered; at lower temperatures the raveling susceptibility is expected to increase (refer to the Literature Review chapter for details).

These parameters include three conditions that can be controlled in road infrastructure projects. The first one is the quality of the compaction process during the construction of the OGFC. An increase in 5 percent in this parameter was the condition presenting the highest impact on the probability of raveling in Base Model 2, and the second highest impact on promoting raveling in Base Model 1. Also, there are three factors associated with traffic that were identified to increase the possibilities of raveling: (a) low-speed traffic, (b) vehicle braking, and (c) very high-load traffic. Indeed, the durability of these mixtures could be compromised if used in low-speed roads—which justifies FDOT current specification that prescribes the use of OGFC mixtures only on high-speed facilities—, in areas where vehicles need to brake regularly, or in zones where a high frequency of unusually heavy vehicles is expected. Finally, binder content was observed to be another important factor that could impact the durability of the mixtures, and it is another element that can be engineered in order to prevent raveling. In this sense, the development and application of mix design methodologies that consider durability issues, and not only workability issues, could be of help for extending the service life of these mixtures. The results reported herein suggest that the design binder content values (i.e., OBC) of the mixtures evaluated do not necessarily correspond to the values that would optimize their durability.

Although the impact of the materials used in the mixture was not ranked among the top five factors affecting raveling, the results obtained from all the simulations were consistent in demonstrating that the mixture with LS aggregate and ARB binder is the most susceptible to raveling. This finding is due to the fact that this mixture has the lowest structural capacity, and as was observed in this study, raveling is mainly a mechanical problem related with fracture processes. Even though it is true that this mixture has a low susceptibility to moisture damage, this condition does not seem to provide an advantage in preventing raveling when compared to the capacity of the material to resist fracture.

In terms of moisture damage, although the results are not comparable with the other sets of simulations, the evaluation parameters obtained make it clear that the sensitivity to raveling of the different material combinations used in the mixtures is exacerbated when moisture is present. In this sense, the decision of using antistripping agents in OGFC is a prudent and effective choice.

Also, the results obtained from Base Models 1 and 2 showed that the combination of gradation and material selection has a strong influence in determining the probability of an OGFC surface to degrade. However, more so than the gradation of the mixture itself, the relationship between the thickness of the layer and the maximum nominal aggregate size, which determines the total amount of aggregates in the mixture (59 aggregates in Base Model 2 in comparison to 70 aggregates in Base Model 1) and partially defines the amount of stone-on-stone contacts and the quality of the aggregate skeleton, seems to be a critical aspect in affecting the mechanical capacity of the mixture to resist fracture. The average difference between the raveling parameters of the two base models when subjected to an equivalent set of external conditions was near 60 percent. However, the results from using the CZM technique suggest that the differences in the mechanical response of the mixtures due to the selection of materials become less relevant with the progression of time (i.e., with aging). This result does not imply that one specific mixture will reduce its susceptibility to raveling with time, since the opposite is expected to occur.

It is also important to mention that the FE simulations demonstrated that the structural capacity of the pavement located underneath the OGFC has a minimum effect in the susceptibility of a mixture to raveling, This, of course, was an expected result since raveling is recognized to be a pavement surface-related phenomenon.

CHAPTER 7 . CONCLUSIONS AND RECOMMENDATIONS

The objective of this project was to understand the mechanisms of raveling in OGFC mixtures. The project had two components: experimental measurements and FE numerical modeling. For the experimental component of the project, FDOT helped identify two mixtures with good field performance and one mixture with poor field performance with respect to raveling. Another three mixtures were added by modifying the aggregate and binder type. Morphological and physiochemical properties of the component materials were examined to reveal their propensity for moisture susceptibility. Volumetrics, binder stiffness, aggregate morphology, and SFE were evaluated. Laboratory specimens prepared in the SGC of all six asphalt mixtures were tested using permeability, Cantabro loss, IDT strength, and HWTT.

Two conditioning protocols were used to evaluate the effect of moisture on the mixture's IDT strength and Cantabro loss: (a) modified Lottman per AASHTO T 283using one freeze/thaw cycle and subjecting the specimens to 87.8 kPa of vacuum for 10 min without regard to the degree of saturation achieved by the specimen; and (b) the MIST device according to ASTM D7870 with 1,000 cycles, 40 psi pressure, and a water temperature of 60°C. The specimens were air dried for 48–72 hr and also subjected to CoreDry to ensure all free moisture had been removed before performance testing. Based on the experimental results from the IDT and Cantabro loss tests, the moisture conditioning protocols did not produce the desired level of moisture damage. In the case of the IDT strength after MIST, five of the six mixtures had TSR values above 100 percent, suggesting that the MIST protocol actually made the specimens stronger. In fact, statistical analysis showed that moisture conditioning was a significant factor, but opposite to the expected behavior. The IDT strength results after AASHTO T 283 showed slightly better trends, but still two of the six mixtures had TSR values above 100 percent.

For the Cantabro loss test after MIST, four of the six specimens showed a decrease in Cantabro loss, again suggesting that the asphalt mixtures improved with moisture conditioning, which is counter to the existing body of research. Again, the Cantabro loss after AASHTO T 283 showed slightly better trends, with only two of the six mixtures showing less or equivalent abrasion loss after conditioning. In addition, HWTT test results showed that all six asphalt mixtures never reached the SN and thus were likely not susceptible to moisture damage. In general, the six mixtures that were evaluated demonstrated adequate moisture resistance in the laboratory, and further investigation to develop adequate moisture conditioning methods or adjust the protocols of existing methods to FDOT OGFC mixtures may be beneficial.

Other conclusions and recommendations made based on the experimental component of the project included:

- Comparison of the angularity, texture, and sphericity values determined by the AIMS indicated that there was no significant difference in the morphological properties of the limestone and granite aggregates commonly used in FDOT OGFC mixtures. These similar properties would seem to exclude aggregate morphology as a factor in the moisture susceptibility of asphalt mixtures made using these two aggregates.
- The G-R parameter showed that the ARB binder had a faster progression toward the damage zone with aging as compared to the PMA binder. This finding indicates that OGFC mixtures employing ARB binder may be more susceptible to raveling as they age.

- The SFE of the component materials was used to evaluate the moisture susceptibility of the aggregate-binder combinations. There was a moderate correlation between the results and field observations. However, future research could examine the effect of the larger film thickness of OGFC mixtures on moisture susceptibility and whether it is controlled by adhesive failure at the aggregate-binder interface or cohesive failure within the binder.
- During specimen fabrication, researchers noted that the specimens expanded in the vertical and diametral directions when extracted from the SGC molds. This phenomenon occurred even when specimens were placed in PVC pipes after extraction. The expansion varied from 0.5 to 1.5 mm and had to be accounted for in order to achieve the target AV content since dimensional analysis was used to estimate that quantity.
- Comparison of the number of gyrations required to make the SGC specimens revealed that mixtures 5 and 6 required a considerably higher compaction effort to meet the target AV content of 20 percent. This finding indicates that standard field compaction may lead to higher than field air voids in the granite mixtures as compared to the limestone mixtures, and thus a potentially higher susceptibility to raveling. In addition, the standard laboratory mix design method prescribes preparing SGC specimens to a fixed number of gyrations (i.e., 50). Therefore, exploring the differences in AV content, permeability, and moisture susceptibility when controlling the level of compaction is recommended.
- The Cantabro loss test resulted in the best performance test in terms of its ability to predict the durability of OGFC mixtures when compared to observed field performance. While moisture conditioning was not a statistically significant factor in the test results (as noted above), the average Cantabro loss values for mixtures 1, 2, and 3 correlated well with the observed field performance of those mixtures, while the IDT and HWTT results did not correlate with field performance.

These results of the materials and mixture characterizations were used as inputs in the 2D FE numerical modeling component of the project. The model used the microstructure of OGFC mixtures coupled with mechanical-moisture formulations to evaluate the impact of internal and external factors on the onset and progression of raveling. The following observations were derived from the modeling effort:

- Raveling is mainly a mechanical and surface-related problem associated with a Mode I of failure. The propensity of the mixture to develop this degradation phenomenon is increased by the presence of moisture (vapor diffusion and liquid pore pressure), which justifies the use of antistripping materials. The number of aggregates, the number of stone-on-stone contacts, and the percentage of the perimeter of an aggregate that is in contact with other aggregates determine the quality of the mixture skeleton, which in turn influences the mechanical distribution and localization of stresses and strains within the microstructure, as well as the susceptibility of the mixture to raveling. These factors are determined by three features: (a) the gradation of the mixture, (b) the thickness of the layer, and (c) the compaction process. Therefore, it seems important to verify that proper sets of [NMAS – layer thickness – AV] are being obtained in the field.
- Although temperature and moisture were observed to significantly raise the chances of raveling, these parameters are not controllable in the field. However, engineers could effectively control the AV content and the binder content of the mixture, as well as the OGFC specifications to ensure that this type of mixtures are not placed on low-speed, high

truck traffic and repeated braking roadways. Specifically, the results suggest that it could be convenient to limit the maximum AV content in the field (probably by making it dependent on OGFC layer thickness) and to use a mixture design methodology that takes durability into account. With respect to the first aspect, it is true that controlling compaction quality in very thin layers is a challenge; therefore, it would be interesting to evaluate the possibility of specifying a minimum OGFC layer thickness that could permit researchers to obtain the target AV content in the field, or to specify not only a minimum but also a maximum value of in-place drainability during construction. Also, the results suggest that the durability of OGFC could be compromised if used in low or low-medium speed roads, in zones where vehicles need to brake repeatedly, or in roads with a high frequency of trucks with unusual high axle loads.

- Long-term aging was observed to decrease the differences in the raveling sensitivity of different types of OGFC mixtures. This finding does not imply that the overall propensity of a mixture to raveling decreases with time but only that the impact in raveling susceptibility of a road exclusively due to differences in material properties diminishes with time. In fact, since the fracture resistance of the materials tends to decrease due to oxidative aging, it is expected that all OGFC mixtures increase their chances of raveling during service life.
- Although the effects of pore pressure were not observed to be relevant in increasing the chances of raveling, it was observed that the impact of pore pressure under saturated undrained conditions was higher than under saturated drained conditions. In other words, maintenance activities that prevent clogging are not only important to guarantee the functionality of the mixture but also to extend its durability.

REFERENCES

Alvarez, A. E., A. Epps Martin, C. Estakhri, J. W. Button, C. Glover, and S. H. M. Jung (2006), "Synthesis of Current Practice on the Design Construction and Maintenance of Porous Friction Courses," Report No. FHWA/TX-06-0-5262-1, Texas A&M Transportation Institute, College Station, TX.

Alvarez, A. E., A. Epps Martin, C. Estakhri, and R. Izzo (2009), "Determination of Volumetric Properties for Permeable Friction Course Mixtures," Journal of Testing and Evaluation, 37(1), 1–10.

Alvarez, A. E., A. Epps Martin, C. Estakhri, and R. Izzo (2010), "Evaluation of Durability Tests for Permeable Friction Course Mixtures," International Journal of Pavement Engineering, 11(1), 49–60.

Alvarez, A. E., E. Mahmoud, A. Epps Martin, E. Masad, and C. Estakhri (2010), "Stone-on-Stone Contact of Permeable Friction Course Mixtures," Materials in Civil Engineering, 22(11), 1129–1138.

Alvarez, A. E., E. Ovalles, and S. Caro (2012), "Assessment of the Effect of Mineral Filler on Asphalt-Aggregate Interfaces Based on Thermodynamic Processes," Construction and Building Materials, 28, 599–606.

Arambula, E., S. Caro, and E. Masad (2010), "Experimental Measurement and Numerical Simulation of Water Vapor Diffusion through Asphalt Pavement Materials," ASCE Journal of Materials in Civil Engineering, 6, 588–598.

Arambula, E., C. K. Estakhri, A. Epps Martin, M. Trevino, A. de Fortier Smit, and J. Prozzi (2012), "Performance and Cost Effectiveness of Permeable Friction Course (PFC) Pavements," Report No. FHWA/TX-12/0-5836-2, Texas A&M Transportation Institute, College Station, TX.

ASTM (2013), "Standard Practice for Moisture Conditioning Compacted Asphalt Mixture Specimens by Using Hydrostatic Pore Pressure," ASTM D7870 / D7870M-13, ASTM International, West Conshohocken, PA.

Bendtsen, H., C. B. Nielsen, J. Raaberg, and R. A. McDonald (2002), "Clogging of Porous Bituminous Surfacings: An Investigation in Copenhagen," Proceedings from the 4th European Symposium on Performance of Bituminous and Hydraulic Materials in Pavements, Nottingham, UK, April.

Bennert, T., and L. A. Cooley (2014), "Evaluate the Contribution of the Mixture Components on the Longevity and Performance of FC-5," Draft Final Report, Center for Advanced Infrastructure and Transportation Rutgers University and Burns Cooley Denis.

Bhasin, A., D. Little, K. Vasconcelos, and E. Masad (2007), "Surface Free Energy to Identify Moisture Sensitivity of Materials for Asphalt Mixes," Transportation Research Record: Journal of the Transportation Research Board, 2001, 37–45.

Birgisson, B., R. Roque, A. Varadhan, T. Thai, and L. Jaiswal (2006), "Evaluation of Thick Open Graded and Bonded Friction Courses for Florida," UF Project No. 4504-968-12, University of Florida, Gainesville, FL.

Brown, J. R. (1973), “Pervious Bitumen—Macadam Surfacings Laid to Reduce Splash and Spray at Stonebridge, Warwickshire,” Report No. LR 563, Transportation Road Research Laboratory, England.

Button, J. W., E. G. Fernando, and D. R. Middleton (2004), “Synthesis of Pavement Issues Related to High-Speed Corridors,” Report No. 0-4756-1, Texas A&M Transportation Institute, College Station, TX.

California Department of Transportation (Caltrans) (2006), “Open Graded Friction Course Usage Guide,” MS # 5, California Department of Transportation, Division of Engineering Services, Sacramento, CA.

Caro, S., E. Masad, A. Bhasin, and D. Little (2010), “Coupled Micromechanical Model of Moisture-Induced Damage in Asphalt Mixtures,” ASCE Journal of Materials in Civil Engineering, 22, 380–388.

Chen, J.-S., Y.-C. Sun, M.-C. Liao, C.-C. Huang, and K.-W. Tsou (2013), “Evaluation of Permeable Friction Course Mixes with Various Binders and Additives,” Journal of Materials in Civil Engineering, 25(5), 573–579.

Chen, X., and B. Huang (2008), “Evaluation of Moisture Damage in Hot Mix Asphalt Using Simple Performance and Superpave Indirect Tensile Tests,” Construction and Building Materials, 22(9), 1950–1962.

Coleri, E., J. T. Harvey, K. Yang, and J. M. Boone (2013), “Micromechanical Investigation of Open-Graded Asphalt Friction Courses’ Rutting Mechanisms,” Construction and Building Materials, 44, 25–34.

Cooley Jr., L. A., R. S. James (2008), “Hot Mix Asphalt Mix Selection Guide for Mississippi,” Report No. FHWA/MS-DOT-RD-08-204, Burns Cooley Dennis, Inc., Jackson, MS.

Cooley Jr., L. A., J. W. Brumfield, R. B. Mallick, W. S. Mogawer, M. Partl, L. Poulikakos, and G. Hicks (2009), “Construction and Maintenance Practices for Permeable Friction Courses,” NCHRP Report 640, National Cooperative Highway Research Program, Washington, DC.

Cui, X., W. Cao, S. Liu, and L. Dong (2009), “On Dynamic Pore Pressure in Moisture Damage of Asphalt Pavement,” Performance Modeling and Evaluation of Pavement Systems and Materials, GeoHunan International Conference, 122–128.

Cui, X. (2010), “Dynamic Numerical Analysis of Antimoisture-Damage Mechanism of Permeable Pavement Base,” Geomechanics, 10(6), 230–236.

European Standard (2006), “Bituminous Mixtures—Material Specifications Part 7: Porous Asphalt,” EN 13108-7, European Committee for Standardization.

FDOT (2003), “Flexible Pavement Condition Survey Handbook,” State Materials Office, Florida Department of Transportation, Gainesville, FL.

FDOT (2008), “Flexible Pavement Design Manual,” Document No. 625-010-002-g, Pavement Management Office, Florida Department of Transportation, Tallahassee, FL.

FDOT (2014a), “Determining the Optimum Asphalt Binder Content of an Open-Graded Friction Course Mixture Using the Pie Plate Method,” FM 5-588.

FDOT (2014b), “Measurement of Water Permeability of Compacted Asphalt Paving Mixtures,” FM 5-565.

FDOT (2014c), “Standard Specifications for Road and Bridge Construction.” Florida Department of Transportation.

FHWA (1990), “Open-Grade Friction Courses FHWA Mix Design Method,” Technical Advisory T 5040.31, Federal Highway Administration, U.S. Department of Transportation, Washington, DC.

Frolov, A. F., V. V. Vasil’eva, E. A. Frolova, and V. N. Ovchinnikova (1983), “Strength and Structure of Asphalt Films,” Chemistry and Technology of Fuels and Oils (Historical Archive), 19(8), 415–419.

Gates, L., E. A. Masad, R. Pyle, and D. Bushee (2011) “Aggregate Image Measurement System 2 (AIMS2): Final Report,” FHWA-HIF-11-030, Highways for LIFE Program Office, Pine Instrument Company.

Glover, C. J., R. R. Davison, C. H. Domke, Y. Ruan, P. Juristyarini, D. B. Knorr, and S. H. Jung (2005), “Development of a New Method For Assessing Asphalt Binder Durability with Field Validation,” FHWA/TX-05/1872-2, Texas A&M Transportation Institute, College Station, TX.

Gunaratne, M., and Y. Mejias de Pernia (2014), “Determination of the Optimum Binder Content of Open-Graded Friction Course (OGFC) Mixtures Using Digital Image Processing,” Final Report, Contract No. BDV25, TWO #820-1, University of South Florida, Tampa, FL.

Hernández, S. (2013), “Influencia De La Humedad Relativa en el Comportamiento y el Deterioro De Matrices Asfálticas Finas,” Universidad de los Andes, Bogotá, Colombia.

Highways Agency (1999), “Design Manual 71 for Roads and Bridges, Volume 7: Pavement Design and Maintenance Bituminous Surfacing Materials and Techniques,” The Scottish Office Development Department, The Welsh Office Y Swyddfa Gymreig, The Department of the Environment for Northern Ireland.

Huber, G. (2000), “Performance Survey on Open-Graded Friction Course Mixes,” Synthesis of Highway Practice 284, Transportation Research Board, National Research Council, Washington, DC.

Huurman, M., and L. T. Mo (2007), “Lifetime Optimization Tool: User’s Guide,” Report 7-07-170-5, Delft University of Technology, Laboratory of Road and Railway Engineering, The Netherlands.

Huurman, M., L. T. Mo, and M. F. Woldekidan (2010a), “Mechanistic Design of Silent Asphalt Mixtures and Its Validation,” Association of Asphalt Paving Technologists, 79, 365–402.

Huurman, M., L. T. Mo, and M. F. Woldekidan (2010b), “Porous Asphalt Ravelling in Cold Weather Conditions,” Pavement Research and Technology, 3, 110–118.

Isenring, T., H. Koster, and I. Scazziga (1990), “Experiences with Porous Asphalt in Switzerland,” Transportation Research Record: Journal of the Transportation Research Board, 1265, 41–53.

Kandhal, P. S. (2002), "Design, Construction, and Maintenance of Open-Graded Asphalt Friction Courses," Information Series 115, National Asphalt Pavement Association.

Kandhal, P. S. (2004), "'Quiet Pavements': Asphalt Pavements Mitigate Tire/Pavement Noise," Hot Mix Asphalt Technology, 9(2), 22–31.

Kearfott, P., M. Barrett, and J. F. Malina, Jr. (2005), "Stormwater Quality Documentation of Roadside Shoulders Borrow Ditches," CRWR Online Report 05-02, Center for Research in Water Resources, The University of Texas, Austin, TX.

Khalid, H., and F. Pérez (1996), "Performance Assessment of Spanish and British Porous Asphalts," In Performance and Durability of Bituminous Materials, E&FN Spon, London, pp. 137–157.

Kim, Y., D. H. Allen, and D. Little (2005), "Damage-Induced Modeling of Asphalt Mixtures through Computational Micromechanics and Cohesive Zone Fracture," ASCE Journal of Materials in Civil Engineering, 17, 477–484.

Kim, Y., and J. Lutiff (2008), "Computational Micromechanics Modeling For Damage-Induced Behavior of Asphalt Mixtures Considering Viscoelasticity and Cohesive Zone Fracture," Pavement and Materials, 17–25.

Kim, Y. R., B. Underwood, M. Sakhaeifar, N. Jackson, and J. Puccinelli (2011), "LTPP Computed Parameter: Dynamic Modulus," FHWA-HRT-10-035, FHWA, Turner-Fairbank Highway Research Center.

Kringos, N., A. Scarpas, and A. Bondt (2008), "Determination of Moisture Susceptibility of Mastic-Stone Bond Strength and Comparison to Thermodynamical Properties," Journal of the Association of Asphalt Paving Technologists, 77, 435–471.

Little, D. N., and A. Bhasin (2006), "Using Surface Energy Measurements to Select Materials for Asphalt Pavement," NCHRP Web-Only Document 104, Transportation Research Board of the National Academies.

Little, D. N., and D. R. Jones (2003), "Chemical and Mechanical Processes of Moisture Damage in Hot-Mix Asphalt Pavements," In Moisture Sensitivity of Asphalt Pavements: A National Seminar," San Diego, CA, Feb 4–6, pp. 37–70.

LTPP (2015), "Traffic MEPDG Axle Distribution—States AL to IL," LTPP InfoPave data.

LTPPBind (2015), LTPPBind Version 2.1, http://www.fhwa.dot.gov/research/tfhrc/programs/infrastructure/pavements/ltpp/install.cfm.

Mallick, R., P. Kandhal, A. Cooley, and D. Watson (2000), "Design, Construction and Performance of New Generation Open-Graded Friction Courses," National Center for Asphalt Technology Report 00-01, NCAT, Auburn, AL.

Masad, E. A. (2005) "Aggregate Imaging System (AIMS): Basics and Applications," FHWA/TX-05/5-1707-01-1, Texas A&M Transportation Institute, College Station, TX.

Masad, E., J. E. Howson, A. Bhasin, S. Caro, and D. Little (2010), "Relationship of Ideal Work of Fracture to Practical Work of Fracture: Background and Experimental Results," Journal of the Association of Asphalt Paving Technologists, 79, 181–218.

Milne, T. I., M. Huurman, M. F. C. Van de Men, J. Jenkins, A. Scarpas, and C. Kasbergen (2004), "Towards Mechanistic Behaviour of Flexible Road Surfacing Seals Using a Prototype FEM Model," Proceedings of the 8th Conference on Asphalt Pavements for Southern Africa (CAPSA'04).

Mitchell, J. K., and K. Soga (2005), *Fundamentals of Soil Behavior*, 3rd ed., John Wiley & Sons, Hoboken, NJ.

Mo, L. T., M. Huurman, S. P. Wu, and A. A. A. Molenaar (2007), "Investigation into Stress States in Porous Asphalt Concrete on the Basis of FE-Modelling," Finite Elements in Analysis and Design, 43, 333–343.

Mo, L. T., M. Huurman, S. P. Wu, and A. A. A. Molenaar (2008), "2D and 3D Meso-Scale Finite Element Models for Ravelling Analysis of Porous Asphalt Concrete," Finite Elements in Analysis and Design, 44, 186–196.

Mo, L. T., M. Huurman, S. P. Wu, and A. A. A. Molenaar (2011), "Bitumen–Stone Adhesive Zone Damage Model for the Meso-Mechanical Mixture Design of Ravelling Resistant Porous Asphalt Concrete," International Journal of Fatigue, 33, 1490–1503.

Mo, L. T., M. Huurman, S. P. Wu, and A. A. A. Molenaar (2014), "Mortar Fatigue Model for Meso-Mechanistic Mixture Design of Ravelling Resistant Porous Asphalt Concrete," Materials and Structures, 47, 947–961.

Mo, L. T., M. Huurman, S. Wu, M. F. Woldekidan, and A. Molenaar, A. (2010), "Investigation into Material Optimization and Development for Improved Ravelling Resistant Porous Asphalt Concrete," Materials and Design, 31, 3194–3206.

Molenaar, J. M. M., and A. A. A. Molenaar (2000), "An Investigation into the Contribution of the Bituminous Binder to the Resistance to Raveling of Porous Asphalt," 2nd Eurasphalt & Eurobitume Congress, Barcelona, Spain, pp. 500–508.

Moore, L., R. Hicks, and D. Rogge (2001), "Design, Construction, and Maintenance Guidelines for Porous Asphalt Pavements," Transportation Research Record: Journal of the Transportation Research Board, 1778, 91–99.

New Jersey Department of Transportation (NJDOT) (2007), "Standard Specifications for Road and Bridge Construction," Retrieved March 2016 from: http://www.state.nj.us/transportation/eng/specs/2007/spec900.shtm#s90203+D20

Nicholls, J. C., and I. G. Carswell (2001), "The Design of Porous Asphalt Mixtures to Performance-Related Criteria," TRL Report 497, TRL, United Kingdom.

Nielsen, C. B. (2006), "Ravelling of Porous Pavements—Experimental Procedures (Draft)," Danish Road Institute, Hedehusene, Denmark.

Nielsen, C. B., J. Raaberg, and E. Nielsen (2005), "Holdbarhed af Drænasfalt," Rapport 139, Vejteknisk Institut, Vejdirektoratet.

Ongel, A., J. Harvey, and E. Kohler (2007), "State of the Practice in 2006 for Open-Graded Asphalt Mix Design," Report No. UCPRC-TM-2008-07, University of California Pavement Research Center, December.

Ranieri, V. (2002), "Runoff Control in Porous Pavements," Transportation Research Record: Journal of the Transportation Research Board, 1789, 46–55.

Rogge, D. (2002), "Development of Maintenance Practices for Oregon F-Mix," Report FHWA-OR-RD-02-09, Federal Highway Administration, U.S. Department of Transportation, Washington, DC.

Roque, R., C. Koh, Y. Chen, X. Sun, and G. Lopp (2009), "Introduction of Fracture Resistance to the Design and Evaluation of Open-Graded Friction Courses in Florida," Final Report Submitted to Florida Department of Transportation, Tallahassee, FL, July.

Rowe, G. M., G. King, and M. Anderson (2014), "The Influence of Binder Rheology on the Cracking of Asphalt Mixes in Airport and Highway Projects," Journal of Testing & Evaluation, 42(5), 1063–1072.

Ruiz, A., R. Alberola, F. Pérez, and B. Sanchez (1990), "Porous Asphalt Mixtures in Spain," Transportation Research Record: Journal of the Transportation Research Board, 1265, 87–94.

Rummel, F. (1991), "Physical Properties of the Rock in the Granitic Section of Borehole GPK1," Geothern, Sci. and Tech, 3, 199–216.

Sandberg, U., and Y. Masuyama (2005), "Japanese Machines for Laying and Cleaning Double-Layer Porous Asphalt—Observations from a Study Tour," Report Produced by Direction of Rijkswaterstaat-DWW, Co-Sponsored by Chalmers University of Technology DWW/IPG, Order Number 64520946.

Schram, S. (2012), "Ranking of HMA Moisture Sensitivity Tests in Iowa," Report RB00-012, FHWA, Iowa Department of Transportation.

Shaowen, D. U., and L. I. Shanshan (2011), "The Raveling Characteristic of Porous Asphalt Mixture," Conference ICTE 2011, 1880–1885. doi: 10.1061/41184(419)310.

Stanard, C., R. Candaele, R. Charbeneau, and M. Barrett (2007), "State of Practice: Permeable Friction Courses", Report No. FHWA/TX-08/0-5220-1, Center for Transportation Research, The University of Texas at Austin, Austin, TX.

Stotz, G., and K. Krauth (1994), "The Pollution of Effluents from Pervious Pavements of an Experimental Highway Section: First Results," The Science of the Total Environment, 146/147, 465–470.

Tang, Y., X. Zhang, D. Zhang, G. Zhao, and X. Guan (2013), "Frictional Order Sliding Mode Controller Design for Antilock Braking Systems," Neurocomputing, 111, 122–130.

Tappeiner, W. (1993), "Open-Graded Asphalt Friction Course," Information Series 115, National Asphalt Pavement Association, Lanham, MD.

Thomsen, S. N., J. Kragh, E. Nielsen, H. Bendtsen, and B. Andersen (2005), "Noise Reducing Pavements—State of the Art in Denmark," Report 141, Danish Road Directorate, Ministry of Transport, Denmark.

TxDOT (2004), "Standard Specifications for Construction and Maintenance of Highways, Streets, and Bridges—Special Specification 3269: Permeable Friction Course (PFC)."

TxDOT (2009), "Permeability or Water Flow of Hot Mix Asphalt," Tex-246-F, Construction Division.

Van der Zwan, J. T., T. Goeman, H. Gruis, J. H. Swart, and R. H. Oldenburger (1990), "Porous Asphalt Wearing Courses in the Netherlands: State of the Art Review," Transportation Research Record: Journal of the Transportation Research Board, 1265, 95–110.

Van der Zwan, J. T. (2011), "Developing Porous Asphalt for Freeways in the Netherlands: Reducing Noise, Improving Safety, Increasing Service Life," Transportation Research News, 272, January–February.

Van Heystraeten, G., and C. Moraux (1990), "Ten Years' Experience of Porous Asphalt in Belgium," Transportation Research Record: Journal of the Transportation Research Board, 1265, 34–40.

Voskuilen, J. (2005), "Experiences with Porous Asphalt in the Netherlands," EPFL Journee de Lavoc, Lausanne, Switzerland.

Watson, D., A. Johnson, and D. Jared (1998), "Georgia Department of Transportation's Progress in Open-Graded Friction Course Development," Transportation Research Record: Journal of the Transportation Research Board, 1616, 30–33.

Watson, D. E., K. A. Moore, K. Williams, and L. A. Cooley (2003), "Refinement of New-Generation Open-Graded Friction Course Mix Design," Transportation Research Record: Journal of the Transportation Research Board, 1832, 78–85.

Weldegiorgis, M. T., and R. A. Tarefder (2015), "Towards a Mechanistic Understanding of Moisture Damage in Asphalt Concrete," ASCE Journal of Materials in Civil Engineering, 27(3).

West, R., D. Timm, J. R. Willis, R. B. Powell, N. Tran, D. Watson, M. Sakhaeifar, M. Robbins, R. Brown, A. Vargas-Nordcbeck, F. L. Villacorta, X. Guo, and J. Nelson (2012), "Phase IV NCAT Pavement Test Track Findings," NCAT Report 12-10, National Center for Asphalt Technology, Auburn University, Auburn, AL.

Yildirim, Y., T. Dossey, K. Fults, M. Tahmoressi, and M. Trevino (2007), "Winter Maintenance Issues Associated with New Generation of Open-Graded Friction Courses," Report FHWA/TX-08-0-4834-2, Center for Transportation Research, Austin, TX.

Yin, F., E. Arambula, R. Lytton, A. Epps Martin, and L. Garcia-Cucalon (2014), "Novel Method for Moisture Susceptibility and Rutting Evaluation Using Hamburg Wheel Tracking Test," Transportation Research Record: Journal of the Transportation Research Board, 2446, 1–7.

Zhang, L., G. P. Ong, and T. F. Fwa (2013), "Evaluating the Influence of Aggregate Size on Permeability of Porous Pavements Using Finite Volume Simulation," International Journal of Pavement Research and Technology, 6(5), 520–526.

Zofka, A., M. Maliszewski, and A. Bernier (2014), "Alternative Moisture Sensitivity Test," 9th International Conference of Environmental Engineering, Vilnius, Lithuania, May 22–23.

APPENDIX A. REVIEW OF QC/QA DATA ON FIU PROJECTS

A.1. Mix Design Data for FC-5 Projects Monitored in FIU Study

Group	Contractor	Mix Design	Mixing Temperature (°F)	Compaction Temperature (°F)	19.0mm (3/4") 100%*	12.5mm (1/2") 85% - 100%*	9.5mm (3/8") 55% - 75%*	4.75mm (#4) 15% - 25%*	2.36mm (#8) 5% - 10%*	1.18mm (#16)	600um (#30)	300um (#50)	150um (#100)	75um (#200) 2% - 4%*	Gsb	Total Binder Content (%)	Binder Type
Good	Elmo Greer	SPM 06-4749C	320	320	100	87	62	21	10	6	5	4	3	2.1	2.411	5.8	PG 76-22
Good	Asphalt Group	SPM 07-5654A	320	320	100	90	66	24	10	8	7	6	5	3.5	2.415	5.8	PG 76-22
Good	Dickerson	SPM 08-6360B	320		100	92	71	25	10	8	6	5	3	2.3	2.416	5.7	PG 76-22
Good	Community	SP 05-3979A	320	310	100	90	66	24	10	8	7	6	5	3.5	2.415	7.1	ARB-12
Good	Community	SP 05-3979A	320	310	100	90	66	24	10	8	7	6	5	3.5	2.415	7.1	ARB-12
Good	East Coast	SP 03-2484A	320		100	86	67	25	10	9	8	6	5	4.0		7.1	ARB-12
Bad	APAC	SPM 05-3987A	320	315	100	93	69	23	9	5	4	3	3	3.0	2.411	6.7	PG 76-22
Bad		SPM 05-3987B	320	315	100	93	69	23	9	5	4	3	3	3.0	2.411	6.0	PG 76-22
Bad	East Coast	SP 03-2484A	320		100	86	67	25	10	9	8	6	5	4.0		7.1	ARB-12
Bad	Hardrives	SP 04-3684A	320	320	100	86	70	24	8	6	5	4	3	2.8	2.345	6.8	ARB-12
	Sieve Size				19.0mm (3/4")	12.5mm (1/2")	9.5mm (3/8")	4.75mm (#4)		2mm (#10)	425 µm (#40)	180 µm (#80)		#200	Sp. Gr.		
Bad	Community	QA 01-10128B	320		100	90	70	24		10	7	6		3.5	2.415	7.10/6.34**	AC-30
Bad	Hardrives	QA 02-10412A	320		100	86	67	25		8	7	4		3.3		7.10/6.34**	RA-3000/PG 76-22

* allowable gradation design range for specified sieve size

** Total asphalt rubber (GTR content of 0.76%)/Optimum asphalt content

A.2. Projects Considered To Have Good Performance

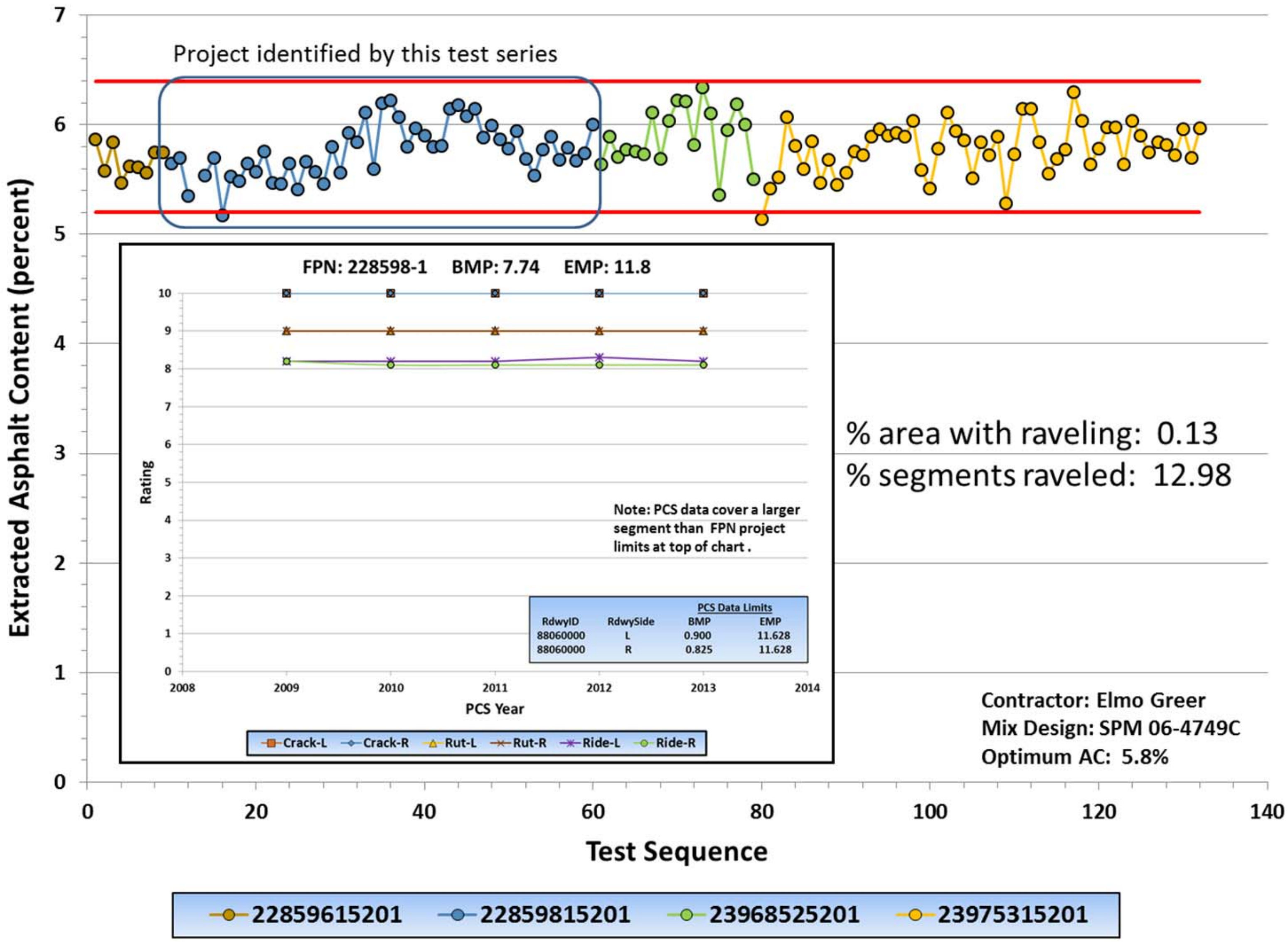

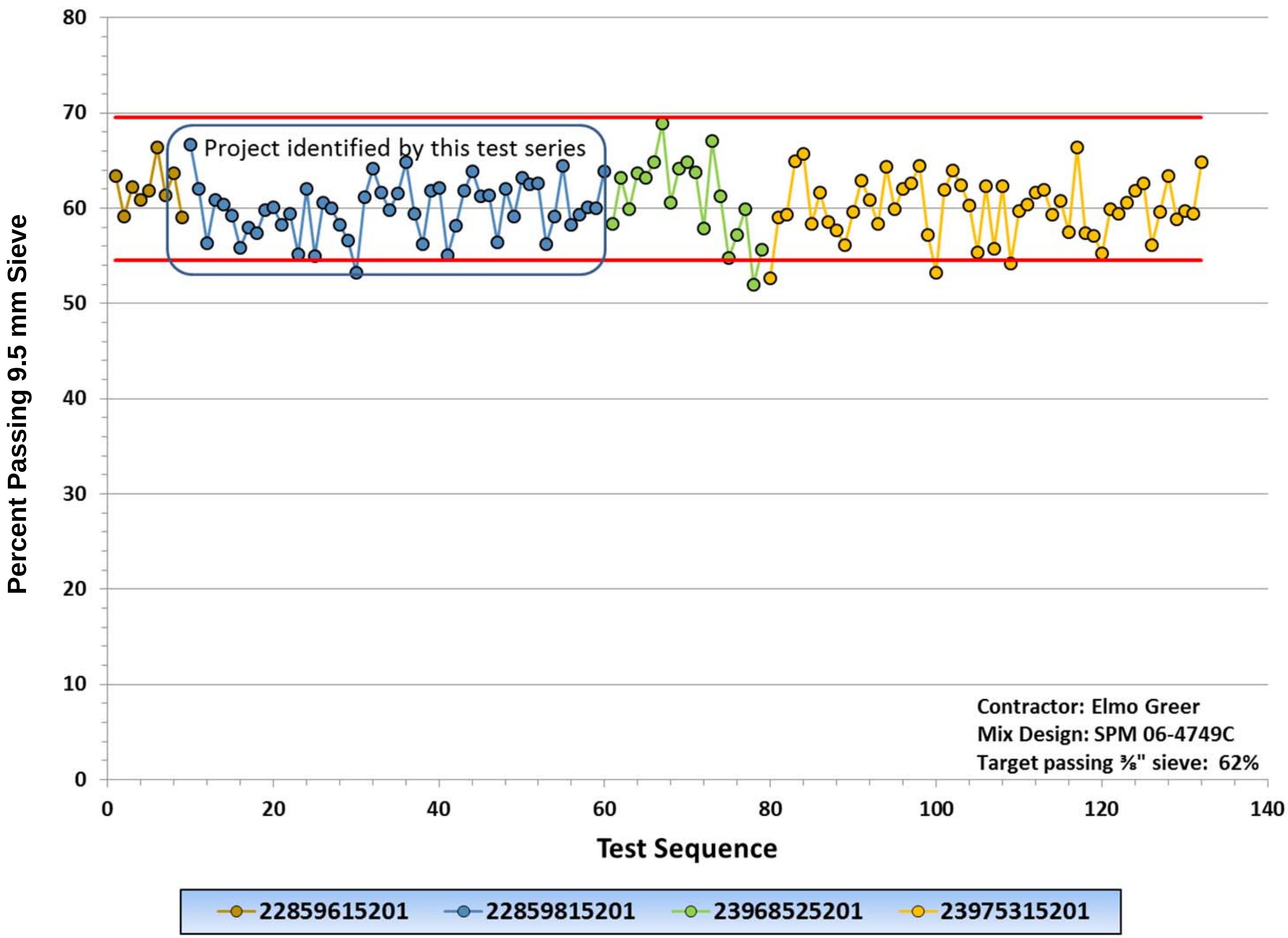

Percent Passing 9.5 mm Sieve
80
70
60
50
40
30
20
10
0
0
20
40
60
80
100
120
140
Test Sequence
Project identified by this test series
Contractor: Elmo Greer
Mix Design: SPM 06-4749C
Target passing ⅜" sieve: 62%
22859615201
22859815201
23968525201
23975315201

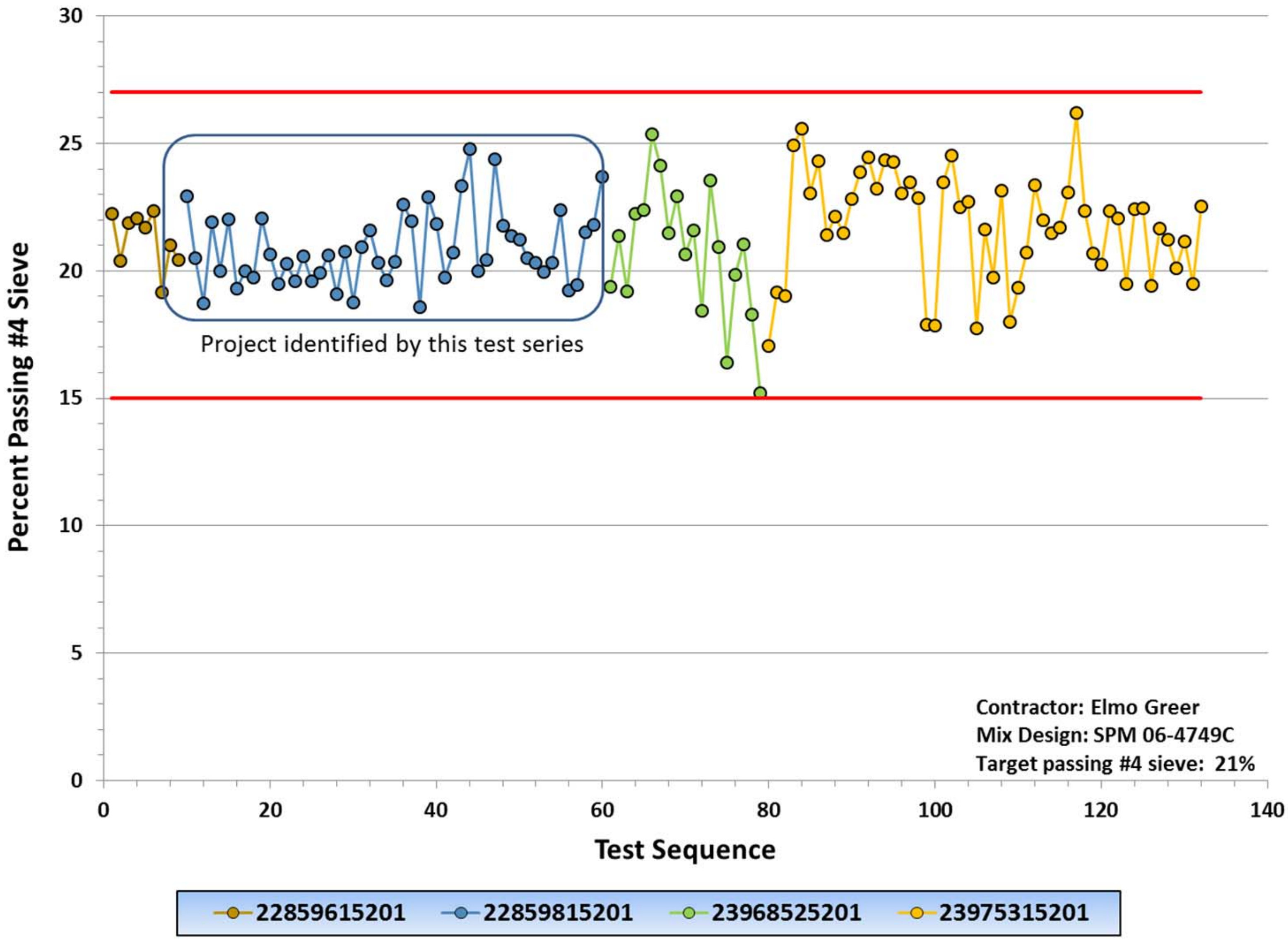
Percent Passing #4 Sieve
Test Sequence
Project identified by this test series
Contractor: Elmo Greer
Mix Design: SPM 06-4749C
Target passing #4 sieve: 21%
22859615201
22859815201
23968525201
23975315201

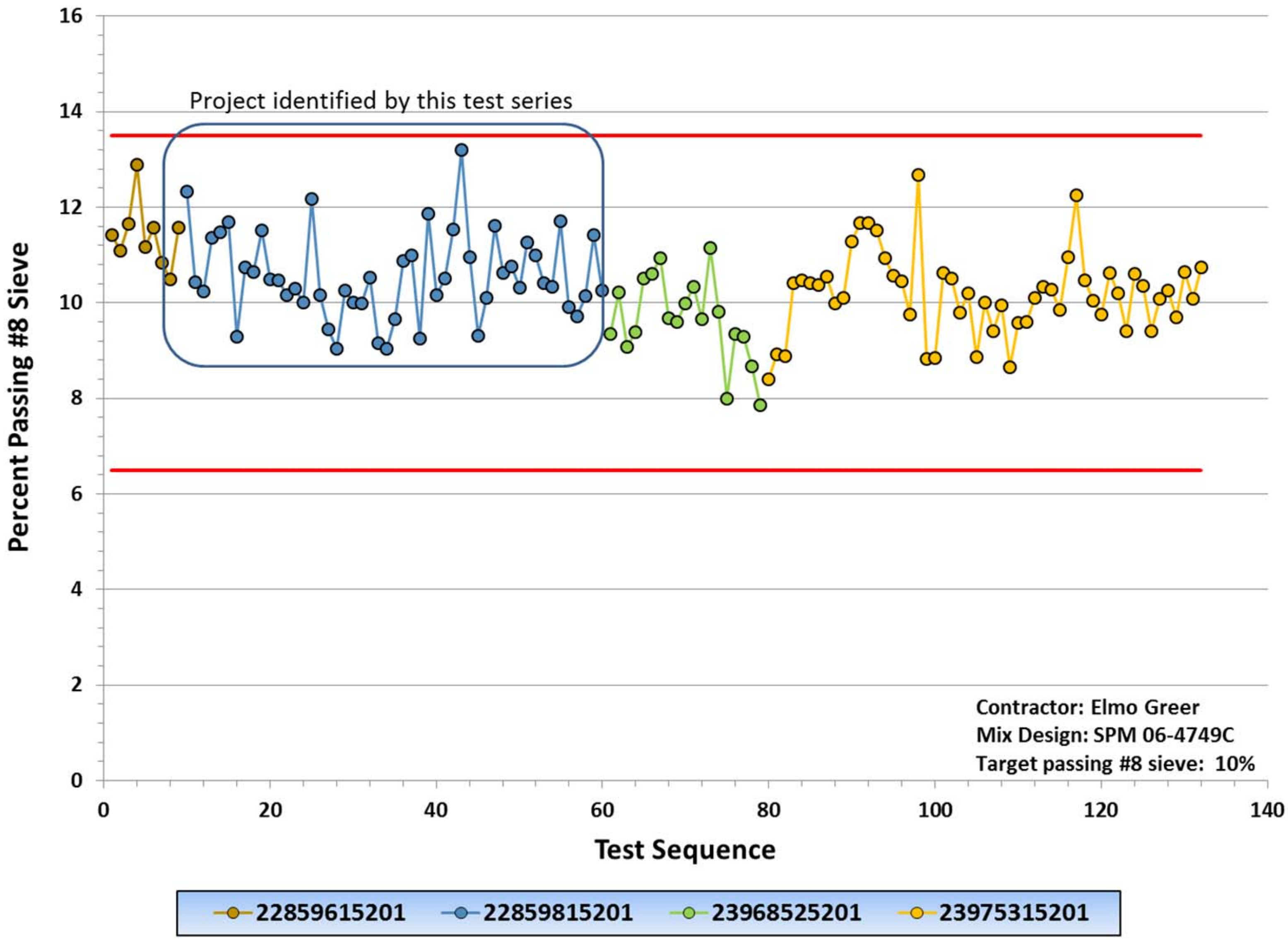

Project identified by this test series
Percent Passing #8 Sieve
Test Sequence
Contractor: Elmo Greer
Mix Design: SPM 06-4749C
Target passing #8 sieve: 10%
22859615201
22859815201
23968525201
23975315201

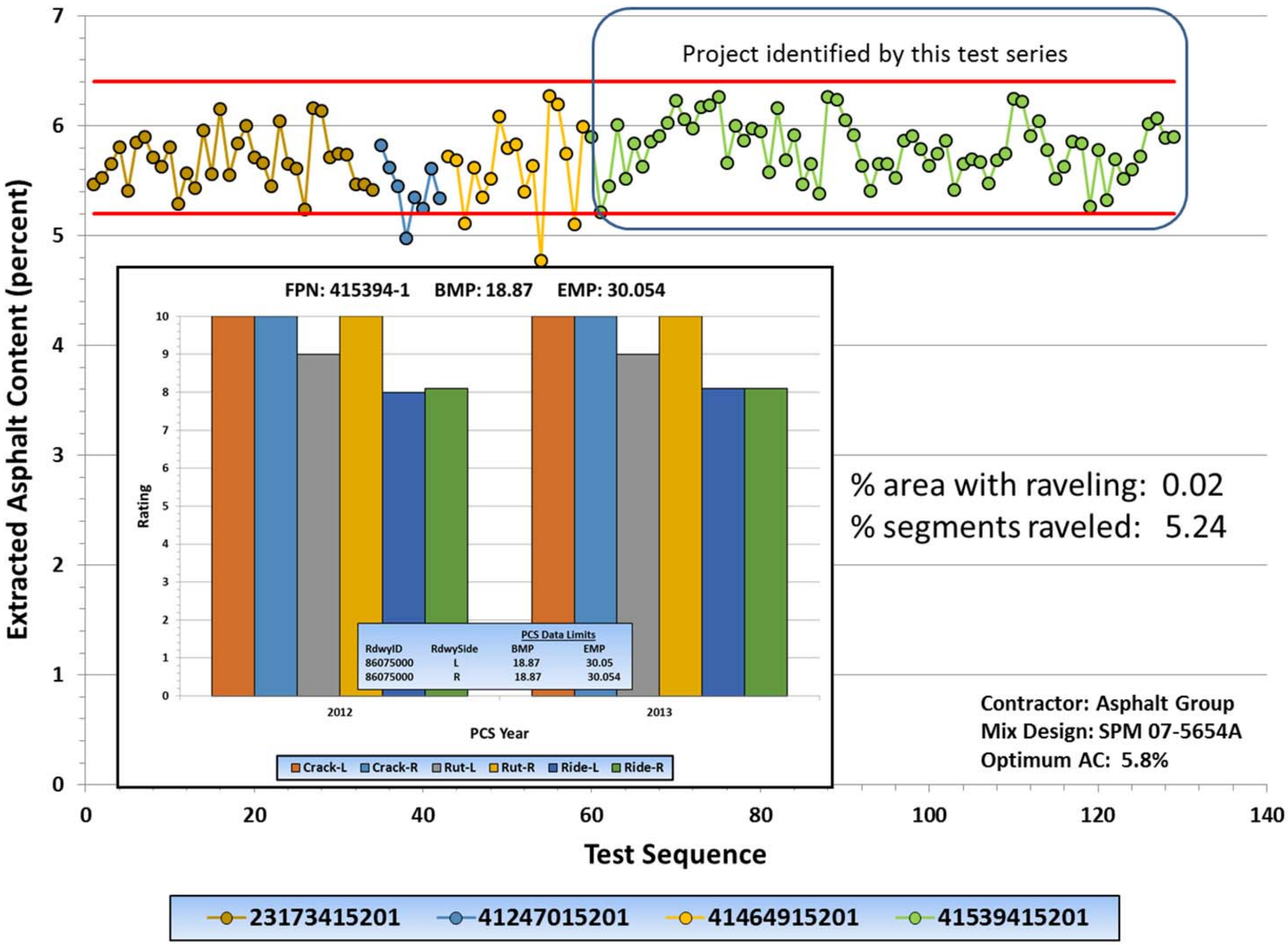

Project identified by this test series
Extracted Asphalt Content (percent)
Test Sequence
FPN: 415394-1 BMP: 18.87 EMP: 30.054
Rating
PCS Year
2012
2013
PCS Data Limits
RdwyID RdwySide BMP EMP
86075000 L 18.87 30.05
86075000 R 18.87 30.054
Crack-L Crack-R Rut-L Rut-R Ride-L Ride-R
% area with raveling: 0.02
% segments raveled: 5.24
Contractor: Asphalt Group
Mix Design: SPM 07-5654A
Optimum AC: 5.8%
23173415201
41247015201
41464915201
41539415201

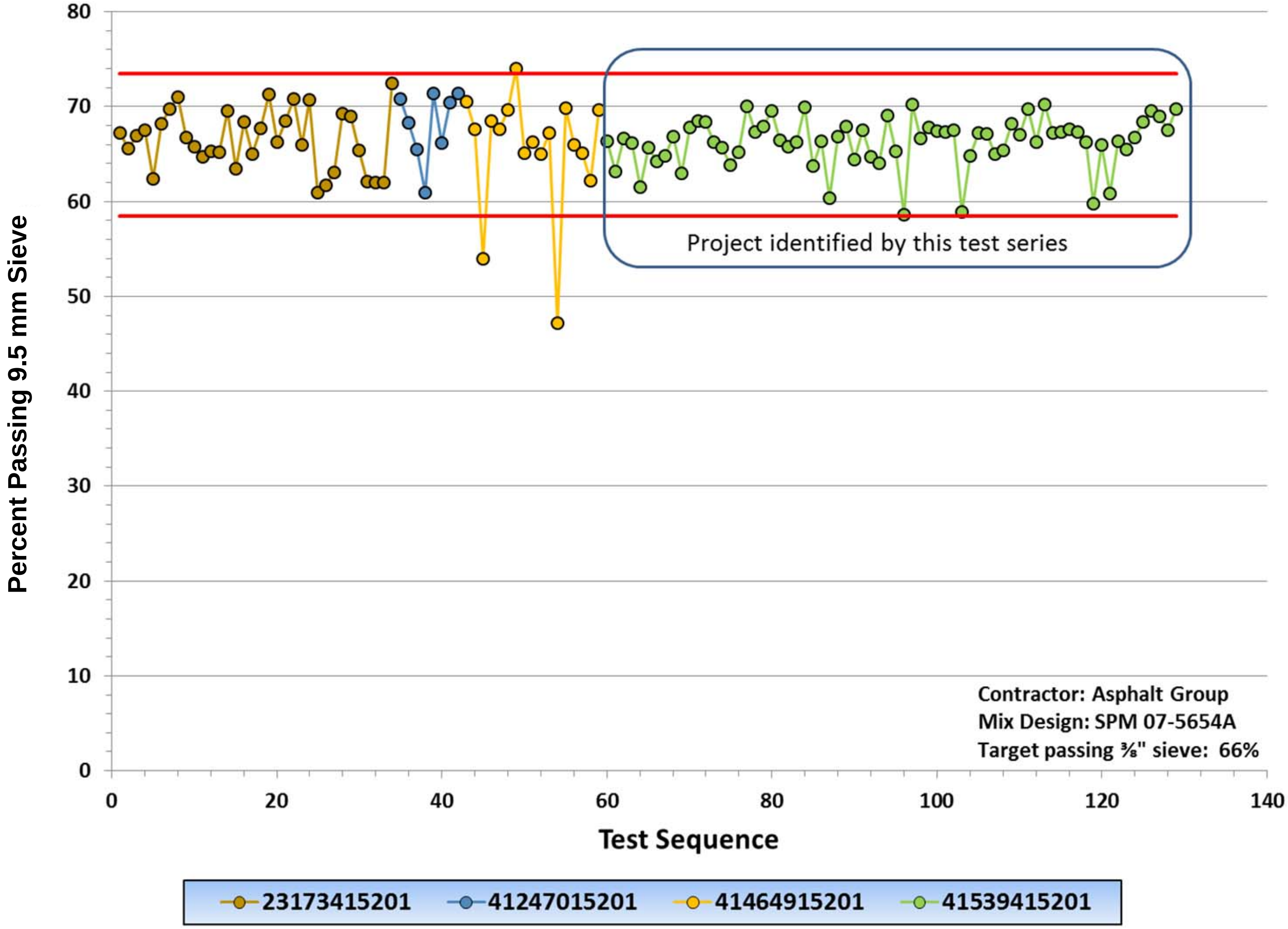

Percent Passing 9.5 mm Sieve
80
70
60
50
40
30
20
10
0
0
20
40
60
80
100
120
140
Test Sequence
Project identified by this test series
Contractor: Asphalt Group
Mix Design: SPM 07-5654A
Target passing ⅜" sieve: 66%
23173415201
41247015201
41464915201
41539415201

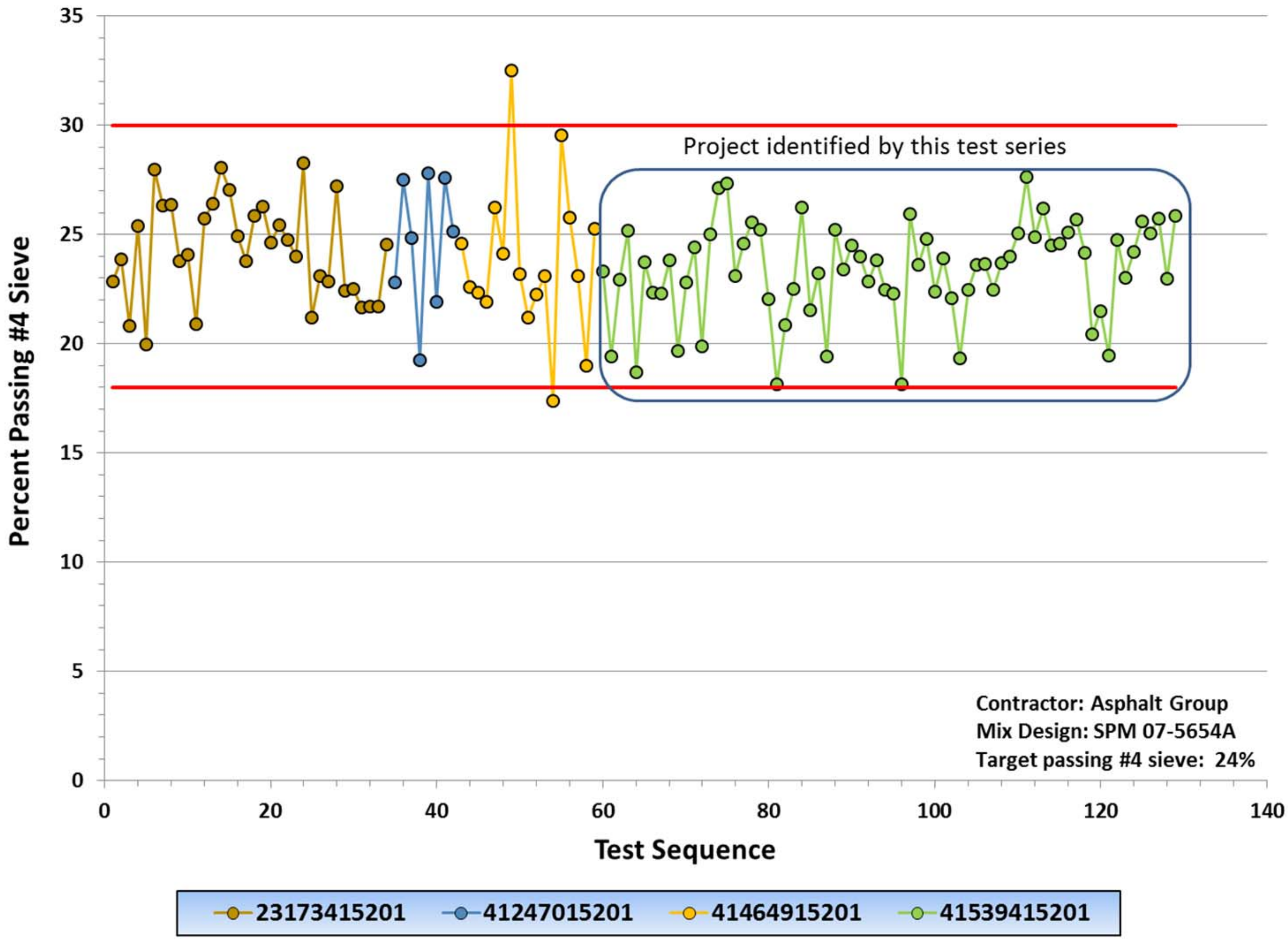
Percent Passing #4 Sieve
Test Sequence
Project identified by this test series
Contractor: Asphalt Group
Mix Design: SPM 07-5654A
Target passing #4 sieve: 24%
23173415201
41247015201
41464915201
41539415201
0
5
10
15
20
25
30
35
0
20
40
60
80
100
120
140

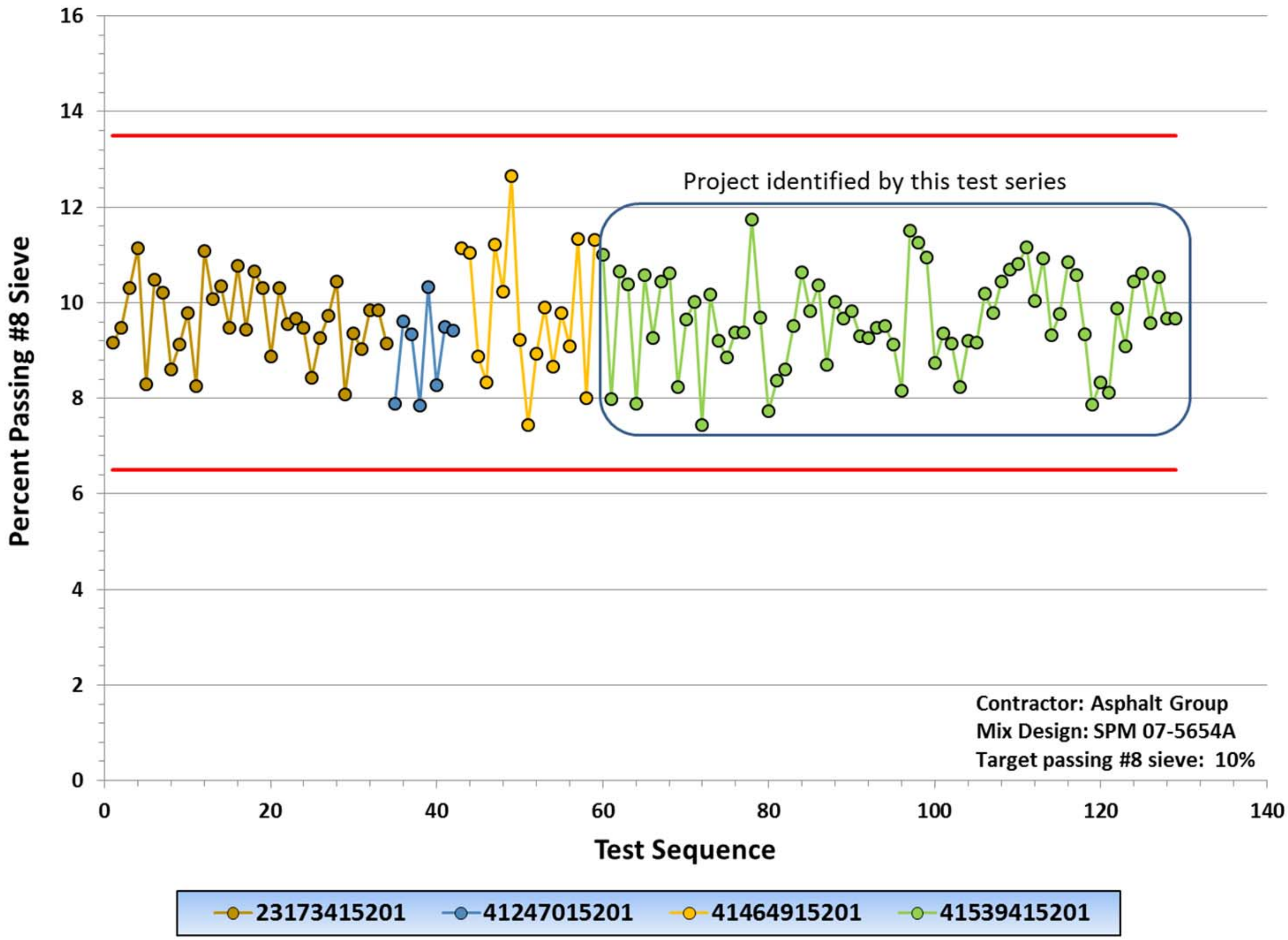

Project identified by this test series
Percent Passing #8 Sieve
Test Sequence
Contractor: Asphalt Group
Mix Design: SPM 07-5654A
Target passing #8 sieve: 10%
23173415201
41247015201
41464915201
41539415201

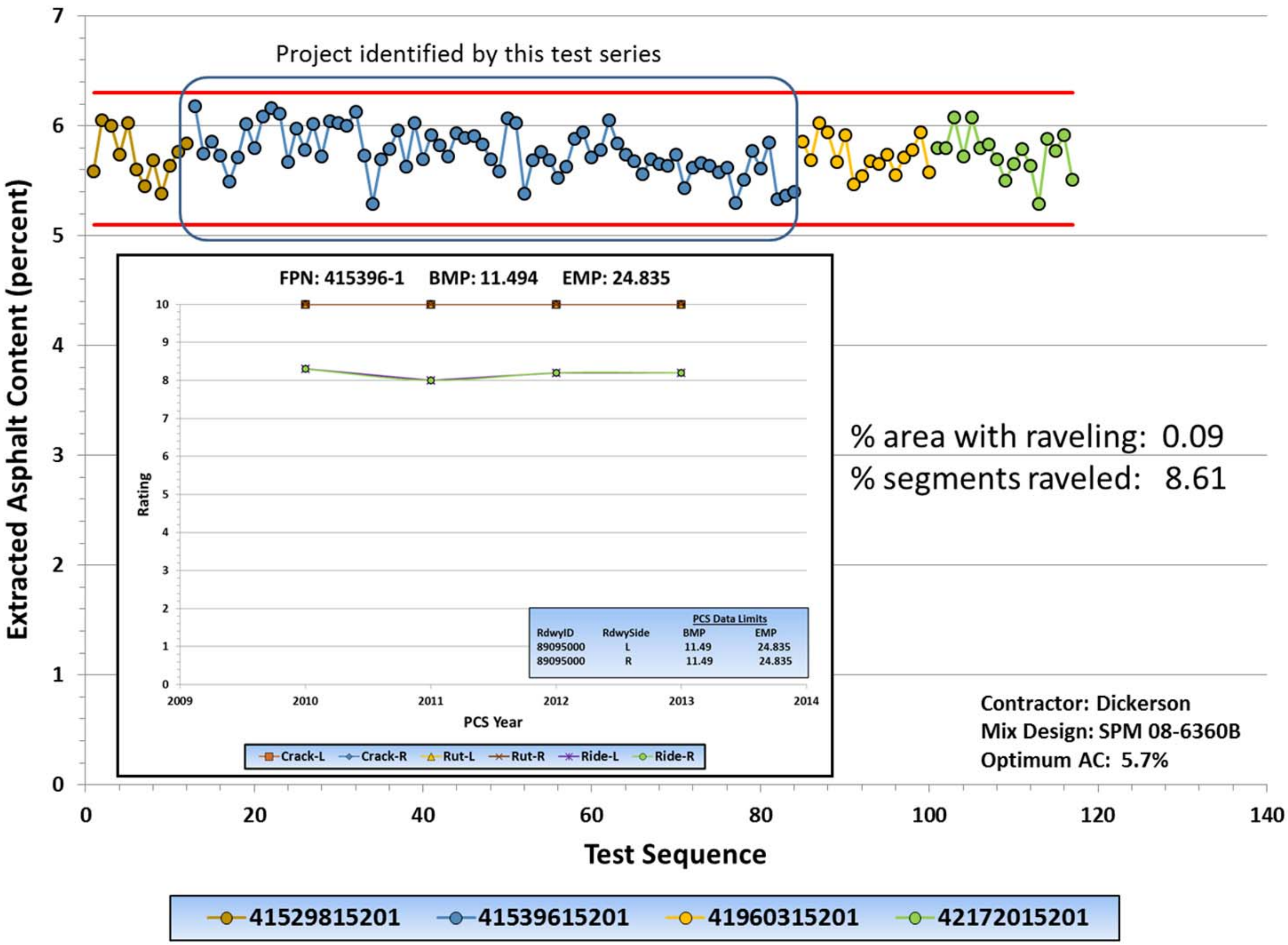

Project identified by this test series
FPN: 415396-1 BMP: 11.494 EMP: 24.835
Rating
PCS Year
PCS Data Limits
RdwyID RdwySide BMP EMP
89095000 L 11.49 24.835
89095000 R 11.49 24.835
Crack-L Crack-R Rut-L Rut-R Ride-L Ride-R
% area with raveling: 0.09
% segments raveled: 8.61
Contractor: Dickerson
Mix Design: SPM 08-6360B
Optimum AC: 5.7%
Extracted Asphalt Content (percent)
Test Sequence
41529815201 41539615201 41960315201 42172015201

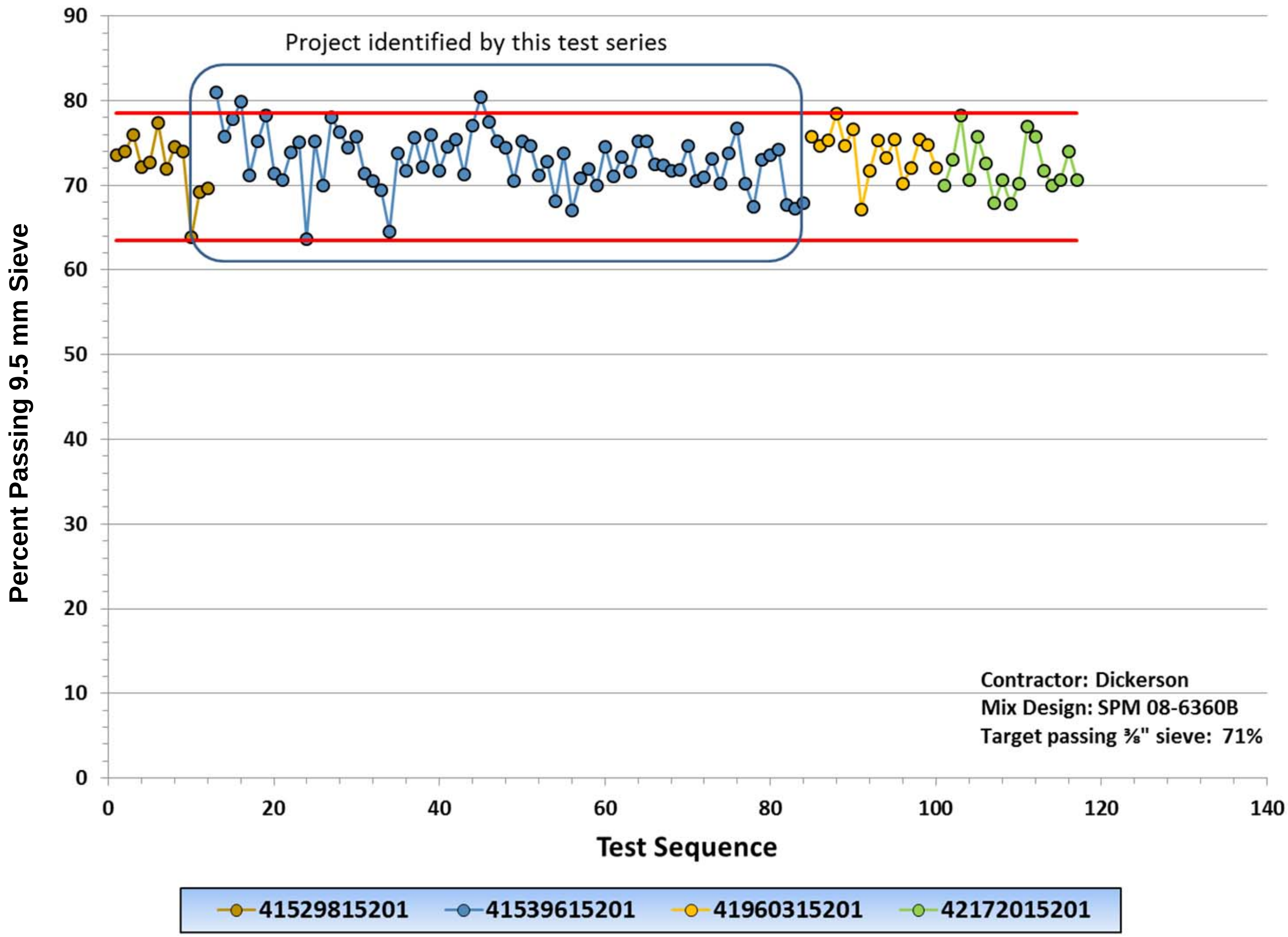

Project identified by this test series
Percent Passing 9.5 mm Sieve
Test Sequence
Contractor: Dickerson
Mix Design: SPM 08-6360B
Target passing ⅜" sieve: 71%
41529815201
41539615201
41960315201
42172015201

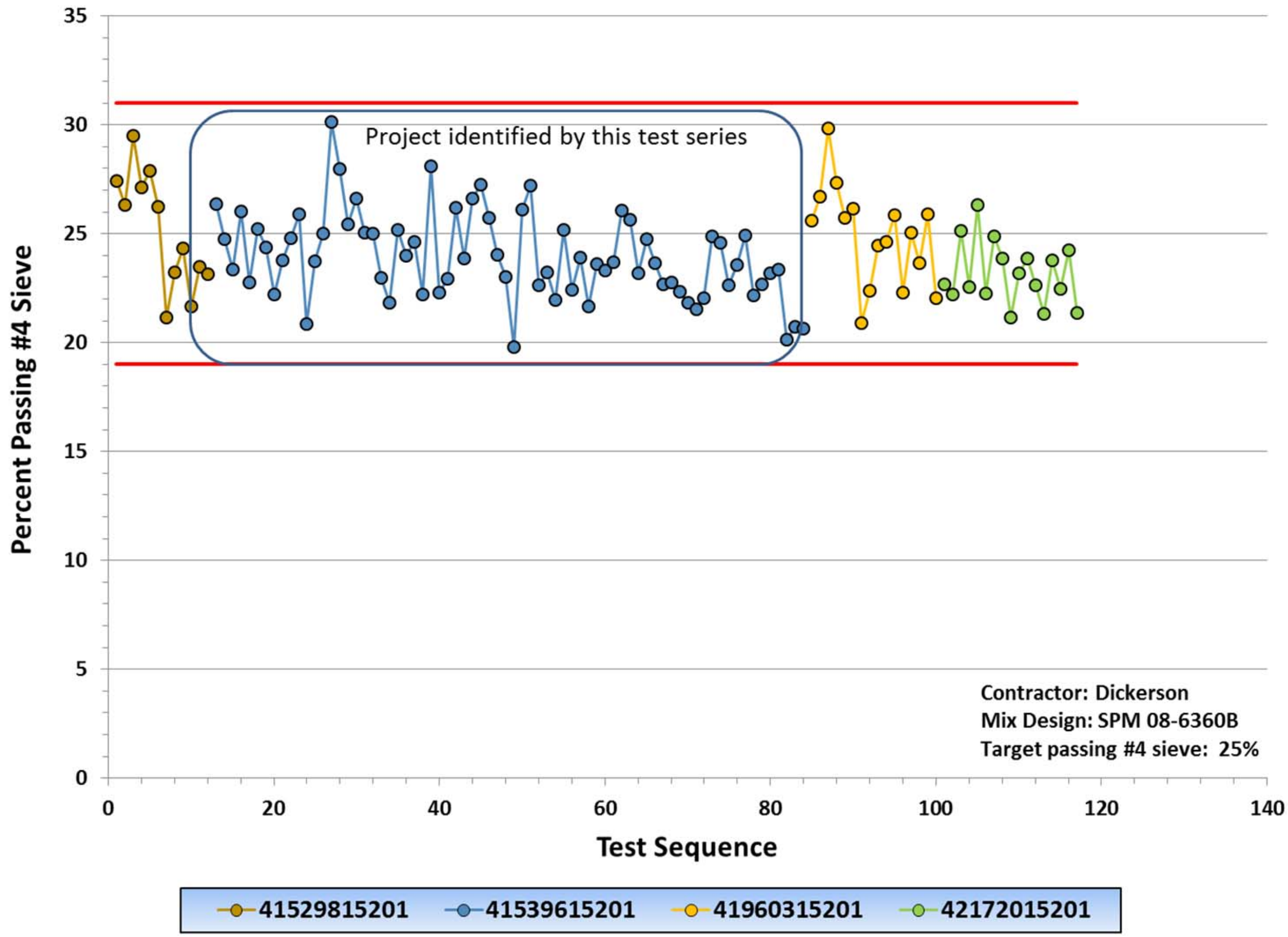

35
30
25
20
15
10
5
0
Percent Passing #4 Sieve
0
20
40
60
80
100
120
140
Test Sequence
Project identified by this test series
Contractor: Dickerson
Mix Design: SPM 08-6360B
Target passing #4 sieve: 25%
41529815201
41539615201
41960315201
42172015201

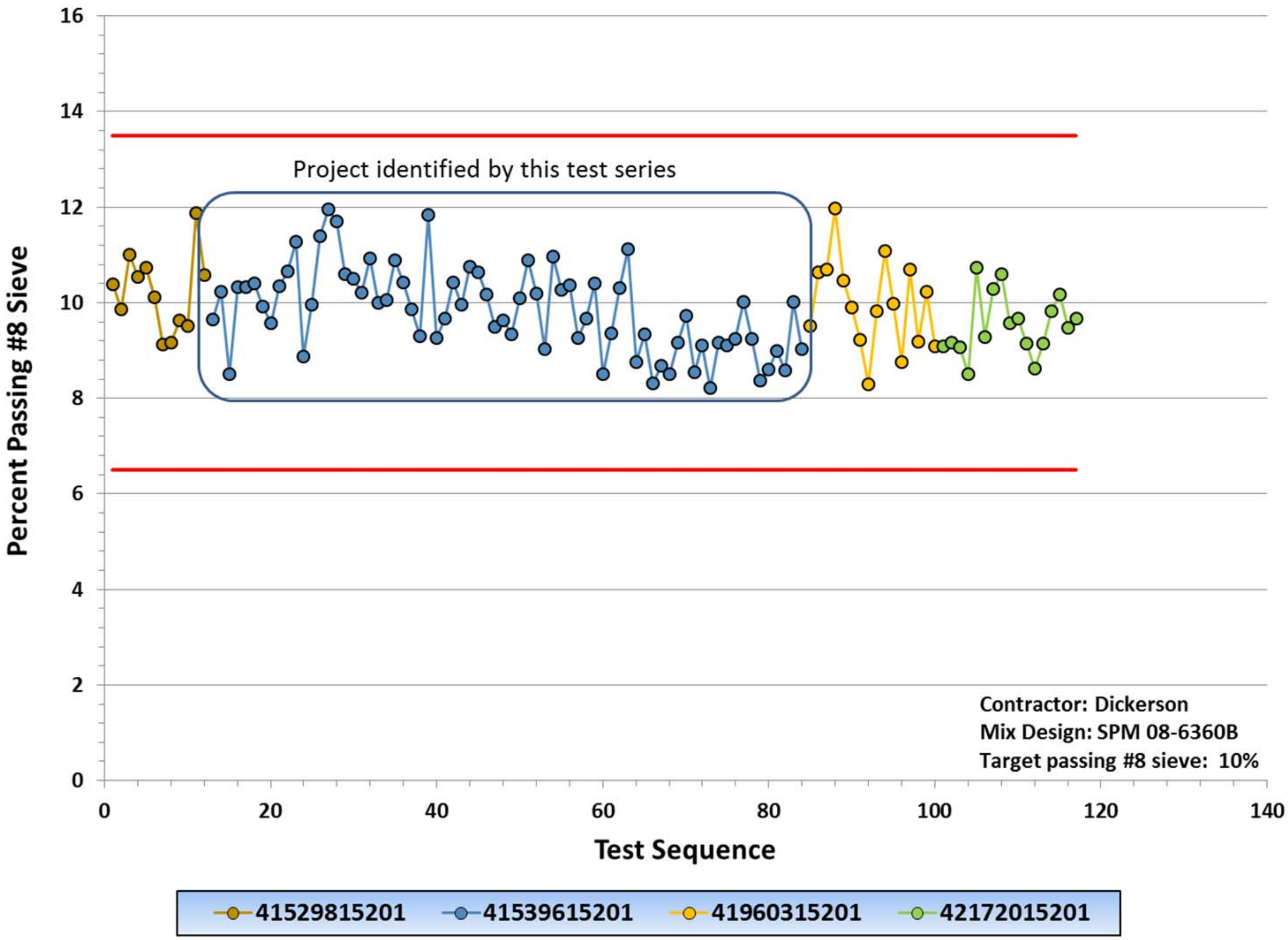

Project identified by this test series
Percent Passing #8 Sieve
Test Sequence
16
14
12
10
8
6
4
2
0
0
20
40
60
80
100
120
140
Contractor: Dickerson
Mix Design: SPM 08-6360B
Target passing #8 sieve: 10%
41529815201
41539615201
41960315201
42172015201

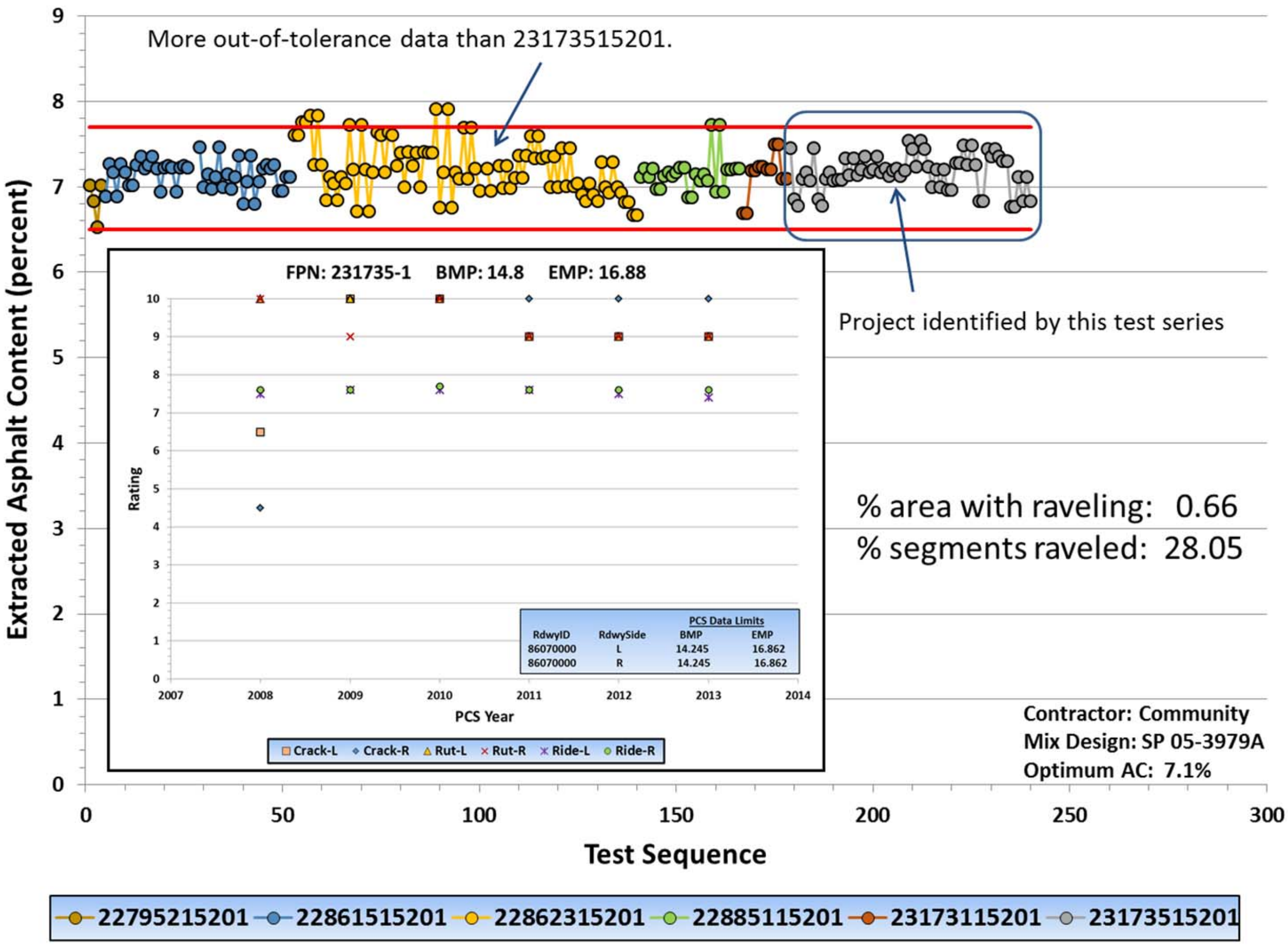
More out-of-tolerance data than 23173515201.
Project identified by this test series
% area with raveling: 0.66
% segments raveled: 28.05
Contractor: Community
Mix Design: SP 05-3979A
Optimum AC: 7.1%
Extracted Asphalt Content (percent)
Test Sequence
FPN: 231735-1 BMP: 14.8 EMP: 16.88
Rating
PCS Year
PCS Data Limits
RdwyID RdwySide BMP EMP
86070000 L 14.245 16.862
86070000 R 14.245 16.862
Crack-L Crack-R Rut-L Rut-R Ride-L Ride-R
22795215201 22861515201 22862315201 22885115201 23173115201 23173515201

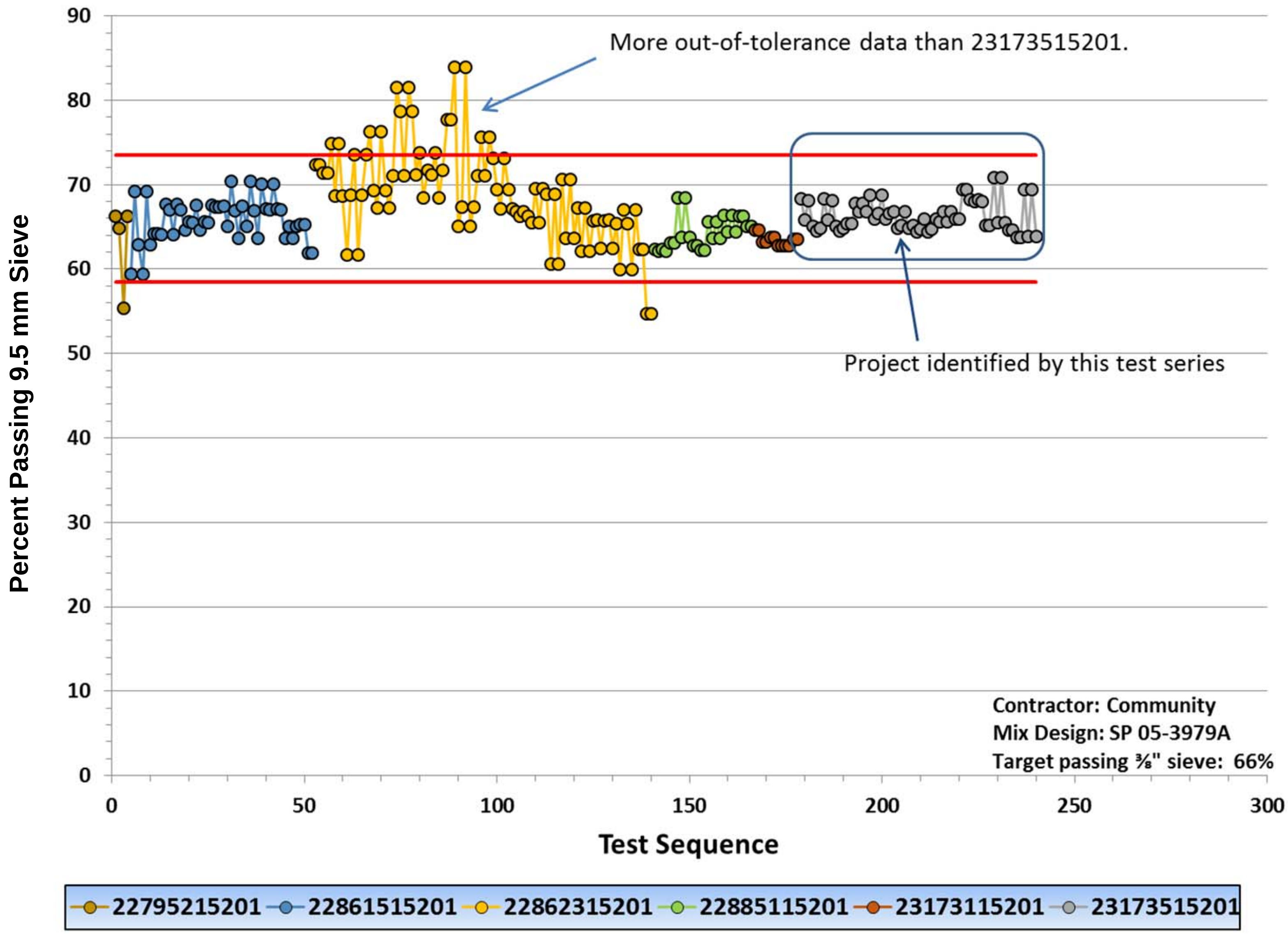

More out-of-tolerance data than 23173515201.
Project identified by this test series
Percent Passing 9.5 mm Sieve
Test Sequence
Contractor: Community
Mix Design: SP 05-3979A
Target passing ⅜" sieve: 66%
22795215201
22861515201
22862315201
22885115201
23173115201
23173515201

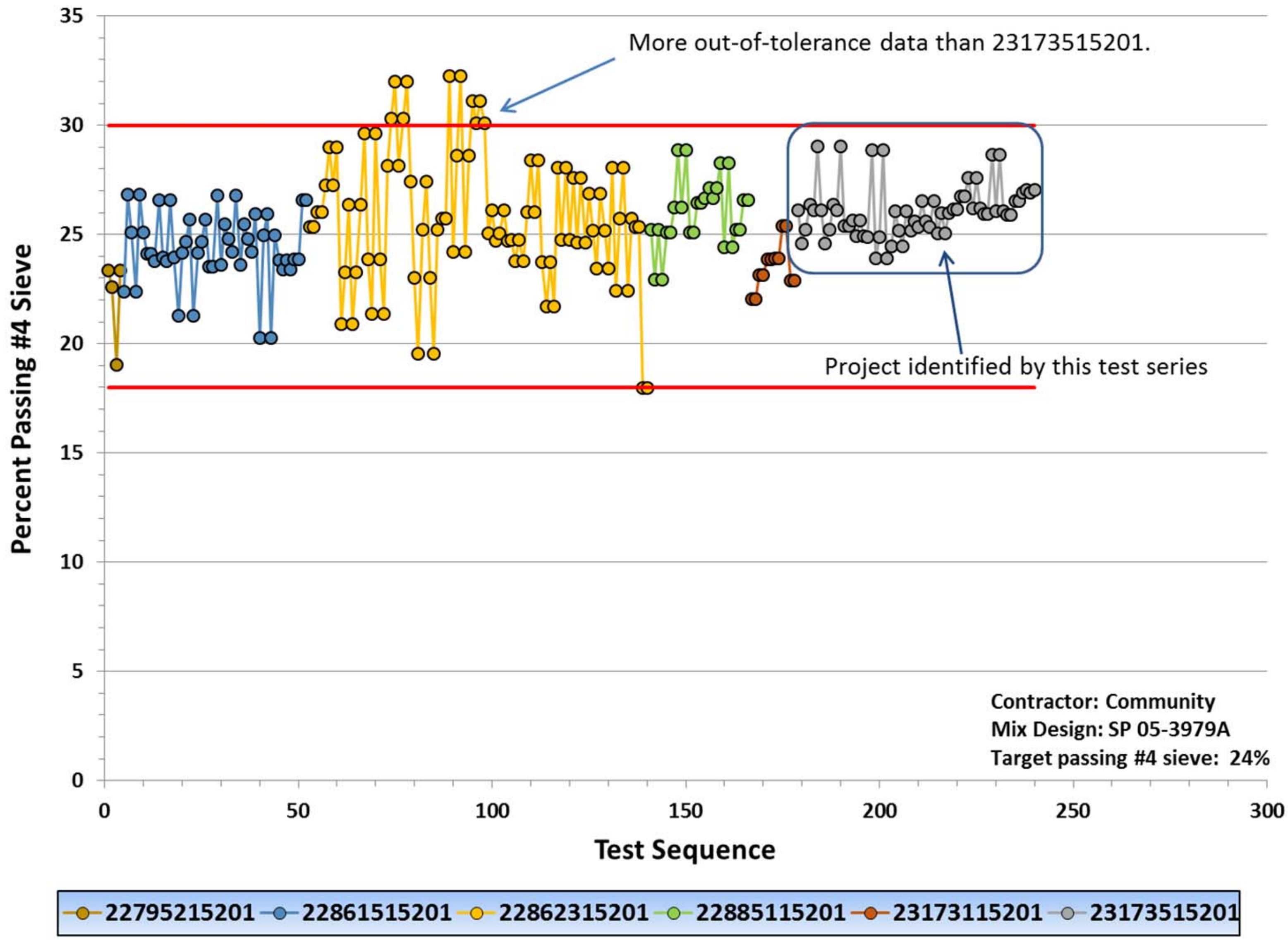

More out-of-tolerance data than 23173515201.
Project identified by this test series
Percent Passing #4 Sieve
Test Sequence
Contractor: Community
Mix Design: SP 05-3979A
Target passing #4 sieve: 24%
22795215201
22861515201
22862315201
22885115201
23173115201
23173515201

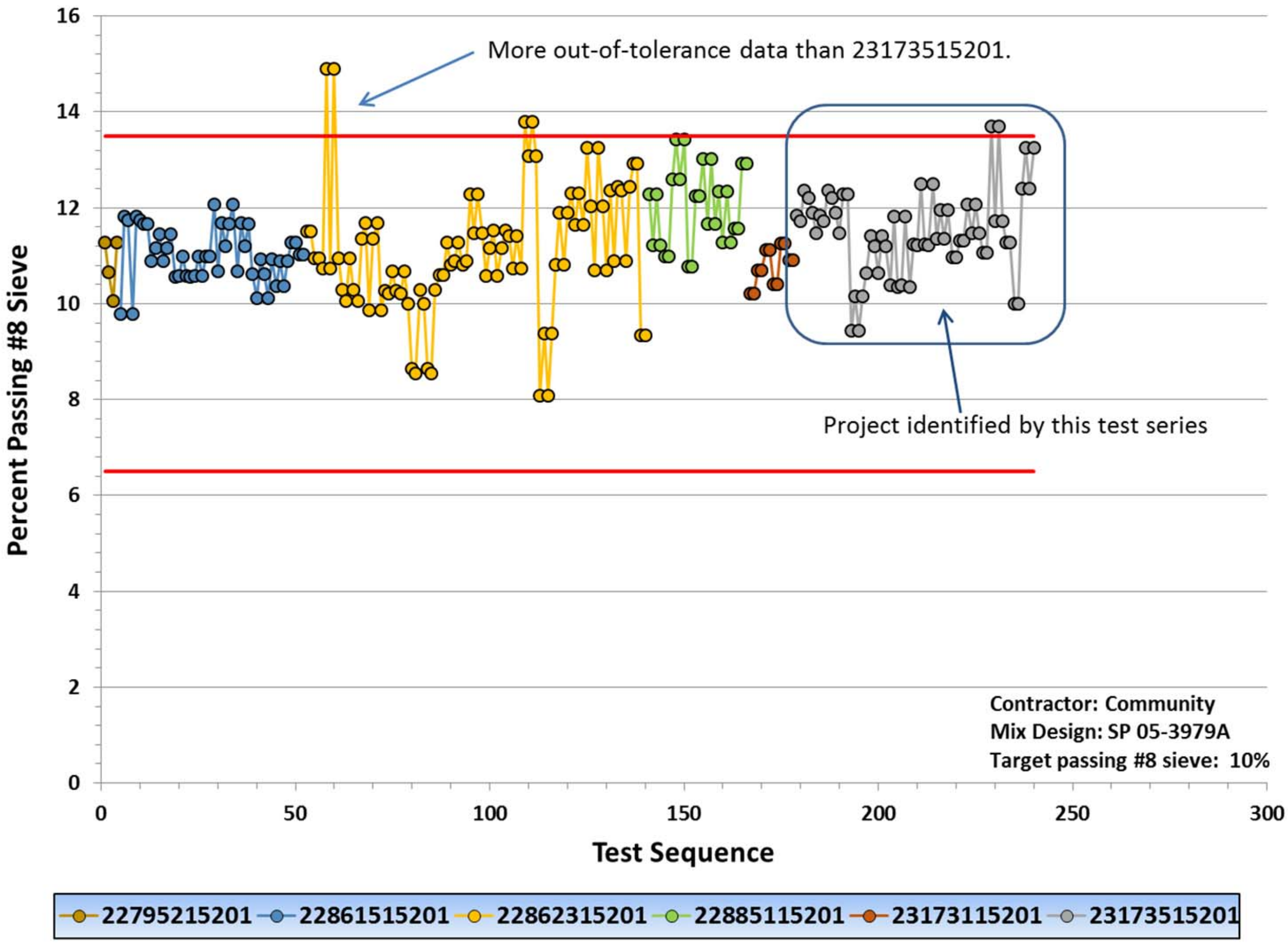

More out-of-tolerance data than 23173515201.
Project identified by this test series
Contractor: Community
Mix Design: SP 05-3979A
Target passing #8 sieve: 10%
Percent Passing #8 Sieve
Test Sequence
0
2
4
6
8
10
12
14
16
0
50
100
150
200
250
300
22795215201
22861515201
22862315201
22885115201
23173115201
23173515201

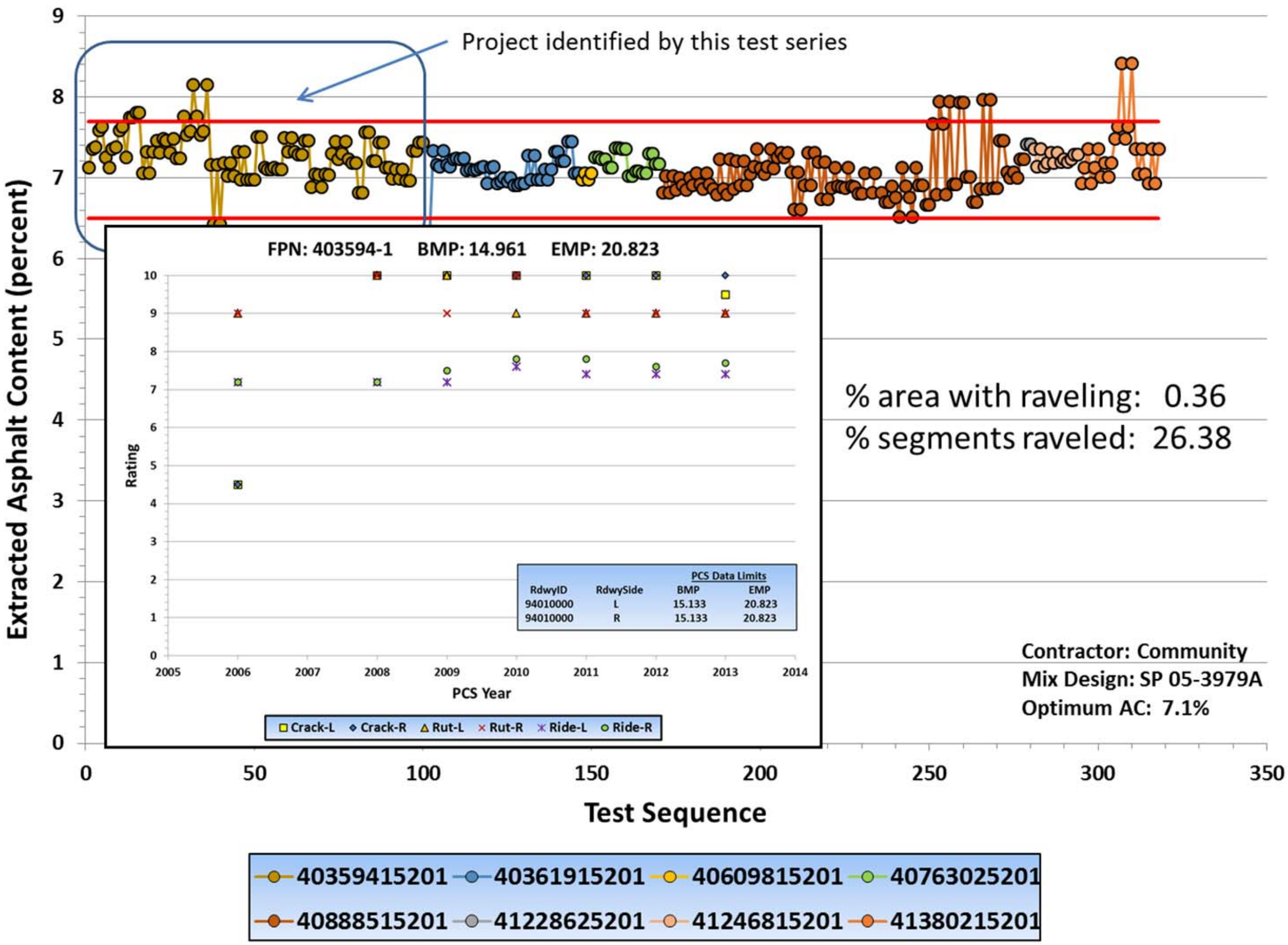

Project identified by this test series
Extracted Asphalt Content (percent)
Test Sequence
FPN: 403594-1 BMP: 14.961 EMP: 20.823
Rating
PCS Year
PCS Data Limits
RdwyID RdwySide BMP EMP
94010000 L 15.133 20.823
94010000 R 15.133 20.823
Crack-L Crack-R Rut-L Rut-R Ride-L Ride-R
% area with raveling: 0.36
% segments raveled: 26.38
Contractor: Community
Mix Design: SP 05-3979A
Optimum AC: 7.1%
40359415201 40361915201 40609815201 40763025201
40888515201 41228625201 41246815201 41380215201

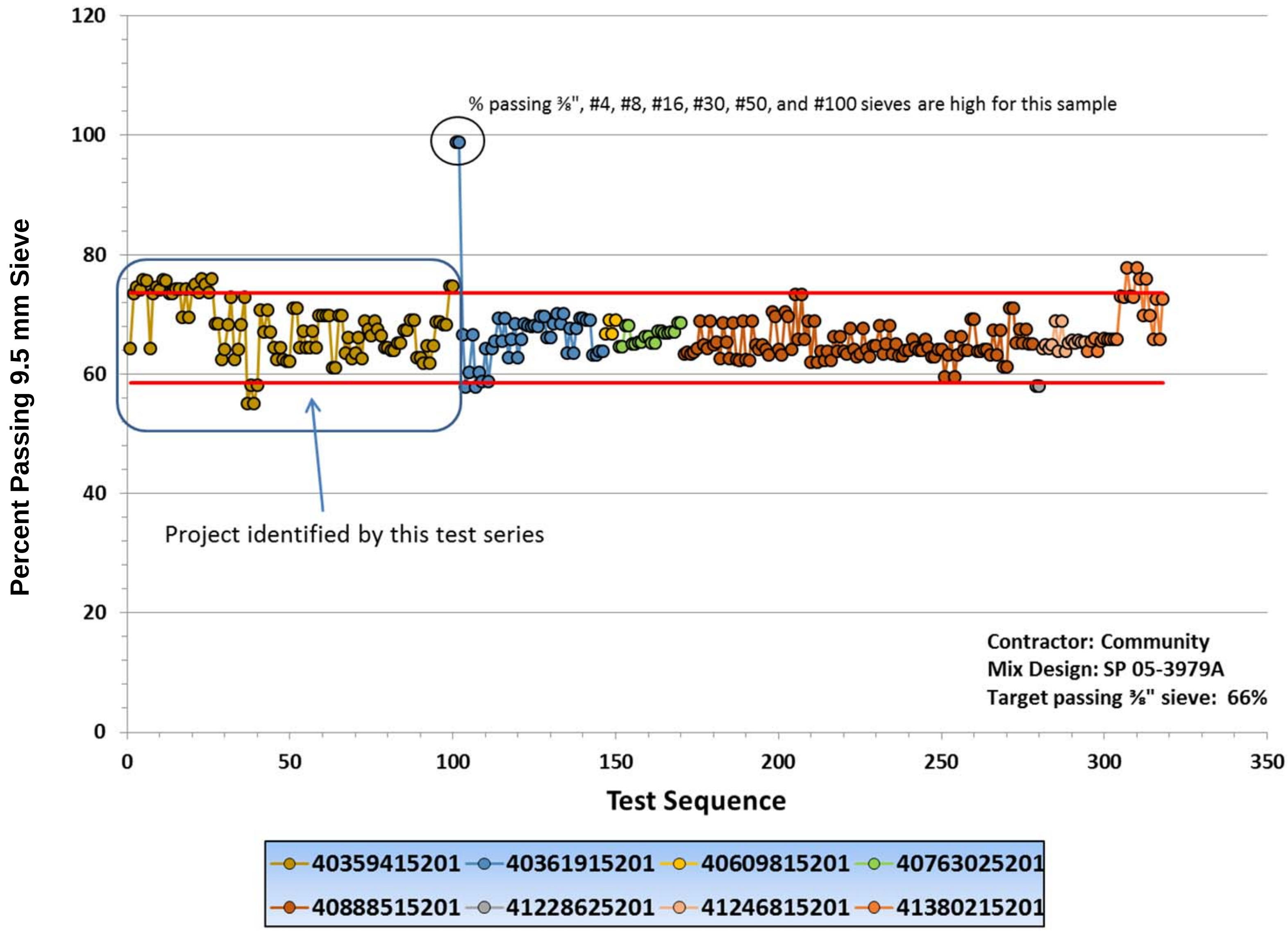

Percent Passing 9.5 mm Sieve
120
100
80
60
40
20
0
% passing ⅜", #4, #8, #16, #30, #50, and #100 sieves are high for this sample
Project identified by this test series
Contractor: Community
Mix Design: SP 05-3979A
Target passing ⅜" sieve: 66%
0
50
100
150
200
250
300
350
Test Sequence
40359415201
40361915201
40609815201
40763025201
40888515201
41228625201
41246815201
41380215201

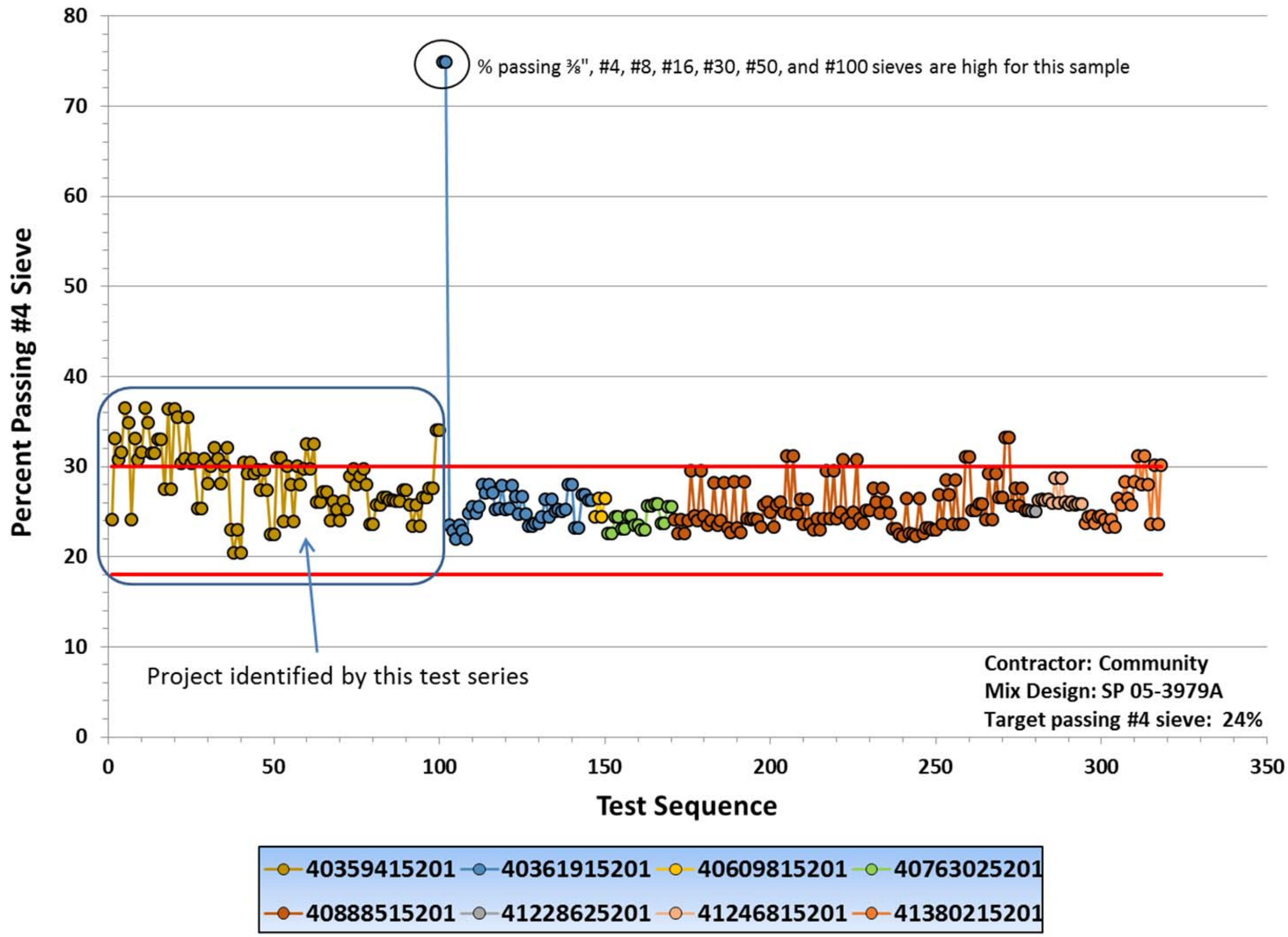

Percent Passing #4 Sieve
Test Sequence
% passing ⅜", #4, #8, #16, #30, #50, and #100 sieves are high for this sample
Project identified by this test series
Contractor: Community
Mix Design: SP 05-3979A
Target passing #4 sieve: 24%
40359415201
40361915201
40609815201
40763025201
40888515201
41228625201
41246815201
41380215201

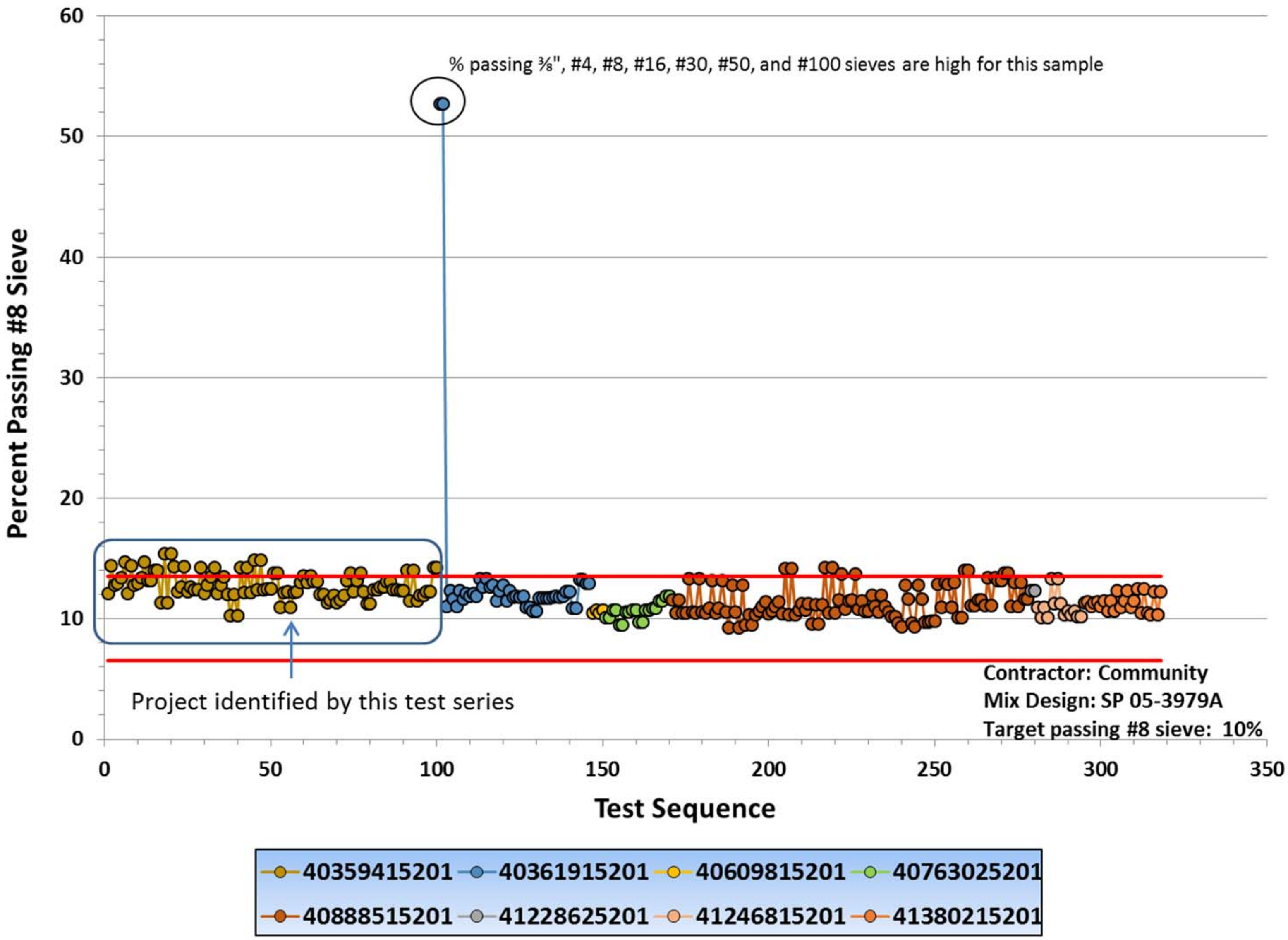

% passing ⅜", #4, #8, #16, #30, #50, and #100 sieves are high for this sample
Percent Passing #8 Sieve
60
50
40
30
20
10
0
Project identified by this test series
Contractor: Community
Mix Design: SP 05-3979A
Target passing #8 sieve: 10%
0
50
100
150
200
250
300
350
Test Sequence
40359415201
40361915201
40609815201
40763025201
40888515201
41228625201
41246815201
41380215201

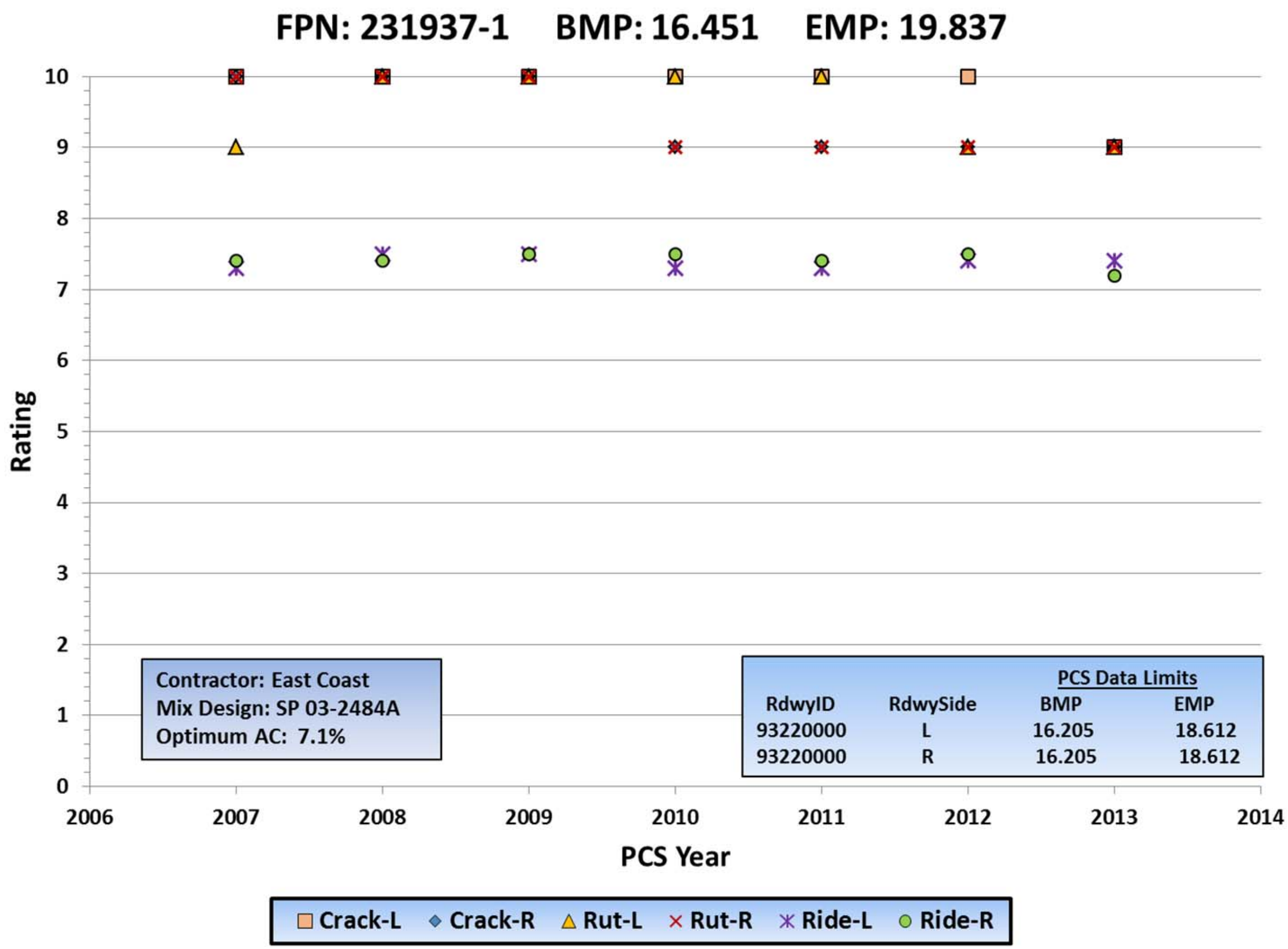
FPN: 231937-1 BMP: 16.451 EMP: 19.837
Rating
PCS Year
Contractor: East Coast
Mix Design: SP 03-2484A
Optimum AC: 7.1%
PCS Data Limits
RdwyID RdwySide BMP EMP
93220000 L 16.205 18.612
93220000 R 16.205 18.612
Crack-L Crack-R Rut-L Rut-R Ride-L Ride-R

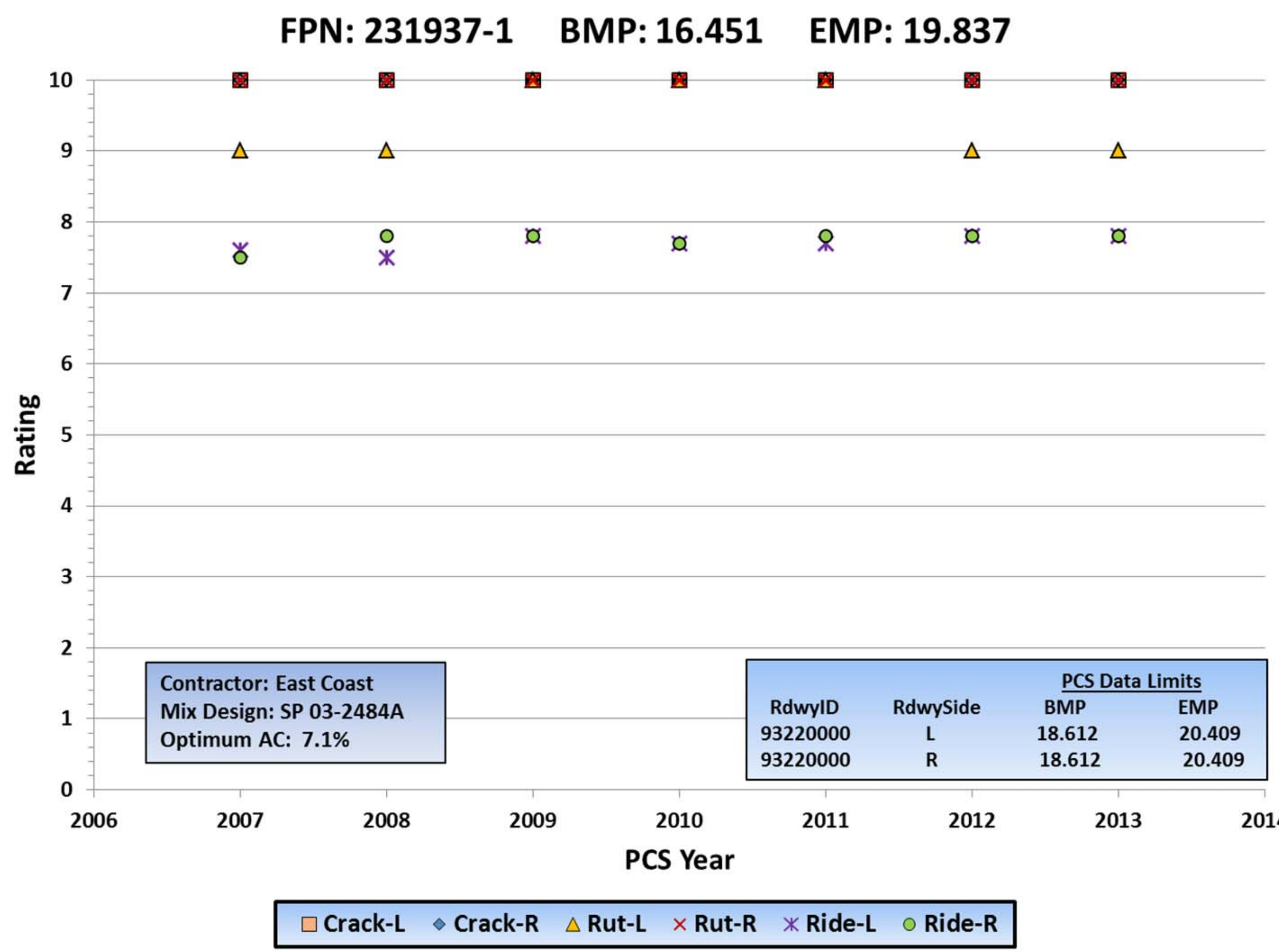

FPN: 231937-1 BMP: 16.451 EMP: 19.837
Rating
PCS Year
Contractor: East Coast
Mix Design: SP 03-2484A
Optimum AC: 7.1%
PCS Data Limits
RdwyID RdwySide BMP EMP
93220000 L 18.612 20.409
93220000 R 18.612 20.409
Crack-L Crack-R Rut-L Rut-R Ride-L Ride-R

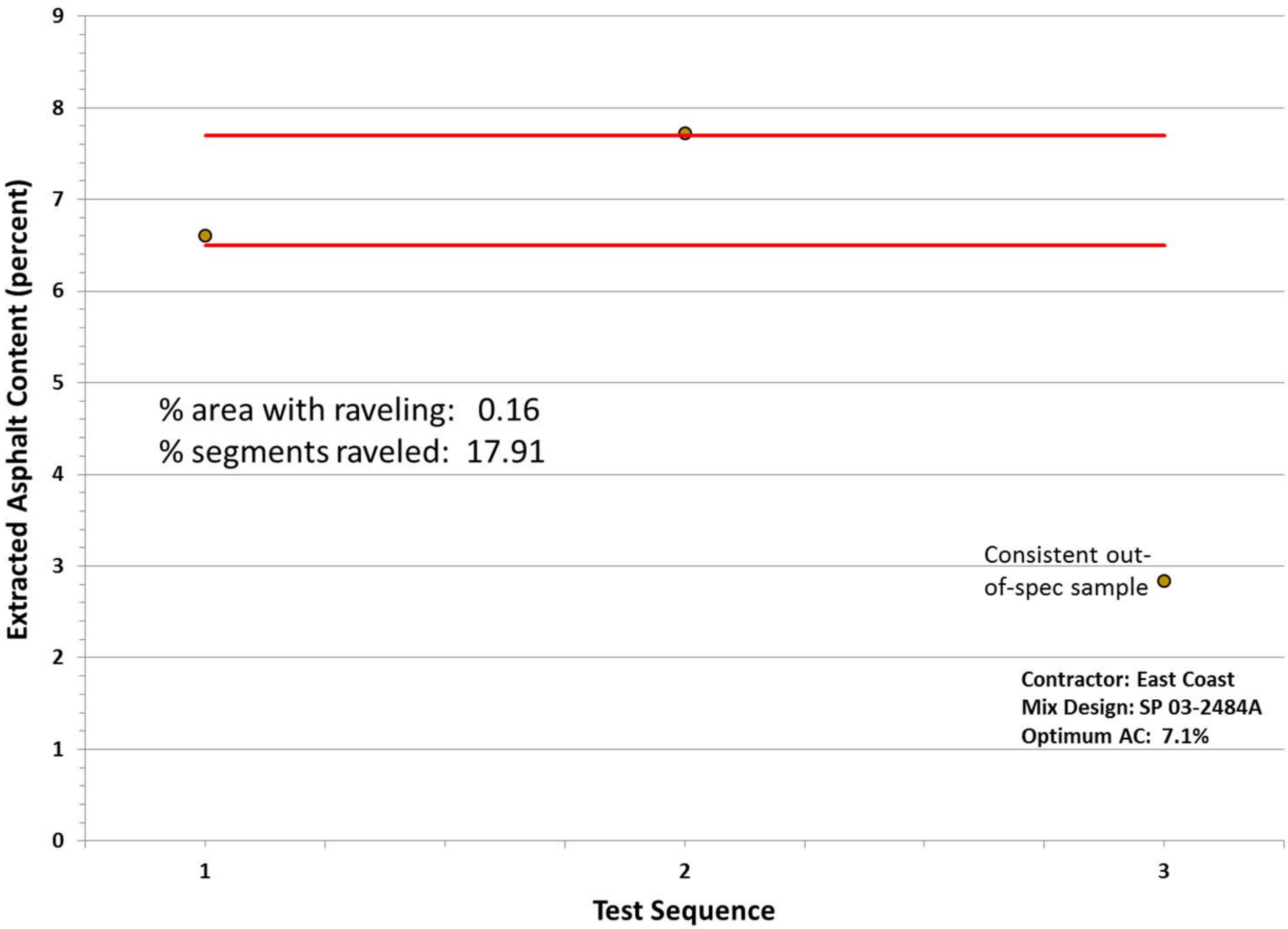

Extracted Asphalt Content (percent)
9
8
7
6
5
4
3
2
1
0
% area with raveling: 0.16
% segments raveled: 17.91
Consistent out-of-spec sample
Contractor: East Coast
Mix Design: SP 03-2484A
Optimum AC: 7.1%
1
2
3
Test Sequence

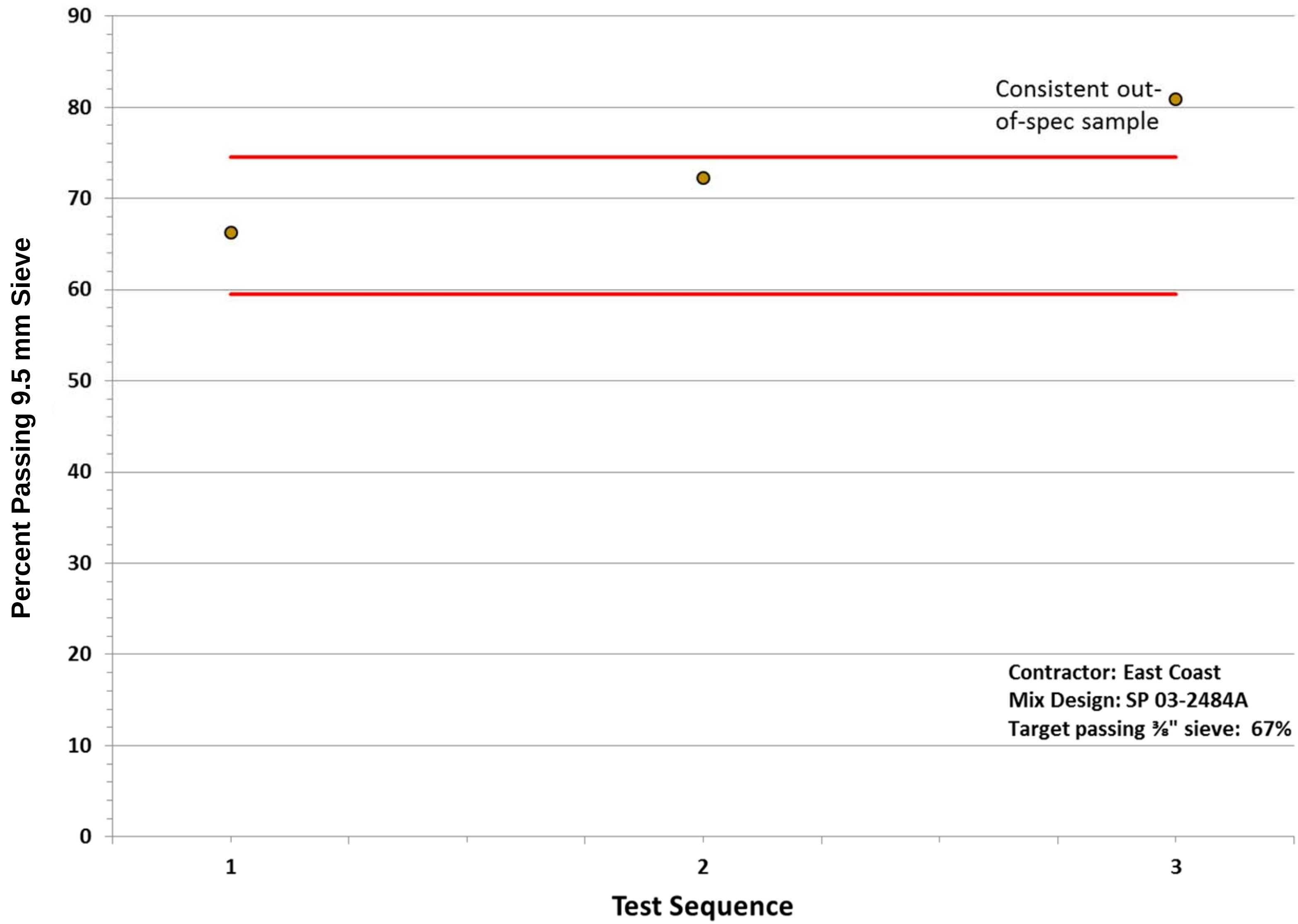

Percent Passing 9.5 mm Sieve
90
80
70
60
50
40
30
20
10
0
1
2
3
Test Sequence
Consistent out-of-spec sample
Contractor: East Coast
Mix Design: SP 03-2484A
Target passing ⅜" sieve: 67%

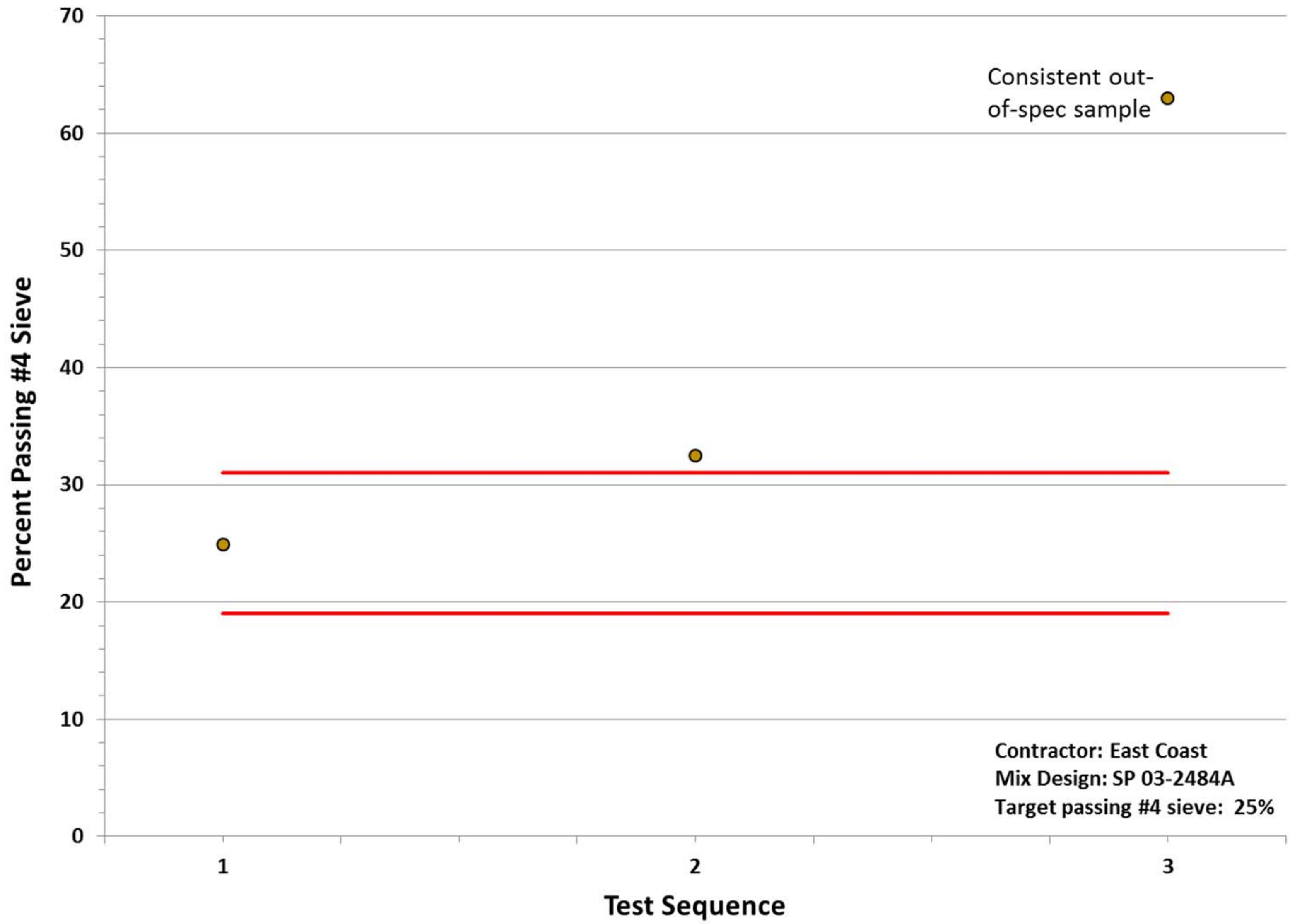

70
60
50
40
30
20
10
0
Percent Passing #4 Sieve
Consistent out-of-spec sample
Contractor: East Coast
Mix Design: SP 03-2484A
Target passing #4 sieve: 25%
1
2
3
Test Sequence

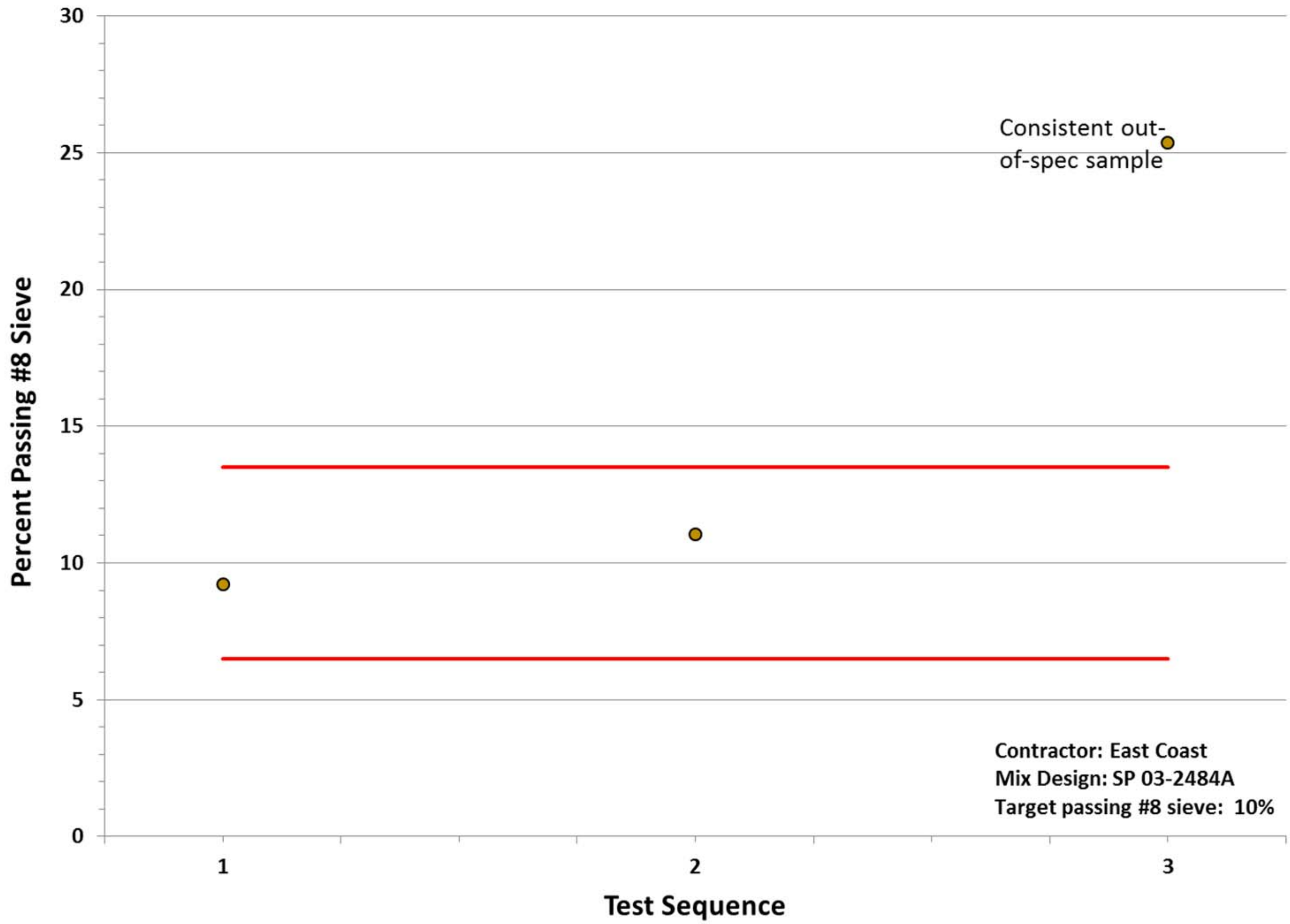
Percent Passing #8 Sieve
30
25
20
15
10
5
0
1
2
3
Test Sequence
Consistent out-of-spec sample
Contractor: East Coast
Mix Design: SP 03-2484A
Target passing #8 sieve: 10%

A.3. Projects Considered To Have Poor Performance

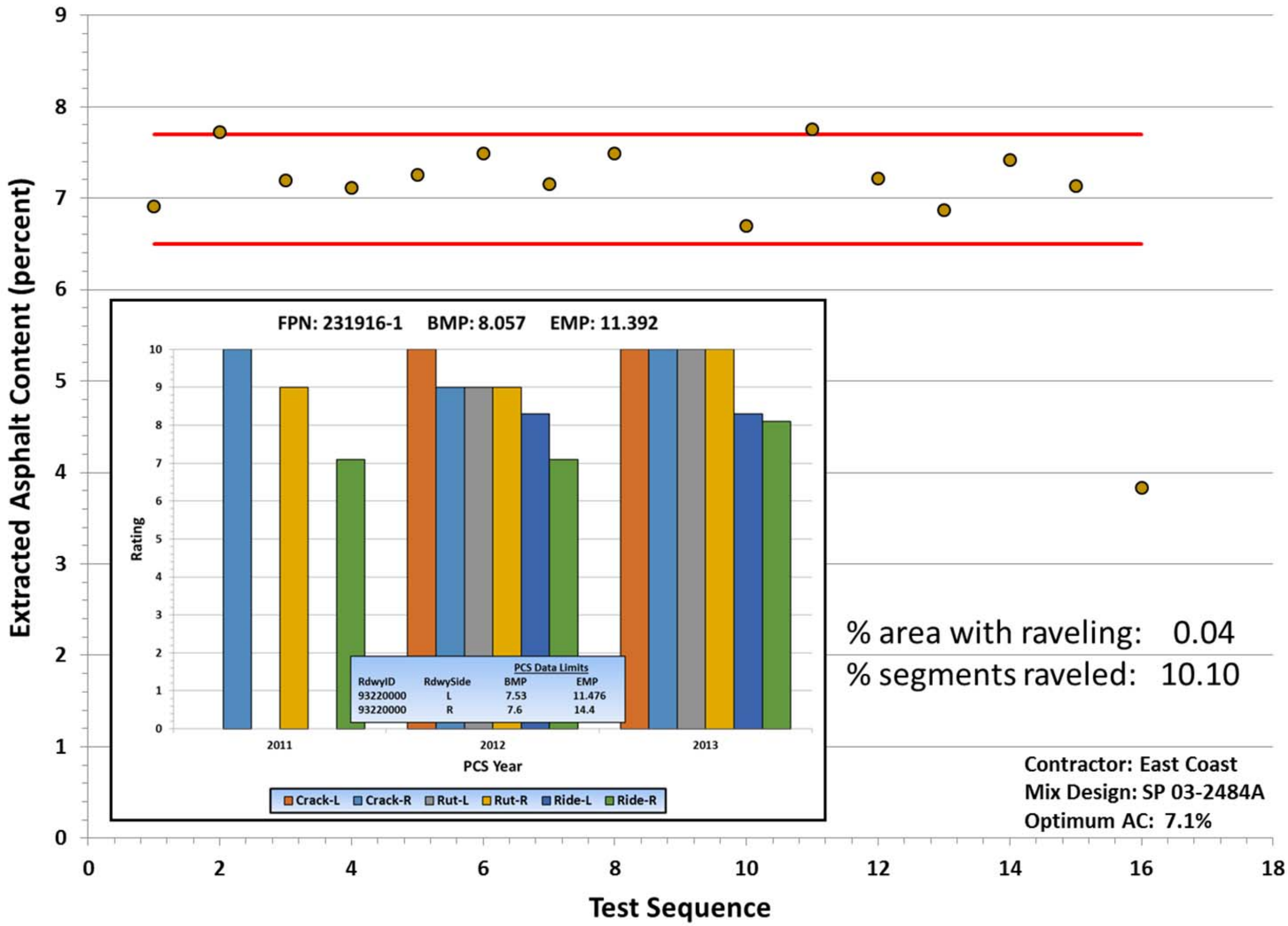

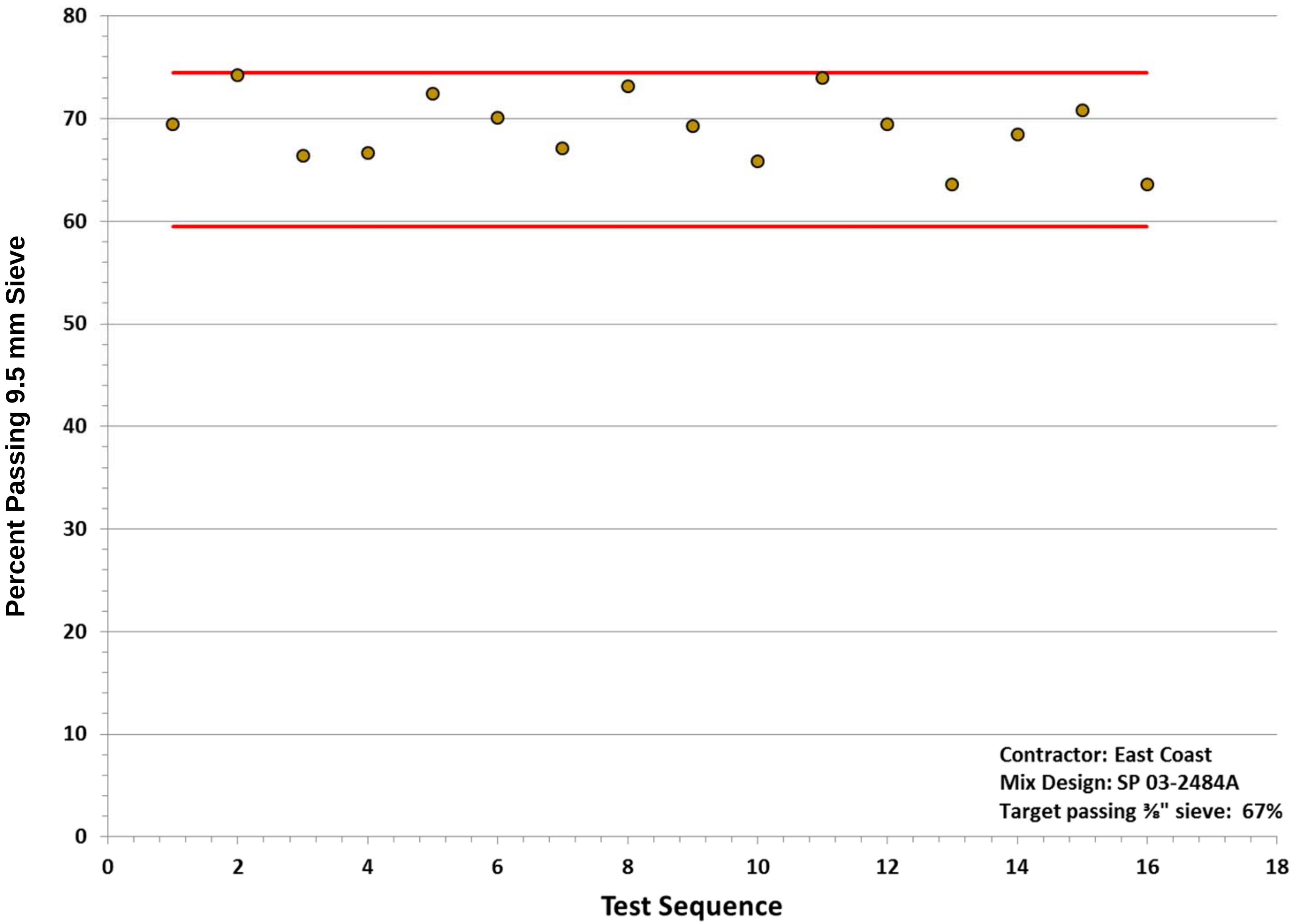

Percent Passing 9.5 mm Sieve
Test Sequence
Contractor: East Coast
Mix Design: SP 03-2484A
Target passing ⅜" sieve: 67%

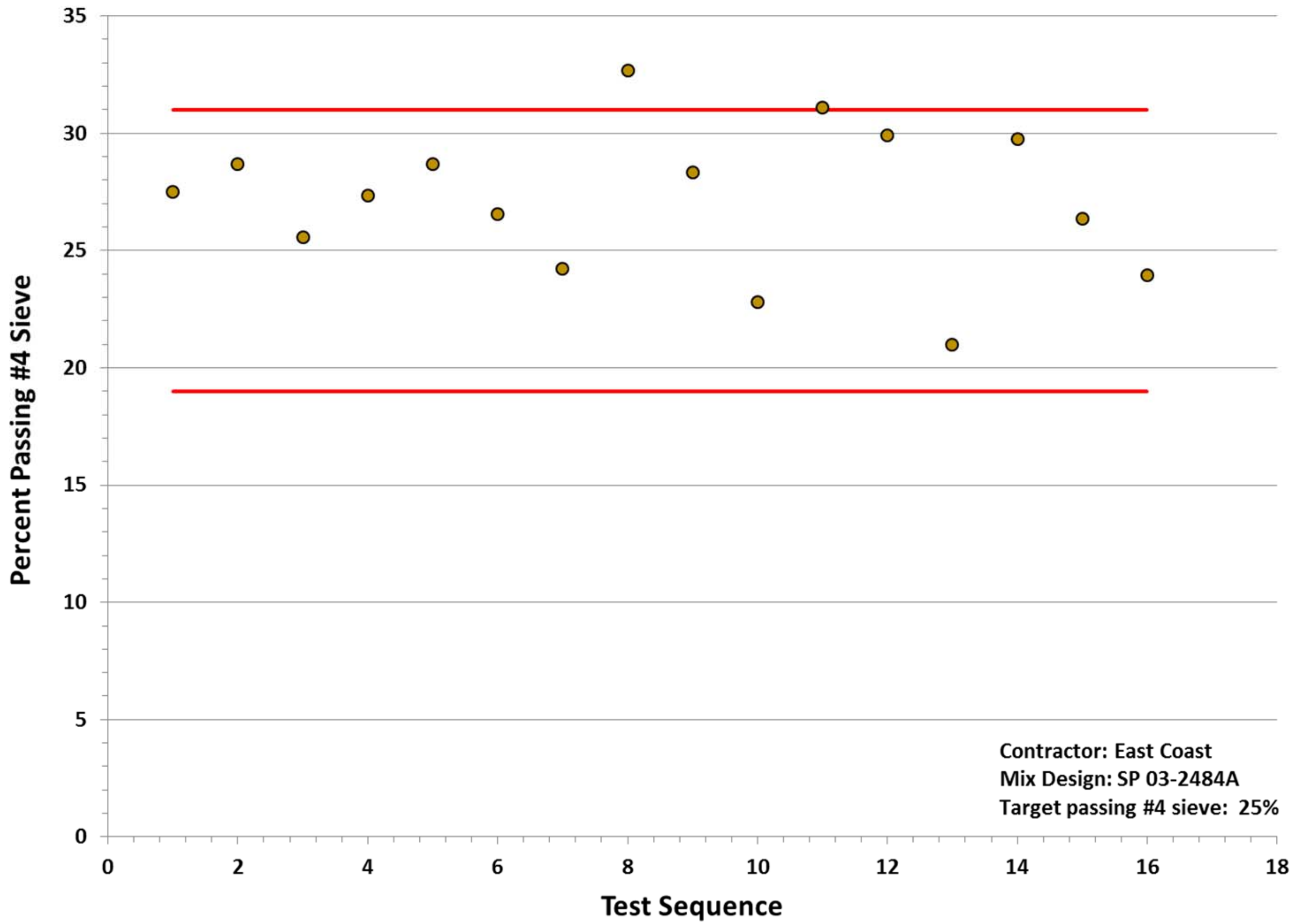
Percent Passing #4 Sieve
Test Sequence
Contractor: East Coast
Mix Design: SP 03-2484A
Target passing #4 sieve: 25%
0
5
10
15
20
25
30
35
0
2
4
6
8
10
12
14
16
18

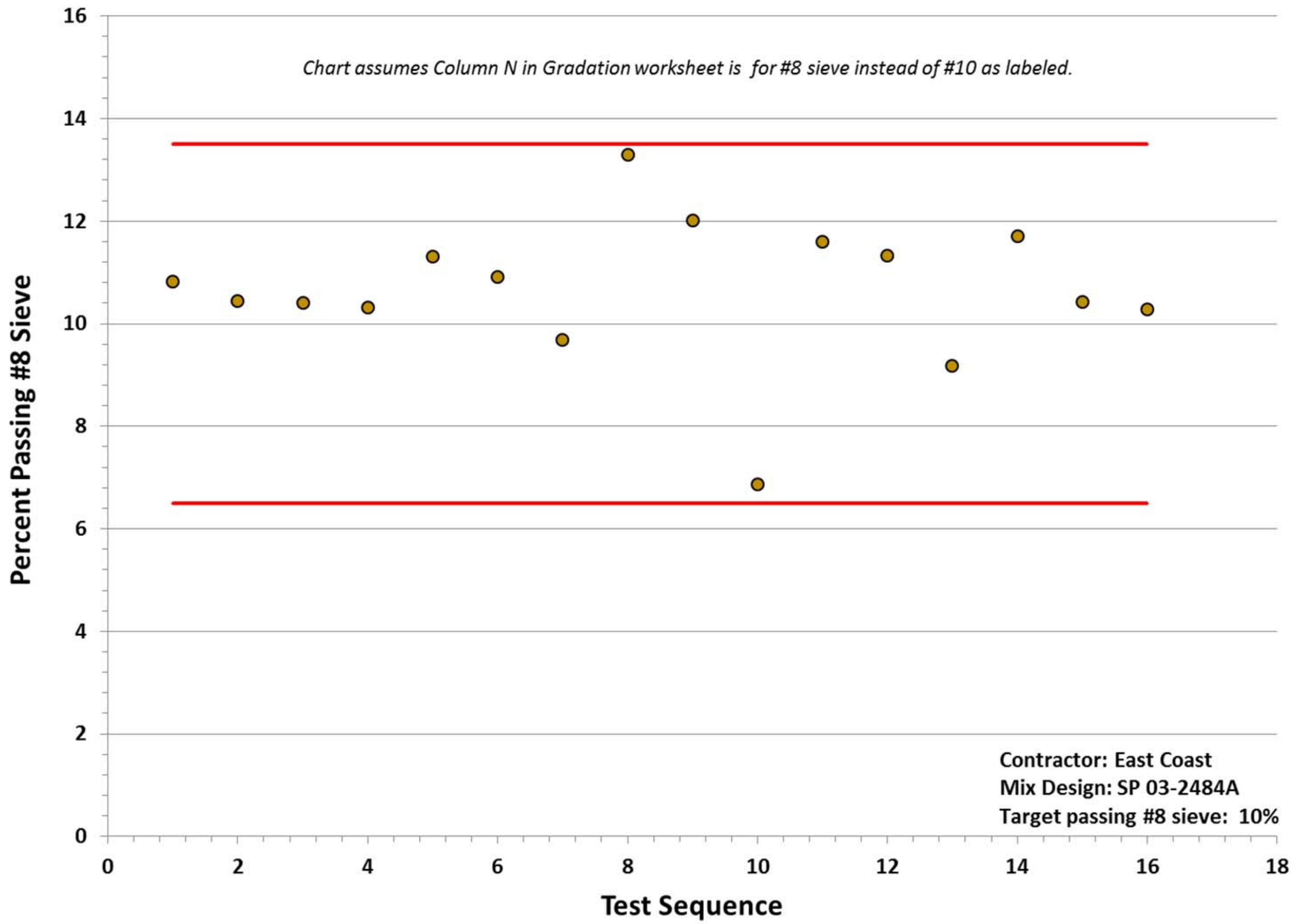
Chart assumes Column N in Gradation worksheet is for #8 sieve instead of #10 as labeled.
Percent Passing #8 Sieve
Test Sequence
Contractor: East Coast
Mix Design: SP 03-2484A
Target passing #8 sieve: 10%
0
2
4
6
8
10
12
14
16
18

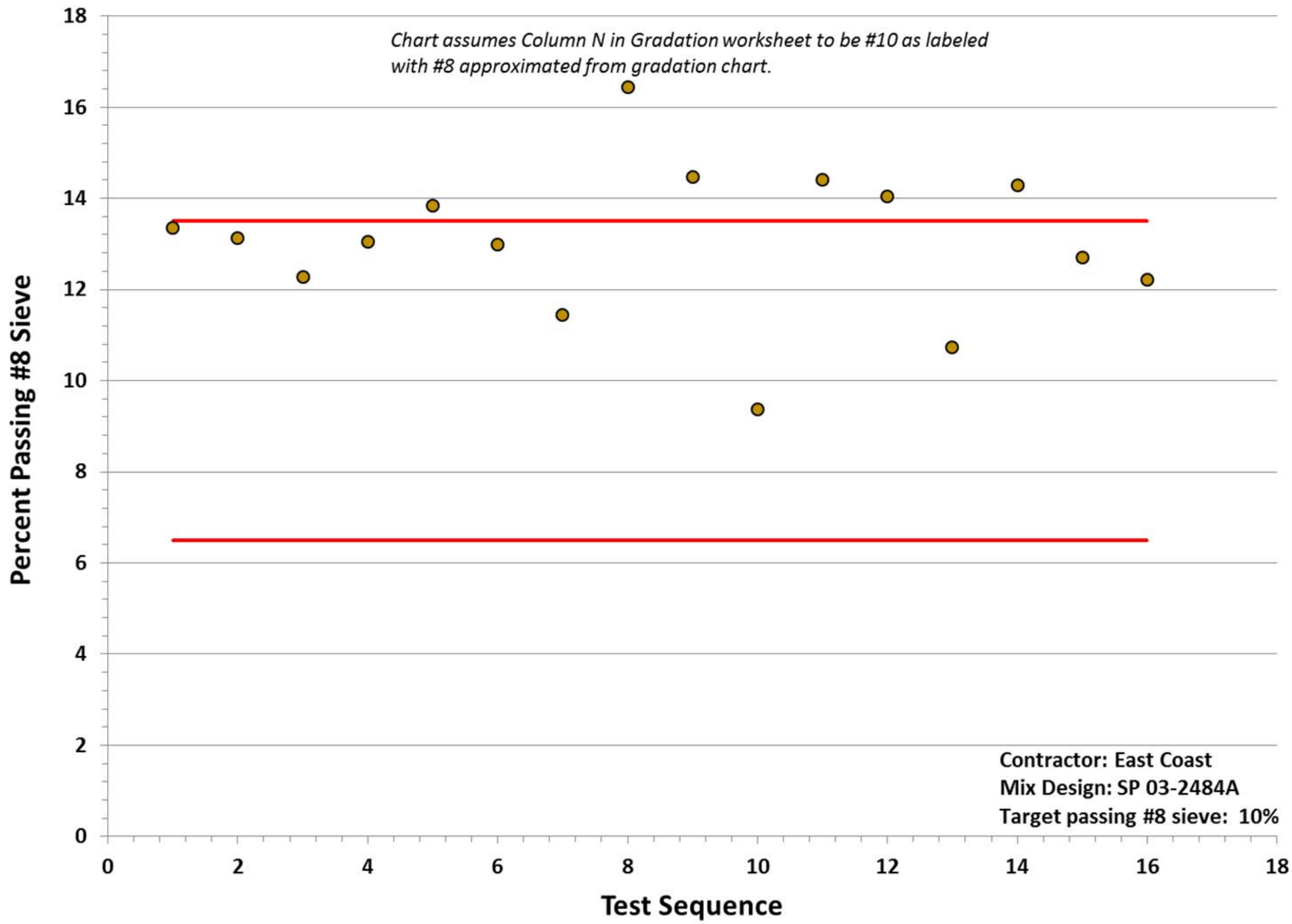

Chart assumes Column N in Gradation worksheet to be #10 as labeled
with #8 approximated from gradation chart.
Percent Passing #8 Sieve
Test Sequence
Contractor: East Coast
Mix Design: SP 03-2484A
Target passing #8 sieve: 10%
0
2
4
6
8
10
12
14
16
18

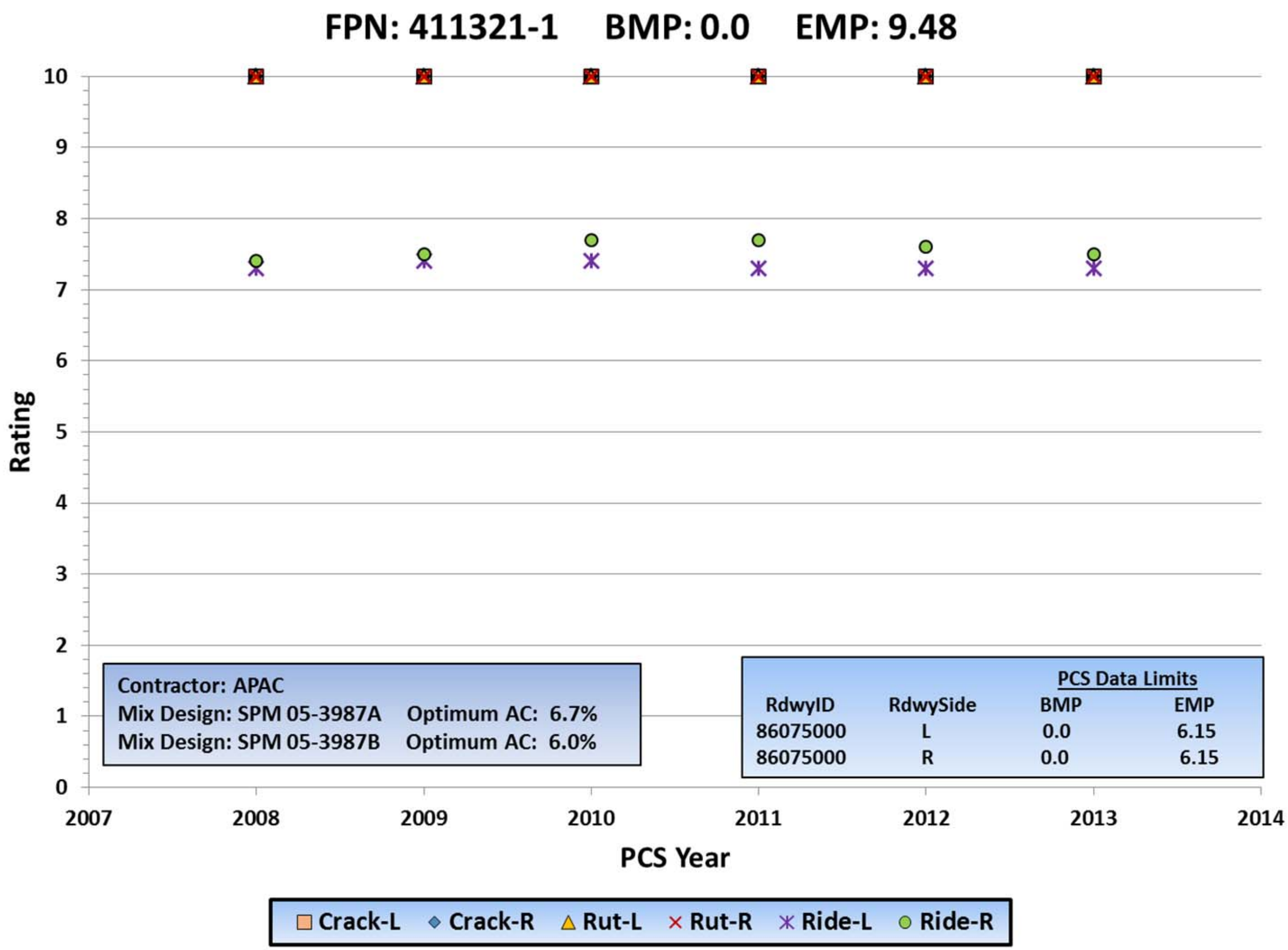
FPN: 411321-1 BMP: 0.0 EMP: 9.48
Rating
10
9
8
7
6
5
4
3
2
1
0
2007
2008
2009
2010
2011
2012
2013
2014
PCS Year
Contractor: APAC
Mix Design: SPM 05-3987A Optimum AC: 6.7%
Mix Design: SPM 05-3987B Optimum AC: 6.0%
PCS Data Limits
RdwyID RdwySide BMP EMP
86075000 L 0.0 6.15
86075000 R 0.0 6.15
Crack-L
Crack-R
Rut-L
Rut-R
Ride-L
Ride-R

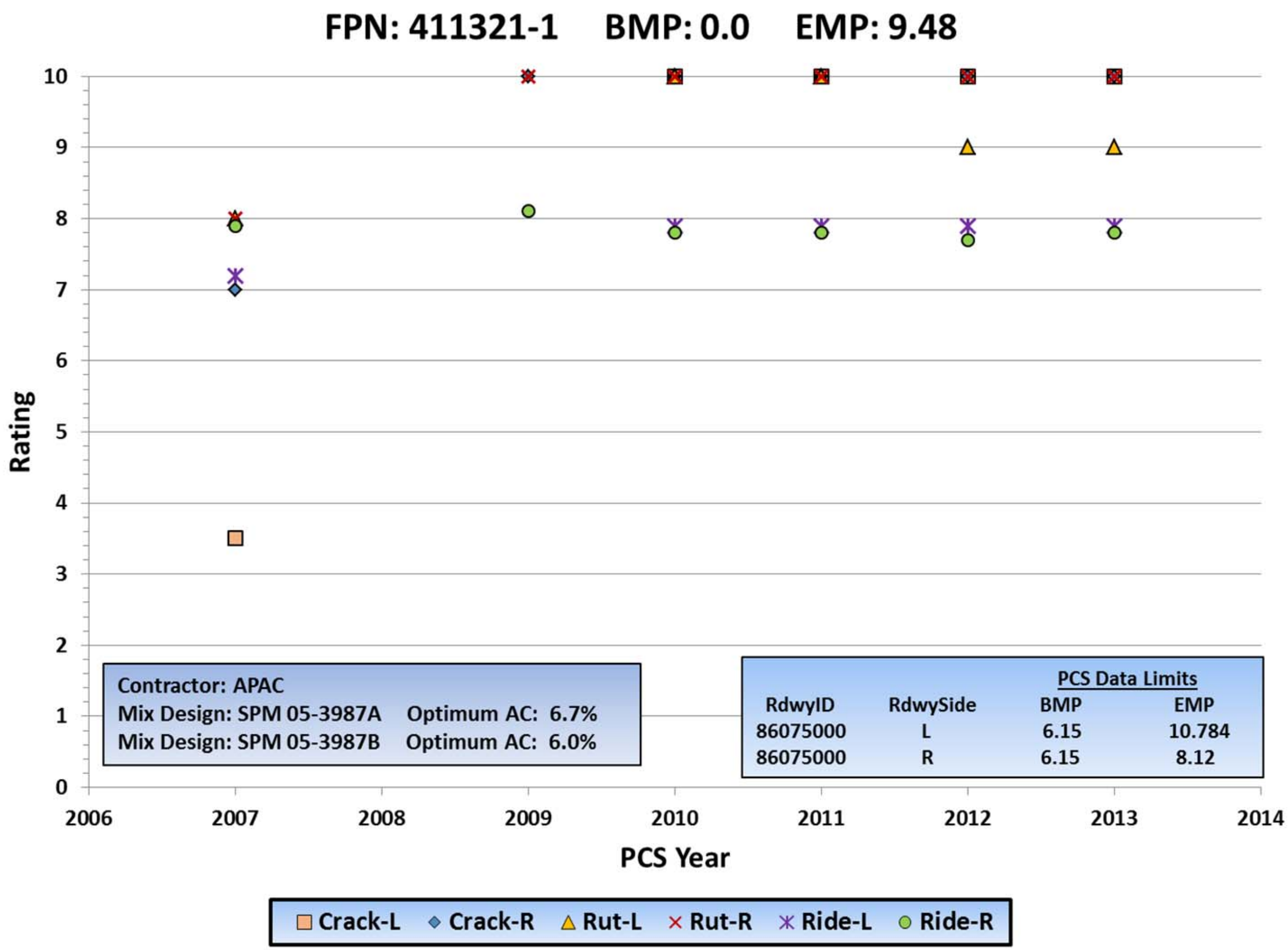
FPN: 411321-1 BMP: 0.0 EMP: 9.48
Rating
PCS Year
Contractor: APAC
Mix Design: SPM 05-3987A Optimum AC: 6.7%
Mix Design: SPM 05-3987B Optimum AC: 6.0%
PCS Data Limits
RdwyID RdwySide BMP EMP
86075000 L 6.15 10.784
86075000 R 6.15 8.12
Crack-L Crack-R Rut-L Rut-R Ride-L Ride-R

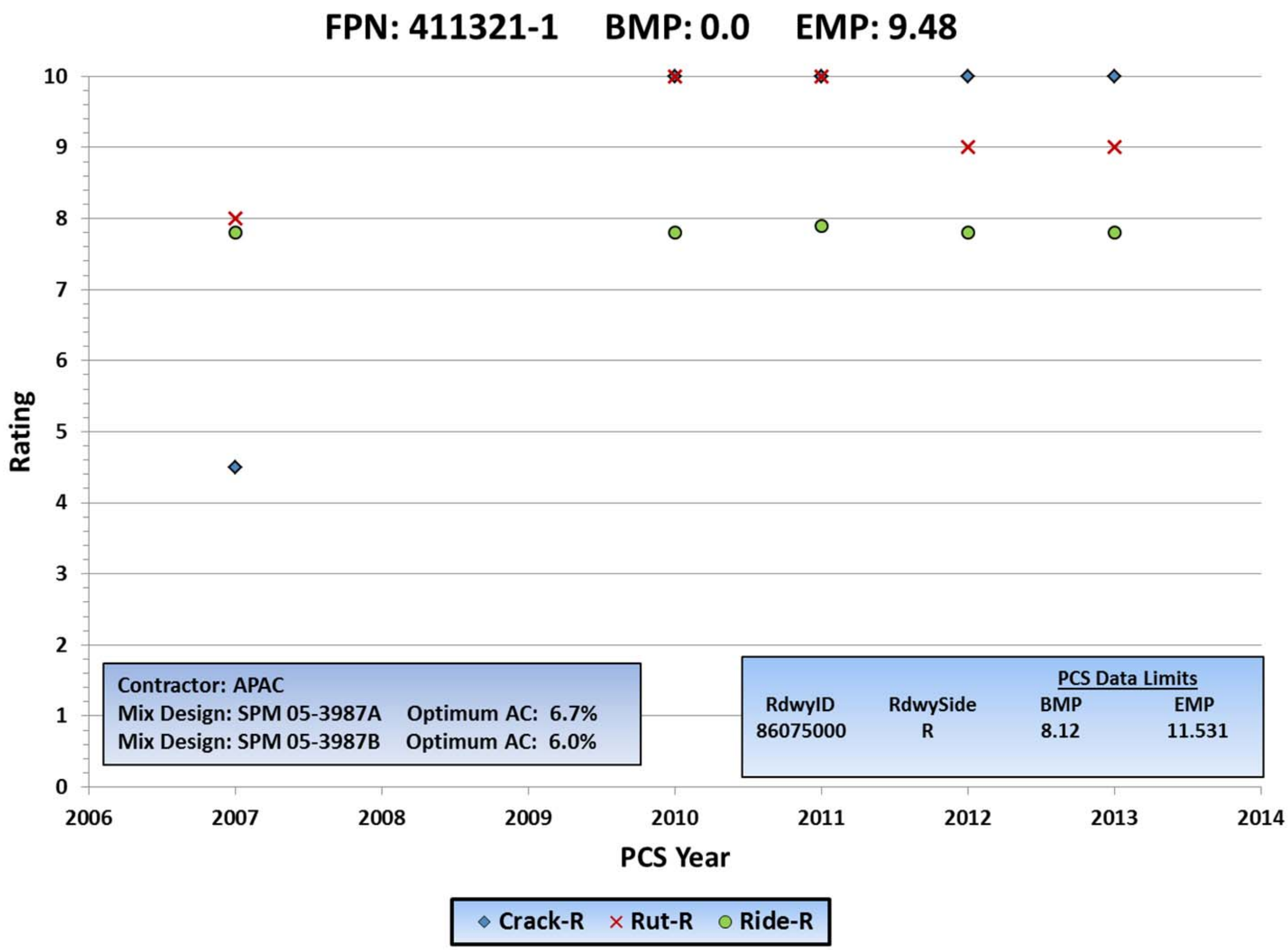

FPN: 411321-1 BMP: 0.0 EMP: 9.48
Rating
PCS Year
Contractor: APAC
Mix Design: SPM 05-3987A Optimum AC: 6.7%
Mix Design: SPM 05-3987B Optimum AC: 6.0%
PCS Data Limits
RdwyID RdwySide BMP EMP
86075000 R 8.12 11.531
Crack-R
Rut-R
Ride-R

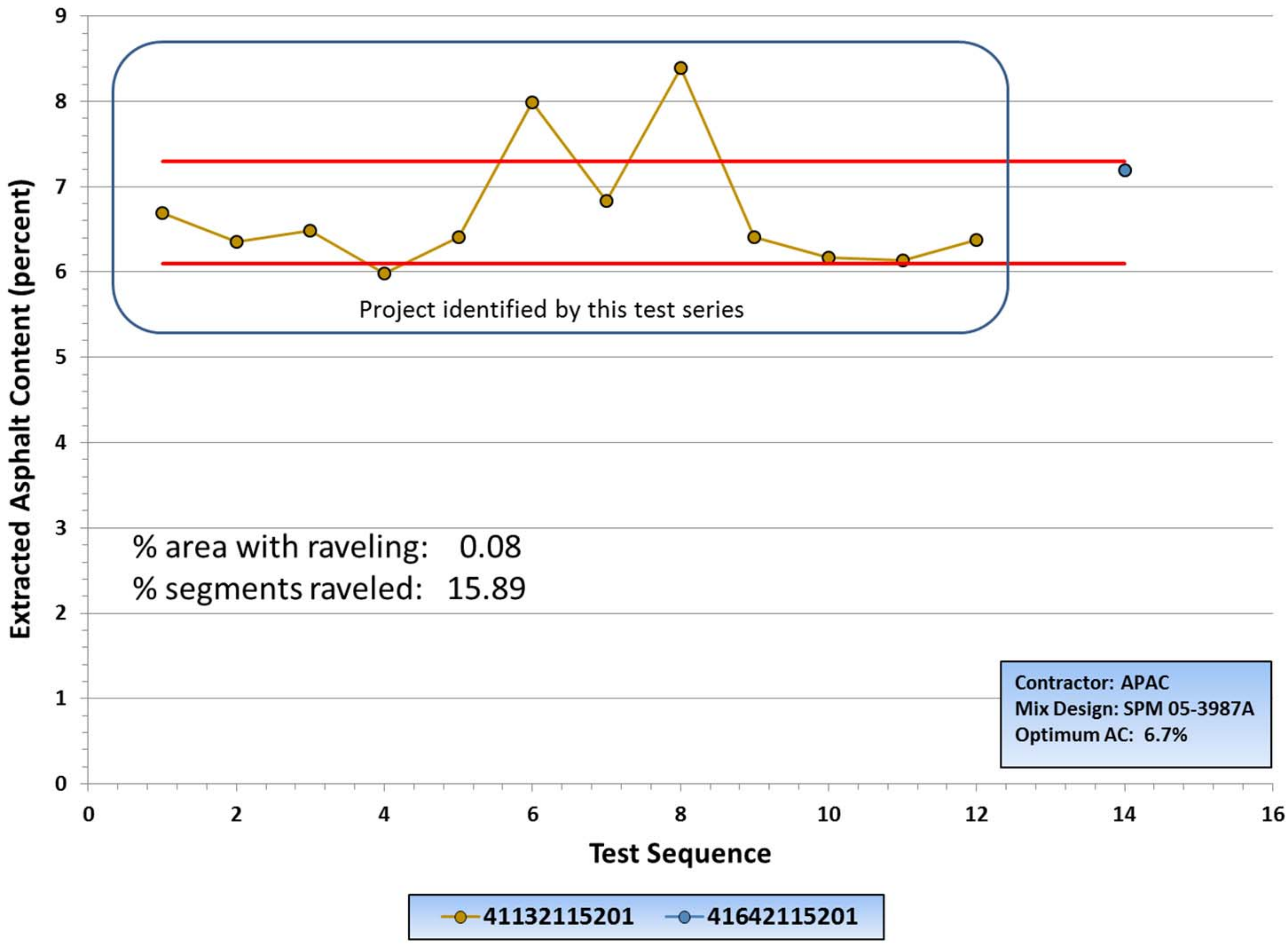

Extracted Asphalt Content (percent)
9
8
7
6
5
4
3
2
1
0
Project identified by this test series
% area with raveling: 0.08
% segments raveled: 15.89
Contractor: APAC
Mix Design: SPM 05-3987A
Optimum AC: 6.7%
0
2
4
6
8
10
12
14
16
Test Sequence
41132115201
41642115201

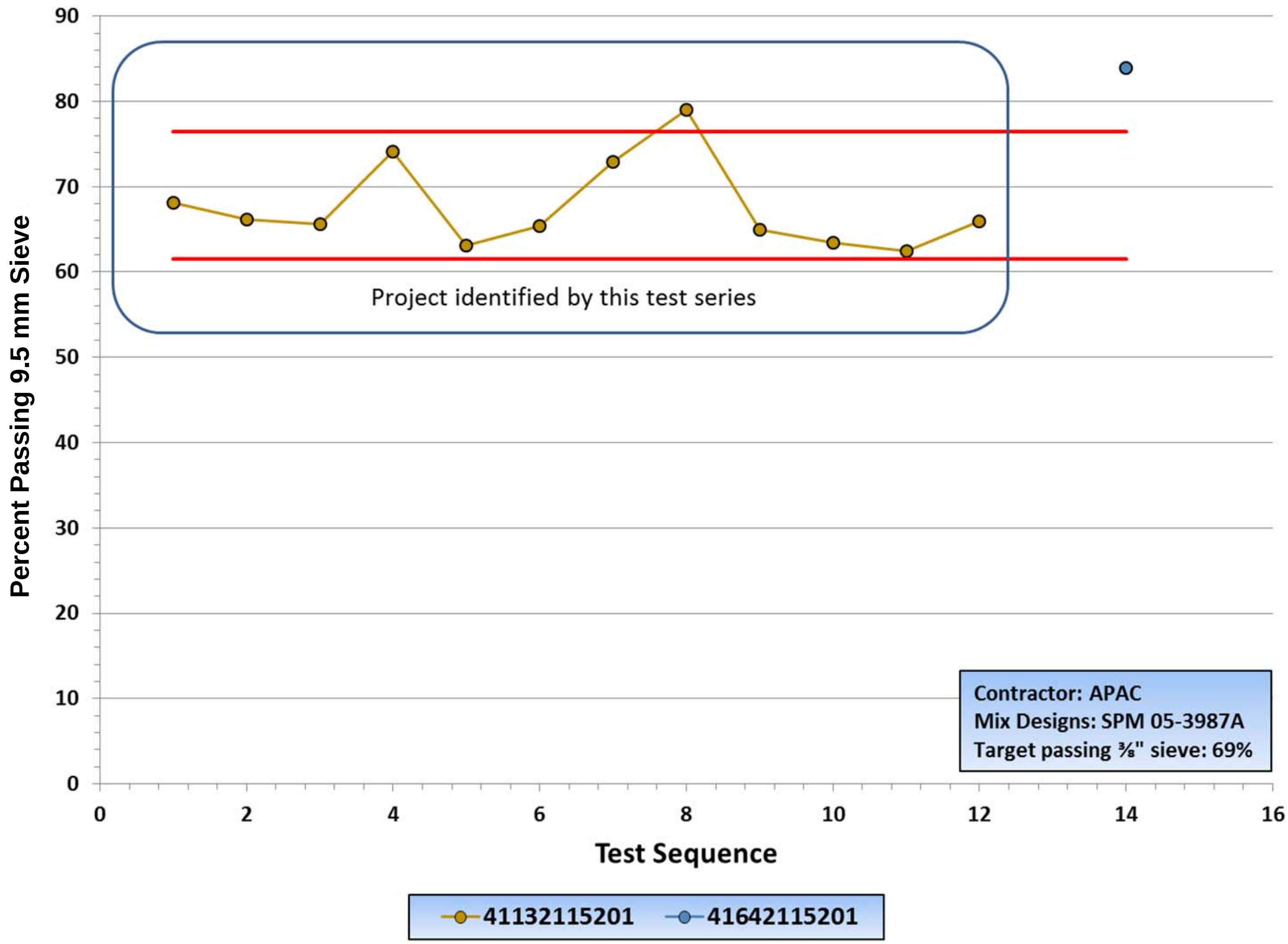

Percent Passing 9.5 mm Sieve
Project identified by this test series
Contractor: APAC
Mix Designs: SPM 05-3987A
Target passing ⅜" sieve: 69%
Test Sequence
41132115201
41642115201

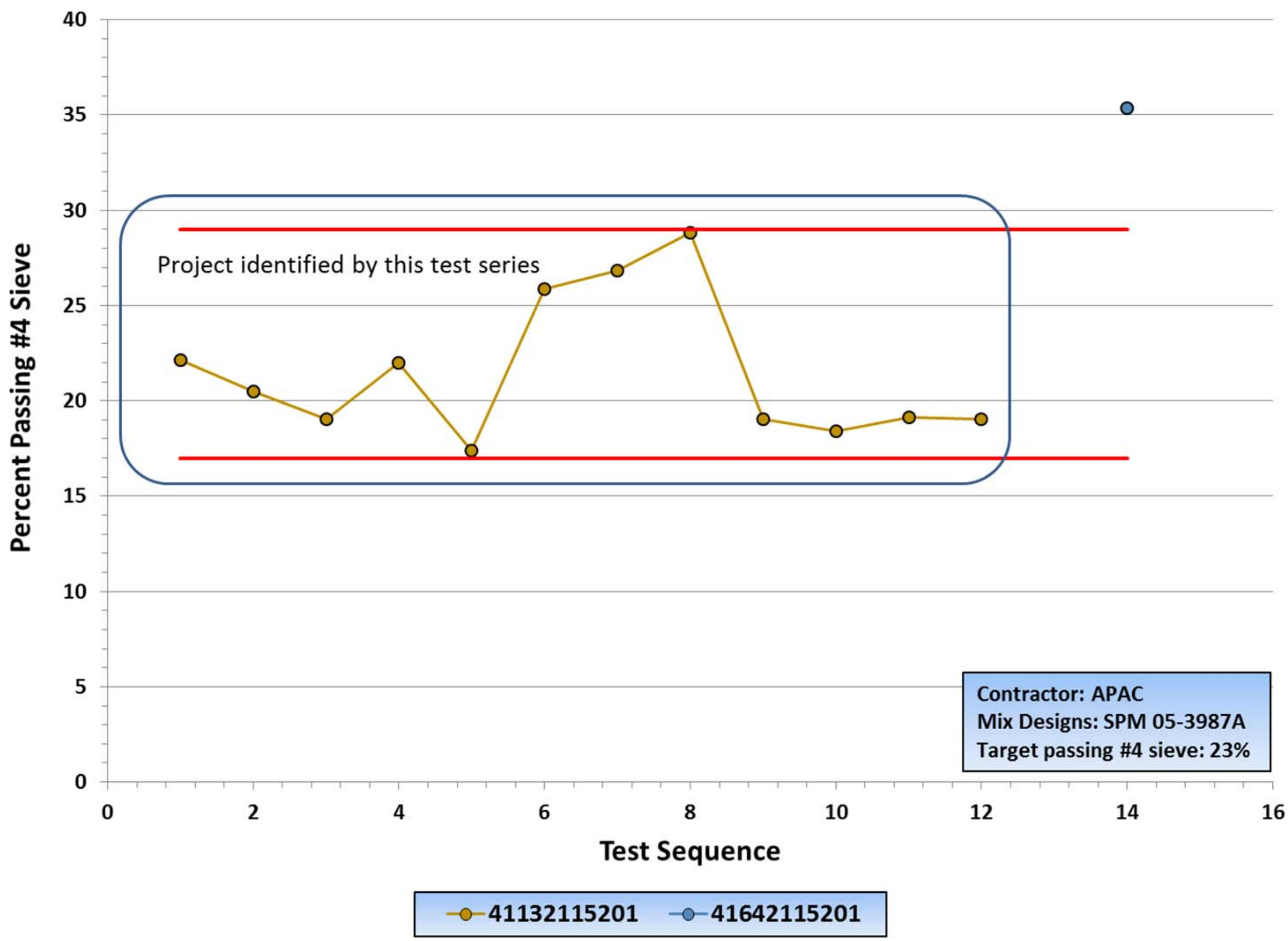

Percent Passing #4 Sieve
Test Sequence
Project identified by this test series
Contractor: APAC
Mix Designs: SPM 05-3987A
Target passing #4 sieve: 23%
41132115201
41642115201
0
5
10
15
20
25
30
35
40
0
2
4
6
8
10
12
14
16

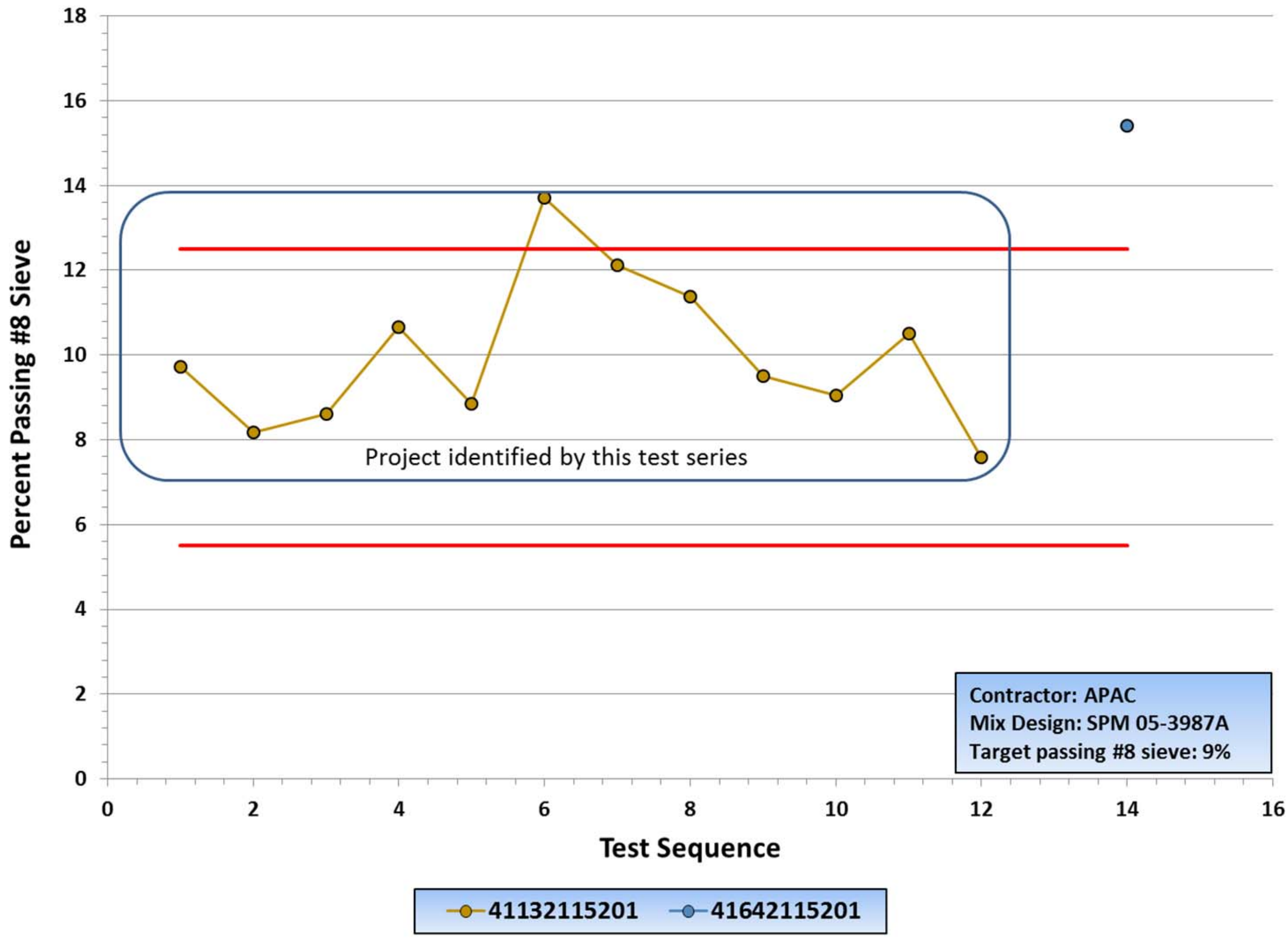

Percent Passing #8 Sieve
18
16
14
12
10
8
6
4
2
0
0
2
4
6
8
10
12
14
16
Test Sequence
Project identified by this test series
Contractor: APAC
Mix Design: SPM 05-3987A
Target passing #8 sieve: 9%
41132115201
41642115201

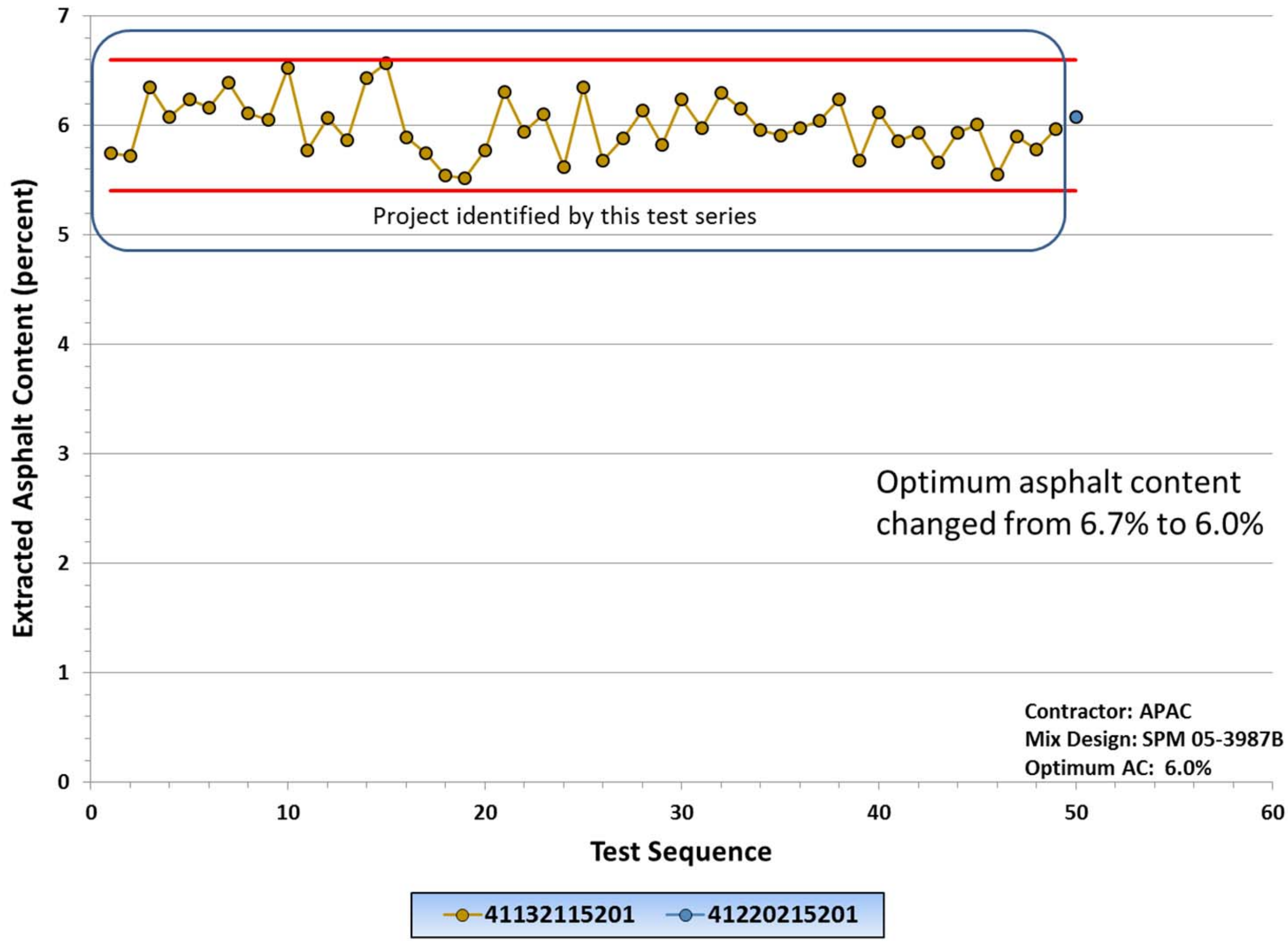

7
6
5
4
3
2
1
0
Extracted Asphalt Content (percent)
Project identified by this test series
Optimum asphalt content changed from 6.7% to 6.0%
Contractor: APAC
Mix Design: SPM 05-3987B
Optimum AC: 6.0%
0
10
20
30
40
50
60
Test Sequence
41132115201
41220215201

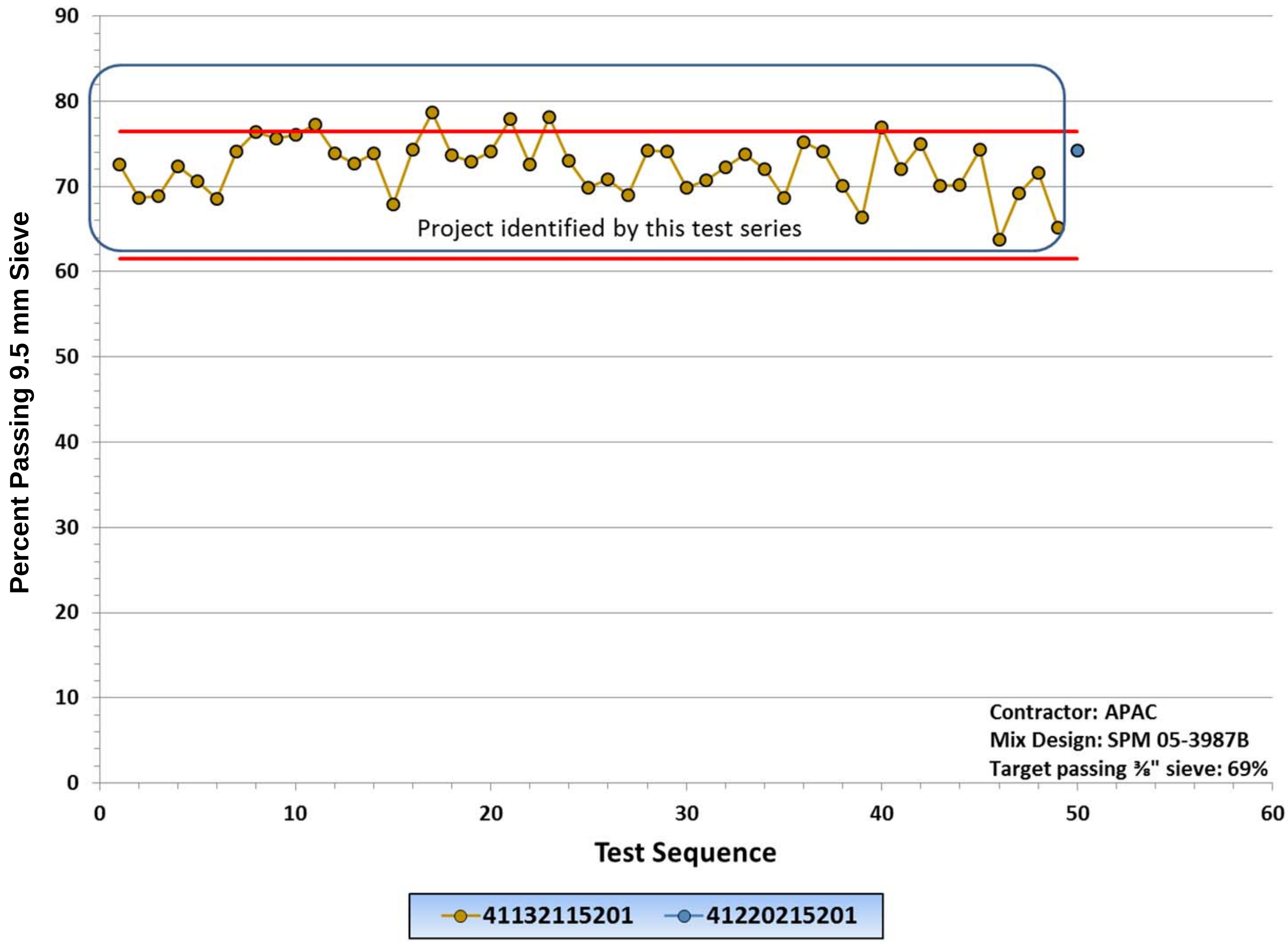

90
80
70
60
50
40
30
20
10
0
Percent Passing 9.5 mm Sieve
Project identified by this test series
Contractor: APAC
Mix Design: SPM 05-3987B
Target passing ⅜" sieve: 69%
0
10
20
30
40
50
60
Test Sequence
41132115201
41220215201

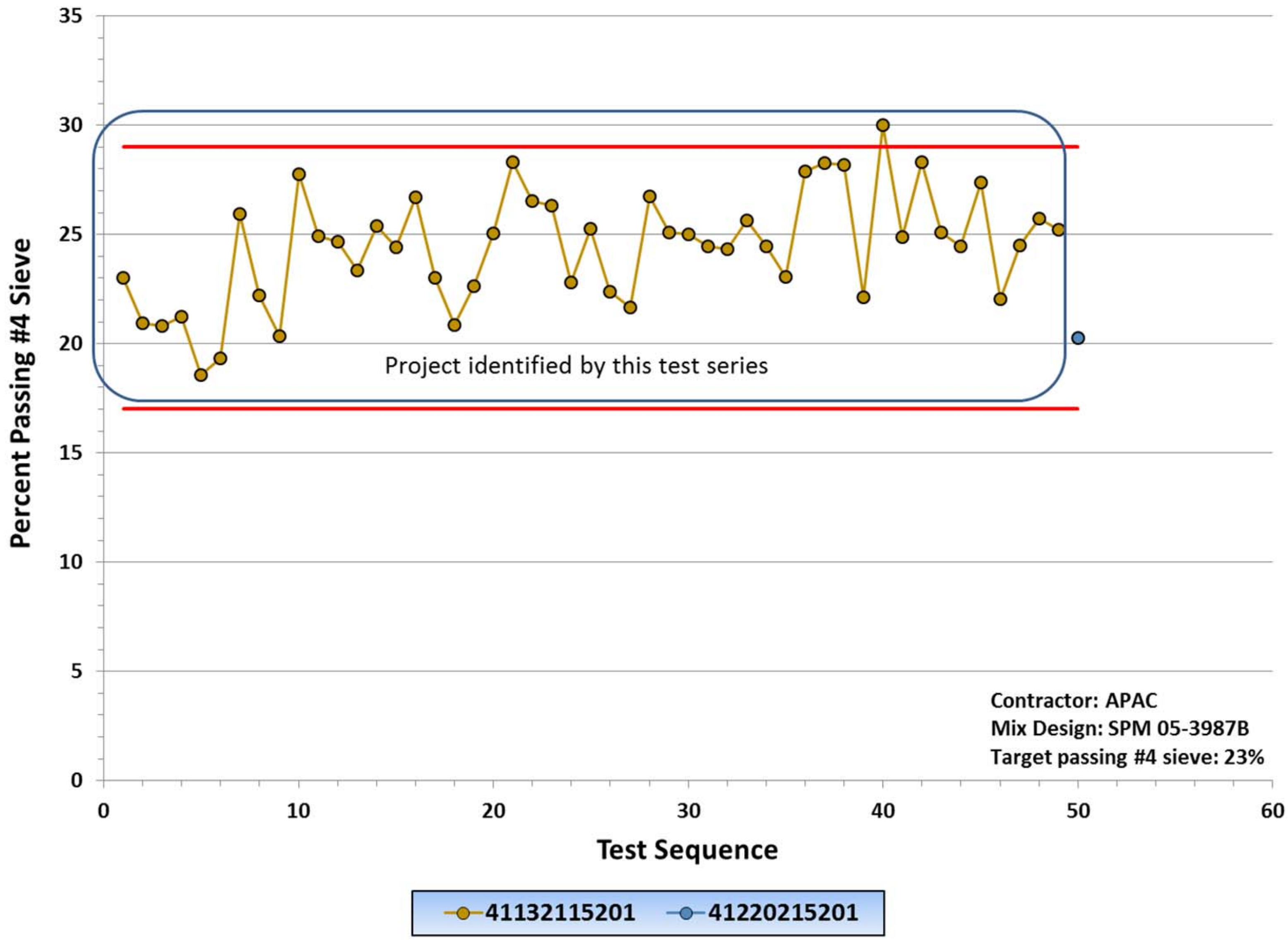
35
30
25
20
15
10
5
0
Percent Passing #4 Sieve
Project identified by this test series
Contractor: APAC
Mix Design: SPM 05-3987B
Target passing #4 sieve: 23%
0
10
20
30
40
50
60
Test Sequence
41132115201
41220215201

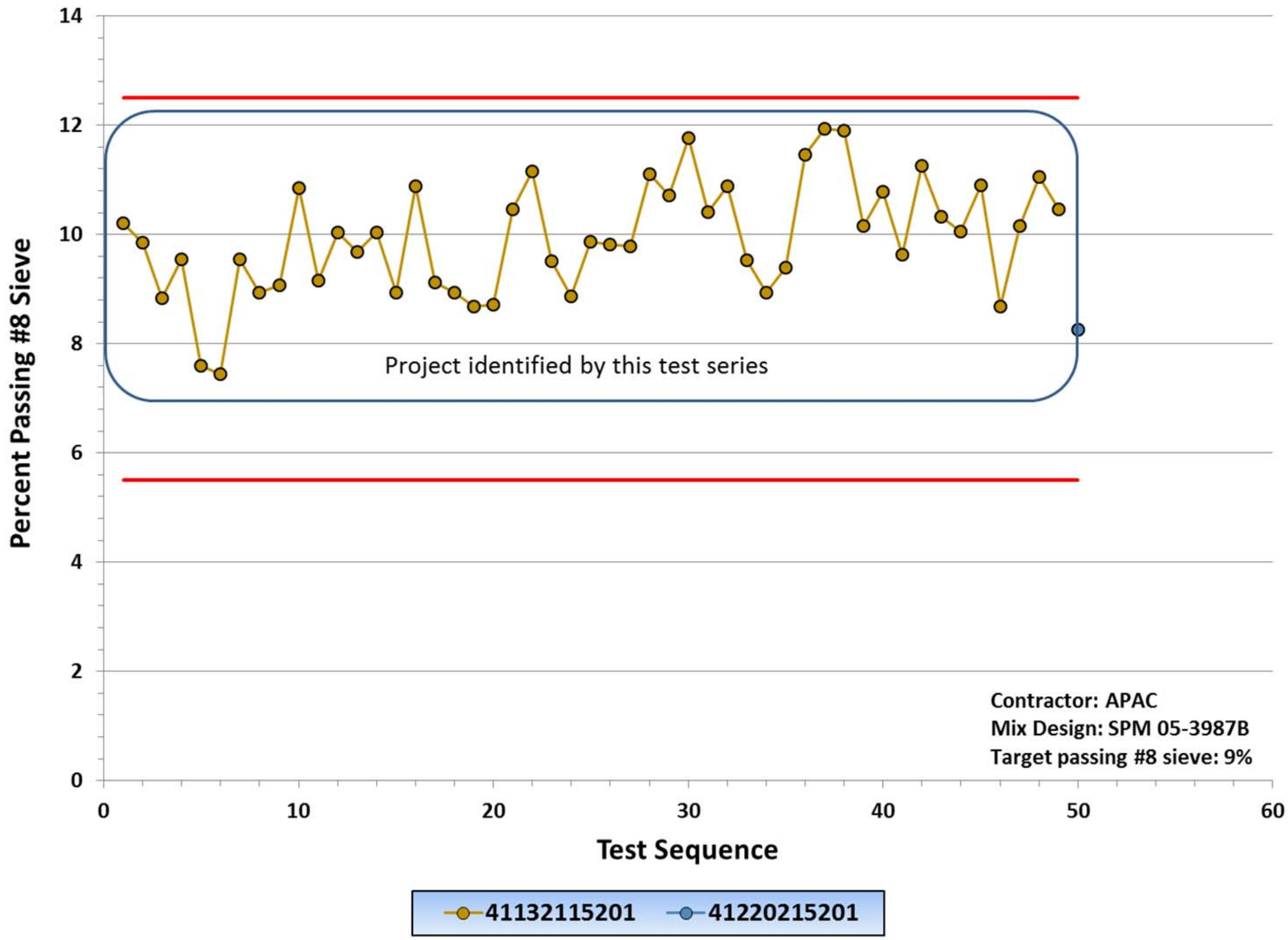

Percent Passing #8 Sieve
Test Sequence
Project identified by this test series
Contractor: APAC
Mix Design: SPM 05-3987B
Target passing #8 sieve: 9%
41132115201
41220215201
0
2
4
6
8
10
12
14
0
10
20
30
40
50
60

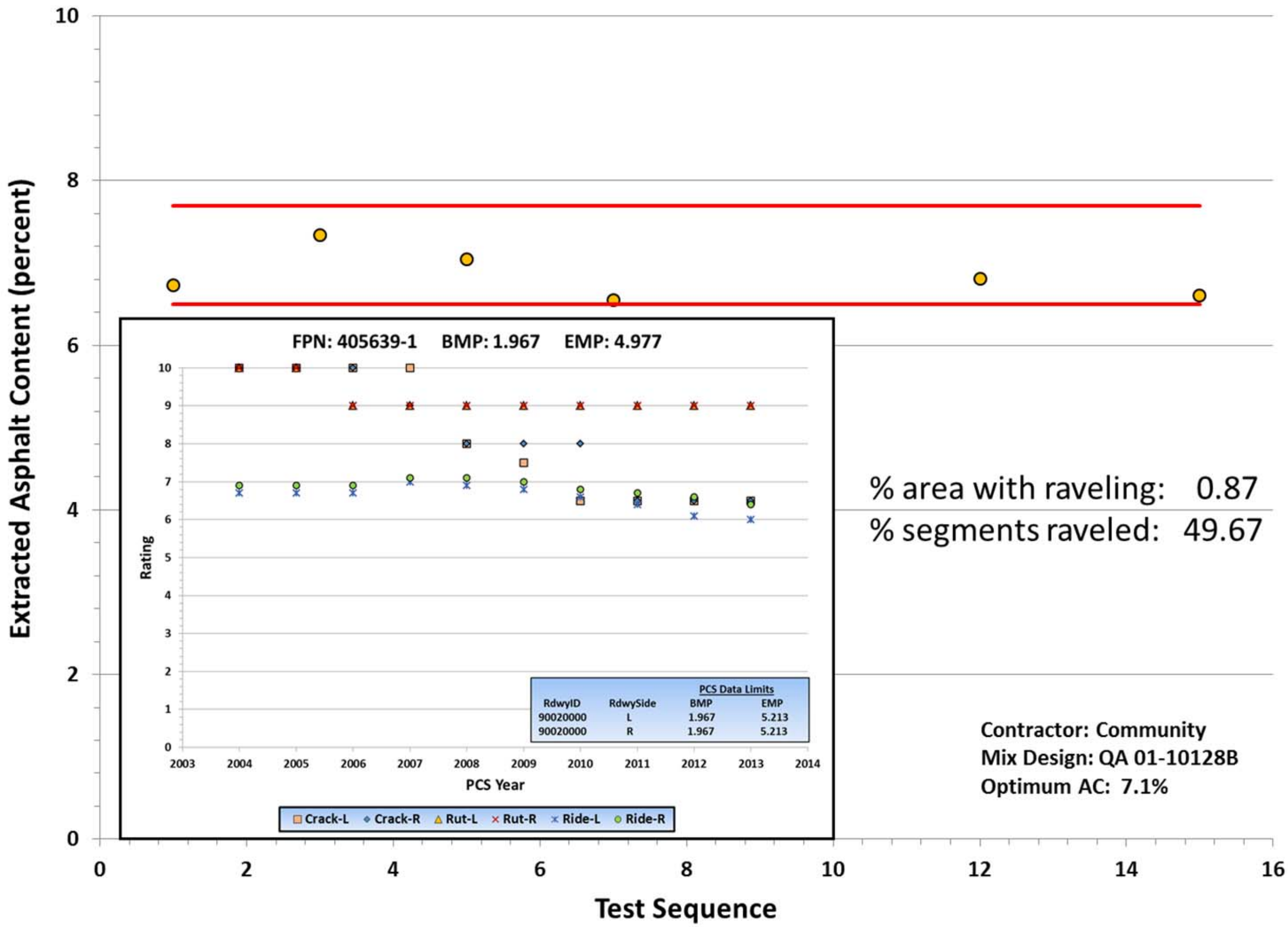
FPN: 405639-1 BMP: 1.967 EMP: 4.977
Rating
PCS Year
PCS Data Limits
RdwyID RdwySide BMP EMP
90020000 L 1.967 5.213
90020000 R 1.967 5.213
Crack-L Crack-R Rut-L Rut-R Ride-L Ride-R
% area with raveling: 0.87
% segments raveled: 49.67
Contractor: Community
Mix Design: QA 01-10128B
Optimum AC: 7.1%
Extracted Asphalt Content (percent)
Test Sequence

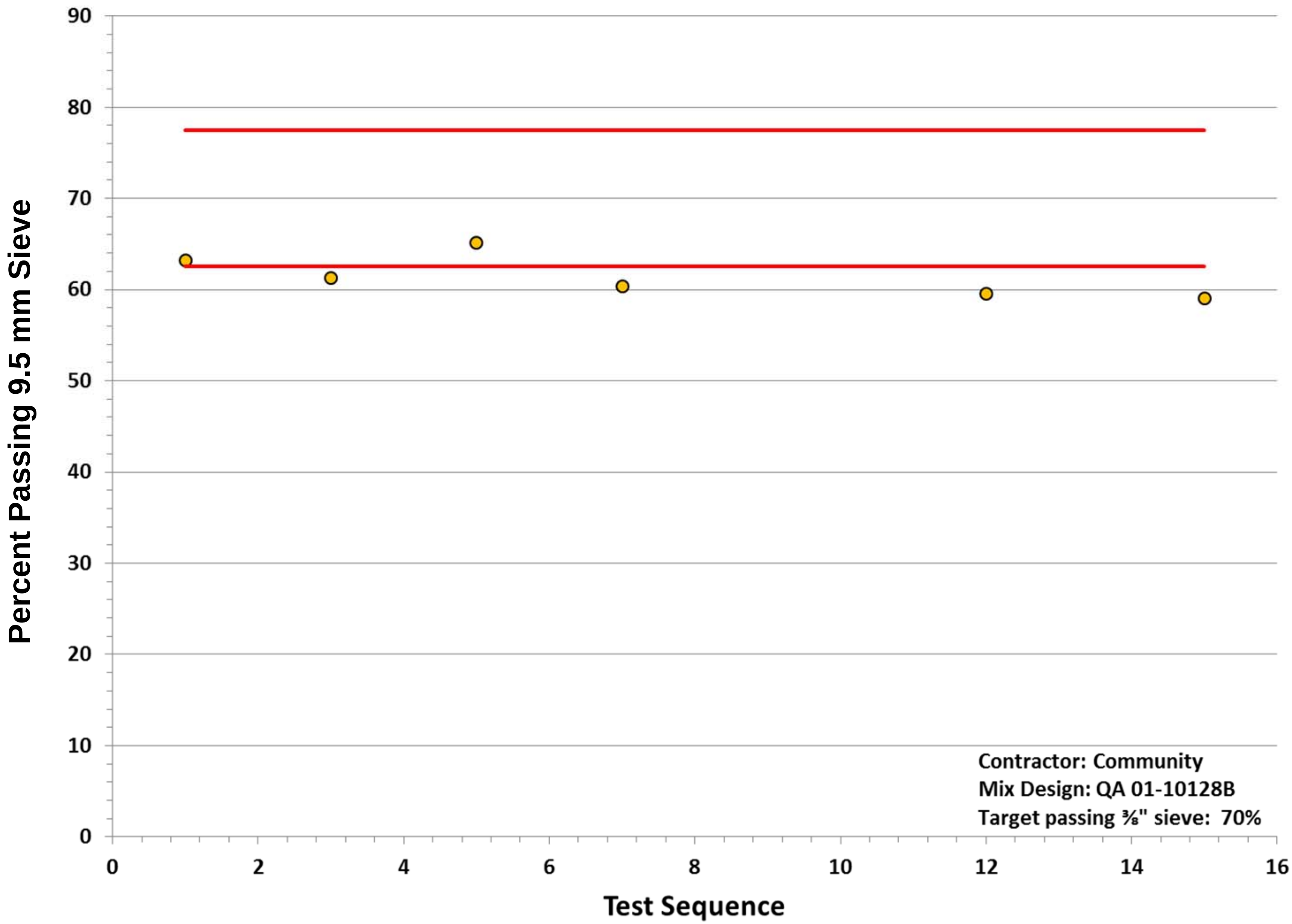
Percent Passing 9.5 mm Sieve
Test Sequence
Contractor: Community
Mix Design: QA 01-10128B
Target passing ⅜" sieve: 70%
0
10
20
30
40
50
60
70
80
90
0
2
4
6
8
10
12
14
16

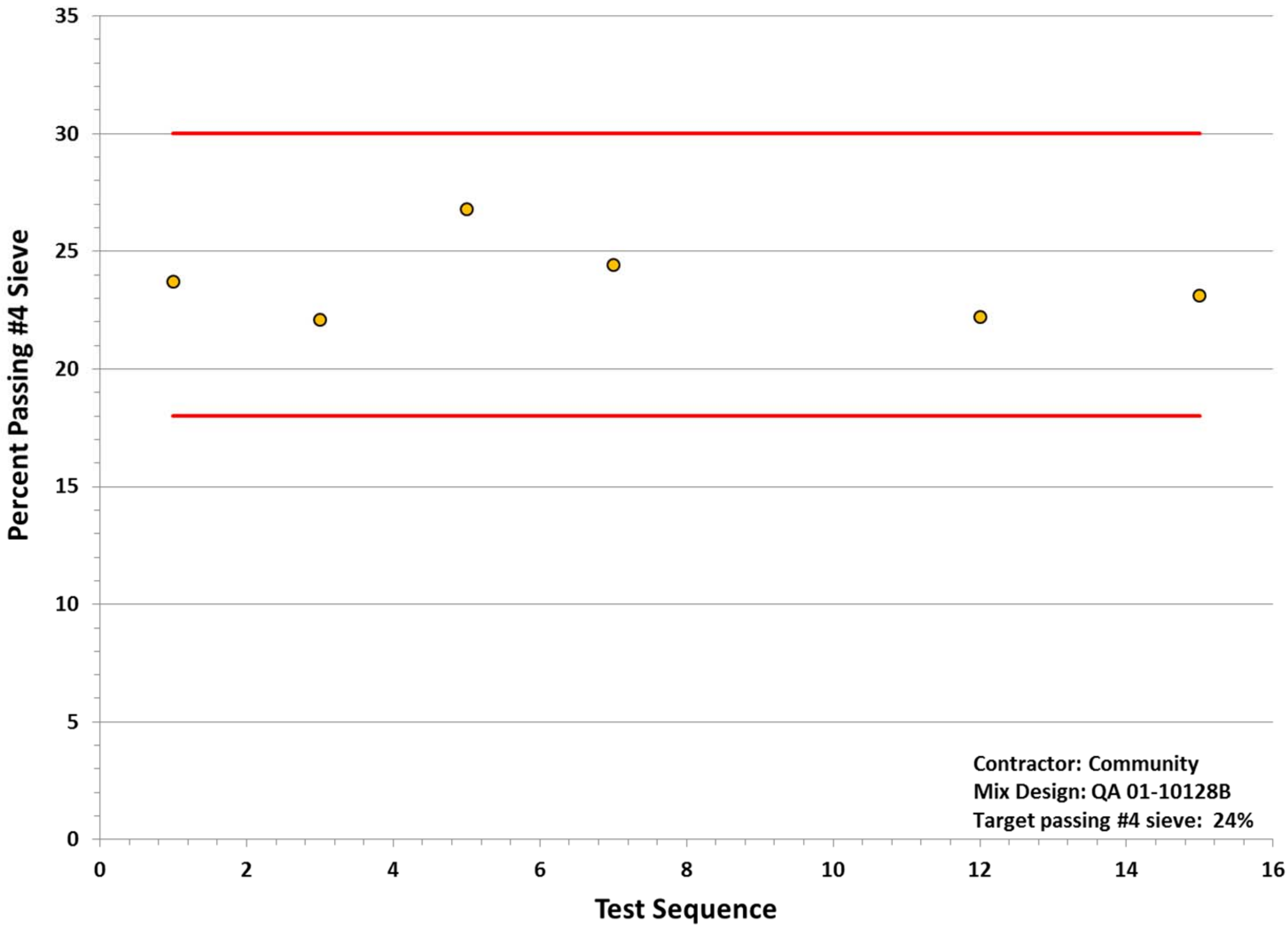
35
30
25
20
15
10
5
0
Percent Passing #4 Sieve
0
2
4
6
8
10
12
14
16
Test Sequence
Contractor: Community
Mix Design: QA 01-10128B
Target passing #4 sieve: 24%

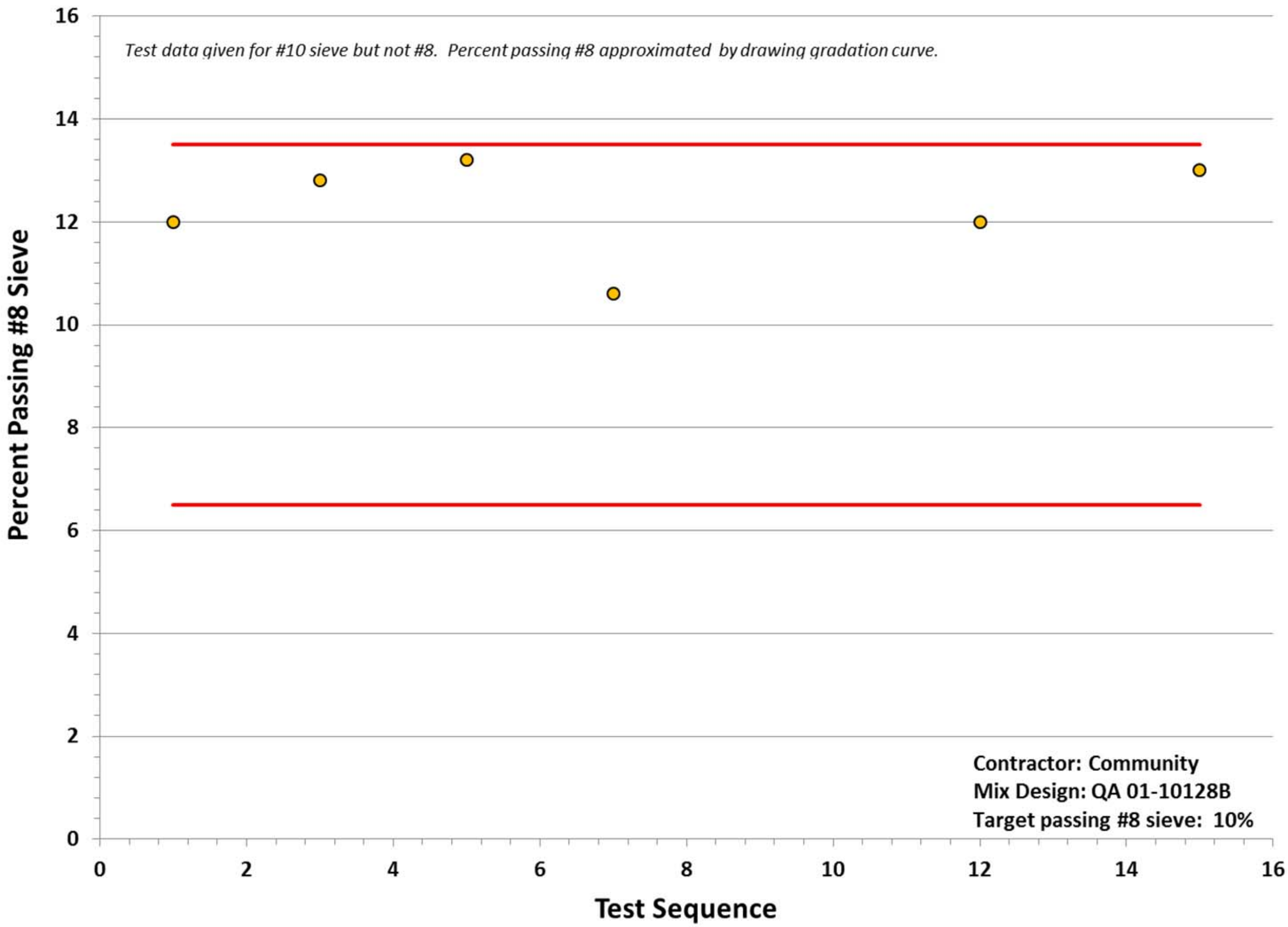
Test data given for #10 sieve but not #8. Percent passing #8 approximated by drawing gradation curve.
Percent Passing #8 Sieve
Test Sequence
Contractor: Community
Mix Design: QA 01-10128B
Target passing #8 sieve: 10%
0
2
4
6
8
10
12
14
16

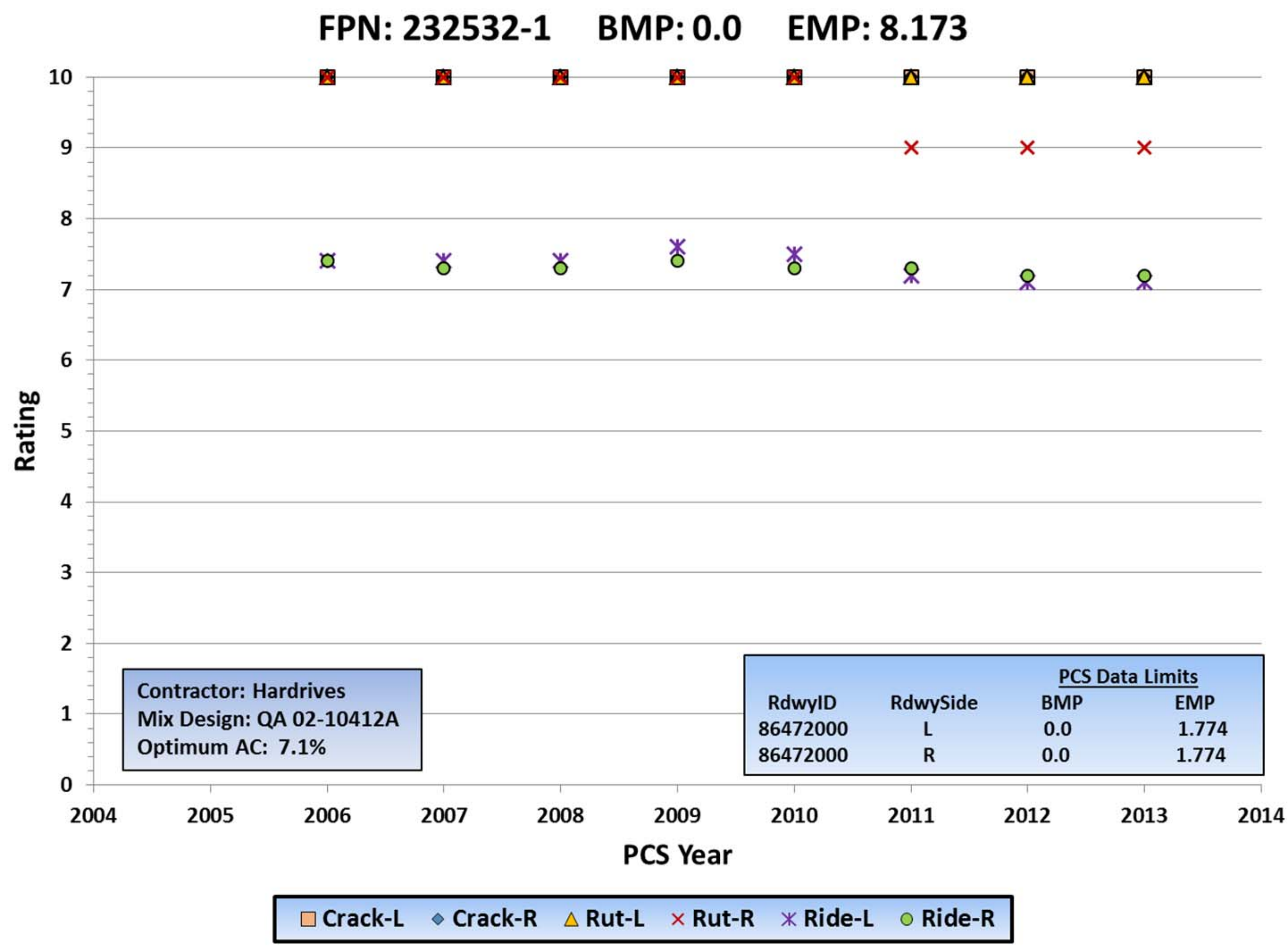
FPN: 232532-1 BMP: 0.0 EMP: 8.173
Rating
10
9
8
7
6
5
4
3
2
1
0
2004
2005
2006
2007
2008
2009
2010
2011
2012
2013
2014
PCS Year
Contractor: Hardrives
Mix Design: QA 02-10412A
Optimum AC: 7.1%
PCS Data Limits
RdwyID RdwySide BMP EMP
86472000 L 0.0 1.774
86472000 R 0.0 1.774
Crack-L
Crack-R
Rut-L
Rut-R
Ride-L
Ride-R

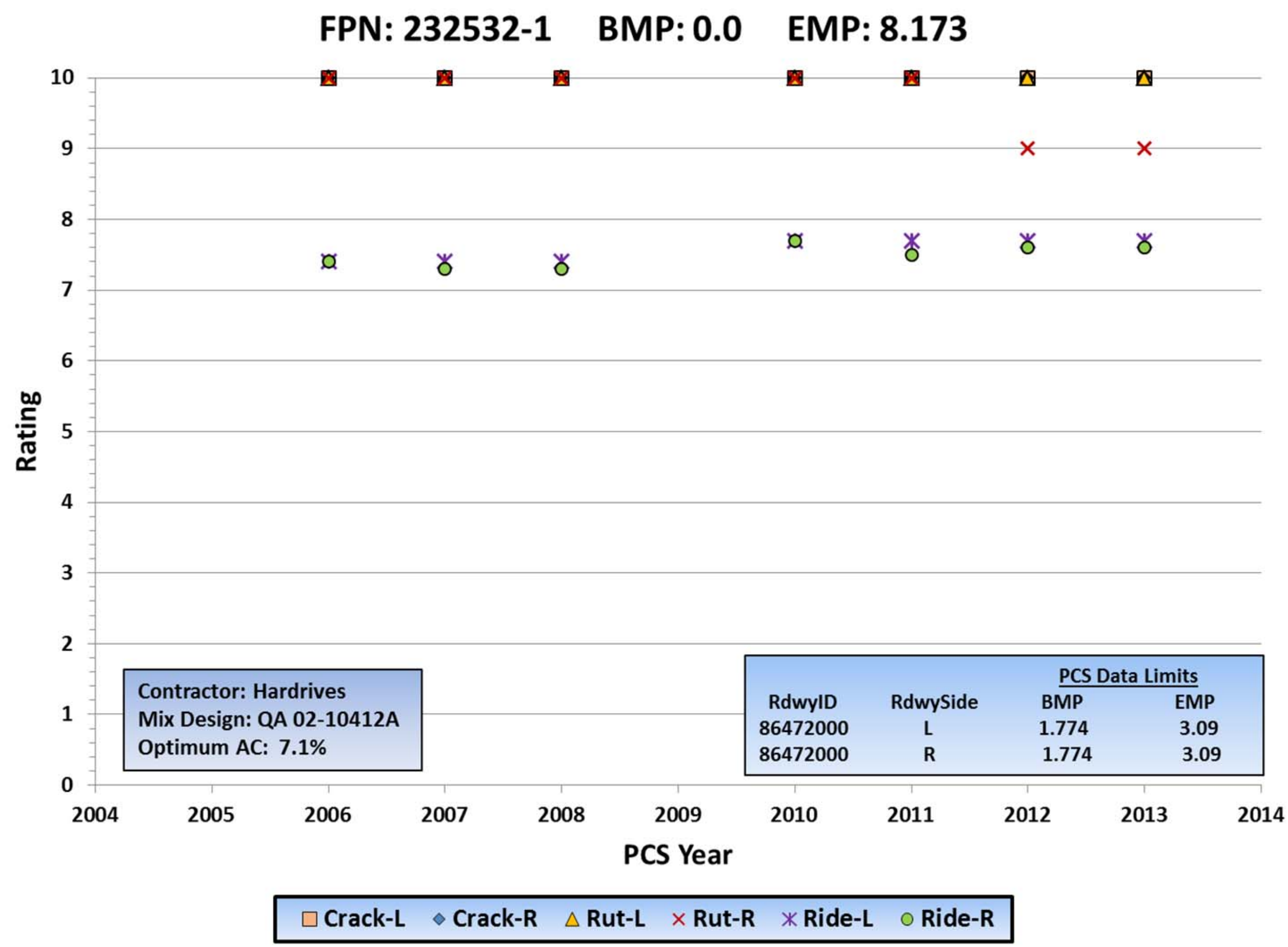
FPN: 232532-1 BMP: 0.0 EMP: 8.173
Rating
PCS Year
Contractor: Hardrives
Mix Design: QA 02-10412A
Optimum AC: 7.1%
PCS Data Limits
RdwyID RdwySide BMP EMP
86472000 L 1.774 3.09
86472000 R 1.774 3.09
Crack-L Crack-R Rut-L Rut-R Ride-L Ride-R

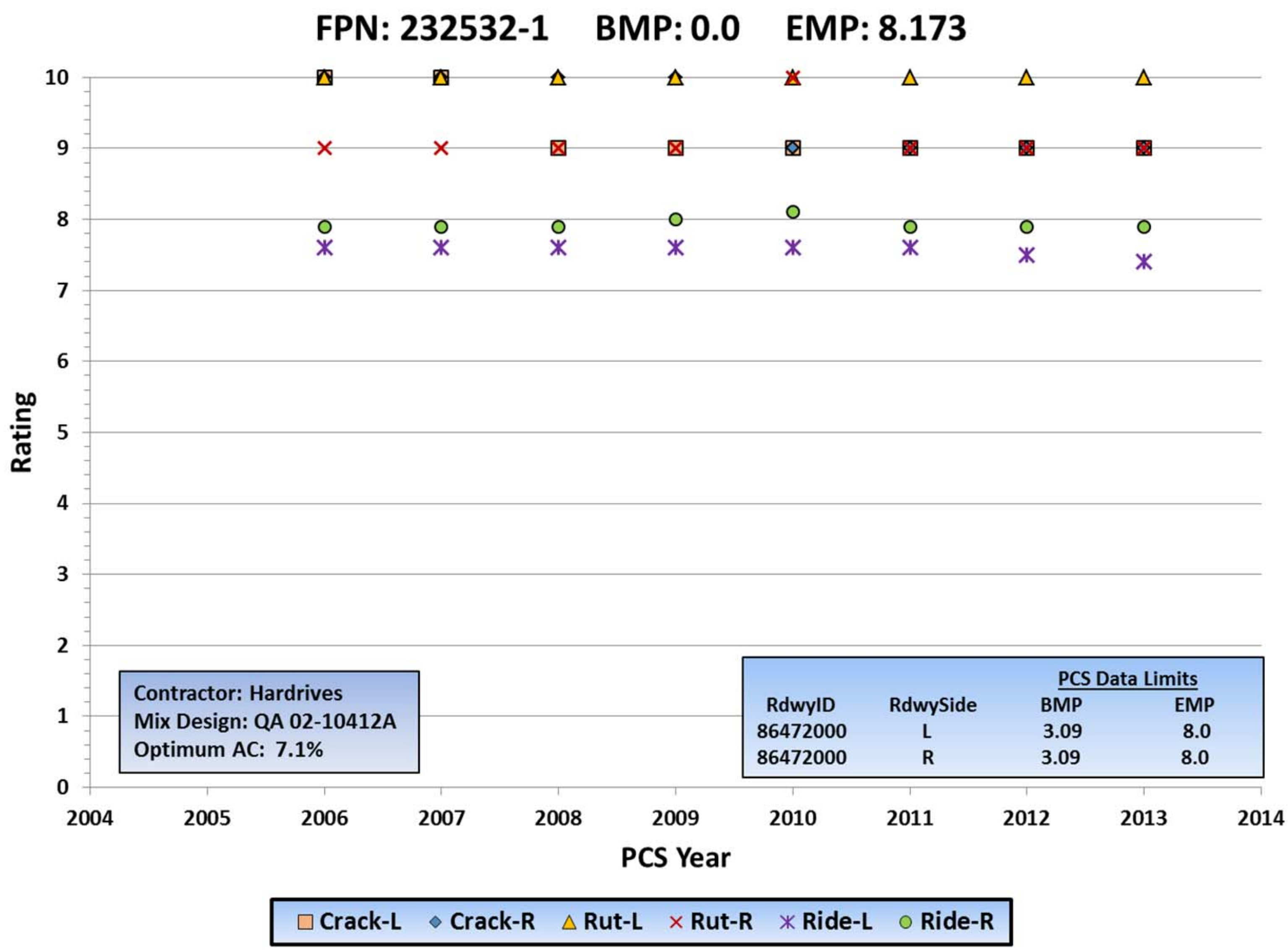
FPN: 232532-1 BMP: 0.0 EMP: 8.173
Rating
PCS Year
10
9
8
7
6
5
4
3
2
1
0
2004
2005
2006
2007
2008
2009
2010
2011
2012
2013
2014
Contractor: Hardrives
Mix Design: QA 02-10412A
Optimum AC: 7.1%
PCS Data Limits
RdwyID RdwySide BMP EMP
86472000 L 3.09 8.0
86472000 R 3.09 8.0
Crack-L
Crack-R
Rut-L
Rut-R
Ride-L
Ride-R

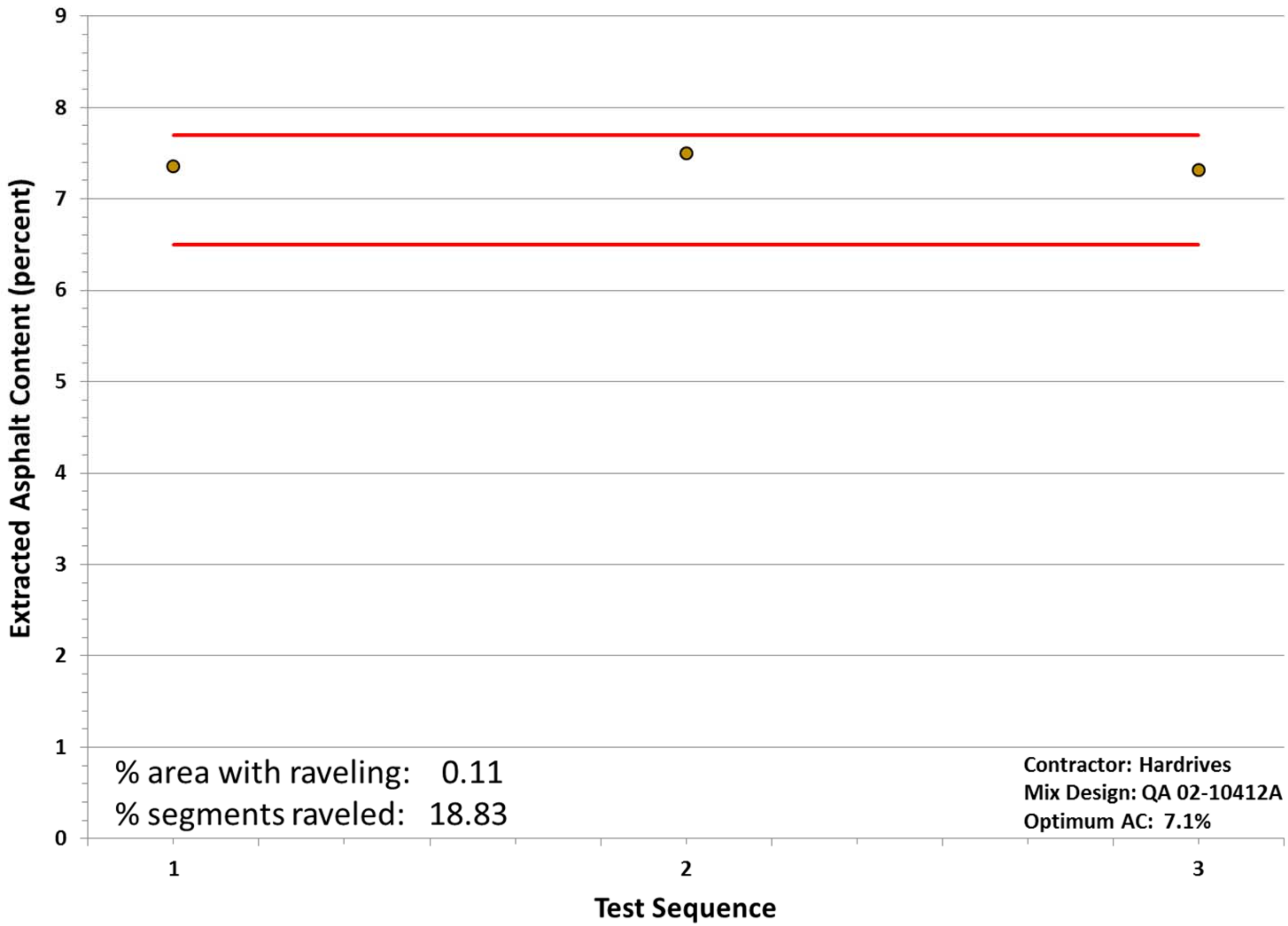

Extracted Asphalt Content (percent)
9
8
7
6
5
4
3
2
1
0
% area with raveling: 0.11
% segments raveled: 18.83
Contractor: Hardrives
Mix Design: QA 02-10412A
Optimum AC: 7.1%
1
2
3
Test Sequence

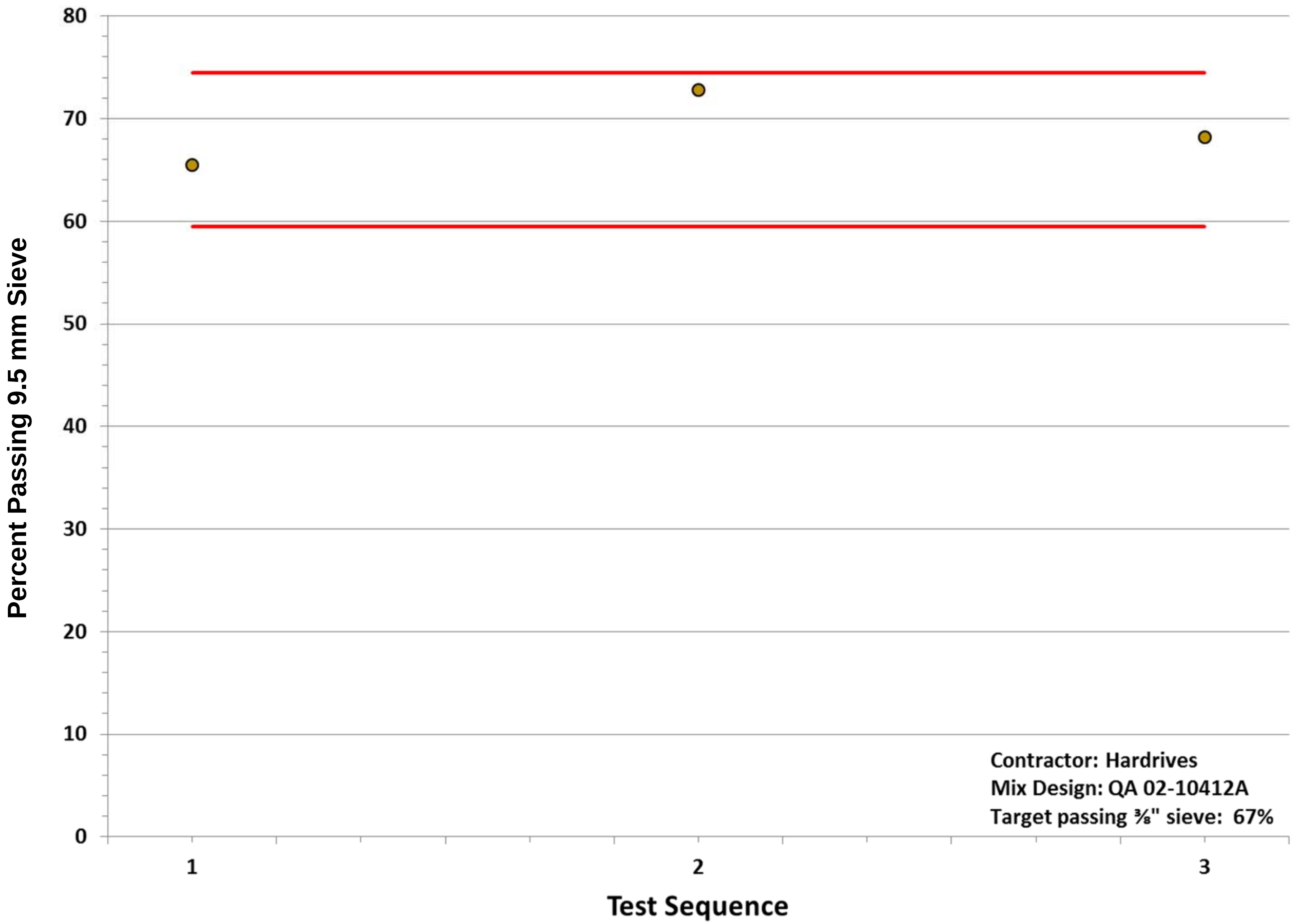
80
70
60
50
40
30
20
10
0
Percent Passing 9.5 mm Sieve
1
2
3
Test Sequence
Contractor: Hardrives
Mix Design: QA 02-10412A
Target passing ⅜" sieve: 67%

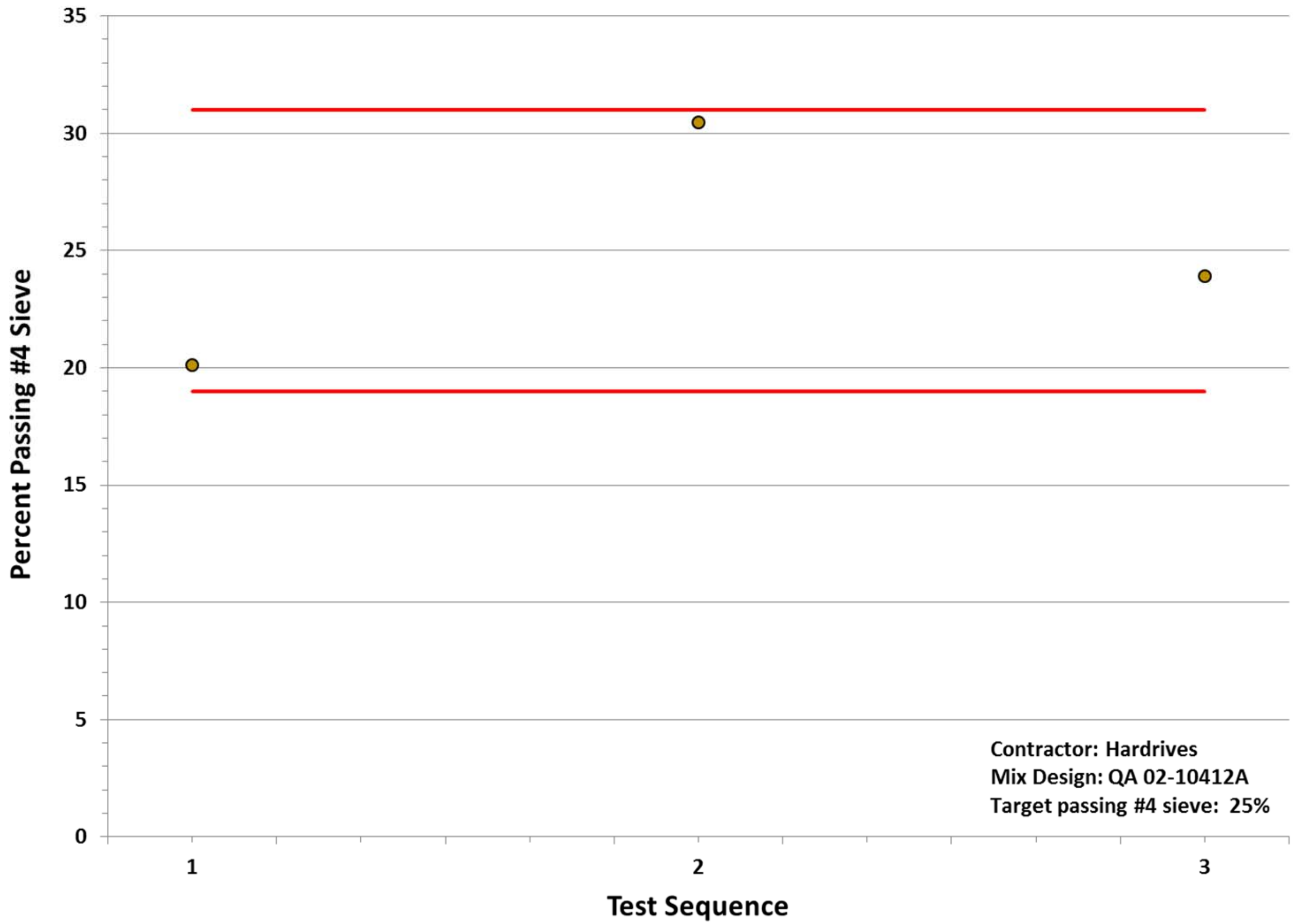

35
30
25
20
15
10
5
0
Percent Passing #4 Sieve
1
2
3
Test Sequence
Contractor: Hardrives
Mix Design: QA 02-10412A
Target passing #4 sieve: 25%

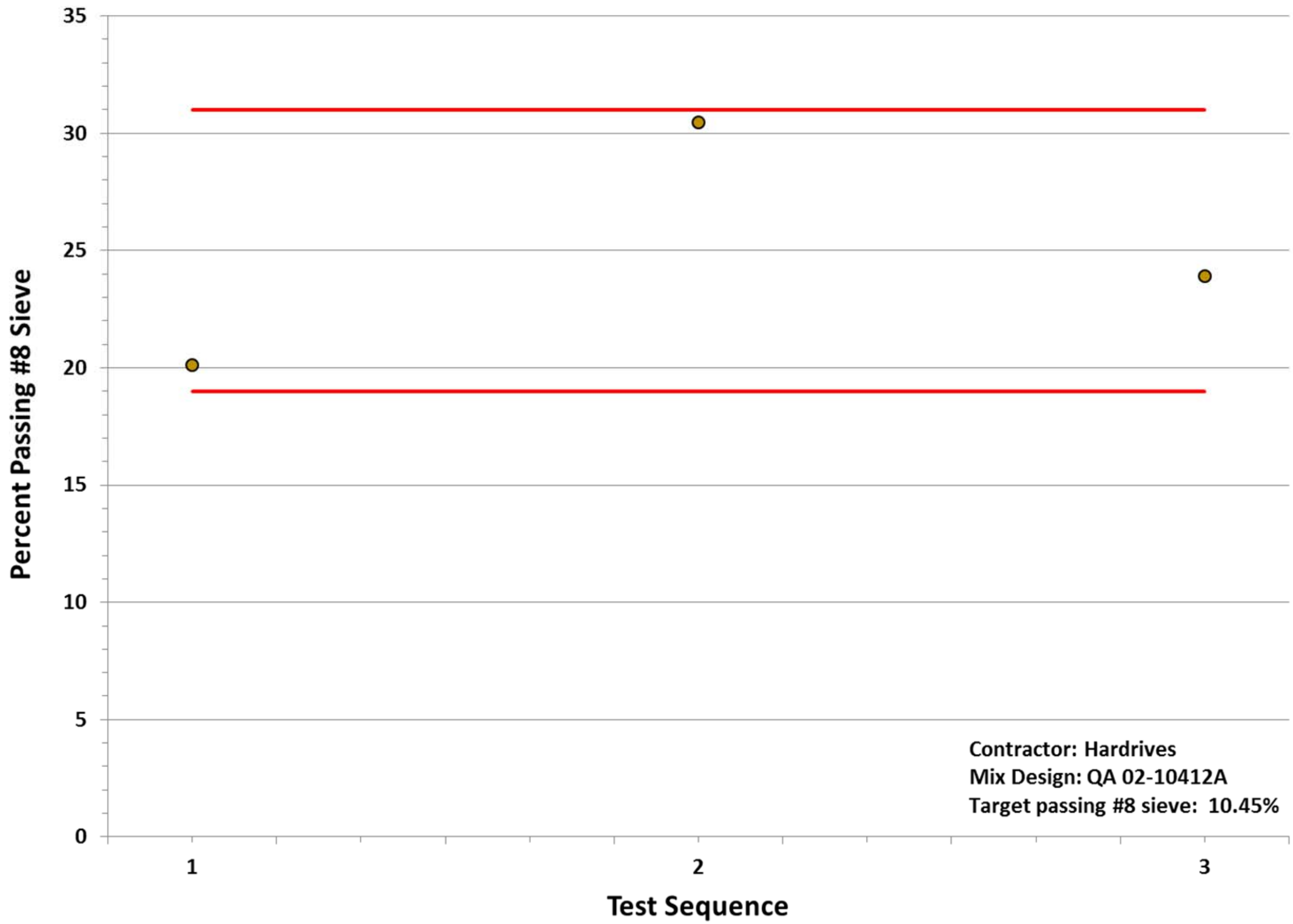

35
30
25
20
15
10
5
0
Percent Passing #8 Sieve
1
2
3
Test Sequence
Contractor: Hardrives
Mix Design: QA 02-10412A
Target passing #8 sieve: 10.45%

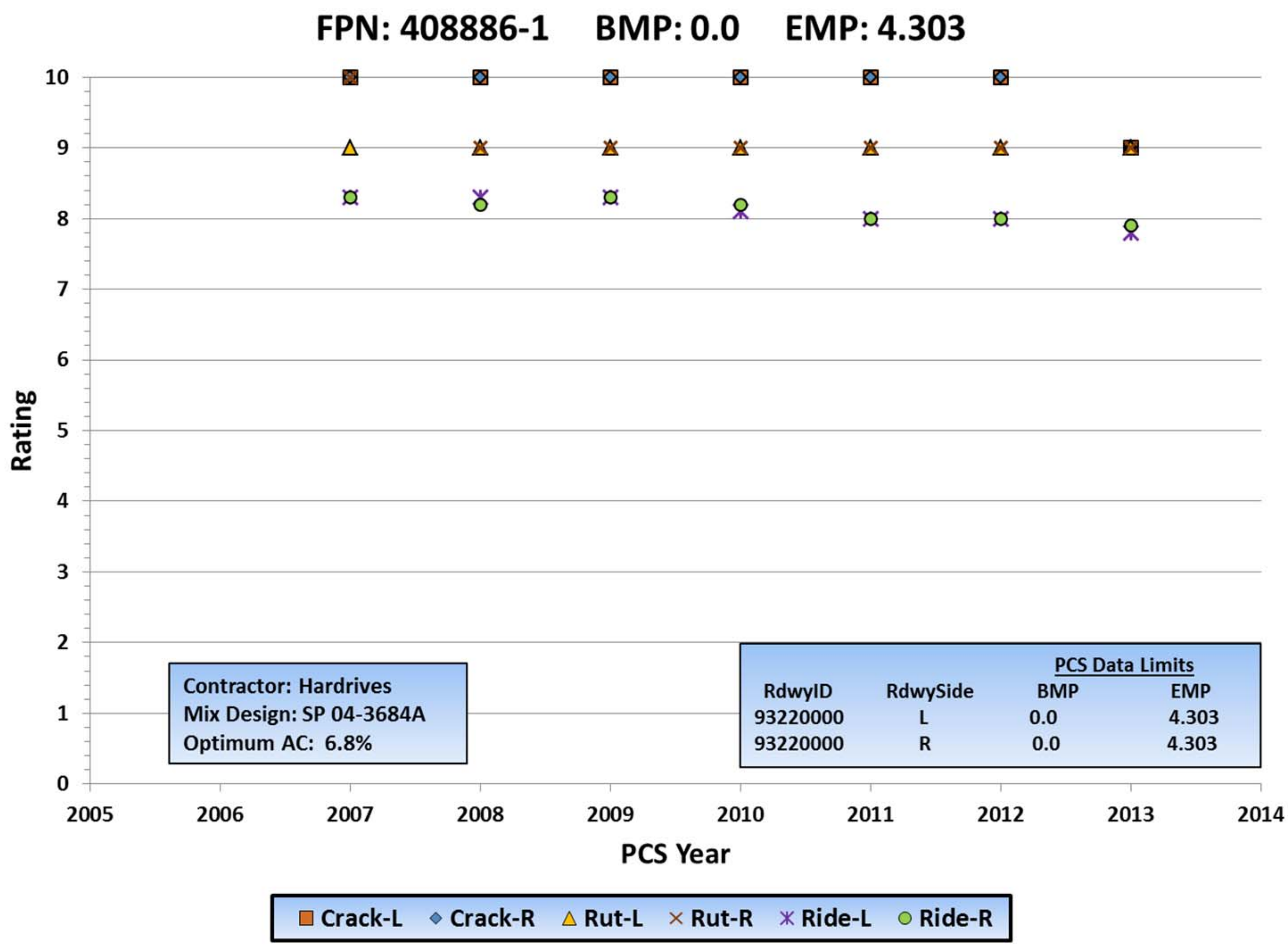
FPN: 408886-1 BMP: 0.0 EMP: 4.303
Rating
PCS Year
10
9
8
7
6
5
4
3
2
1
0
2005
2006
2007
2008
2009
2010
2011
2012
2013
2014
Contractor: Hardrives
Mix Design: SP 04-3684A
Optimum AC: 6.8%
PCS Data Limits
RdwyID RdwySide BMP EMP
93220000 L 0.0 4.303
93220000 R 0.0 4.303
Crack-L Crack-R Rut-L Rut-R Ride-L Ride-R

APPENDIX B.
SURFACE FREE ENERGY

The following discussion on SFE is adapted extensively from Bhasin et al. (2007), Little and Jones (2003), and Little and Bhasin (2006).

SFE (γ in ergs/cm^2) is a fundamental material property defined as the work required to create a new unit area of surface of a material. Acid-Base theory divides the total SFE into three components: a nonpolar or dispersive component known as the Lifshitz-van der Waals (LW) component, the Lewis acid component, and the Lewis base component. The total surface free energy of a material is represented as follows:

$$\gamma^{\text{total}} = \gamma^{\text{LW}} + \gamma^{+-} = \gamma^{\text{LW}} + 2\sqrt{\gamma^{+}\gamma^{-}} \quad \text{(B-1)}$$

Where:
γ = total surface free energy of the material.
γ^{LW} = LW component.
γ^{+-} = acid-base component.
γ^{+} = Lewis acid component.
γ^{-} = Lewis base component.

When the SFE components of two materials are known, Equation B-2 can be used to determine the work of adhesion between those materials:

$$W_{\text{AB}} = 2\sqrt{\gamma_{\text{A}}{}^{\text{LW}}\gamma_{\text{B}}{}^{\text{LW}}} + 2\sqrt{\gamma_{\text{A}}{}^{+}\gamma_{\text{B}}{}^{-}} + 2\sqrt{\gamma_{\text{A}}{}^{-}\gamma_{\text{B}}{}^{+}} \quad \text{(B-2)}$$

where, in an asphalt mixture, the subscripts A and B represent the aggregate and binder, respectively. For an aggregate to be durable and resistant to moisture damage, the work of adhesion between the aggregate and binder, W_{AB}, should be as high as possible. A higher magnitude of work of adhesion means that it takes more work to separate the binder from the aggregate surface.

In a three-phase system (as in the presence of moisture in an asphalt pavement), water is represented by the subscript W. According to Little and Jones (2003), water reduces the free energy of the three-phase system more than the binder does, which produces a thermodynamically favorable condition of minimum surface energy. This means that the aggregate has a strong preference for water over binder. When water displaces the binder from the aggregate surface, as illustrated in Figure B-1, the work of debonding, $W_{\text{ABW}}^{\text{wet}}$, is determined using Equation B-3:

$$W_{\text{ABW}}^{\text{wet}} = \gamma_{\text{AW}} + \gamma_{\text{BW}} - \gamma_{\text{AB}} \quad \text{(B-3)}$$

where the subscripts AW, BW, and AB represent the interfacial energy between the aggregate and water, binder and water, and aggregate and binder, respectively. The work of debonding can also be thought of as the reduction in free energy of the system when water displaces the binder from the aggregate surface. A higher magnitude of $W_{\text{ABW}}^{\text{wet}}$ indicates a high thermodynamic potential for water to cause debonding; therefore, it is desirable that this quantity be as small as possible to reduce moisture sensitivity.

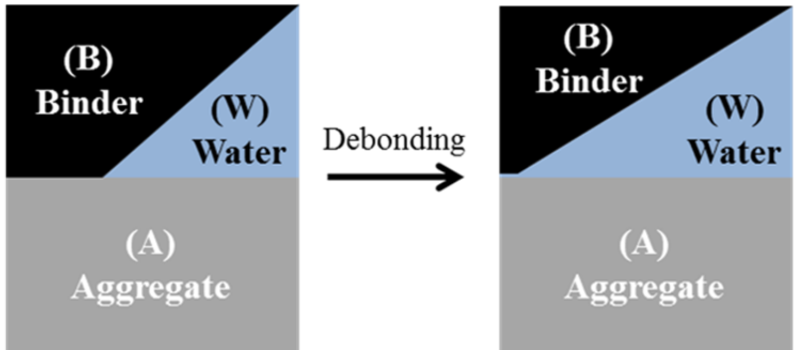

Figure B-1. Displacement of the binder from Aggregate-Binder Interface by water (Little and Bhasin 2006).

The interfacial energy between any two materials, i and j, is calculated using each material's SFE components from the relationship given in Equation B-4:

$$\gamma_{ij} = \gamma_i + \gamma_j - 2\sqrt{\gamma_i^{LW}\gamma_j^{LW}} - 2\sqrt{\gamma_i^{+}\gamma_j^{-}} - 2\sqrt{\gamma_i^{-}\gamma_j^{+}} \qquad \text{(B-4)}$$

The work of cohesion, W_{BB}, can be defined as the amount of work required to separate a column of liquid (or solid) in two and is given by Equation B-5. This component plays an important role in the loss of cohesion and degradation of the binder in the presence of water.

$$W_{BB} = 2\gamma_B \qquad \text{(B-5)}$$

Equations B-1 through B-5 provide for the calculation of the three quantities needed to evaluate the thermodynamic potential of the asphalt mixture in the presence of water: W_{AB}, the work of adhesion between the aggregate and the binder; W_{ABW}^{wet}, the work of debonding of that system in the presence of water; and W_{BB}, the work of cohesion of the binder. Four additional energy parameters, which combine these quantities, provide for an enhanced method to assess the mixture's susceptibility to moisture damage.

The ratio of the work of adhesion to the work of debonding is the first energy parameter, ER_1, and it is directly proportional to the moisture resistance of the asphalt mixture. Combinations of binders that produce a higher value of ER_1 are less sensitive to moisture.

$$ER_1 = \left|\frac{W_{AB}}{W_{ABW}^{wet}}\right| \qquad \text{(B-6)}$$

An important factor not considered in ER_1 is the wettability of an aggregate by the binder. Wettability refers to the ability of one material to wet the surface of another material. It also refers to the ability of a material to penetrate into the microtextural surface of another material. Therefore, a binder with better wettability has a stronger affinity to coat the surface of an aggregate than does a binder with lower wettability. A higher wettability value allows for fewer weak points at the aggregate-binder interface and thus a lower susceptibility to moisture damage.

ER_2 is the ratio of the wettability of the aggregate by the binder to the magnitude of the work of debonding and is given by Equation B-7. Again, a higher value of ER_2 would suggest that the aggregate-binder combination would be less sensitive to moisture.

$$\mathrm{ER}_2 = \left|\frac{W_{AB}-W_{BB}}{W_{ABW}^{wet}}\right| \tag{B-7}$$

Given the energy parameters, ER_1 and ER_2, it is necessary to consider SSA of the aggregate. A higher SSA will enhance the chance of the binder bonding with the aggregate. In addition, a higher SSA would mean a greater microtexture on the surface of the aggregate and a greater contact area for the aggregate-binder bond. The two energy parameters are therefore modified in Equations B-8 and B-9 to account for the SSA of the aggregate.

$$\mathrm{ER}_1 \times \mathrm{SSA} = \left|\frac{W_{AB}}{W_{ABW}^{wet}}\right| \times \mathrm{SSA} \tag{B-8}$$

$$\mathrm{ER}_2 \times \mathrm{SSA} = \left|\frac{W_{AB}-W_{BB}}{W_{ABW}^{wet}}\right| \times \mathrm{SSA} \tag{B-9}$$

In summary, the aggregate and binder SFE components can be obtained through laboratory testing. The SFE components can be combined using thermodynamic principles to calculate four energy parameters: ER_1, ER_2, $ER_1 \times SSA$, and $ER_2 \times SSA$. These energy parameters have been shown to be an effective tool to use in selecting materials with adequate moisture damage resistance in the field.

APPENDIX C. STATISTICAL ANALYSIS

This appendix contains details of the statistical analysis done on the performance test results.

C.1. Permeability

The objective of this analysis was to assess the effects of aggregate gradation and binder type on permeability. The factors of interest and their levels were gradation with three levels (A: limestone with fines; B: coarser limestone; C: coarser granite) and binder with two levels (PMA, ARB). Other extraneous factors that could potentially affect permeability such as AV content, specimen height, and specimen diameter were controlled throughout the experiment

There were 18 permeability measurements obtained at each factor-level combination with three replications. An ANOVA having gradation and binder as main effects and a two-way interaction effect between them was fitted to the data. Table C-1 contains the analysis outputs obtained by the JMP statistical package (SAS product). It can be observed from Table C-1 (see Effect Tests) that the effect of the two-way interaction Gradation*Binder was statistically significant at α=0.05. Table C-2 presents the predicted values for permeability for each factor. The Tukey's honest significant differences (HSD) test was carried out for the levels of Gradation*Binder to determine which of those levels were statistically different. It can be seen in Figure C-1 and Table C-3 that when Binder=PMA, the predicted permeability value for Gradation Level C was significantly lower than A or B, while there were not statistically significant differences across the levels of gradation when Binder=ARB.

Table C-1. Results of Fitting ANOVA to Permeability Data with Gradation and Binder as Factors

Summary of Fit

RSquare	0.814785
RSquare Adj	0.737612
Root Mean Square Error	0.008309
Mean of Response	0.050633
Observations (or Sum Wgts)	18

Analysis of Variance

Source	DF	Sum of Squares	Mean Square	F Ratio
Model	5	0.00364432	0.000729	10.5579
Error	12	0.00082842	0.000069	**Prob > F**
C. Total	17	0.00447274		0.0005*

Effect Tests

Source	Nparm	DF	Sum of Squares	F Ratio	Prob > F
Gradation	2	2	0.00275665	19.9656	0.0002*
Binder	1	1	0.00009068	1.3135	0.2741
Gradation*Binder	2	2	0.00079699	5.7724	0.0175*

Table C-2. Effect Details for Permeability Data with Gradation and Binder as Factors

Gradation

Least Squares Means Table

Level	Least Sq Mean	Std Error	Mean
A	0.05920000	0.00339202	0.059200
B	0.05956667	0.00339202	0.059567
C	0.03313333	0.00339202	0.033133

Binder

Least Squares Means Table

Level	Least Sq Mean	Std Error	Mean
ARB	0.04838889	0.00276958	0.048389
PMA	0.05287778	0.00276958	0.052878

Gradation*Binder

Least Squares Means Table

Level	Least Sq Mean	Std Error
A,ARB	0.04790000	0.00479705
A,PMA	0.07050000	0.00479705
B,ARB	0.05963333	0.00479705
B,PMA	0.05950000	0.00479705
C,ARB	0.03763333	0.00479705
C,PMA	0.02863333	0.00479705

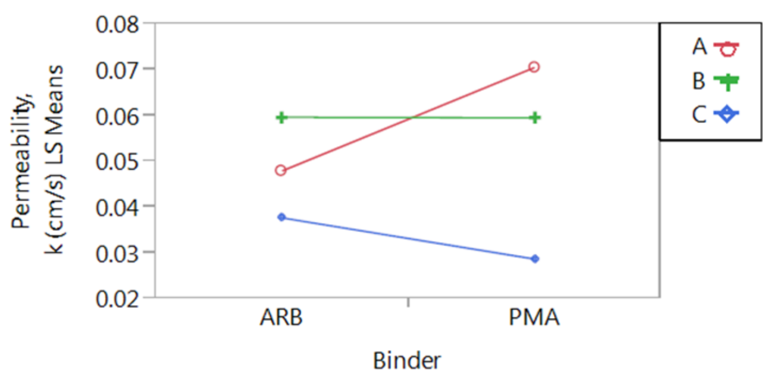

Figure C-1. Least squares mean (LSM) plot for permeability data with gradation and binder as factors.

Table C-3. Tukey's HSD for Permeability Data with Gradation and Binder as Factors

Level [a]				Least Sq Mean
A,PMA	A			0.07050000
B,ARB	A	B		0.05963333
B,PMA	A	B		0.05950000
A,ARB	A	B	C	0.04790000
C,ARB		B	C	0.03763333
C,PMA			C	0.02863333

[a] *Levels not connected by the same letter are significantly different.*

Researchers identified an observation (highlighted in red in Figure C-2) that could be considered an outlier. To examine the effect of the outlier, the observation was removed from the data and the ANOVA model refitted. Table C-4 shows the result of fitting the ANOVA after excluding the potential outlier. It can be observed from the Effect Tests that Gradation*Binder was statistically significant at α=0.05 along with the main effects. From the LSM results for Gradation*Binder and the corresponding interaction plot shown in Table C-4 and Figure C-3, it can be seen that the predicted value of permeability for the level (C, ARB) was mainly affected by the exclusion of the outlier. Tukey's HSD results, which are listed in Table C-6, again suggested that the predicted permeability value for Gradation Level C was significantly lower than A or B, while there were not statistically significant differences across the levels of gradation when Binder=ARB.

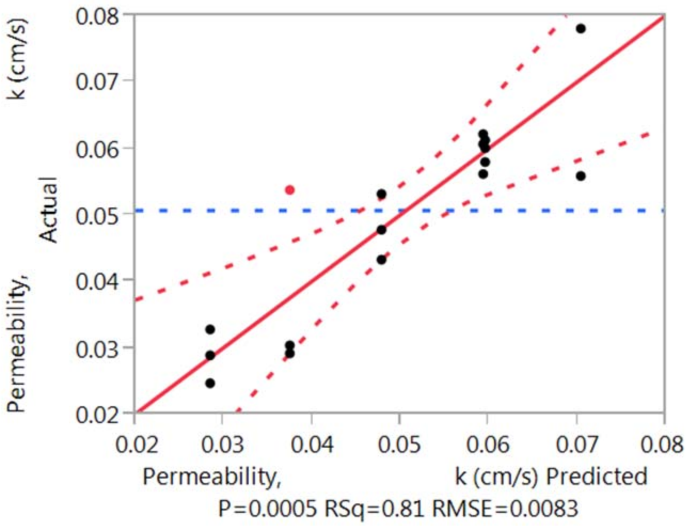

Figure C-2. Actual vs. predicted permeability plot.

Table C-4. Results of Fitting the ANOVA to Permeability Data after Excluding the Outlier with Gradation and Binder as Factors

Summary of Fit

RSquare	0.901135
RSquare Adj	0.856196
Root Mean Square Error	0.006333
Mean of Response	0.050453
Observations (or Sum Wgts)	17

Analysis of Variance

Source	DF	Sum of Squares	Mean Square	F Ratio
Model	5	0.00402157	0.000804	20.0525
Error	11	0.00044121	0.000040	**Prob > F**
C. Total	16	0.00446278		<.0001*

Effect Tests

Source	Nparm	DF	Sum of Squares	F Ratio	Prob > F
Gradation	2	2	0.00314122	39.1573	<.0001*
Binder	1	1	0.00021335	5.3190	0.0416*
Gradation*Binder	2	2	0.00051518	6.4220	0.0142*

Table C-5. Effect Details for Permeability Data after Excluding the Outlier with Gradation and Binder as Factors

Gradation

Least Squares Means Table

Level	Least Sq Mean	Std Error	Mean
A	0.05920000	0.00258555	0.059200
B	0.05956667	0.00258555	0.059567
C	0.02911667	0.00289073	0.029020

Binder

Least Squares Means Table

Level	Least Sq Mean	Std Error	Mean
ARB	0.04571111	0.00228024	0.047725
PMA	0.05287778	0.00211109	0.052878

Gradation*Binder

Least Squares Means Table

Level	Least Sq Mean	Std Error
A,ARB	0.04790000	0.00365651
A,PMA	0.07050000	0.00365651
B,ARB	0.05963333	0.00365651
B,PMA	0.05950000	0.00365651
C,ARB	0.02960000	0.00447830
C,PMA	0.02863333	0.00365651

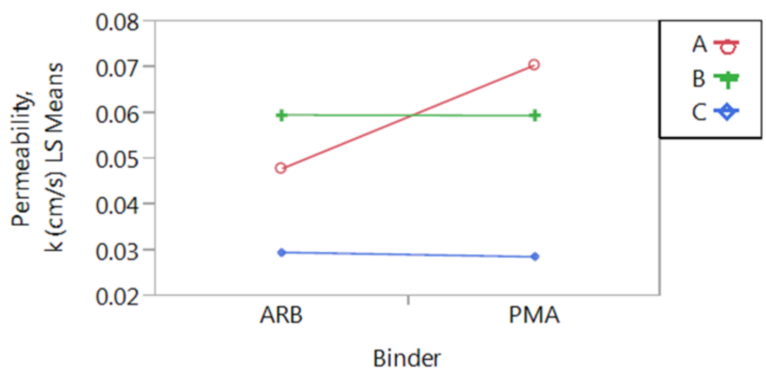

Figure C-3. LSM plot for permeability data after excluding the outlier.

Table C-6. Tukey's HSD for Permeability Data after Excluding the Outlier with Gradation and Binder as Factors

Level [a]					Least Sq Mean
A,PMA	A				0.07050000
B,ARB	A	B			0.05963333
B,PMA	A	B			0.05950000
A,ARB		B	C		0.04790000
C,ARB			C	D	0.02960000
C,PMA				D	0.02863333

[a] *Levels not connected by the same lette, are significantly different.*

The ANOVA results using mixture as single main factor (instead of gradation and binder separately) are presented in Table C-7 and Table C-8. The dataset considered was the one after excluding the outlier. The results did show statistically significant differences at α=0.05 (Table C-7), especially between mixtures 1 and 5 (Table C-9 and Figure C-4).

Table C-7. Results of Fitting the ANOVA to Permeability Data with Mixture as a Factor

Summary of Fit

RSquare	0.901135
RSquare Adj	0.856196
Root Mean Square Error	0.006333
Mean of Response	0.050453
Observations (or Sum Wgts)	17

Analysis of Variance

Source	DF	Sum of Squares	Mean Square	F Ratio
Model	5	0.00402157	0.000804	20.0525
Error	11	0.00044121	0.000040	**Prob > F**
C. Total	16	0.00446278		<.0001*

Effect Tests

Source	Nparm	DF	Sum of Squares	F Ratio	Prob > F
Mixture	5	5	0.00402157	20.0525	<.0001*

Table C-8. Effect Details for Permeability Data with Mixture as a Factor

Least Squares Means Table

Level	Least Sq Mean	Std Error	Mean
1	0.07050000	0.00365651	0.070500
2	0.04790000	0.00365651	0.047900
3	0.05950000	0.00365651	0.059500
4	0.05963333	0.00365651	0.059633
5	0.02863333	0.00365651	0.028633
6	0.02960000	0.00447830	0.029600

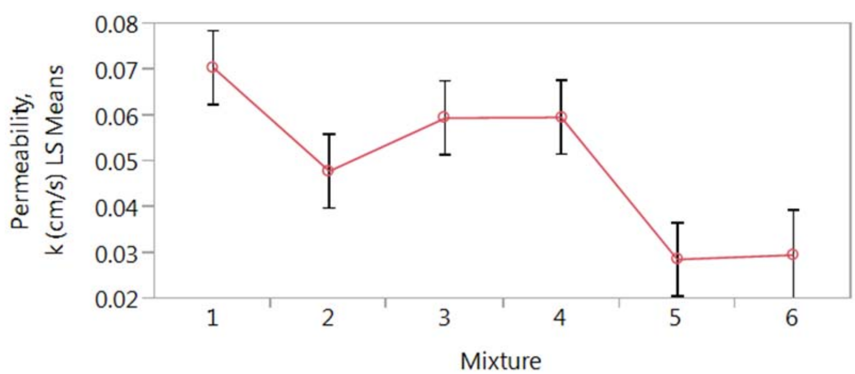

Figure C-4. LSM plot for permeability data with mixture as a factor.

Table C-9. Tukey's HSD for Permeability Data with Mixture as a Factor

Level [a]					Least Sq Mean
1	A				0.07050000
4	A	B			0.05963333
3	A	B			0.05950000
2		B	C		0.04790000
6			C	D	0.02960000
5				D	0.02863333

[a] *Levels not connected by the same letter are significantly different.*

C.2. Cantabro

C.2.1. MIST Moisture Conditioning

The objective of this analysis was to assess the effects of aggregate gradation, binder type, and moisture conditioning on Cantabro loss. The factors of interest and their levels were gradation with three levels (A: limestone w/fines, B: coarser limestone, C: coarser granite), binder with two levels (PMA, ARB), and conditioning with two levels (no MIST, MIST). Other extraneous factors that could potentially affect Cantabro loss such as AV content, specimen height, and specimen diameter were controlled throughout the experiment.

There were 36 Cantabro loss measurements obtained at each factor-level combination with three replications. An ANOVA with gradation, binder, and conditioning as main effects along with all possible two-way interaction effects among them was fitted to the data. Table C-10 contains the analysis outputs obtained by the JMP statistical package (SAS product). It can be observed from Table C-10 (see Effect Tests) that only gradation and binder were statistically significant at α=0.05.

Table C-11 presents the predicted values for Cantabro loss for each level of factors (see LSM results) and Tukey's HSD test for gradation (main effect that was statistically significant and had more than three levels). It can be seen that Gradation Level A led to a significantly lower Cantabro loss than B or C, while Gradation Levels B and C were not significantly different from each other. Also, for binder, ARB led to a significantly lower Cantabro loss than PMA.

Table C-10. Results of Fitting the ANOVA to Cantabro Loss Data with Gradation, Binder, and MIST Conditioning as Factors

Summary of Fit

RSquare	0.828361
RSquare Adj	0.768948
Root Mean Square Error	2.003752
Mean of Response	8.733333
Observations (or Sum Wgts)	36

Analysis of Variance

Source	DF	Sum of Squares	Mean Square	F Ratio
Model	9	503.80944	55.9788	13.9423
Error	26	104.39056	4.0150	**Prob > F**
C. Total	35	608.20000		<.0001*

Lack of Fit

Source	DF	Sum of Squares	Mean Square	F Ratio
Lack Of Fit	2	9.14389	4.57194	1.1520
Pure Error	24	95.24667	3.96861	**Prob > F**
Total Error	26	104.39056		0.3329
				Max RSq

Effect Tests

Source	Nparm	DF	Sum of Squares	F Ratio	Prob > F
Gradation	2	2	189.27167	23.5704	<.0001*
Binder	1	1	268.96000	66.9884	<.0001*
Conditioning	1	1	1.96000	0.4882	0.4909
Gradation*Binder	2	2	15.08167	1.8782	0.1730
Gradation*Conditioning	2	2	26.38500	3.2858	0.0534
Binder*Conditioning	1	1	2.15111	0.5358	0.4707

Table C-11. Effect Details and Tukey's HSD for Cantabro Loss Data with Gradation, Binder, and MIST Conditioning as Factors

Gradation

Least Squares Means Table

Level	Least Sq Mean	Std Error	Mean
A	5.491667	0.57843333	5.4917
B	10.283333	0.57843333	10.2833
C	10.425000	0.57843333	10.4250

LSMeans Differences Tukey HSD

α=0.050

Level [a]			Least Sq Mean
C	A		10.425000
B	A		10.283333
A		B	5.491667

[a] Levels not connected by same letter are significantly different.

Binder

Least Squares Means Table

Level	Least Sq Mean	Std Error	Mean
ARB	6.000000	0.47228883	6.0000
PMA	11.466667	0.47228883	11.4667

Researchers noted that the more extreme observation highlighted in red in Figure C-5 could be considered an outlier. To examine its effect, that observation was removed from the data and the ANOVA model was refitted. Table C-12 shows the result of fitting the ANOVA after excluding that observation. The effect tests in Table C-12 show that Gradation*Binder and Gradation*Conditioning were then statistically significant two-way interactions at α=0.05.

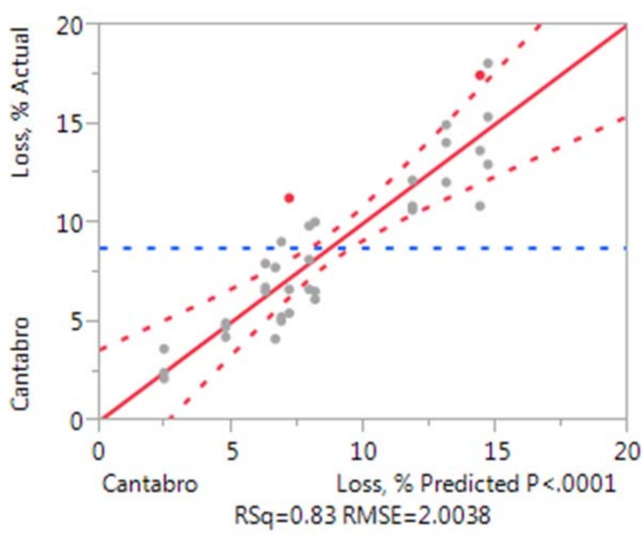

Figure C-5. Actual vs. predicted Cantabro loss plot.

Table C-12. Results of Fitting the ANOVA to Cantabro Loss Data after Excluding the Outlier with Gradation, Binder, and MIST Conditioning as Factors

Summary of Fit

RSquare	0.862821
RSquare Adj	0.813436
Root Mean Square Error	1.817403
Mean of Response	8.662857
Observations (or Sum Wgts)	35

Analysis of Variance

Source	DF	Sum of Squares	Mean Square	F Ratio
Model	9	519.36784	57.7075	17.4715
Error	25	82.57388	3.3030	**Prob > F**
C. Total	34	601.94171		<.0001*

Lack Of Fit

Source	DF	Sum of Squares	Mean Square	F Ratio
Lack Of Fit	2	5.353878	2.67694	0.7973
Pure Error	23	77.220000	3.35739	**Prob > F**
Total Error	25	82.573878		0.4626
				Max RSq

Effect Tests

Source	Nparm	DF	Sum of Squares	F Ratio	Prob > F
Gradation	2	2	169.88354	25.7169	<.0001*
Binder	1	1	288.73938	87.4185	<.0001*
Conditioning	1	1	0.22556	0.0683	0.7960
Gradation*Binder	2	2	22.51723	3.4086	0.0491*
Gradation*Conditioning	2	2	26.11771	3.9537	0.0322*
Binder*Conditioning	1	1	5.46696	1.6552	0.2100

From the LSM and the Tukey's HSD results shown in Table C-13 as well as the LSM plots shown in Figure C-6, it can be observed that for Gradation*Binder, PMA led to higher predicted Cantabro loss than ARB, and the effect was stronger when Gradation=B or C. For Gradation*Conditioning, significantly lower Cantabro loss occurred when Conditioning=No MIST and Gradation=A.

Table C-13. Effect Details and Tukey's HSD Test for Cantabro Loss Data after Excluding the Outlier with Gradation, Binder, and MIST Conditioning as Factors

Gradation

Least Squares Means Table

Level	Least Sq Mean	Std Error	Mean
A	5.491667	0.52463917	5.4917
B	10.283333	0.52463917	10.2833
C	9.966987	0.55408072	10.3545

LSMeans Differences Tukey HSD

α=0.050

Level [a]			Least Sq Mean
B	A		10.283333
C	A		9.966987
A		B	5.491667

[a] Levels not connected by same letter are significantly different.

Binder

Least Squares Means Table

Level	Least Sq Mean	Std Error	Mean
ARB	5.694658	0.44453650	5.6941
PMA	11.466667	0.42836609	11.4667

Conditioning

Least Squares Means Table

Level	Least Sq Mean	Std Error	Mean
MIST	8.5000000	0.42836609	8.50000
No MIST	8.6613248	0.44453650	8.83529

Gradation*Binder

Least Squares Means Table

Level	Least Sq Mean	Std Error
A,ARB	3.650000	0.74195183
A,PMA	7.333333	0.74195183
B,ARB	7.283333	0.74195183
B,PMA	13.283333	0.74195183
C,ARB	6.150641	0.82312165
C,PMA	13.783333	0.74195183

LSMeans Differences Tukey HSD

α=0.050

Level [a]				Least Sq Mean
C,PMA	A			13.783333
B,PMA	A			13.283333
A,PMA		B		7.333333
B,ARB		B		7.283333
C,ARB		B	C	6.150641
A,ARB			C	3.650000

[a] Levels not connected by same letter are significantly different.

Gradation*Conditioning

Least Squares Means Table

Level	Least Sq Mean	Std Error
A,MIST	6.383333	0.74195183
A,No MIST	4.600000	0.74195183
B,MIST	9.100000	0.74195183
B,No MIST	11.466667	0.74195183
C,MIST	10.016667	0.74195183
C,No MIST	9.917308	0.82312165

LSMeans Differences Tukey HSD

α=0.050

Level [a]				Least Sq Mean
B,No MIST	A			11.466667
C,MIST	A			10.016667
C,No MIST	A			9.917308
B,MIST	A	B		9.100000
A,MIST		B	C	6.383333
A,No MIST			C	4.600000

[a] Levels not connected by same letter are significantly different.

Binder*Conditioning

Least Squares Means Table

Level	Least Sq Mean	Std Error
ARB,MIST	6.011111	0.60580113
ARB,No MIST	5.378205	0.65073480
PMA,MIST	10.988889	0.60580113
PMA,No MIST	11.944444	0.60580113

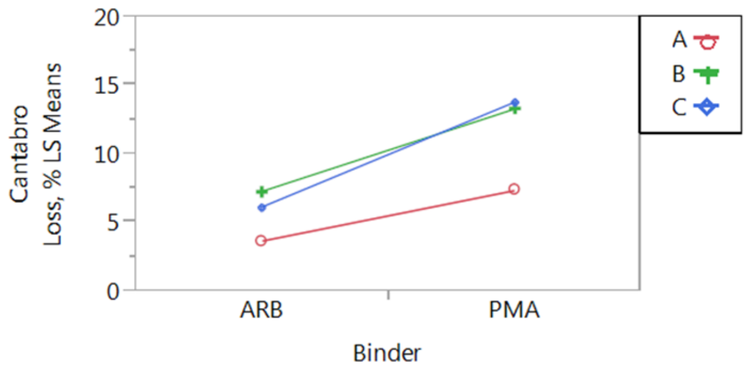

(a)

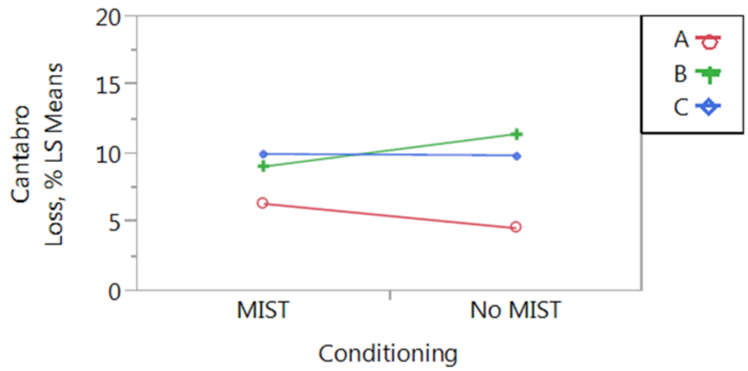

(b)

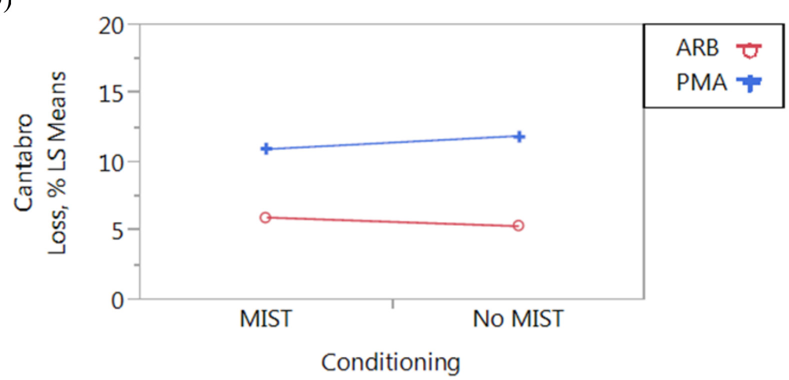

(c)

Figure C-6. LSM plot for Cantabro loss data after excluding outlier: (a) gradation*binder, (b) gradation*conditioning, (c) binder*conditioning.

The ANOVA using mixture (instead of gradation and binder separately) and conditioning as main factors and their two-way interaction is detailed next. The dataset considered was the one after excluding the outlier. The results showed that the two-way interaction between Mixture*Conditioning was not significant, and that conditioning as a main effect was not significant either (Table C-14). The effect of mixture on Cantabro loss was statistically significant at α=0.05 (Table C-14), especially between mixtures 2 and 5, as shown in Table C-15, Table C-16, and Figure C-7.

Table C-14. Results of Fitting the ANOVA to Cantabro Loss Data with Mixture and MIST Conditioning as Factors

Summary of Fit

RSquare	0.871715
RSquare Adj	0.810362
Root Mean Square Error	1.832319
Mean of Response	8.662857
Observations (or Sum Wgts)	35

Analysis of Variance

Source	DF	Sum of Squares	Mean Square	F Ratio
Model	11	524.72171	47.7020	14.2080
Error	23	77.22000	3.3574	**Prob > F**
C. Total	34	601.94171		<.0001*

Effect Tests

Source	Nparm	DF	Sum of Squares	F Ratio	Prob > F
Mixture	5	5	487.31793	29.0296	<.0001*
Conditioning	1	1	0.27307	0.0813	0.7781
Mixture*Conditioning	5	5	36.82529	2.1937	0.0900

Table C-15. Effect Details for Cantabro Loss Data with Mixture and MIST Conditioning as Factors

Mixture

Least Squares Means Table

Level	Least Sq Mean	Std Error	Mean
1	7.333333	0.74804092	7.3333
2	3.650000	0.74804092	3.6500
3	13.283333	0.74804092	13.2833
4	7.283333	0.74804092	7.2833
5	13.783333	0.74804092	13.7833
6	6.200000	0.83633517	6.2400

Conditioning

Least Squares Means Table

Level	Least Sq Mean	Std Error	Mean
MIST	8.5000000	0.43188163	8.50000
No MIST	8.6777778	0.44951665	8.83529

Mixture*Conditioning

Least Squares Means Table

Level	Least Sq Mean	Std Error
1,MIST	8.166667	1.0578896
1,No MIST	6.500000	1.0578896
2,MIST	4.600000	1.0578896
2,No MIST	2.700000	1.0578896
3,MIST	11.166667	1.0578896
3,No MIST	15.400000	1.0578896
4,MIST	7.033333	1.0578896
4,No MIST	7.533333	1.0578896
5,MIST	13.633333	1.0578896
5,No MIST	13.933333	1.0578896
6,MIST	6.400000	1.0578896
6,No MIST	6.000000	1.2956449

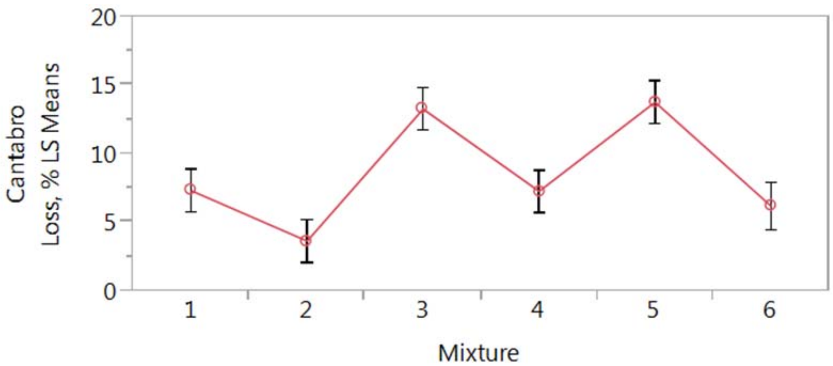

(a)

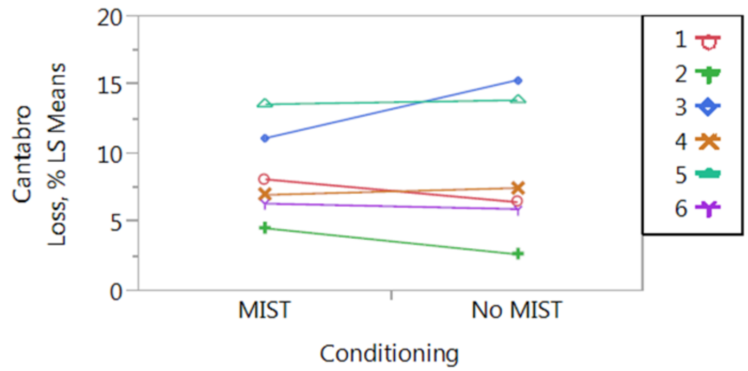

(b)

Figure C-7. LSM plot for Cantabro loss data: (a) mixture, (b) mixture*conditioning.

Table C-16. Tukey's Multiple Comparison Test for Cantabro Loss Data with Mixture as a Factor

Level [a]				**Least Sq Mean**
5	A			13.783333
3	A			13.283333
1		B		7.333333
4		B		7.283333
6		B	C	6.200000
2			C	3.650000

[a] Levels not connected by same letter are significantly different.

C.2.2. AASHTO T 283 Moisture Conditioning

The same factors of interest included in the MIST conditioning analysis were used, with the exception of conditioning, which in this case had two levels (T283, no T283). There were 30 IDT strength measurements obtained at each factor-level combination. The ANOVA with gradation, binder, and conditioning as main effects along with all possible two-way interaction effects among them was fitted to the Cantabro loss data. Table C-17 contains the analysis outputs obtained by the JMP statistical package (SAS product). It can be observed from the effect tests that the main effects of gradation, binder, and conditioning as well as the two-way interaction effect of Binder*Conditioning were statistically significant at α=0.05.

Table C-17. Results of Fitting ANOVA to Cantabro Loss Data with Gradation, Binder, and AASHTO T 283 Conditioning as Factors

Summary of Fit

RSquare	0.830489
RSquare Adj	0.754209
Root Mean Square Error	2.234947
Mean of Response	9.716667
Observations (or Sum Wgts)	30

Analysis of Variance

Source	DF	Sum of Squares	Mean Square	F Ratio
Model	9	489.44189	54.3824	10.8874
Error	20	99.89978	4.9950	**Prob > F**
C. Total	29	589.34167		<.0001*

Lack Of Fit

Source	DF	Sum of Squares	Mean Square	F Ratio
Lack Of Fit	2	15.444778	7.72239	1.6459
Pure Error	18	84.455000	4.69194	**Prob > F**
Total Error	20	99.899778		0.2206
				Max RSq

Effect Tests

Source	Nparm	DF	Sum of Squares	F Ratio	Prob > F
Gradation	2	2	286.87033	28.7158	<.0001*
Binder	1	1	63.48672	12.7101	0.0019*
Conditioning	1	1	25.31250	5.0676	0.0358*
Gradation*Binder	2	2	2.66467	0.2667	0.7686
Gradation*Conditioning	2	2	6.23033	0.6237	0.5461
Binder*Conditioning	1	1	64.20139	12.8532	0.0019*

Table C-18 presents the predicted values for Cantabro loss for each factor (see LSM). Tukey's HSD tests were also carried out (when the effects were significant) to determine which specific factor levels were statistically different, and the results are included in Table C-18. From these results and the interaction plots in Figure C-8, it can be seen that Conditioning=No T283 led to a significantly lower Cantabro loss than Conditioning=T283 when Binder=ARB, while there was no statistically significant difference in Cantabro loss for different levels of conditioning when Binder=PMA. Also, for gradation, Gradation A led to a significantly lower Cantabro loss than B or C.

.

Table C-18. Effect Details and Tukey's HSD for Cantabro Loss Data with Gradation, Binder, and AASHTO T 283 Conditioning as Factors

Gradation

Least Squares Means Table

Level	Least Sq Mean	Std Error	Mean
A	5.450000	0.72132610	5.2800
B	11.883333	0.72132610	11.8000
C	12.379167	0.72132610	12.0700

LSMeans Differences Tukey HSD

Level [a]			Least Sq Mean
C	A		12.379167
B	A		11.883333
A		B	5.450000

[a] Levels not connected by same letter are significantly different.

Binder

Least Squares Means Table

Level	Least Sq Mean	Std Error	Mean
ARB	8.419444	0.58896029	7.9333
PMA	11.388889	0.58896029	11.5000

Conditioning

Least Squares Means Table

Level	Least Sq Mean	Std Error	Mean
No T283	8.966667	0.52678210	8.9667
T283	10.841667	0.64517368	10.8417

Gradation*Binder

Least Squares Means Table

Level	Least Sq Mean	Std Error
A,ARB	4.228611	1.0132856
A,PMA	6.671389	1.0132856
B,ARB	9.981944	1.0132856
B,PMA	13.784722	1.0132856
C,ARB	11.047778	1.0132856
C,PMA	13.710556	1.0132856

Gradation*Conditioning

Least Squares Means Table

Level	Least Sq Mean	Std Error
A,No T283	4.600000	0.9124134
A,T283	6.300000	1.1174736
B,No T283	11.466667	0.9124134
B,T283	12.300000	1.1174736
C,No T283	10.833333	0.9124134
C,T283	13.925000	1.1174736

Binder*Conditioning

Least Squares Means Table

Level	Least Sq Mean	Std Error
ARB,No T283	5.988889	0.74498239
ARB,T283	10.850000	0.91241336
PMA,No T283	11.944444	0.74498239
PMA,T283	10.833333	0.91241336

LSMeans Differences Tukey HSD

Level [a]			Least Sq Mean
PMA,No T283	A		11.944444
ARB,T283	A		10.850000
PMA,T283	A		10.833333
ARB,No T283		B	5.988889

[a] Levels not connected by same letter are significantly different.

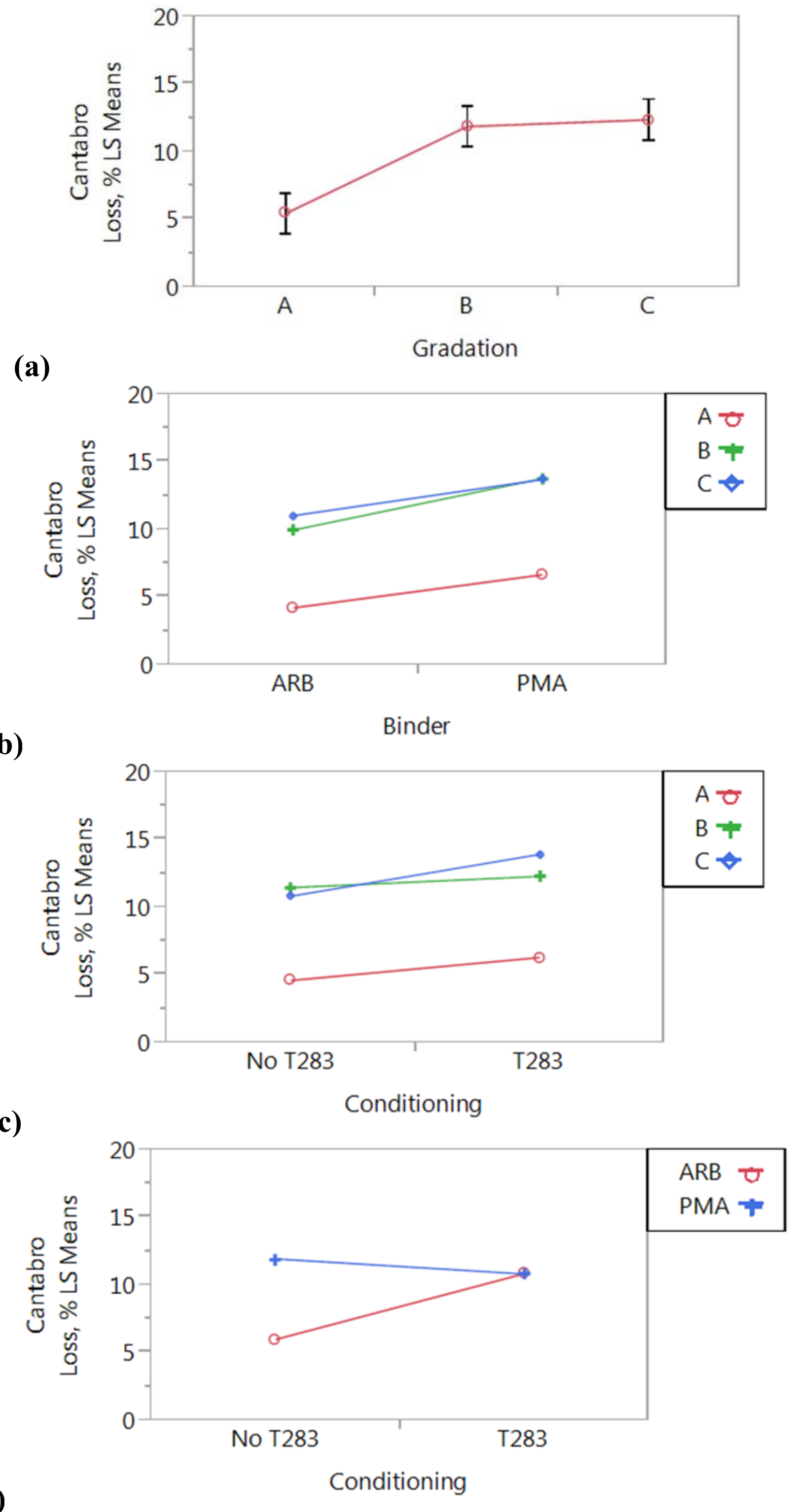

Figure C-8. LSM plot for Cantabro loss data with AASHTO T 283 conditioning: (a) gradation, (b) gradation*binder, (c) gradation*conditioning, (d) binder*conditioning.

C.3. IDT Strength

C.3.1. MIST Moisture Conditioning

The objective of this analysis was to assess the effects of aggregate gradation, binder, and moisture conditioning on IDT strength. The factors of interest and their levels were gradation with three levels (A: limestone with fines; B: coarser limestone; C: coarser granite), binder with two levels (PMA, ARB), and conditioning with two levels (no MIST, MIST). Other extraneous factors that could potentially affect IDT strength such as AV content, specimen height, and specimen diameter were controlled throughout the experiment.

There were 36 IDT strength measurements obtained at each factor-level combination with three replications. The ANOVA having gradation, binder, and conditioning as main effects along with all possible two-way interaction effects among them was fitted to the IDT strength data. Table C-19 contains the analysis outputs obtained by the JMP statistical package (SAS product). It can be observed from Table C-19 (see Effect Tests) that the two-way interactions Gradation*Conditioning and Binder*Conditioning were statistically significant at α=0.05, while the Gradation*Binder interaction effect was not statistically significant.

Table C-19. Results of Fitting the ANOVA to IDT Strength Data with Gradation, Binder, and MIST Conditioning as Factors

Summary of Fit

RSquare	0.836116
RSquare Adj	0.779387
Root Mean Square Error	64.96535
Mean of Response	700.8292
Observations (or Sum Wgts)	36

Analysis of Variance

Source	DF	Sum of Squares	Mean Square	F Ratio
Model	9	559844.98	62205.0	14.7388
Error	26	109732.92	4220.5	**Prob > F**
C. Total	35	669577.89		<.0001*

Lack Of Fit

Source	DF	Sum of Squares	Mean Square	F Ratio
Lack Of Fit	2	23434.94	11717.5	3.2587
Pure Error	24	86297.98	3595.7	**Prob > F**
Total Error	26	109732.92		0.0560
				Max RSq

Effect Tests

Source	Nparm	DF	Sum of Squares	F Ratio	Prob > F
Gradation	2	2	221645.88	26.2583	<.0001*
Binder	1	1	153976.45	36.4830	<.0001*
Conditioning	1	1	68362.20	16.1977	0.0004*
Gradation*Binder	2	2	3085.62	0.3656	0.6973
Gradation*Conditioning	2	2	91835.29	10.8797	0.0004*
Binder*Conditioning	1	1	20939.54	4.9614	0.0348*

Table C-20 presents the LSM for each factor and Tukey's HSD results for the statistically significant interaction factors. Figure C-9 illustrates the interaction plots for all two-way interactions. It can be seen from the interaction plot for Gradation*Conditioning that the effect of conditioning was much stronger when Gradation=C as compared to A or B. Tukey's HSD test indicated that for Gradation=C, the predicted IDT strength was significantly higher when Conditioning=MIST than Conditioning=No MIST, while for the other two gradation levels, the level of conditioning did not seem to matter. Likewise, from the interaction plot for Binder*Conditioning and the corresponding Tukey's HSD test, it can be observed that only for Binder=PMA, the level of conditioning mattered (the predicted IDT strength was higher when Conditioning=MIST).

Table C-20. Effect Details and Tukey's HSD for IDT Strength Data with Gradation, Binder, and MIST Conditioning as Factors

Gradation

Least Squares Means Table

Level	Least Sq Mean	Std Error	Mean
A	659.15667	18.753881	659.157
B	810.73167	18.753881	810.732
C	632.59917	18.753881	632.599

Binder

Least Squares Means Table

Level	Least Sq Mean	Std Error	Mean
ARB	635.42944	15.312480	635.429
PMA	766.22889	15.312480	766.229

Conditioning

Least Squares Means Table

Level	Least Sq Mean	Std Error	Mean
MIST	744.40611	15.312480	744.406
No MIST	657.25222	15.312480	657.252

Gradation*Binder

Least Squares Means Table

Level	Least Sq Mean	Std Error
A,ARB	605.32000	26.521994
A,PMA	712.99333	26.521994
B,ARB	734.23167	26.521994
B,PMA	887.23167	26.521994
C,ARB	566.73667	26.521994
C,PMA	698.46167	26.521994

Gradation*Conditioning

Least Squares Means Table

Level	Least Sq Mean	Std Error
A,MIST	668.25667	26.521994
A,No MIST	650.05667	26.521994
B,MIST	817.37167	26.521994
B,No MIST	804.09167	26.521994
C,MIST	747.59000	26.521994
C,No MIST	517.60833	26.521994

LSMeans Differences Tukey HSD

Level [a]				Least Sq Mean
B,MIST	A			817.37167
B,No MIST	A			804.09167
C,MIST	A	B		747.59000
A,MIST		B		668.25667
A,No MIST		B		650.05667
C,No MIST			C	517.60833

[a] Levels not connected by same letter are significantly different.

Binder*Conditioning

Least Squares Means Table

Level	Least Sq Mean	Std Error
ARB,MIST	654.88889	21.655117
ARB,No MIST	615.97000	21.655117
PMA,MIST	833.92333	21.655117
PMA,No MIST	698.53444	21.655117

LSMeans Differences Tukey HSD

Level [a]			Least Sq Mean
PMA,MIST	A		833.92333
PMA,No MIST		B	698.53444
ARB,MIST		B	654.88889
ARB,No MIST		B	615.97000

[a] Levels not connected by the same letter are significantly different.

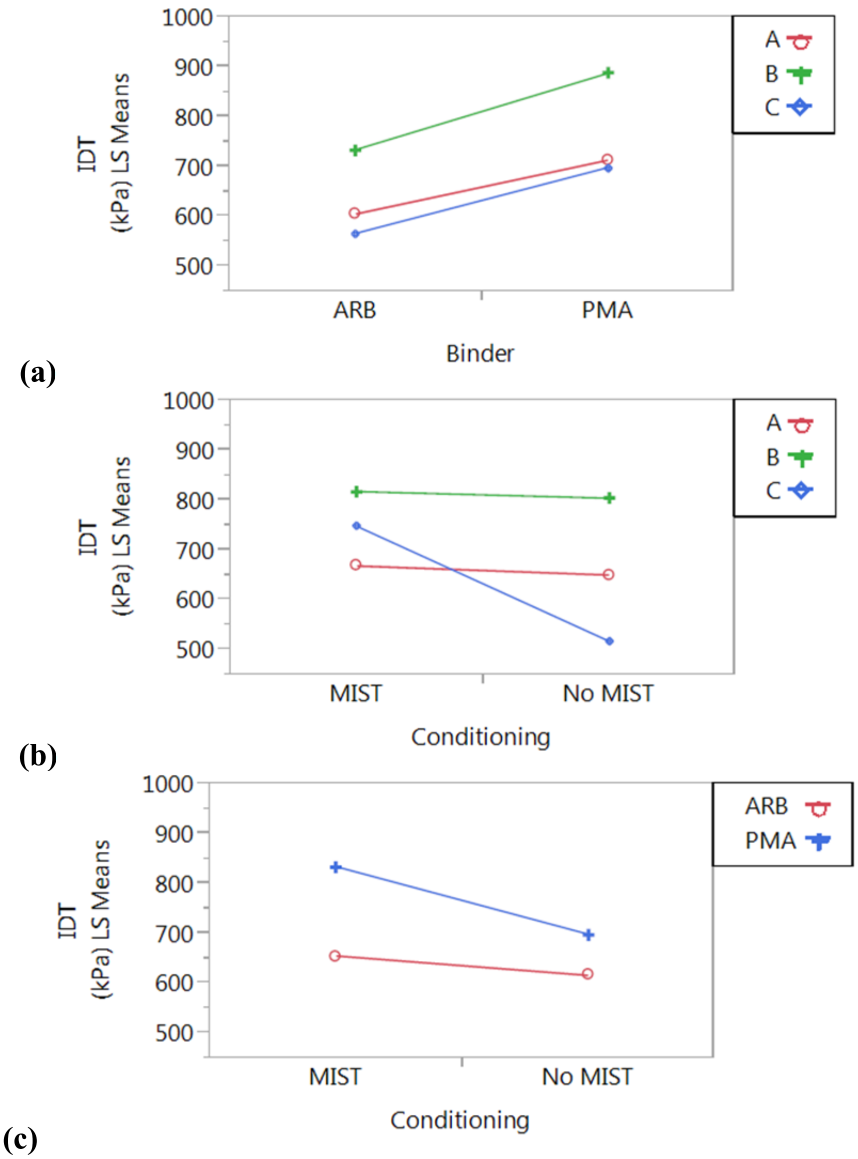

Figure C-9. LSM plot for IDT strength data: (a) gradation*binder, (b) gradation*conditioning, (c) binder*conditioning.

Researchers identified two observations, highlighted in red in the actual vs. predicted plot shown in Figure C-10, that could be considered outliers. To examine their effect, these two observations were removed from the data and the ANOVA model was refitted. Table C-21 shows the result of fitting the ANOVA after excluding these two data points. It can be observed from the effect tests that Gradation*Binder became a statistically significant two-way interaction at $\alpha=0.05$ (along with the other two-way interactions).

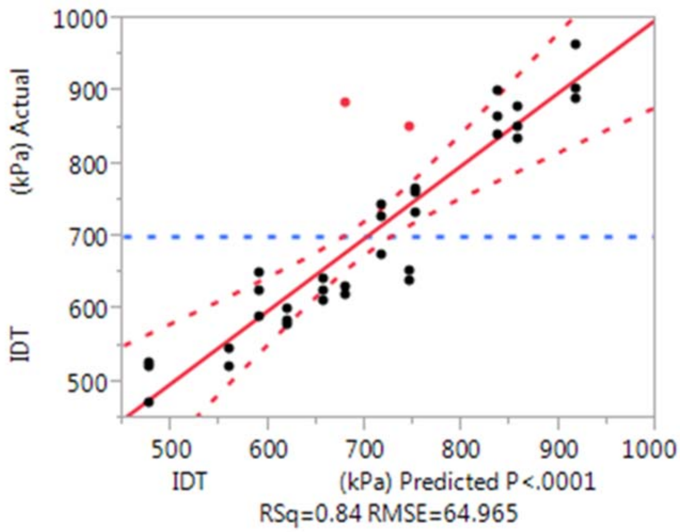

Figure C-10. Actual vs. predicted IDT strength plot.

Table C-21. Results of Fitting the ANOVA to IDT Strength Data after Excluding Outliers with Gradation, Binder, and Conditioning as Factors

Summary of Fit

RSquare	0.947612
RSquare Adj	0.927967
Root Mean Square Error	36.50093
Mean of Response	691.0376
Observations (or Sum Wgts)	34

Analysis of Variance

Source	DF	Sum of Squares	Mean Square	F Ratio
Model	9	578387.24	64265.2	48.2357
Error	24	31975.64	1332.3	**Prob > F**
C. Total	33	610362.88		<.0001*

Lack Of Fit

Source	DF	Sum of Squares	Mean Square	F Ratio
Lack Of Fit	2	18034.398	9017.20	14.2296
Pure Error	22	13941.240	633.69	**Prob > F**
Total Error	24	31975.638		0.0001*
				Max RSq

Effect Tests

Source	Nparm	DF	Sum of Squares	F Ratio	Prob > F
Gradation	2	2	260450.01	97.7432	<.0001*
Binder	1	1	91739.21	68.8568	<.0001*
Conditioning	1	1	74613.14	56.0025	<.0001*
Gradation*Binder	2	2	22119.63	8.3012	0.0018*
Gradation*Conditioning	2	2	82249.85	30.8672	<.0001*
Binder*Conditioning	1	1	25714.17	19.3003	0.0002*

From the predicted values for IDT strength and the Tukey's HSD test results for Gradation*Binder shown in Table C-22 and the corresponding interaction plot shown in Figure C-11, it can be observed that PMA led to higher predicted IDT strength values than ARB for Gradation Levels B and C, but not for A. The effects of the other interaction effects were similar to those previously shown in Table C-20 and Figure C-9.

Table C-22. Effect Details and Tukey's HSD for IDT Strength Data after Excluding Outliers with Gradation, Binder, and MIST Conditioning as Factors

Gradation

Least Squares Means Table

Level	Least Sq Mean	Std Error	Mean
A	620.58375	11.780626	617.531
B	810.73167	10.536912	810.732
C	632.59917	10.536912	632.599

Binder

Least Squares Means Table

Level	Least Sq Mean	Std Error	Mean
ARB	635.42944	8.6033529	635.429
PMA	740.51361	9.2926832	753.597

Conditioning

Least Squares Means Table

Level	Least Sq Mean	Std Error	Mean
MIST	735.09508	8.9300190	738.145
No MIST	640.84798	8.9300190	643.931

Gradation*Binder

Least Squares Means Table

Level	Least Sq Mean	Std Error
A,ARB	605.32000	14.901444
A,PMA	635.84750	18.250467
B,ARB	734.23167	14.901444
B,PMA	887.23167	14.901444
C,ARB	566.73667	14.901444
C,PMA	698.46167	14.901444

LSMeans Differences Tukey HSD

Level [a]					Least Sq Mean
B,PMA	A				887.23167
B,ARB		B			734.23167
C,PMA		B	C		698.46167
A,PMA			C	D	635.84750
A,ARB				D	605.32000
C,ARB				D	566.73667

[a] Levels not connected by same letter are significantly different.

Gradation*Conditioning

Least Squares Means Table

Level	Least Sq Mean	Std Error
A,MIST	640.32357	16.540891
A,No MIST	600.84393	16.540891
B,MIST	817.37167	14.901444
B,No MIST	804.09167	14.901444
C,MIST	747.59000	14.901444
C,No MIST	517.60833	14.901444

LSMeans Differences Tukey HSD

Level [a]					Least Sq Mean
B,MIST	A				817.37167
B,No MIST	A	B			804.09167
C,MIST		B			747.59000
A,MIST			C		640.32357
A,No MIST			C		600.84393
C,No MIST				D	517.60833

[a] Levels not connected by same letter are significantly different.

Binder*Conditioning

Least Squares Means Table

Level	Least Sq Mean	Std Error
ARB,MIST	654.88889	12.166978
ARB,No MIST	615.97000	12.166978
PMA,MIST	815.30127	13.074616
PMA,No MIST	665.72595	13.074616

LSMeans Differences Tukey HSD

Level [a]				Least Sq Mean
PMA,MIST	A			815.30127
PMA,No MIST		B		665.72595
ARB,MIST		B	C	654.88889
ARB,No MIST			C	615.97000

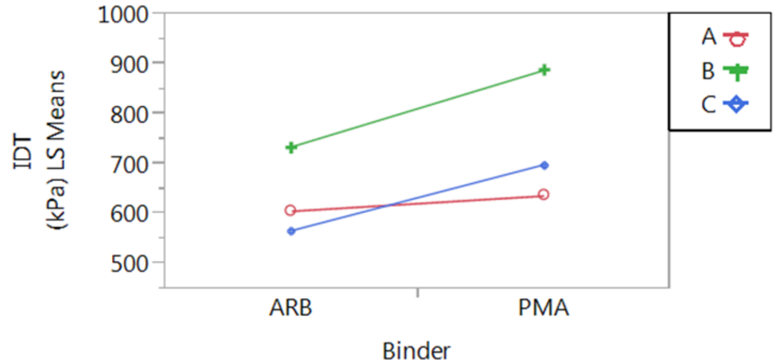

(a)

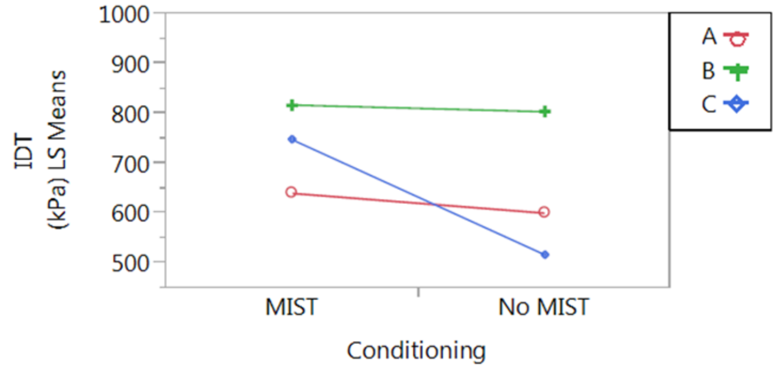

(b)

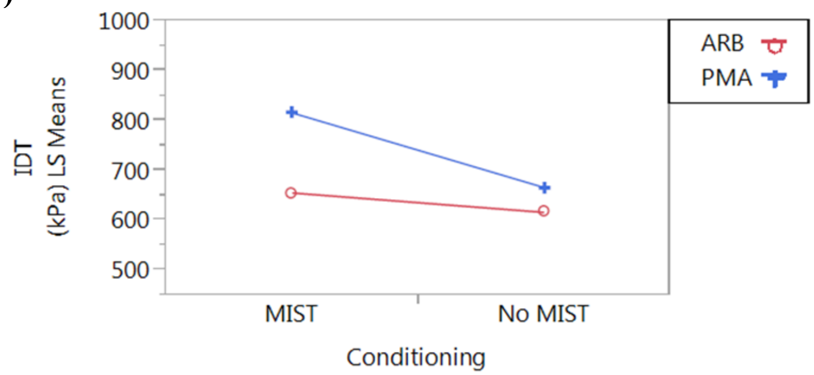

(c)

Figure C-11. LSM plot for IDT strength data after excluding outliers: (a) gradation*binder, (b) gradation*conditioning, (c) binder*conditioning.

The ANOVA using mixture (instead of gradation and binder separately) and conditioning as main factors and their two-way interaction is detailed next. The dataset considered was the one after excluding the outliers. The results showed that the main effects and the two-way interaction between them (i.e., Mixture*Conditioning) were all significant, as shown in Table C-23. The most pronounced difference was between mixtures 3 and 6, as detailed in Table C-24 and Figure C-12.

Table C-23. Results of Fitting the ANOVA to IDT Strength Data with Mixture as a Factor

Summary of Fit

RSquare	0.977159
RSquare Adj	0.965739
Root Mean Square Error	25.17325
Mean of Response	691.0376
Observations (or Sum Wgts)	34

Analysis of Variance

Source	DF	Sum of Squares	Mean Square	F Ratio
Model	11	596421.64	54220.1	85.5622
Error	22	13941.24	633.7	**Prob > F**
C. Total	33	610362.88		<.0001*

Effect Tests

Source	Nparm	DF	Sum of Squares	F Ratio	Prob > F
Mixture	5	5	391450.90	123.5460	<.0001*
Conditioning	1	1	67445.67	106.4328	<.0001*
Mixture*Conditioning	5	5	129522.19	40.8785	<.0001*

Table C-24. Effect Details and Tukey's HSD for IDT Strength Data with Mixture as a Factor

Mixture

Least Squares Means Table

Level	Least Sq Mean	Std Error	Mean
1	635.84750	12.586627	635.848
2	605.32000	10.276938	605.320
3	887.23167	10.276938	887.232
4	734.23167	10.276938	734.232
5	698.46167	10.276938	698.462
6	566.73667	10.276938	566.737

Conditioning

Least Squares Means Table

Level	Least Sq Mean	Std Error	Mean
MIST	733.02278	6.1756711	738.145
No MIST	642.92028	6.1756711	643.931

Mixture*Conditioning

Least Squares Means Table

Level	Least Sq Mean	Std Error
1,MIST	645.95000	17.800179
1,No MIST	625.74500	17.800179
2,MIST	622.26333	14.533785
2,No MIST	588.37667	14.533785
3,MIST	919.46667	14.533785
3,No MIST	854.99667	14.533785
4,MIST	715.27667	14.533785
4,No MIST	753.18667	14.533785
5,MIST	868.05333	14.533785
5,No MIST	528.87000	14.533785
6,MIST	627.12667	14.533785
6,No MIST	506.34667	14.533785

LSMeans Differences Tukey HSD

Level [a]							Least Sq Mean
3,MIST	A						919.46667
5,MIST	A						868.05333
3,No MIST	A						854.99667
4,No MIST		B					753.18667
4,MIST		B	C				715.27667
1,MIST			C	D			645.95000
6,MIST				D			627.12667
1,No MIST				D			625.74500
2,MIST				D			622.26333
2,No MIST				D	E		588.37667
5,No MIST					E	F	528.87000
6,No MIST						F	506.34667

[a] Levels not connected by same letter are significantly different.

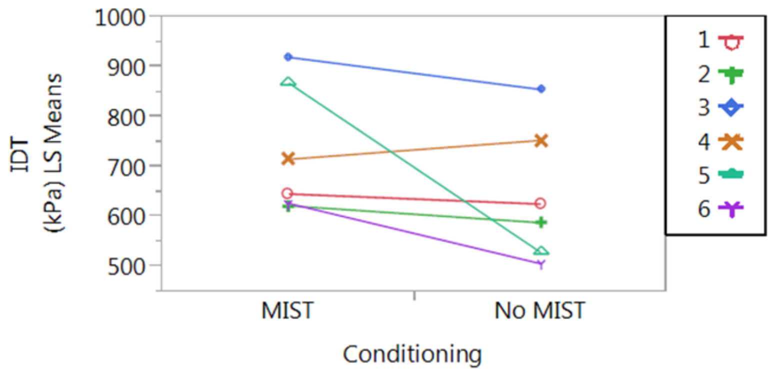

Figure C-12. LSM plot for mixture*conditioning IDT strength data.

C.3.2. AASHTO T 283 Moisture Conditioning

The same factors of interest included in the MIST conditioning analysis were used, with the exception of conditioning, which in this case had two levels (T283, no T283). There were 30 IDT strength measurements obtained at each factor-level combination. The ANOVA with gradation, binder, and conditioning as main effects along with all possible two-way interaction effects among them was fitted to the IDT strength data. Table C-25 details the outputs obtained by the JMP statistical package (SAS product). From the effect tests, it can be observed that Gradation*Conditioning was a significant interaction effect at α=0.05, as were the main effects of binder and gradation.

Table C-25. Results of Fitting the ANOVA to IDT Strength Data with Gradation, Binder, and AASHTO T 283 Conditioning as Factors

Summary of Fit

RSquare	0.777442
RSquare Adj	0.67729
Root Mean Square Error	72.25008
Mean of Response	637.8957
Observations (or Sum Wgts)	30

Analysis of Variance

Source	DF	Sum of Squares	Mean Square	F Ratio
Model	9	364695.41	40521.7	7.7627
Error	20	104401.49	5220.1	**Prob > F**
C. Total	29	469096.89		<.0001*

Lack Of Fit

Source	DF	Sum of Squares	Mean Square	F Ratio
Lack Of Fit	2	45516.57	22758.3	6.9568
Pure Error	18	58884.92	3271.4	**Prob > F**
Total Error	20	104401.49		0.0058*
				Max RSq

Effect Tests

Source	Nparm	DF	Sum of Squares	F Ratio	Prob > F
Gradation	2	2	137447.94	13.1653	0.0002*
Binder	1	1	78833.68	15.1020	0.0009*
Conditioning	1	1	16860.43	3.2299	0.0874
Gradation*Binder	2	2	14670.00	1.4052	0.2685
Gradation*Conditioning	2	2	69064.15	6.6152	0.0062*
Binder*Conditioning	1	1	3508.16	0.6721	0.4220

Table C-26 presents the predicted values for IDT strength for each factor (see LSM) and Tukey's HSD test results to determine which of those factor levels were statistically different. Figure C-13 illustrates the interaction plot for the two-way interactions. The predicted IDT strength was statistically higher when Binder=PMA as compared to Binder=ARB. The interaction plot also showed that the effect of conditioning was stronger when Gradation=B as compared to A or C. Tukey's HSD indicated that for Gradation=B, the predicted IDT strength was significantly higher when Conditioning=No T283 as compared to Conditioning=T283, while for the other two gradation levels, the level of conditioning was not statistically different.

Table C-26. Effect Details and Tukey's HSD for IDT Strength Data with Gradation, Binder, and AASHTO T 283 Conditioning as Factors

Gradation

Least Squares Means Table

Level	Least Sq Mean	Std Error	Mean
A	639.43333	23.318614	641.558
B	714.29708	23.318614	732.256
C	545.43917	23.318614	539.873

Binder

Least Squares Means Table

Level	Least Sq Mean	Std Error	Mean
ARB	580.73750	19.039568	587.784
PMA	685.37556	19.039568	688.007

Conditioning

Least Squares Means Table

Level	Least Sq Mean	Std Error	Mean
No T283	657.25222	17.029508	657.252
T283	608.86083	20.856802	608.861

Gradation*Binder

Least Squares Means Table

Level	Least Sq Mean	Std Error
A,ARB	564.94197	32.756912
A,PMA	713.92469	32.756912
B,ARB	692.16372	32.756912
B,PMA	736.43044	32.756912
C,ARB	485.10681	32.756912
C,PMA	605.77153	32.756912

Gradation*Conditioning

Least Squares Means Table

Level	Least Sq Mean	Std Error
A,No T283	650.05667	29.495973
A,T283	628.81000	36.125041
B,No T283	804.09167	29.495973
B,T283	624.50250	36.125041
C,No T283	517.60833	29.495973
C,T283	573.27000	36.125041

LSMeans Differences Tukey HSD

Level [a]				Least Sq Mean
B,No T283	A			804.09167
A,No T283		B		650.05667
A,T283		B	C	628.81000
B,T283		B	C	624.50250
C,T283		B	C	573.27000
C,No T283			C	517.60833

[a] Levels not connected by same letter are significantly different.

Binder*Conditioning

Least Squares Means Table

Level	Least Sq Mean	Std Error
ARB,No T283	615.97000	24.083361
ARB,T283	545.50500	29.495973
PMA,No T283	698.53444	24.083361
PMA,T283	672.21667	29.495973

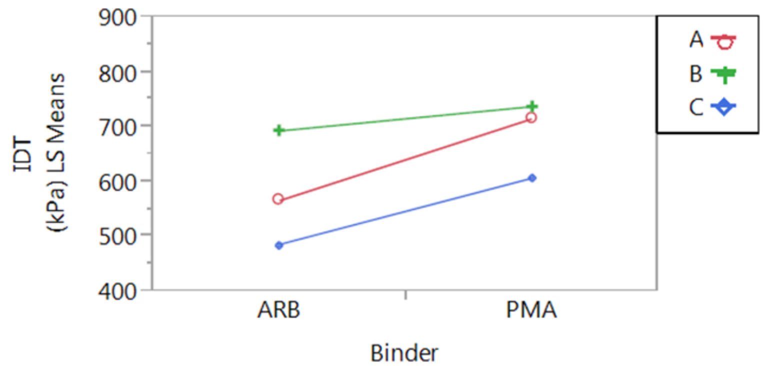

(a)

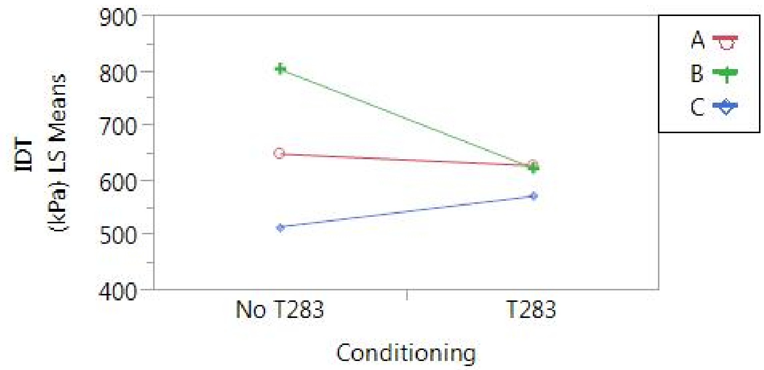

(b)

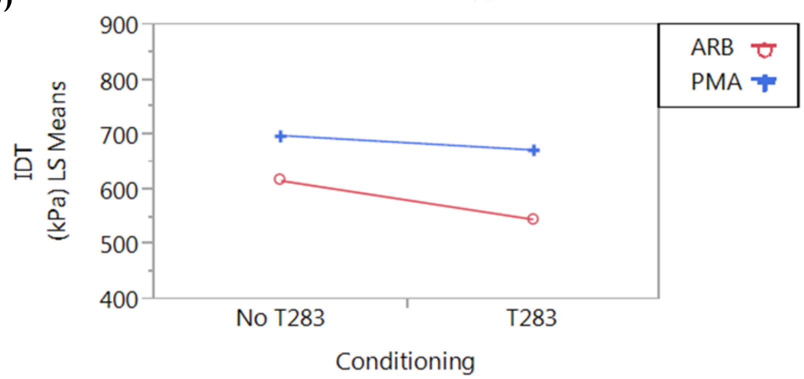

(c)

Figure C-13. LSM plot for IDT strength data with AASHTO T 283 conditioning: (a) gradation*binder, (b) gradation*conditioning, (c) binder*conditioning.

C.4. Hamburg Wheel Tracking Test

The objective of this analysis was to assess the effect of aggregate gradation and binder on rut depth measured by the HWTT test. The factors of interest and their levels were gradation with three levels (A: limestone with fines; B: coarser limestone; C: coarser granite) and binder with two levels (PMA, ARB). Another factor considered in the experiment was wheel with two levels (left wheel [LW] or right wheel [RW]). Other extraneous factors that could possibly affect rut depth such as AV content, specimen height, and specimen diameter were controlled throughout the experiment.

There were 12 rut depth measurements obtained at each factor-level combination. An ANOVA with gradation, binder, and wheel as main effects and a two-way interaction effect, Gradation*Binder, was fitted to the rut depth data. Table C-27 contains the analysis outputs obtained by the JMP statistical package (SAS product). It can be observed from the effect tests in Table C-27 that only the main effects of gradation and wheel were statistically significant at α=0.05.

Table C-27. Results of Fitting the ANOVA to HWTT Data with Gradation, Binder, and Wheel as Factors

Summary of Fit

RSquare	0.901429
RSquare Adj	0.783145
Root Mean Square Error	0.89886
Mean of Response	4.865917
Observations (or Sum Wgts)	12

Analysis of Variance

Source	DF	Sum of Squares	Mean Square	F Ratio
Model	6	36.943533	6.15726	7.6208
Error	5	4.039748	0.80795	**Prob > F**
C. Total	11	40.983281		0.0208*

Effect Tests

Source	Nparm	DF	Sum of Squares	F Ratio	Prob > F
Gradation	2	2	10.004617	6.1914	0.0444*
Binder	1	1	2.109247	2.6106	0.1671
Gradation*Binder	2	2	0.726499	0.4496	0.6614
Wheel	1	1	24.103171	29.8325	0.0028*

Table C-28 presents the LSM values for rut depth for each factor. The Fisher's Least Significant Differences test (denoted as LSMeans Differences Student's t in Table C-28), employed to determine which levels of gradation were statistically different, suggested that the predicted rut depth for Gradation Level A was significantly higher than that for B or C, while there were not statistically significant differences between B and C. This conclusion was further confirmed by the interaction plot shown in Figure C-14. In addition, the predicted rut depth for RW was also significantly higher than that for LW.

Table C-28. Effect Details and Student's t-test for HWTT Data with Gradation, Binder, and Wheel as Factors

Gradation

Least Squares Means Table

Level	Least Sq Mean	Std Error	Mean
A	6.1570000	0.44943007	6.15700
B	4.2002500	0.44943007	4.20025
C	4.2405000	0.44943007	4.24050

LSMeans Differences Student's t

Level [a]			Least Sq Mean
A	A		6.1570000
C		B	4.2405000
B		B	4.2002500

[a] Levels not connected by same letter are significantly different.

Binder

Least Squares Means Table

Level	Least Sq Mean	Std Error	Mean
ARB	5.2851667	0.36695812	5.28517
PMA	4.4466667	0.36695812	4.44667

Gradation*Binder

Least Squares Means Table

Level	Least Sq Mean	Std Error
A,ARB	6.7985000	0.63559010
A,PMA	5.5155000	0.63559010
B,ARB	4.2765000	0.63559010
B,PMA	4.1240000	0.63559010
C,ARB	4.7805000	0.63559010
C,PMA	3.7005000	0.63559010

Wheel

Least Squares Means Table

Level	Least Sq Mean	Std Error	Mean
LW	3.4486667	0.36695812	3.44867
RW	6.2831667	0.36695812	6.28317

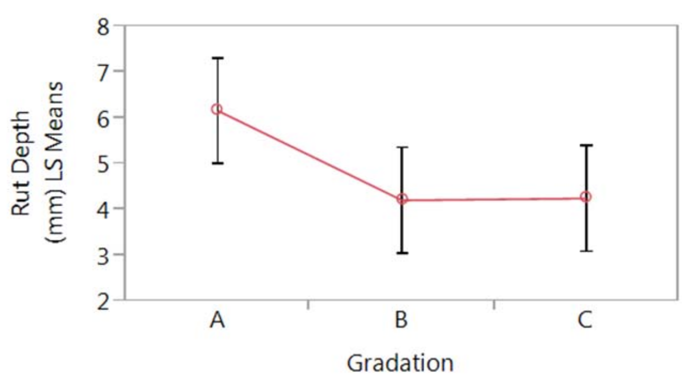

Figure C-14. LSM plot for HWTT data.

The ANOVA using mixture (instead of gradation and binder separately) and wheel as main factors is detailed next. The effect tests in Table C-29 show that only wheel was statistically significant; the LW had a lower recorded rut depth as compared to the RW (Table C-30). In addition, the mixture with the highest rut depth was mixture 1, and the one with the lowest was mixture 6, although the differences were not statistically significant (Table C-30).

Table C-29. Results of Fitting the ANOVA to HWTT Data with Mixture and Wheel as Factors

Summary of Fit

RSquare	0.901429
RSquare Adj	0.783145
Root Mean Square Error	0.89886
Mean of Response	4.865917
Observations (or Sum Wgts)	12

Analysis of Variance

Source	DF	Sum of Squares	Mean Square	F Ratio
Model	6	36.943533	6.15726	7.6208
Error	5	4.039748	0.80795	**Prob > F**
C. Total	11	40.983281		0.0208*

Effect Tests

Source	Nparm	DF	Sum of Squares	F Ratio	Prob > F
Mixture	5	5	12.840362	3.1785	0.1151
Wheel	1	1	24.103171	29.8325	0.0028*

Table C-30. Effect Details for HWTT Data with Mixture and Wheel as Factors

Mixture

Least Squares Means Table

Level	Least Sq Mean	Std Error	Mean
1	5.5155000	0.63559010	5.51550
2	6.7985000	0.63559010	6.79850
3	4.1240000	0.63559010	4.12400
4	4.2765000	0.63559010	4.27650
5	3.7005000	0.63559010	3.70050
6	4.7805000	0.63559010	4.78050

Wheel

Least Squares Means Table

Level	Least Sq Mean	Std Error	Mean
LW	3.4486667	0.36695812	3.44867
RW	6.2831667	0.36695812	6.28317

%